

Tesi di Dottorato di ALBERTO CUOCI
Matricola D02339

POLITECNICO DI MILANO



**DIPARTIMENTO
DI
CHIMICA,
MATERIALI
E
INGEGNERIA CHIMICA
"Giulio Natta"**

**Dottorato di Ricerca in
Chimica Industriale e
Ingegneria Chimica (CII)**

XX Ciclo
2005-2008

**POLLUTANT FORMATION IN
TURBULENT REACTIVE FLOWS:
INTERACTIONS BETWEEN
CHEMISTRY AND TURBULENCE**

Coordinatore: Prof. Renato Rota

Tutore: Prof. Eliseo Ranzi

Relatore: Prof. Tiziano Faravelli

Ai miei genitori

Acknowledgements

I wish to express my sincere gratitude to my supervisors Prof. Tiziano Faravelli and Prof. Eliseo Ranzi for their continuous and warm interest and constructive criticism on my work. Without their support and guidance, this work would not have been possible.

I would also like to thank my colleague and friend, Prof. Alessio Frassoldati, who has assisted and helped me in numerous ways.

I am indebted to Prof. Philip J. Smith and Prof. Adel F. Sarofim, for giving me the opportunity to spend one year of my Ph.D. at the University of Utah as a visiting scholar.

I cannot end without thanking my family, on whose constant encouragement and help I have relied throughout my time at the University.

Alberto

Publications

Publications on international journals

A. Cuoci, A. Frassoldati, G. Buzzi Ferraris, T. Faravelli, E. Ranzi, “*The ignition, combustion and flame structure of carbon monoxide/hydrogen mixtures. Note 2: Fluid dynamics and kinetic aspects of syngas combustion*”, International Journal of Hydrogen Energy, 32 (2007), pp. 3486-3500

A. Cuoci, A. Frassoldati, T. Faravelli, E. Ranzi, “*Frequency response of counter flow diffusion flames to strain rate harmonic oscillations*”, Combustion Science and Technology, 180 (2008), pp. 767-784

A. Cuoci, A. Frassoldati, T. Faravelli, E. Ranzi, “*Kinetic Modeling of Soot Formation in Turbulent Flames*”, Environmental Engineering Science, Accepted, In press

A. Cuoci, A. Frassoldati, T. Faravelli, E. Ranzi, “*Soot formation in unsteady counter-flow diffusion flames*”, Accepted at the “32nd International Symposium on Combustion”, McGill University, Montréal (Canada)

Papers presented at international conferences

A. Cuoci, A. Frassoldati, T. Faravelli, E. Ranzi, C. Accordini and G. Toniato, “*Experimental and Modeling study of NO_x formation in a Turbulent Gasoil Burner*”, 30th Meeting of the Italian Section of The Combustion Institute, June 20-23, 2007 Ischia (Italy), paper II9-1:II9-6

A. Cuoci, A. Frassoldati, T. Faravelli and E. Ranzi, “*Fluid dynamics and kinetic aspects of syngas combustion*”, 29th Meeting of the Italian Section of The Combustion Institute, June 14-17, 2006 Pisa (Italy), pp. IV6-1:IV6-6

M. Valenza, A. Frassoldati, **A. Cuoci**, T. Faravelli and E. Ranzi, “*NO_x formation in burners firing gases with low calorific value. An experimental and modeling study*”, Proceedings of the 6th International Symposium on High Temperature Air Combustion and Gasification (HiTACG), paper 47, October 17-19, 2005 Essen (Germany), pp. 47_1 – 47_10

A. Frassoldati, **A. Cuoci**, T. Faravelli, G. Buzzi Ferraris, E. Ranzi and M.Valenza, “*Optimal design of burners and furnaces with CFD simulations and detailed kinetics*”, Proceedings of the 6th International Symposium on High Temperature Air Combustion and Gasification (HiTACG), paper 68, October 17-19, 2005 Essen (Germany), pp. 68_1–68_9

A. Cuoci, T. Faravelli, E. Ranzi and P. J. Smith, “*Effects Of Turbulent Fluctuations On The Numerical Predictions Of Soot Formation And Oxidation In Turbulent Non-Premixed Flames Using A Coupled Radiation/flamelet Model*”, 2007 AIChE Annual Meeting, November 4-9, 2007 Salt Lake City (USA)

A. Frassoldati, **A. Cuoci**, B. Kanoczova, T. Faravelli and G. Buzzi Ferraris, “*Kinetic Modeling of Soot Formation in Turbulent Flames*”, 10th International Congress on Combustion By-Products and their Health Effects, June 17-20, 2007 Ischia (Italy), Book of Abstract p. 119

A. Cuoci, A. Frassoldati, T. Faravelli and E. Ranzi, “*Frequency response of counter flow diffusion flames to strain rate harmonic oscillations*”, Fifth International Mediterranean Combustion Symposium, September 9-13, 2007 Monastir (Tunisia)

S. Barendregt, M. van Goethem, I. Risseeuw, A. Frassoldati, T. Faravelli, **A. Cuoci**, X. J. Li, “*The Design Of Ultra-Low NO_x Critical Furnaces*”, Proceedings of the 8th European Conference on Industrial Furnaces and Boilers, March 25-28, 2008 Vilamoura (Portugal)

A. Frassoldati , **A. Cuoci**, T. Faravelli, E. Ranzi, S. Colantuoni, P. Di Martino and G. Cinque, “*Fluid dynamics and kinetic modelling of a low NO_x combustor for aero-engine turbofan*”, Submitted to the “32nd International Symposium on Combustion”, McGill University, Montréal (Canada)

Table of Contents

Sommario	XIX
Abstract	XXI
Introduction	XXIII
1 Numerical modeling of turbulent flows	1
1.1 Governing equations	1
1.1.1 Conservation of mass	2
1.1.2 Conservation of momentum	3
1.1.3 Conservation of species	4
1.1.4 Conservation of energy	5
1.2 Constitutive equations	6
1.2.1 Newton's law	6
1.2.2 Diffusion velocities (Fick's law)	7
1.2.3 Fourier's law	8
1.2.4 Equation of state	8
1.3 Navier-Stokes equations for a Newtonian fluid	9
1.3.1 Mass conservation	9
1.3.2 Momentum conservation	9
1.3.3 Species conservation	9
1.3.4 Energy conservation	9
1.4 Chemical kinetics	11
1.5 Modeling of turbulence	12
1.5.1 Reynolds averaging	14
1.5.2 Favre averages	15

II Table of Contents

1.6	RANS simulations for turbulent combustion	16
1.6.1	Species and enthalpy turbulent fluxes	17
1.6.2	Reynolds stresses.....	18
1.7	Conclusions	21
2	Modeling of combustion in turbulent flows	23
2.1	Introduction	23
2.2	Interactions between turbulence and chemistry.....	24
2.2.1	Oscillating Perfectly Stirred Reactor.....	26
2.3	Series expansion closure.....	32
2.4	Eddy Dissipation model.....	33
2.5	Eddy Dissipation Concept model.	34
2.6	Steady Laminar Flamelet Model	36
2.6.1	Mixed-Burned approach.....	40
2.6.2	Equilibrium approach	40
2.6.3	Flamelets approach.....	41
2.7	Unsteady Laminar Flamelet Model	43
2.8	Reaction Time Flamelet Model	44
2.9	Transported Probability Density Function.....	45
2.10	Conclusions	47
3	NO_x predictions in turbulent non premixed flames.....	49
3.1	Introduction	49
3.2	The Kinetic Post-Processor (KinPP)	50
3.2.1	Grouping of cells and grid sensitivity.....	51
3.2.2	Reaction rate evaluation	53
3.2.3	Mass balance equations	58
3.2.4	Numerical method and control of convergence.....	59
3.3	Experimental data.....	61
3.4	Flame modeling	62
3.5	Kinetic schemes.....	63
3.6	Preliminary analysis	63

3.6.1	Effect of turbulence models	63
3.6.2	Grid Sensitivity	66
3.6.3	Effect of different kinetic mechanisms	66
3.6.4	Effect of Radiative Heat transfer.....	67
3.7	NO _x predictions in Flames A and B	70
3.7.1	CFD results.....	70
3.7.2	KinPP results	72
3.8	NO _x predictions in Flame C.....	77
3.8.1	CFD results.....	77
3.8.2	KinPP results	78
3.9	Conclusions	81
4	Soot modeling in turbulent non premixed flames	83
4.1	Introduction	83
4.2	The soot population balance equation	86
4.2.1	Method of moments	89
4.3	Modeling of soot formation.....	89
4.4	Semi-empirical kinetic models.....	91
4.4.1	Nucleation Rate	91
4.4.2	Growth Rate	92
4.4.3	Coagulation Rate.....	92
4.4.4	Oxidation Rate.....	93
4.5	Flamelet library and enthalpy defect	94
4.6	Radiative heat transfer.....	97
4.7	Closure of soot source terms	98
4.7.1	Mean Properties.....	98
4.7.2	Uncorrelated closure	99
4.7.3	Correlated Closure.....	100
4.8	Kinetic mechanism.....	102
4.9	Experimental flames.....	102
4.10	Construction of the Flamelet Library	103
4.11	CFD simulation of experimental flames.....	109

IV Table of Contents

4.12	Combustion regimes	109
4.13	CFD results.....	112
4.13.1	Flame A	112
4.13.2	Flame B	114
4.14	Soot predictions	116
4.14.1	Flame A	116
4.14.2	Flame B	119
4.15	Sensitivity analysis to the nucleation rate.....	122
4.16	Conclusions	125
5	Soot modeling in turbulent non premixed flames - DQMOM.....	127
5.1	Introduction	127
5.2	Modeling of Soot Formation using DQMOM.....	128
5.2.1	Quadrature Method of Moments	129
5.2.2	Direct Quadrature Method of Moments	130
5.2.3	Nucleation.....	132
5.2.4	Molecular growth	132
5.2.5	Coagulation.....	133
5.2.6	Oxidation.....	134
5.3	Semi-empirical kinetic models	135
5.3.1	Nucleation Rate	135
5.3.2	Growth Rate.....	135
5.3.3	Coagulation Rate	136
5.3.4	Oxidation Rate.....	136
5.4	Flamelet library and enthalpy defect	137
5.5	Closure of soot source terms	139
5.5.1	Mean Properties.....	139
5.5.2	Uncorrelated closure.....	140
5.6	Radiative heat transfer.....	141
5.7	Kinetic mechanism	141
5.8	CFD Simulation of Experimental Flames.....	141
5.9	CFD results.....	142

5.9.1	Flame A.....	142
5.9.2	Flame B.....	143
5.10	Soot predictions.....	143
5.10.1	Flame A.....	143
5.10.2	Flame B.....	146
5.11	Sensitivity analysis to the nucleation rate.....	147
5.12	Conclusions.....	148
6	Unsteady counter flow diffusion flames.....	151
6.1	Introduction.....	152
6.2	Counter-flow diffusion flames.....	154
6.3	Mathematical model of unsteady counter-flow diffusion flames.....	156
6.3.1	Governing equations.....	157
6.3.2	Boundary conditions.....	158
6.3.3	Initial conditions.....	158
6.4	Numerical methodology.....	159
6.5	PAH formation in unsteady counter flow diffusion flames.....	160
6.5.1	Flames Investigated.....	160
6.5.2	Kinetic Scheme.....	160
6.5.3	Steady Flame Results.....	161
6.5.4	Unsteady Flame Results.....	164
6.5.5	Stokes' number.....	169
6.5.6	Comparison with experimental measurements.....	171
6.6	Soot formation in unsteady counter flow diffusion flames.....	172
6.6.1	Flames Investigated.....	172
6.6.2	Kinetic Scheme.....	172
6.6.3	Steady Flame Results.....	173
6.6.4	Unsteady Flame Results.....	175
6.7	Conclusions.....	181
	Conclusions.....	183
	References.....	187
	Nomenclature.....	199

Appendix A	205
Governing equations of steady flamelets.....	205
Extension to non adiabatic combustion.....	206
Transient solution method	207
Finite difference discretization	208
Non adiabatic flamelet library construction	208
The β -PDF	209
The Clipped-Gaussian PDF.....	210
The log-normal distribution.....	211
Numerical integration.....	211
 Appendix B.....	 215
Governing equations of counter flow diffusion flames	215
Conservation equation of mass.....	215
Conservation equation of momentum.....	216
Conservation equations of species.....	219
Conservation equation of energy	219
Governing equations for counter flow diffusion flames.....	219
Boundary conditions.....	220
Finite difference discretization	221
 Appendix C	 223

List of Figures

Figure 1. Comparison between chemical time scales and fluid flow time scales in turbulent reacting systems.

Figure 2. Oscillating perfectly stirred reactor fed with propane and air. The reactor temperature oscillates according to a sinusoidal function, while the residence time is kept fixed.

Figure 3. Responses of CO, CO₂, PAH and soot to the imposed temperature oscillations in a perfectly stirred reactor. The mean temperature is 1800K, the semi-amplitude of oscillations is 360K and the frequency 100 Hz.

Figure 4. Comparison between steady state and mean compositions of CO, CO₂, PAH and soot at the exit of an oscillating perfectly stirred reactor. The operating conditions are the same reported in Figure 3.

Figure 5. Response of soot to the imposed temperature oscillations in a perfectly stirred reactor at the mean temperatures of 1500K and 2100K. The semi-amplitude of oscillations is 20% of the mean value of temperature and the frequency 100 Hz.

Figure 6. Response of NO to the imposed temperature oscillations in a perfectly stirred reactor at the mean temperatures of 1800K and 2100K. The semi-amplitude of oscillations is 20% of the mean value of temperature and the frequency 100 Hz.

Figure 7. Comparison between steady state and mean compositions of nitrogen oxides at the exit of an oscillating perfectly stirred reactor. The operating conditions are the same reported in Figure 3.

Figure 8. Predicted CO and NO emissions in the exhaust gases as a function of the number of reactors used in kinetic post-processing procedure.

Figure 9. NO mass fraction map as a function of the number of reactors used in the post-processing procedure by the KinPP.

VIII List of Figures

Figure 10. Correction coefficient of the rate constants versus the intensity of temperature fluctuations at average temperatures of 1500 and 2000K. Continuous lines refer to series truncated at the eighth order. (a) activation energy = 20,000 cal/mol; (b) activation energy=40,000 cal/mol; (c) activation energy=70,000 cal/mol.

Figure 11. Correction coefficient of the rate constants versus the intensity of temperature fluctuations. The correction coefficients are calculated using the sinusoidal function approach proposed in this thesis, a Beta-PDF and a 2 Dirac delta approach. The mean temperature is assumed equal to 1500K.

Figure 12. (a) Average kinetic temperature versus the intensity of temperature fluctuations; (b) average kinetic temperature versus the intensity of energy activation. The mean temperature is equal to 1500K.

Figure 13. Effects of temperature and concentration oscillation on a second order reaction. The ratio between the reaction rate calculated at $T(\delta) = T_{\text{mean}}(1+\delta)$ or $c(\delta) = c_{\text{mean}}(1+\delta)$ is plotted versus δ for two different activation energies.

Figure 14. NO mole fraction versus the time in an oscillating perfectly stirred reactor fed with ethylene and air in stoichiometric proportions. (a) Reactor mean temperature equal to 1500K; (b) reactor mean temperature equal to 2000K.

Figure 15. (a) Example of a Boolean structure of the whole matrix system for a simple structured 2D computational mesh. (b) Zoom of the diagonal region (square in panel a). (c) Zoom of the single block structure (square in panel b).

Figure 16. Numerical procedure to solve the mass balances for the reactor network resulting from the clustering procedure.

Figure 17. Comparison between the different turbulence models investigated: temperature profile along the axis and in radial direction at $x/d=60$.

Figure 18. Comparison between the different turbulence models investigated: mixture fraction and carbon dioxide mass fraction profiles along the axis.

Figure 19. Comparison between the different structured mesh: coarse mesh (~30000 cells) and fine mesh (~90000 cells). Profiles of temperature, mixture fraction, H₂O and CO₂ mass fraction along the axis

Figure 20. Comparison between the CRECK kinetic scheme [7] and the GRI 3.0 kinetic scheme [58].

Figure 21. *Effects of radiative heat transfer on temperature, mixture fraction and H₂O and CO₂ mass fraction profiles.*

Figure 22. *Temperature profiles along the axis: comparison between experimental measurements [7, 8] and numerical calculations (a) in physical space and (b) in the dimensionless axial coordinate. Predicted contours of temperature in physical space and in dimensionless axial coordinate (c). The results refer to the EDC simulation.*

Figure 23. *Flame A: comparison between numerical results and experimental measurements in radial direction at several axial locations. (a) Axial velocity; (b) turbulent kinetic energy.*

Figure 24. *Flame A: temperature and mass fraction profiles along the axis and at several distances from the burner surface in radial direction (d is the internal diameter of the nozzle, x is the axial distance from the nozzle outlet): --- EDC model, --- ED model, --- SLF model.*

Figure 25. *Flame A: predicted contours of NO_x mass fractions. The results refer to the post-processing procedure applied to the CFD predictions obtained using the EDC model.*

Figure 26. *Flames A and B: comparison between experimental measurements of NO mass fraction [7, 8] and numerical results obtained from the KinPP. The red lines were obtained considering the effects of temperature fluctuation on reaction rates; the green lines neglecting the temperature fluctuations; the purple lines were calculated neglecting the thermal mechanism.*

Figure 27. *Flames A and B: comparison between numerical predictions and experimental measurements [7, 8] of NO mass fraction in radial direction at several axial locations.*

Figure 28. *Flame A: predicted contours of NO_x mass fractions. Comparison between results obtained taking into account the temperature fluctuations for estimating the reaction rates and results obtained neglecting the effects of temperature fluctuations.*

Figure 29. *Flame B: NO mass fraction at different distances from the nozzle. Comparison between singles hot measurements (symbols) [7, 8] and average model results (lines). The red lines are the result of the KinPP with the correction for taking into account the fluctuations of temperature on reaction rates; the green lines were obtained from the KinPP neglecting the temperature fluctuation effects on the reaction rates; the blue lines refer to the predicted results calculated without considering the thermal NO_x mechanism.*

Figure 30. *Flame B: OH mass fraction at different distances from the nozzle. Comparison between singles hot measurements (symbols) [7, 8] and average model results (lines). The red lines are the result of the KinPP with the correction for taking into account the fluctuations of temperature on reaction rates; the green lines were obtained from the KinPP neglecting the temperature fluctuation effects on the reaction rates.*

Figure 31. Predicted maximum NO and N₂O mass fractions in the flame as a function of the number of reactors used in kinetic post-processing procedure (Flame A).

Figure 32. Flame C: temperature and mass fraction profiles along the axis and at several distances from the burner surface in radial direction (d is the internal diameter of the nozzle, x is the axial distance from the nozzle outlet) with 0.80% of total amount of added NH₃: --- EDC model, --- ED model, --- SLF model.

Figure 33. Flame C: predicted contours of temperature and NO_x mass fractions. The results refer to the post-processing procedure applied to the CFD predictions obtained using the EDC model.

Figure 34. Flame C: comparison of experimental measurements and predictions in radial direction at $x/d=100$ with 0.80% of total amount of added NH₃. (a) Mean temperature; (b) NO mole fraction.

Figure 35. Flame C: comparison between predicted NO mole fraction profiles in radial direction at $x/d=100$ for different total amounts of added NH₃.

Figure 36. Flame C: (a) comparison of measurements and predictions of the molar yield of NO from NH₃. The NO flux has been obtained by integration over the cross section at $x/d=100$; (b) radially integrated values of NO at $x/d=100$ divided by the amount of inflow NH₃.

Figure 37. Flame C: radially integrated values of NO, NO₂ and NO_x at $x/d=100$ divided by the amount of inflow NH₃ versus axial position (0.80% of added NH₃).

Figure 38. Flame A: temperature and species profiles versus the mixture fraction at different scalar dissipation rate.

Figure 39. Flame B: temperature and species profiles versus the mixture fraction at different scalar dissipation rate.

Figure 40. Flame A: temperature and species profiles versus the mixture fraction at different enthalpy defects and equilibrium conditions.

Figure 41. Flame B: temperature and species profiles versus the mixture fraction at different enthalpy defects and equilibrium conditions.

Figure 42. Flame A: profiles of source terms in the soot properties transport equations at adiabatic conditions for different values of scalar dissipation rate: nucleation rate (a); growth rate (b); oxidation rate (c).

Figure 43. Flame B: profiles of source terms in the soot properties transport equations at adiabatic conditions for different values of scalar dissipation rate: nucleation rate (a); growth rate (b); oxidation rate (c).

Figure 44. *Flame A: soot particle number density (a) and soot volume fraction (b) profiles versus the mixture fraction as predicted by the flamelet calculations at different scalar dissipation rates.*

Figure 45. *Flame B: soot particle number density (a) and soot volume fraction (b) profiles versus the mixture fraction as predicted by the flamelet calculations at different scalar dissipation rates.*

Figure 46. *Normalized soot volume fraction profiles versus the mixture fraction as predicted by the flamelet calculations at different scalar dissipation rates: (a) Flame A; (b) Flame B.*

Figure 47. *Regimes of turbulent combustion for Flame A [72] and B [21]. Continuous lines represent fast reactions (combustion), dashed lines soot formation (nucleation).*

Figure 48. *Karlovitz number (left side) and combustion regimes (right side) for turbulent diffusion Flame A [72] and B [21].*

Figure 49. *Flame A: temperature, enthalpy defect and acetylene mole fraction contours calculated using the totally uncorrelated closure model.*

Figure 50. *Flame A: comparison between experimental measurements of temperature field and numerical results obtained using the totally uncorrelated closure model.*

Figure 51. *Flame A: comparison between experimental measurements of temperature field and numerical results obtained using the totally uncorrelated closure model. Radial profiles at $x=138$ mm, $x=241$ mm and $x=345$ mm.*

Figure 52. *Flame B: temperature, enthalpy defect and acetylene mole fraction contours calculated using the totally uncorrelated closure model.*

Figure 53. *Flame B: comparison between experimental measurements of temperature field and numerical results obtained using the totally uncorrelated closure model.*

Figure 54. *Flame B: comparison between experimental measurements of temperature field and numerical results obtained using the totally uncorrelated closure model. Radial profiles at $x=350$ mm and $x=425$ mm.*

Figure 55. *Flame A: soot volume fraction, particle number density and particle mean diameter contours calculated using the totally uncorrelated closure model.*

Figure 56. *Flame A: nucleation, growth and oxidation rate contours calculated using the totally uncorrelated closure model.*

Figure 57. *Flame A: comparison between experimental measurements of soot volume fraction and numerical results obtained using different closure models.*

XII List of Figures

Figure 58. *Flame B: comparison between experimental measurements of soot volume fraction and numerical results obtained using different closure models. Radial profiles at $x=138$ mm, $x=241$ mm and $x=345$ mm.*

Figure 59. *Flame A: comparison between predicted nucleation, growth and oxidation rates along the flame axis. Mean properties closure (a), uncorrelated closure (b), correlated closure (c).*

Figure 60. *Flame B: soot volume fraction, particle number density and particle mean diameter contours calculated using the totally uncorrelated closure model.*

Figure 61. *Flame B: nucleation, growth and oxidation rate contours calculated using the totally uncorrelated closure model.*

Figure 62. *Flame B: comparison between experimental measurements of soot volume fraction and numerical results obtained using different closure models.*

Figure 63. *Flame B: comparison between experimental measurements of soot volume fraction and numerical results obtained using different closure models. (I) mean properties closure (continuous line); (II) uncorrelated closure (dashed line); (III) correlated closure (dotted line).*

Figure 64. *Flame B. Comparison between predicted nucleation, growth and oxidation rates along the flame axis. Mean properties closure (a), uncorrelated closure (b), correlated closure (c).*

Figure 65. *Flame B. Main results of sensitivity analysis to the nucleation model: a. Comparison of nucleation rates along the axis (a), the soot volume fraction profiles along the axis (b), soot particles mean diameter along the axis (c).*

Figure 66. *Flame A: comparison between experimental measurements of temperature [72] and numerical predictions along the axis.*

Figure 67. *Flame B: comparison between experimental measurements of temperature [20] and numerical predictions along the axis.*

Figure 68. *Flame A: soot volume fraction and soot particle mean diameter maps obtained using the uncorrelated approach.*

Figure 69. *Flame A: comparison between experimental measurements of soot volume fraction and numerical results obtained using different closure models. Mean properties closure (dotted line) and uncorrelated closure (continuous line).*

Figure 70. *Flame B: soot volume fraction and soot particle mean diameter maps obtained using the uncorrelated approach.*

Figure 71. *Flame B: comparison between experimental measurements of soot volume fraction and numerical results obtained using different closure models. Mean properties closure (dotted line) and uncorrelated closure (continuous line).*

Figure 72. *Flame A: main results of sensitivity analysis to the nucleation model. (a) Soot volume fraction profile along the axis; (b) soot mass fraction along the axis.*

Figure 73. *Flame A: main results of sensitivity analysis to the nucleation model. (a) Soot particle mean diameter (d_{10}) along the axis; (b) Soot particle mean diameter (d_{32}) along the axis.*

Figure 74. *(a) Geometry of the axisymmetric opposed-flow diffusion flame; (b) geometry of the planar opposed-flow diffusion flame. The dashed lines represent the stagnation plane (SP).*

Figure 75. *Undiluted hydrocarbon/air counterflow diffusion flame geometry and sooting structure (from Zhang et al.[140]).*

Figure 76. *Comparison between the numerical results obtained for the flames fed with methane in steady state conditions: (a) Axial velocity profiles; (b) temperature profiles; (c) normalized (by their free stream values) mole fraction profiles of methane and oxygen; (d) heat release profiles along the centerline. All profiles are reported along the centerline.*

Figure 77. *Mole fraction profiles of main reactants normalized by their free stream values and temperature profile normalized by its maximum value (methane flame, GSR=30 Hz).*

Figure 78. *Predicted mole fraction profiles of PAH class A, B and C along the centerline for the flames fed with methane.*

Figure 79. *Predicted PAH peak values as a function of strain rate (normalized by the value at the lowest strain rate).*

Figure 80. *Flame II: peak values for each PAH class and maximum flame temperature at different frequencies, with non dimensional time $t' = \text{time}/\text{period}$. (a) Mole fraction peak value of Class A; (b) mole fraction peak value of Class B; (c) mole fraction peak value of Class C; (d) maximum temperature. The semi-amplitude of velocity oscillations is 50% of the steady value.*

Figure 81. *Flame II: detailed frequency response of the oscillation amplitude and phase lag for each class of PAH. The semi-amplitude of velocity oscillations is 50% of the steady value.*

Figure 82. *Flame II: peak values for each PAH class and maximum flame temperature at different oscillation semi-amplitude, with non dimensional time $t' = \text{time}/\text{period}$. (a) Mole fraction peak value of Class A; (b) mole fraction peak value of Class B; (c) mole fraction peak value of Class C; (d) maximum temperature. The frequency of velocity oscillations is 10 Hz.*

XIV List of Figures

Figure 83. *Variation of the maximum flame temperature and peak values for each PAH class at different frequencies, with non dimensional time $t' = \text{time}/\text{period}$. (a) Mole fraction peak value of Class A; (b) mole fraction peak value of Class B; (c) mole fraction peak value of Class C; (d) normalized maximum temperature. The semi-amplitude of velocity oscillations is 50% of the steady value.*

Figure 84. *Mole fraction peak value amplitude of induced oscillations normalized by the corresponding quasi-steady value versus the Stokes' parameter. Comparison between Flames I, II, III for Class A, B and C.*

Figure 85. *Mole fraction peak value amplitude of induced oscillations normalized by the corresponding quasi-steady value versus the Stokes' number. Comparison between Class A, B, C for Flame II.*

Figure 86. *Normalized mole fraction peak values versus the Stokes number compared with experimental measurements [139] (Flame II, oscillation semi-amplitude 70% of the steady state value). The profiles are scaled by the steady state value.*

Figure 87. *Normalized mole fraction peak values versus the non dimensional time (here expressed in $^\circ$) compared with experimental measurements [139] (Flame II, oscillation semi-amplitude 70% of the steady state value). The profiles are scaled by the steady state value.*

Figure 88. *Comparison between predicted and experimental [37] profiles of OH and soot (propane flame, GSR=15 Hz). The profiles are reported in arbitrary units.*

Figure 89. *Peak soot volume fraction versus the global strain rate. The lines refer to the numerical results, while the points are the experimental measurements reported in [37]. The dotted line indicates the minimum experimental amount of detectable soot.*

Figure 90. *Peak soot volume fraction versus the fuel C/H ratio at different values of GSR for the flames fed with propane.*

Figure 91. *Thickness of the soot region versus the square root of strain rate. The lines refer to the predicted results, while the points are the experimental measurements reported in [37].*

Figure 92. *Peak values of PAH mole fraction (a) and soot volume fraction (b) at different oscillation frequencies (propane flame, GSR=60 Hz, $A_u=60\%$).*

Figure 93. *Detailed frequency response of the oscillation amplitude and phase lag of soot (propane flame, GSR=60 Hz, $A_u=60\%$).*

Figure 94. *Peak values of PAH mole fraction (a) and soot volume fraction (b) at different amplitudes of oscillations (propane flame, GSR=60 Hz, $f=30$ Hz).*

Figure 95. Peak values of (a) PAH mole fraction and (b) soot volume fraction for different global strain rates (propane flame, $A_u=60\%$, $f=30$ Hz). The lines are normalized by the steady state value.

Figure 96. Soot volume fraction profiles in steady-state conditions and at different temporal locations (propane flame, $GSR=60$ Hz, $A_u=60\%$, $f=30$ Hz).

Figure 97. Normalized profiles of inlet velocities, peak temperature, peak PAH mole fraction and peak soot volume fraction values (propane flame, $A_u=30\%$, $f=30$ Hz).

Figure 98. Non adiabatic flamelet library structure.

List of Tables

Table 1. *Main data about the turbulent, non-premixed flames fed with syngas*

Table 2. *Reaction rate constants for soot formation and oxidation. Constants are in form of Arrhenius expression $k=A\cdot\exp(-T_a/T)$. Units are [K, kmol, m, s].*

Table 3. *Coefficients in Equation (4.42) for the evaluation of the mean Planck absorption coefficient of carbon monoxide.*

Table 4. *Operating conditions for the two flames investigated*

Table 5. *Constants in the soot models*

Table 6. *Constants in the soot models*

Table 7. *Coagulation kernel*

Table 8. *Operating conditions and main numerical results for the flames fed with methane, experimentally investigated by Xiao et al. [140].*

Table 9. *Mean of peak soot volume fraction for unsteady propane flames normalized to the peak soot volume fraction for the steady flame.*

Table 10. *Experimental [118] and numerical phase shifts (propane flame, $A_u=60\%$, $f=25$ Hz).*

Sommario

La modellazione numerica della formazione di specie inquinanti nelle fiamme turbolente presenta notevoli aspetti problematici. In effetti la possibilità di prevedere in termini affidabili e accurati la presenza di specie la cui concentrazione è talvolta di appena qualche ppm o addirittura ppb richiede in generale l'uso di schemi cinetici dettagliati, costituiti da centinaia di specie chimiche e migliaia di reazioni. A ciò bisogna aggiungere le difficoltà associate alle interazioni e al forte accoppiamento che esiste tra la cinetica e la turbolenza, in grado di condizionare in misura determinante la formazione di taluni inquinanti. Le fluttuazioni turbolente di temperatura e composizione possono spesso influenzare la velocità di formazione delle specie chimiche, secondo delle modalità che spesso non risultano di facile comprensione e semplice previsione.

Nonostante il continuo aumento della velocità degli strumenti di calcolo automatico, l'accoppiamento diretto tra fluidodinamica e cinetica chimica dettagliata è ancora molto difficile quando il moto è di tipo turbolento. Le ragioni principali delle difficoltà sono legate all'esistenza di un largo spettro di scale spaziali e temporali. Le difficoltà aumentano quando vengono utilizzate delle griglie di calcolo di grandi dimensioni e su geometrie complesse, quali generalmente quelle richieste nelle applicazioni di tipo industriale. Nella maggior parte dei casi una affidabile e accurata modellazione delle emissioni di inquinanti dalle fiamme turbolente richiede degli approcci modellistici semplificati e concepiti su misura per le diverse classi di inquinanti.

Il presente lavoro di Tesi si pone come obiettivo principale lo studio approfondito delle interazioni tra turbolenza e cinetica nelle fiamme turbolente non premiscelate, allo scopo di migliorare le predizioni numeriche delle emissioni di inquinanti che possono essere stimate attraverso l'uso di codici di calcolo fluidodinamici. L'attenzione è rivolta in misura particolare agli ossidi di azoto (NO_x) e al particolato carbonioso fine (soot).

Gli ossidi di azoto si formano secondo delle reazioni chimiche molto lente (almeno se confrontate con i tempi caratteristici della fluidodinamica in sistemi reattivi turbolenti), ma non sono in generale in grado di condizionare in misura significativa il processo di combustione propriamente detto. Tali considerazioni consentono l'adozione di un disaccoppiamento parziale tra

la chimica degli ossidi di azoto e la fluidodinamica della fiamma. Nel presente lavoro di Tesi è stata sviluppata una metodologia particolarmente robusta ed efficiente per la modellazione accurata della formazione degli ossidi di azoto nelle fiamme turbolente attraverso la tecnica del post-processamento cinetico. I risultati numerici ottenuti attraverso l'uso di uno schema cinetico semplificato all'interno di un codice di calcolo fluidodinamico sono post-processati attraverso l'impiego di uno schema cinetico dettagliato, in grado di predire accuratamente la formazione degli ossidi di azoto. Attraverso un tale approccio, la modellazione della formazione degli NO_x in fiamme turbolente, anche per geometrie complesse e casi di interesse industriale, viene resa possibile o comunque facilitata rispetto alle tecniche convenzionali.

La stessa metodologia non può essere applicata per la predizione numerica della formazione di soot, dal momento che quest'ultimo è in grado di condizionare il campo termico di una fiamma turbolenta grazie al suo importante ruolo nel trasporto di calore per irraggiamento. Inoltre i tempi caratteristici della chimica del soot e del mescolamento turbolento sono dello stesso ordine di grandezza e di conseguenza gli effetti delle fluttuazioni turbolente sulla velocità di formazione del soot diventano più complessi e di più difficile descrizione rispetto a quanto avviene per gli ossidi di azoto. Prima ancora del tentativo di adozione di schemi cinetici dettagliati (peraltro di dimensioni molto maggiori rispetto a quanto richiesto dagli NO_x), è necessario focalizzare l'attenzione sulla corretta modellazione delle interazioni tra turbolenza e cinetica nella formazione delle particelle di soot. Nel presente lavoro di Tesi sono stati quindi formulati diversi modelli e proposte diverse strategie per la modellazione degli effetti delle fluttuazioni turbolente sulla chimica del soot. Tali approcci sono stati quindi testati e confrontati su diverse fiamme turbolente non-premiscelate, simulate attraverso l'approccio RANS.

Risulta evidente che gli effetti della turbolenza sulla formazione del soot meritano una trattazione più approfondita e delle indagini numeriche più dettagliate. Tuttavia tali indagini non possono essere effettuate in maniera elementare direttamente sulle fiamme turbolente, a causa della loro complessità e dell'esistenza di molti fenomeni di non facile descrizione che si sovrappongono a quelli reattivi propriamente detti. E' stata quindi proposta una metodologia alternativa, basata sull'uso delle fiamme laminari a controdiffusione, nelle quali è possibile rilevare la presenza di molti degli aspetti fisici che caratterizzano le ben più complesse fiamme turbolente non premiscelate. L'idea alla base della metodologia proposta consiste nell'esporre delle fiamme laminari a controdiffusione ad oscillazioni armoniche dello strain rate, allo scopo di simulare gli effetti di fluttuazioni turbolente e di studiarne quindi gli effetti sulla formazione delle specie inquinanti (in particolare PAH e soot). Ciascuna specie chimica in generale offre una risposta diversa alle fluttuazioni turbolente, in funzione dei tempi che ne caratterizzano la chimica. E' chiaro dunque che attraverso un tale approccio è possibile indagare in maniera molto più semplice il ruolo delle fluttuazioni turbolente sulla formazione delle diverse specie chimiche.

Abstract

The numerical modelling of pollutant formation in turbulent flames is usually a very difficult task. The prediction of species whose concentration is of a few ppm or even ppb necessarily requires detailed kinetic mechanisms, involving hundreds of compounds. Moreover, the strong interactions and coupling between chemistry and turbulence strongly affect the amount of pollutants. Fluctuations of temperature and composition can either increase or reduce the concentration of by-products.

Despite the continuous increase in the speed of computational tools, the existence of many spatial and temporal scales of chemical and turbulent phenomena makes unfeasible the direct coupling of fluid dynamics and detailed kinetics, especially when considering the large and complex computational grids used for industrial applications. In most cases, reliable, accurate predictions of pollutant emissions from turbulent flames require simplified approaches, specifically conceived for each class of pollutant species.

The main objective of this work is a deeper understanding of interactions between turbulence and chemistry in turbulent non premixed flames, in order to improve the numerical predictions of pollutant emissions which can be obtained by CFD codes. In particular, the attention is mainly focused on nitrogen oxides (NO_x) and soot.

Since NO_x are ruled by very slow reactions (if compared to the turbulent mixing times) and affect only marginally the main combustion process, a partial decoupling between chemistry and fluid dynamics is possible. An efficient computational procedure is then developed in the present work for the accurate modelling of NO_x formation in turbulent flames through a post-processing technique. In other words, the CFD results (obtained with a simplified kinetic scheme) are post-processed by using a large, detailed kinetic scheme, which is able to accurately predict the formation of NO_x. This approach facilitates and makes possible the predictions of NO_x formation with detailed chemistry even in complex geometries.

The same methodology cannot be used for modeling soot formation, because of strong influence of soot on the temperature field of turbulent flames (due to its important role in radiative

heat transfer) and because characteristic times of mixing and soot chemistry are of the same order and consequently their interactions are more complex than in the case of NO_x. Before trying to apply detailed chemistry, the attention must be devoted to the correct modeling of effects of turbulent mixing on the formation rates of soot particles. Several closure models and strategies for describing the interactions between soot and turbulent mixing were formulated and applied in RANS simulations of turbulent non-premixed flames.

The effects of turbulence on soot chemistry deserve a deeper investigation, which however cannot be easily performed on turbulent flames, because of their complexity and the existence of many coupled phenomena. An alternative approach was proposed and applied in this thesis. Opposed counter-flow diffusion flames (CFDF), which possess much of the physics of turbulent flames, can be exposed to harmonic oscillations of the strain rate in order to simulate turbulent fluctuations and their effects on the formation of pollutant species. Each chemical species responds to the imposed oscillations according to the characteristic times of its chemistry and this allows to accurately investigate the role of turbulent mixing on the formation of pollutant species. The methodology presented in this work can be easily adopted to better understand how turbulent fluctuations affect the chemistry of each chemical species.

Introduction

Turbulent non premixed flames are largely used in many practical combustion devices to convert chemical energy into work, due to the high efficiency, large heat releases and safety reasons. However diffusion flames produce more pollutant species (in particular nitrogen oxides and soot) than premixed flames. Since combustion devices need to respect always more stringent limitations concerning the emissions of pollutants, the design of new burners relying on non premixed flames cannot neglect the issues related to the formation of such pollutant species. This explains the increasing demand for computational tools capable of characterizing the combustion systems in a reliable, accurate way, also in terms of pollutant species.

Even with the continuous increase of computer power and speed, the direct coupling of detailed kinetics (which is usually required to obtain accurate predictions of most pollutants whose concentrations are often of a few ppm or even ppb) and complex CFD is not possible, especially when considering the typical dimensions of the computational grids used for complex geometries and industrial applications. The computational cost significantly increases with the number of cells (N_C) of the computational grid and also with the second or third power of the number of reacting species (N_S). Moreover, the turbulent flow of most practical combustion devices leads to and involves strong interactions between fluid mixing and chemical reactions. Fluctuations of temperature and composition can either increase or reduce the concentration of by-products. The direct use of detailed chemistry in turbulent calculations appears a very difficult task. In most cases, reliable, accurate predictions of pollutant emissions from turbulent flames require simplified approaches, specifically conceived for each class of pollutant species.

Nitrogen oxides (NO_x) are reactive gases that have negative effects on the human health and cause many environmental concerns. Nitrogen dioxide (NO₂) for example is a gas that has been linked with higher susceptibility to respiratory infection, increased airway resistance in asthmatics, and decreased pulmonary function. In particular, increasingly stringent exhaust emission

requirements in terms of NO_x call for enhanced pollution reduction strategies, especially for diesel engines and industrial furnaces.

Since the nitrogen oxide chemistry is governed by very slow reactions if compared to the characteristic times of turbulent mixing, a kinetic post processing procedure can be successfully applied for their numerical modeling in turbulent non premixed flames. Pollutant species like nitrogen oxides only marginally affect the main combustion process and consequently do not significantly influence the overall temperature and flow fields. Consequently it is feasible to evaluate the structure of the flame with simplified kinetic schemes first and then post-process the CFD results with specific techniques which adopt a detailed kinetic scheme. This is the methodology applied in the present thesis, through a newly-conceived numerical tool, the so-called Kinetic Post-Processor (KinPP). The KinPP model, which can be applied for evaluating industrial burner performances, is able to accurately predict the formation of different pollutants, such as NO_x, CO and can be extended, with appropriate modifications, to other by-products.

Understanding the processes controlling soot in combustion has been an important research field for more than three decades. In most combustion processes soot is an undesirable product and therefore there are many reasons explaining this great interest by the scientific community. Usually soot particles in the exhaust gas of a combustion engine indicate an incomplete combustion, which leads to a poor utilization of the fuel. During the combustion or partial combustion in industrial reactors, deposition of soot may take place, leading to stacked process equipment. This problem can be very important for industrial processes using a catalyst. If mixing, temperature and composition of fuel and oxidizer, which are the main parameters controlling the formation of soot particles, are not correctly tuned, soot will start to deposit on the reactor catalyst. The equipment has to be cleaned or replaced and production has to be halted, resulting in an economic loss. Soot released into the atmosphere also represents a threat to the environment and the health of human beings. Soot is formed from large Polycyclic Aromatic Hydrocarbons (PAH) and many of these molecules are known to have a carcinogenic effect. Due to its negative effects on human health, soot emissions from combustion devices are subject to always more stringent limitations.

Soot formation significantly influences thermal radiation, which controls the burning regime in pool fires under most practical fire scenarios. In fact, soot usually dominates the radiative absorption coefficient and controls the heat feedback to the liquid fuel. Furthermore, the soot formed in the flames affects the radiation heat transfer in furnaces and various practical applications. Therefore, soot is not only an unwanted byproduct of combustion. In some combustion processes a controlled amount of soot is desired. Since soot greatly enhances the energy transfer from the flame to its surroundings by radiation, this is often a desired feature in furnaces where the objective is to transfer the heat from the flame to the furnace walls. However, in

such cases it is important to control the combustion in such a way that the soot particles are oxidized before the exhaust gas is released into the atmosphere.

The formation and oxidation of soot particles are highly complex processes, involving a large number of both homogeneous and heterogeneous chemical reactions and additional physical processes such as coagulation. All these processes can be described with a high degree of accuracy and reliability by using the most sophisticated soot models available in literature. However these models are expensive in terms of CPU time, even for simulations of laminar flames. In the numerical modeling of turbulent flames, the detailed soot models should be used together with other models necessary to describe reacting turbulent flow, leading to a very high CPU-time even for simple flames. Such detailed models could be used to help identify the conditions that reduce soot formation, but for predictions of soot particles in turbulent non premixed flames of practical interest, it is often necessary to use simplified models to keep CPU-time at an acceptable level. Such simplified models consider only the phenomena essential for obtaining sufficiently accurate predictions of soot concentrations and reliable CFD calculations of radiative heat transfer.

The numerical modeling of soot formation in turbulent non premixed flames cannot rely on the same methodology proposed for the nitrogen oxides. The main reason is related to the strong interactions between turbulence and soot chemistry, whose characteristic times are in the same range of turbulent mixing times. Moreover, a complete decoupling of soot from the gas-phase computations cannot be adopted due to the effect of soot on thermal radiation. Before trying to apply detailed chemistry, like in the case of NO_x, the attention must be shifted to the correct modeling of effects of turbulent mixing on the formation rates of soot particles. Accurate closure models for describing the interactions between soot chemistry and turbulent mixing must be formulated, keeping the computational time at an acceptable level.

The formation of pollutant species in turbulent diffusion flames is strongly affected by the coupling between the highly non-linear chemical kinetics with three dimensional, unsteady hydrodynamics. In order to accurately predict non-equilibrium effects in the numerical modeling of pollutant formation (especially PAH and soot), it is necessary to better understand this interdependency of transport and kinetic mechanisms. However the effects of turbulence on soot chemistry cannot be easily investigated on turbulent flames, because of their complexity and the existence of many coupled phenomena. Unsteady counter flow diffusion flames can be conveniently used to address the effects of hydrodynamic unsteadiness on the pollutant chemistry, because they possess much of the physics of turbulent diffusion flames and exhibit a large range of combustion conditions with respect to steady flames. Thus, these flames give insights into a variety of chemistry-flow field interactions important in turbulent combustion. Opposed counter-flow diffusion flames (CFDF) can be exposed to harmonic oscillations of the strain rate in order to

simulate turbulent fluctuations and their effects on the formation of pollutant species. Each chemical species responds to the imposed oscillations according to the characteristic times of its chemistry and this allows to accurately investigate the role of turbulent mixing on the formation of pollutant species.

In Chapter 1 the basic equations governing the conservation of mass, species, momentum and energy for turbulent reacting flows are briefly reported and discussed. The main approaches for the modeling of turbulence are shortly outlined, providing a first introduction to the so called problem of *turbulence closure*. The attention is focused on the RANS approach, which is the method used in the present thesis for the modeling of turbulent flames.

In Chapter 2 the so called chemical-source-term closure problem in turbulent reacting flows is introduced. The main issues related to the strong interactions between turbulent fluctuations and formation of chemical species are presented from a Chemical-Reaction-Engineering (CRE) point of view through numerical investigations performed on an oscillating perfectly stirred reactor. The most used approaches for the closure of chemical source terms in the conservation equations of chemical species are briefly summarized.

In Chapter 3 an effective methodology for the prediction of NO_x in turbulent non premixed flames by using Computational Fluid Dynamics (CFD) and detailed chemical kinetics is presented and discussed. The proposed approach is based on the general concept of “Reactor Network Analysis” and can be successfully applied even in complex geometries, which are very usual in industrial cases. The main features of a newly-conceived numerical tool, the Kinetic Post-Processor (KinPP), are summarized and its advantages and limitations are addressed. In order to show the validity and the accuracy of such methodology several turbulent non premixed flames are numerically investigated and the obtained predictions are presented and discussed.

Chapter 4 is devoted to the numerical modeling of soot formation in turbulent non premixed flames. The attention is here shifted from the detailed kinetics to the correct modeling of interactions between soot chemistry and turbulence, which are very complex to describe, since the soot characteristic times are in the same range of turbulent mixing times. Several closure approaches are formulated and applied for the numerical simulation of jet flames fed with ethylene. The formation of soot is numerically modeled using semi-empirical kinetic models available in literature. Predictions of temperature, mixture fraction and soot are compared with experimental measurements. The effect of a two-way coupling of soot and gas-phase chemistry on both soot yield and gas-phase composition is investigated. Also, the effect of radiation on predicted temperatures and soot volume fractions is studied. The main objective is to demonstrate the importance of correctly describing the effects of turbulent mixing on the formation of soot in turbulent non-premixed flames.

In Chapter 5 the methodology proposed in the previous Chapter for predicting the formation of soot in turbulent non premixed flames is extended to non monodispersed soot particle size distributions through the Direct Quadrature Method of Moments. The modeling of turbulence-chemistry interactions was reformulated for its direct application in the DQMOM procedure in order to improve the reliability of the overall method.

Chapter 6 is focused on a deeper investigation on the role of turbulent mixing on the formation of PAH and soot in unsteady counter-flow diffusion flames. A mathematical model for simulating unsteady counterflow diffusion flames is presented and applied to several flames fed with methane, propane and ethylene at different global strain rates and in a large range of strain rate frequencies. From the analyses of the response of each chemical species to the externally imposed oscillations, some important information about the effects of turbulent mixing on the chemistry can be addressed.

In the final Chapter conclusions and suggestions for further work are given.

1 Numerical modeling of turbulent flows

In this chapter the basic equations which govern turbulent fluid flows will be presented both in a coordinate-free form (which can be specialized to various coordinate systems) and in integral form for a finite control volume (which represents the starting point for an important class of numerical methods). The basic conservation principles and laws used to derive these equations will be briefly summarized here; more detailed derivations and discussions can be found in a large number of standard texts on fluid mechanics of reacting flows (for example [17, 107, 133]).

1.1 Governing equations

In this section the conservation equations needed for reacting flows are described and different issues which are specific to the Navier-Stokes equations for a multi-species reacting flow are discussed.

Conservation laws can be derived by considering a certain spatial region, which is usually called control volume (CV), and its extensive properties, such as total mass, species masses, momentum and energy. The conservation law for an extensive property relates the rate of change of the amount of that property in the given control volume to externally determined effects. The governing equations can be written in a common form according to the following integral expression:

$$\int_V \frac{\partial}{\partial t} (\rho\phi) dV + \int_S \rho\phi\vec{u} \cdot \hat{n} dS = \int_S \vec{Q}_s(\phi) \cdot \hat{n} dS + \int_V Q_v(\phi) dV \quad (1.1)$$

This equation represents the conservation of a generic quantity ϕ in the volume V whose surface is S . In Equation (1.1) \hat{n} is the unit vector orthogonal to S and directed outwards and \vec{u} is

the fluid velocity. The first term on the left side is the rate of change of ϕ in this volume. The second term is the convective flux of the quantity ϕ through the surface of the volume control, which is related to the flow convective velocity \vec{u} . On the right side the first term is the diffusion flux of ϕ through the surface S , whilst the second term is the production of ϕ inside the volume. The physical interpretation of this equation is clear: the rate of change of ϕ must be equal to the net sum of all (convective and diffusive) fluxes entering into the volume through the control surface plus the production of ϕ inside the same volume.

By applying the Gauss' divergence theorem to the surface integrals, the surface integral can be transformed into volume integrals. Allowing the control volume to become infinitesimally small leads to a differential coordinate-free form of Equation (1.1):

$$\frac{\partial}{\partial t}(\rho\phi) + \nabla(\rho\vec{u}\phi) = \nabla\vec{Q}_s(\phi) + Q_v(\phi) \quad (1.2)$$

Sometimes the conservation equations can be more conveniently written in terms of the so called total or substantive derivative, which is defined as:

$$\frac{D\phi}{Dt} = \frac{\partial\phi}{\partial t} + \vec{u} \cdot \nabla\phi \quad (1.3)$$

The mass, momentum, species and energy conservation equations will be presented in the next sections. A detailed derivation of these equations is given in many textbooks on fluid dynamics (e.g. in [17, 44, 109, 131]) and will not be repeated here. For convenience, a fixed CV will be considered.

1.1.1 Conservation of mass

The integral form of the mass conservation (continuity) equation follows directly from the control volume equation and states that the mass of a fluid is conserved:

$$\int_V \frac{\partial\rho}{\partial t} dV + \int_S \rho\vec{u} \cdot \hat{n} dS = 0 \quad (1.4)$$

where \vec{u} is velocity and ρ is the density of the fluid. The rate of change of mass in the volume V is due only to the mass fluxes through its surface. By applying the Gauss' divergence theorem to

the convection term, the surface integral can be transformed into a volume integral and the equation of conservation of mass can be written in the following differential form:

$$\frac{\partial \rho}{\partial t} + \nabla(\rho \bar{u}) = 0 \quad (1.5)$$

The Equation (1.5) reported above is written in a differential coordinate-free form, which does not depend on the specific coordinate system adopted. This equation can be transformed into a form specific to a given coordinate system by providing the expression for the divergence operator in such system. For example the Cartesian form of this equation in tensor notation becomes:

$$\frac{\partial \rho}{\partial t} + \frac{\partial \rho u_j}{\partial x_j} = 0 \quad (1.6)$$

1.1.2 Conservation of momentum

The integral form of the equation of conservation of momentum takes into account the forces which may act on the fluid in a CV, and therefore the surface forces (pressure, normal and shear stresses, surface tension, etc.) and the body forces (gravity, centrifugal and Coriolis forces, electromagnetic forces, etc.):

$$\int_V \frac{\partial}{\partial t}(\rho \bar{u}) dV + \int_S \rho \bar{u} \bar{u} \cdot \hat{n} dS = \int_S \underline{\underline{\sigma}} \cdot \hat{n} dS + \int_V \rho \bar{f} dV \quad (1.7)$$

where $\underline{\underline{\sigma}}$ is the stress tensor. The volume source term has the following expression:

$$\rho \bar{f} = \rho \sum_{k=1}^{N_S} \bar{f}_k \omega_k \quad (1.8)$$

where \bar{f} is the volume force acting on the species k and N_S is the total number of species. If only the gravity is taken into account \bar{f} is the same for every species and it is equal to the vector \bar{g} . The momentum conservation equation states that the rate of change of momentum equals the sum of the forces on a fluid particle (Newton's second law).

A coordinate-free vector form of the momentum conservation equation is readily obtained by applying Gauss' divergence theorem to the convective and diffusive flux terms:

$$\frac{\partial}{\partial t}(\rho \bar{u}) + \nabla(\rho \bar{u} \bar{u}) = \rho \bar{f} + \nabla \underline{\underline{\sigma}} \quad (1.9)$$

If the total derivative is introduced and the conservation equation of mass (1.5) is considered, the equation of conservation of momentum reported above can be written as:

$$\rho \frac{D\bar{u}}{Dt} = \rho \bar{f} + \nabla \underline{\underline{\sigma}} \quad (1.10)$$

Equation (1.9) is a vectorial equation which, in the most general case, corresponds to three scalar conservation equations for three velocity components. In particular in a Cartesian reference coordinate system the equation for the single component u_i can be easily written, both in the integral and in the differential forms (where $\bar{\sigma}_i = \underline{\underline{\sigma}} \cdot \hat{i}_i$):

$$\int_V \frac{\partial}{\partial t}(\rho u_i) dV + \int_S \rho u_i \bar{u} \cdot \hat{n} dS = \int_S \bar{\sigma}_i \cdot \hat{n} dS + \int_V \rho f_i dV \quad (1.11)$$

$$\rho \frac{Du_i}{Dt} = \frac{\partial}{\partial t}(\rho u_i) + \nabla(\rho u_i \bar{u}) = \rho f_i + \nabla \bar{\sigma}_i \quad (1.12)$$

1.1.3 Conservation of species

The mass conservation equation for species k is written as following, both in integral and differential forms respectively:

$$\int_V \frac{\partial}{\partial t}(\rho \omega_k) dV + \int_S \rho \bar{u} \omega_k \cdot \hat{n} dS = - \int_S \bar{j}_k \cdot \hat{n} dS + \int_V \dot{\Omega}_k dV \quad k = 1 \dots N_S \quad (1.13)$$

$$\rho \frac{D\omega_k}{Dt} = \frac{\partial}{\partial t}(\rho \omega_k) + \nabla(\rho \bar{u} \omega_k) = - \nabla \bar{j}_k + \dot{\Omega}_k \quad k = 1 \dots N_S \quad (1.14)$$

where N_S is the number of species, \bar{j}_k is the molecular diffusive flux of the k species, $\dot{\Omega}_k$ is the mass reaction rate per unit volume (see Paragraph 1.4) and ω_k is the mass fraction of species k . By definition:

$$\sum_{k=1}^{N_s} \vec{j}_k = \vec{0} \quad (1.15)$$

$$\sum_{k=1}^{N_s} \dot{\Omega}_k = 0 \quad (1.16)$$

The molecular diffusive \vec{j}_k is usually written in terms of a diffusion velocity \vec{V}_k , according to the following definition:

$$\vec{j}_k = \rho \omega_k \vec{V}_k \quad (1.17)$$

The equation of conservation of mass (1.5) can be easily recovered by summing the equations of conservations (1.14) for all chemical species, using the identities (1.15) and (1.16).

1.1.4 Conservation of energy

The energy conservation equation requires particular attention because multiple forms exist. Here the equation is written for the specific total energy \hat{E} , which is defined as the sum of the specific kinetic energy \hat{E}_K and the specific internal energy \hat{U} (which is a function of temperature, pressure and composition):

$$\hat{E} = \hat{E}_K + \hat{U}(p, T, \omega_k) = \frac{1}{2} \vec{u} \cdot \vec{u} + \hat{U}(p, T, \omega_k) \quad (1.18)$$

The conservation equation in the integral form is:

$$\int_V \frac{\partial}{\partial t} (\rho \hat{E}) dV + \int_S \rho \hat{E} \vec{u} \cdot \hat{n} dS = - \int_S \vec{q} \cdot \hat{n} dS + \int_S \underline{\underline{\sigma}} \cdot \vec{u} \cdot \hat{n} dS + \int_V \dot{Q} dV + \int_V \rho \sum_{k=1}^{NS} \omega_k \vec{f}_k \cdot (\vec{u} + \vec{V}_k) dV \quad (1.19)$$

where \vec{q} is the heat flux and \dot{Q} is the volume energy source term (due for example to an electric spark, a laser or a radiative flux), not to be confused with the heat released by combustion. The last term in the equation reported above is the energy power produced by volume forces \vec{f}_k on species k . As usual, a coordinate-free vector form of the energy conservation equation is obtained by applying Gauss' divergence theorem:

$$\rho \frac{D\hat{E}}{Dt} = \frac{\partial}{\partial t}(\rho \hat{E}) + \nabla(\rho \bar{u} \hat{E}) = -\nabla \bar{q} + \nabla(\underline{\underline{\sigma}} \cdot \bar{u}) + \dot{Q} + \rho \sum_{k=1}^{NS} \omega_k \bar{j}_k \cdot (\bar{u} + \bar{V}_k) \quad (1.20)$$

The energy equation is derived from the first law of thermodynamics which states that the rate of change of energy of a fluid particle is equal to the rate of heat addition to the fluid particle plus the rate of work done on the particle.

1.2 Constitutive equations

The conservation laws reported in the previous section are valid for any continuum and correspond to a system of partial differential equations. However, the number of unknown quantities is larger than the number of equations in the system, making the system indeterminate. Besides the main unknowns $(\rho, \bar{u}, p, \hat{E}, \omega_k)$, Equations (1.5), (1.9), (1.14), (1.20) includes the additional unknown variables $(\underline{\underline{\sigma}}, \bar{j}_k, \bar{q})$. Therefore, in order to close the system, it is necessary to introduce additional, so-called “*constitutive equations*” for the stress tensor $\underline{\underline{\sigma}}$, for the mass diffusion fluxes \bar{j}_k (or equivalently for the diffusion velocities \bar{V}_k) and for the energy flux \bar{q} . These variables depend on the properties of the continuous medium in question and must be expressed in terms of the main unknowns $(\bar{u}, p, \hat{E}, \omega_k)$ in order to close the system. Moreover it is necessary to introduce a state equation which relates the thermodynamic variables of gases.

In the next section the constitutive equations for Newtonian fluids and the state equations for perfect gases are briefly summarized.

1.2.1 Newton's law

For Newtonian fluids, the stress tensor $\underline{\underline{\sigma}}$ (which is the molecular rate of transport of momentum) can be written using the generalized form of the Newton's law of viscosity:

$$\underline{\underline{\sigma}} = 2\mu \underline{\underline{D}} - \left(p + \frac{2}{3} \mu \nabla \bar{u} \right) \underline{\underline{I}} = \left(2\mu \underline{\underline{D}} - \frac{2}{3} \mu \nabla \bar{u} \underline{\underline{I}} \right) - p \underline{\underline{I}} = \underline{\underline{\tau}} - p \underline{\underline{I}} \quad (1.21)$$

where μ is the dynamic viscosity, $\underline{\underline{I}}$ is the unit tensor, p is the static pressure and $\underline{\underline{D}}$ is the rate of strain (deformation) tensor:

$$\underline{\underline{D}} = \frac{1}{2} \left[\nabla \cdot \bar{\mathbf{u}} + (\nabla \cdot \bar{\mathbf{u}})^T \right] \quad (1.22)$$

The tensor $\underline{\underline{\tau}}$ describes the viscous part of the stress tensor $\underline{\underline{\sigma}}$. From the (1.21):

$$\underline{\underline{\tau}} = 2\mu\underline{\underline{D}} - \frac{2}{3}\mu\nabla\bar{\mathbf{u}}\underline{\underline{I}} \quad (1.23)$$

In Cartesian coordinates the stress tensor and the rate of strain tensor becomes:

$$\sigma_{ij} = \tau_{ij} - p\delta_{ij} = \left(2\mu D_{ij} - \frac{2}{3}\mu \frac{\partial u_j}{\partial x_j} \delta_{ij} \right) - p\delta_{ij} \quad (1.24)$$

$$D_{ij} = \frac{1}{2} \left(\frac{\partial u_i}{\partial x_j} + \frac{\partial u_j}{\partial x_i} \right) \quad (1.25)$$

where δ_{ij} is Kronecker symbol ($\delta_{ij} = 1$ if $i = j$ and $\delta_{ij} = 0$ otherwise).

1.2.2 Diffusion velocities (Fick's law)

The diffusion velocities (and therefore the diffusion fluxes) can be obtained by solving the following system [107]:

$$\nabla X_k = \sum_{p=1}^{N_s} \frac{X_k X_p}{\Gamma_{kp}} (V_p - V_k) + (\omega_k - X_k) \frac{\nabla p}{p} + \frac{\rho}{p} \sum_{p=1}^{N_s} \omega_k \omega_p (f_k - f_p) \quad \text{for } k = 1, \dots, N_s \quad (1.26)$$

where Γ_{kp} is the binary mass diffusion coefficient of species k into species p and X_k is the mole fraction of species k . The system (1.26) is a linear system of size N_s^2 which must be solved in each direction at each point (and each instant for unsteady flows). This task is usually costly, but in most cases a simplified approach based on the Fick's law can be adopted. According to the Fick's law, the diffusion velocity and the diffusive molecular fluxes can be written as:

$$\omega_k \vec{V}_k = -\Gamma_{k,mix} \nabla \omega_k \quad (1.27)$$

$$\vec{j}_k = -\rho \cdot \Gamma_{k,mix} \nabla \omega_k \quad (1.28)$$

where $\Gamma_{k,mix}$ is the mass diffusion coefficient of species k into the mixture.

1.2.3 Fourier's law

The energy flux is usually expressed as the sum of a first contribution expressed by the Fourier's law and a second term associated with the diffusion of species with different enthalpies, which is specific of multi-species gas:

$$\vec{q} = -\lambda \nabla T + \rho \sum_{k=1}^{N_s} \hat{H}_k \omega_k \vec{V}_k \quad (1.29)$$

In the expression reported above λ is the thermal conductivity and H_k is the specific enthalpy of species k .

1.2.4 Equation of state

The relationship between the thermodynamic variables (ρ, p, \hat{U}, T) can be obtained through the assumption of thermodynamic equilibrium, which is acceptable in most cases with the exception of certain flows with strong shockwaves. According to such hypothesis, the fluid can thermodynamically adjust itself to the new conditions so quickly that the changes are instantaneous if compared to the fluid velocity. The state of a substance in thermodynamic equilibrium can be described by means of just two state variables. Equations of state relate the other variables to the two state variables. For example, if we choose ρ and T as state variables, two state equations allow obtaining the pressure p and the internal energy \hat{U} :

$$p = p(\rho, T) \quad \hat{U} = \hat{U}(\rho, T) \quad (1.30)$$

The equation of perfect gases is usually accurate enough for the turbulent reacting flows studied in the present thesis:

$$p = \rho RT \quad \hat{U} = \hat{C}_v T \quad (1.31)$$

1.3 Navier-Stokes equations for a Newtonian fluid

The constitutive equations reported in the previous Paragraph, together with the governing equations for a continuum, create a closed system of partial differential equations for Newtonian fluids (which are written here only in the differential form):

1.3.1 Mass conservation

$$\frac{\partial \rho}{\partial t} + \nabla(\rho \vec{u}) = 0 \quad (1.32)$$

1.3.2 Momentum conservation

$$\rho \frac{D\vec{u}}{Dt} = \rho \vec{f} - \nabla \left(p + \frac{2}{3} \mu \nabla \cdot \vec{u} \right) + \nabla \left[\mu \left(\nabla \cdot \vec{u} + (\nabla \cdot \vec{u})^T \right) \right] \quad (1.33)$$

1.3.3 Species conservation

$$\rho \frac{D\omega_k}{Dt} = \nabla \cdot \left(\rho \cdot \Gamma_{k,mix} \nabla \omega_k \right) + \dot{\Omega}_k \quad k = 1, \dots, N_s \quad (1.34)$$

1.3.4 Energy conservation

$$\rho \frac{D\hat{E}}{Dt} = -\nabla(p\vec{u}) + \nabla(\underline{\underline{\tau}} \cdot \vec{u}) + \nabla \left(\lambda \nabla T - \rho \sum_{k=1}^{N_s} \hat{H}_k \omega_k \vec{V}_k \right) + \dot{Q} + \rho \sum_{k=1}^{N_s} \omega_k \vec{f}_k \cdot (\vec{u} + \vec{V}_k) \quad (1.35)$$

Usually for reactive systems studied in this thesis the energy equation can be more conveniently written in terms of specific total enthalpy \hat{H}_{tot} and specific enthalpy \hat{H} , defined as:

$$\hat{H}_{tot} = \hat{E} + \frac{p}{\rho} \quad (1.36)$$

$$\hat{H} = \hat{U} + \frac{p}{\rho} \quad (1.37)$$

After some re-arrangements of Equation (1.20), using the definitions (1.36) and (1.37), the following equations of conservation of total enthalpy and specific enthalpy can be obtained:

$$\rho \frac{D\hat{H}_{tot}}{Dt} = \frac{\partial p}{\partial t} - \nabla \bar{q} + \nabla(\underline{\underline{\tau}} \cdot \bar{u}) + \dot{Q} + \rho \sum_{k=1}^{N_s} \omega_k \bar{f}_k \cdot (\bar{u} + \bar{V}_k) \quad (1.38)$$

$$\rho \frac{D\hat{H}}{Dt} = \frac{Dp}{Dt} - \nabla \bar{q} + \underline{\underline{\tau}} : \nabla \bar{u} + \dot{Q} + \rho \sum_{k=1}^{N_s} \omega_k \bar{f}_k \cdot \bar{V}_k \quad (1.39)$$

In the Equation (1.39) reported above, the third term on the right side is the viscous heating source term and is a quantity always positive:

$$\dot{Q}_{diss} = \underline{\underline{\tau}} : \nabla \bar{u} > 0 \quad (1.40)$$

The Equations (1.38) and (1.39) are not always easy to implement in classical CFD codes, because they use expressions for enthalpy including chemical terms $\left(\sum_{k=1}^{N_s} \Delta \hat{H}_{f,k}^0 \cdot \omega_k \right)$ in addition to the sensible enthalpy. Sensible enthalpy \hat{H}_s , whose definition is reported below, is usually preferred:

$$\hat{H}_s = \hat{H} - \sum_{k=1}^{N_s} \Delta \hat{H}_{f,k}^0 \cdot \omega_k \quad (1.41)$$

Using the species conservation equations (1.34), the equation of conservation for sensible enthalpy can be obtained from Equation (1.39):

$$\rho \frac{D\hat{H}_s}{Dt} = \dot{Q}_R + \frac{Dp}{Dt} + \nabla(\lambda \nabla T) - \nabla \left(\rho \sum_{k=1}^{N_s} \hat{H}_{s,k} \omega_k \bar{V}_k \right) + \dot{Q}_{diss} + \dot{Q} + \rho \sum_{k=1}^{N_s} \omega_k \bar{f}_k \cdot \bar{V}_k \quad (1.42)$$

where \dot{Q}_R is the heat release due to combustion:

$$\dot{Q}_R = - \sum_{k=1}^{N_s} \Delta \hat{H}_{f,k}^0 \dot{\omega}_k \quad (1.43)$$

If the Mach number is low, an equation for temperature can be conveniently introduced. The derivative of sensible enthalpy can be written in terms of temperature:

$$\rho \frac{D\hat{H}_s}{Dt} = \sum_{k=1}^{N_S} \hat{H}_{s,k} \rho \frac{D\omega_k}{Dt} + \rho \hat{C}_P \frac{DT}{Dt} \quad (1.44)$$

Replacing this derivative in Equation (1.42) gives:

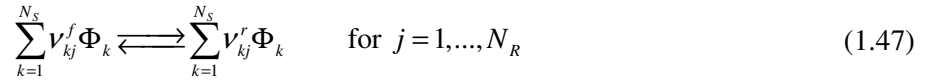
$$\rho \hat{C}_P \frac{DT}{Dt} = \dot{Q}_R^* + \frac{Dp}{Dt} + \nabla(\lambda \nabla T) - \left(\rho \sum_{k=1}^{N_S} \hat{C}_{P,k} \omega_k \vec{V}_k \right) \cdot \nabla T + \dot{Q}_{diss} + \dot{Q} + \rho \sum_{k=1}^{N_S} \omega_k \vec{f}_k \cdot \vec{V}_k \quad (1.45)$$

where \dot{Q}_R^* is the heat release due to combustion, not to be confused with \dot{Q}_R :

$$\dot{Q}_R^* = - \sum_{k=1}^{N_S} \hat{H}_k \dot{\Omega}_k = - \sum_{k=1}^{N_S} \hat{H}_{s,k} \dot{\Omega}_k - \sum_{k=1}^{N_S} \Delta \hat{H}_{f,k}^0 \dot{\Omega}_k = - \sum_{k=1}^{N_S} \hat{H}_{s,k} \dot{\Omega}_k + \dot{Q}_R \quad (1.46)$$

1.4 Chemical kinetics

Let us consider a chemical system of N_S species which react through N_R reactions:



where Φ_k is a symbol for the species k and ν_{kj}^f and ν_{kj}^r are its stoichiometric coefficients in reaction j . The mass formation rate $\dot{\Omega}_k$ of species k is the sum of net reaction rates \dot{r}_j produced by all N_R reactions:

$$\dot{\Omega}_k = W_k \sum_{j=1}^{N_R} (\nu_{kj}^r - \nu_{kj}^f) \dot{r}_j \quad \text{for } k = 1, \dots, N_S \quad (1.48)$$

where W_k is the molecular weight of species k . The net reaction rate \dot{r}_j of reaction j is written:

$$\dot{r}_j = K_j^f \prod_{k=1}^{N_S} (c_k)^{\nu_{kj}^f} - K_j^r \prod_{k=1}^{N_S} (c_k)^{\nu_{kj}^r} \quad \text{for } j = 1, \dots, N_R \quad (1.49)$$

where K_j^f and K_j^r are the forward and reverse rates of reaction j and c_k is the molar concentration of species k . The rates of reactions are usually modeled using the empirical Arrhenius law:

$$K_j^f = A_j^f T^{\beta_j} \exp\left(-\frac{E_j^{att}}{RT}\right) \quad \text{for } j = 1, \dots, N_R \quad (1.50)$$

where A_j^f is the pre-exponential constant, β_j is the temperature exponent and E_j^{att} the activation temperature. The backwards rates K_j^r are calculated from the forward rates through the equilibrium constants:

$$K_j^r = \frac{K_j^f}{\left(\frac{P_a}{RT}\right)^{\sum_{k=1}^{N_S} (v_{kj}^r - v_{kj}^f)} \exp\left(\frac{\Delta\tilde{S}_j^0}{R} - \frac{\Delta\tilde{H}_j^0}{RT}\right)} \quad \text{for } j = 1, \dots, N_R \quad (1.51)$$

where $p_a = 1$ bar. The $\Delta\tilde{H}_j^0$ and $\Delta\tilde{S}_j^0$ symbols refer to enthalpy and entropy changes occurring when passing from reactants to products.

1.5 Modeling of turbulence

Every flow which is met in the engineering practice becomes unstable if the Reynolds number becomes larger than a critical value. At low Reynolds numbers flows are laminar, but if this number becomes larger flows are observed to become turbulent, which can be considered a random state of motion in which the velocity and pressure change continuously with time. Most fluid flows occurring in nature are turbulent. Turbulence can be described as a state of continuous instability in the flow, where it is still possible to separate the fluctuations from the mean flow properties. It is characterized by irregularity in the flow, increased diffusivity and energy dissipation [130]. Turbulent flows are always three-dimensional and time dependent, even if the boundary conditions of the flow do not change in time. The range of scales in such flows is very large, from the smallest turbulent eddies characterized by Kolmogorov micro scales, to the flow features comparable with the size of the geometry. A comprehensive review of simulation techniques for turbulent flows can be found in [44] and [109]. A brief overview of the modeling techniques will be given here.

There are several possible approaches to the simulation of turbulent flows. According to Bardina *et al.* [5], the main approaches for the numerical prediction of turbulent flows can be classified in six main categories, most of which can be divided in sub-categories [44].

- I. The simplest approach involves the use of correlations (such as ones that give the friction factor as a function of the Reynolds number or the Nusselt number of heat transfer as a function of the Reynolds and Prandtl numbers). This approach is useful only for very simple types of flows, ones that can be characterized by just a few parameters.
- II. A more accurate approach uses integral equations which can be derived from the equations of motion by integrating over one or more coordinates. Usually this reduces the problem to one or more ordinary differential equations which are easily solved.
- III. The third approach is based on equations obtained by averaging the equations of motion over time (if the flow is statistically steady), over a coordinate in which the mean flow does not vary. This approach is called one-point closure and leads to a set of partial differential equations called the Reynolds-Averaged Navier-Stokes (RANS) equations. Unfortunately these equations do not form a closed set, so this method requires the introduction of approximations (turbulence models).
- IV. The fourth type is based on two-point closure. It uses equations for the correlation of the velocity components at two spatial points or, more often, the Fourier transform of these equations. These methods are rarely used except for homogeneous turbulence.
- V. The Large Eddy Simulation (LES), solves for the largest scale motions of the flow while approximating or modeling only the small scale motions. It can be regarded as a kind of compromise between one point closure methods and direct numerical simulation.
- VI. The most accurate methodology is the Direct Numerical Simulation (DNS), in which the Navier-Stokes equations are solved for all of the motions in a turbulent flow.

The major difficulty is that turbulent flows contain variations on a much wider range of length and time scales than laminar flows. The equations describing turbulent flows are usually much more difficult and expensive to solve, even though they are similar to the laminar flow equations. The methods close to the bottom in the list can be considered more exact, since more and more of the turbulent motions are computed and fewer are approximated by models, but the computation time is increased considerably [44].

The direct solution of the Navier-Stokes equations in turbulent regime is obviously the most natural choice and does not require any modeling effort. However the main problem is related to the computational cost: the accuracy and reliability of the numerical solution is directly

associated to the discretization of the computational domain on which the conservation equations need to be solved. The computational cells must be fine enough to capture the smallest turbulent scales (Kolmogorov microscale). At high Reynolds number, the Kolmogorov microscale becomes very small and the number of required grid points increases. For example it can be demonstrated that for a finite difference scheme, the number of grid points required for a DNS is proportional to $Re^{9/4}$, where Re is the Reynolds number constructed on the integral scale. Since in many practical applications the Reynolds number is very high (10^4 - 10^6), the required number of grid points is 10^9 - 10^{14} . As a consequence the corresponding numerical problem is intractable with the actual computational tools and power.

When modeling turbulent flows, we have to take into account that turbulence is an unsteady, irregular and non-periodical motion in which the transported quantities fluctuate in time and space in a wide range of space and time scales. Usually, for the majority of applications, we are interested in the mean values of the variables, and therefore the conservation equations for the mass, species, momentum and energy can be averaged over space or time. When this averaging is performed, the equations describing the mean flow-field contain the averages of product of fluctuating velocities. In general this will result in more unknowns than the number of equations available. Such difficulty can be resolved by turbulence modeling with additional equations being provided to match the number of unknowns. Such models are designed to approximate the physical behavior of turbulence. The average balance equations for turbulent flames can be obtained by decomposing the instantaneous quantities into mean and fluctuating quantities and describes only the mean flow field. Two methods of averaging, Reynolds and Favre (or mass weighted) averaging are commonly used.

1.5.1 Reynolds averaging

The mean quantity $\bar{\phi}$ can be defined in many ways, depending on the flow conditions [65, 109]. Here it is defined as the ensemble average, where N is a sample size:

$$\bar{\phi}(x_i, t) = \frac{1}{N} \sum_{k=1}^N \phi^k(x_i, t) \quad (1.52)$$

The value of ϕ can be assumed to be the sum of its mean quantity $\bar{\phi}$ and its fluctuation part ϕ' :

$$\phi(x_i, t) = \bar{\phi}(x_i, t) + \phi'(x_i, t) \quad (1.53)$$

In this expression the mean value $\bar{\phi}$ is defined as the time average of ϕ , where the time step must be chosen to be sufficiently large than the characteristic time of turbulent motions:

$$\bar{\phi}(x_i, t) = \frac{1}{\Delta t} \int_t^{t+\Delta t} \phi(x_i, t) dt \quad (1.54)$$

The time average of fluctuations is zero by definition:

$$\overline{\phi'}(x_i, t) = \frac{1}{\Delta t} \int_t^{t+\Delta t} \phi'(x_i, t) dt = 0 \quad (1.55)$$

On the contrary, the time average of the product of fluctuation parts of two different variables ϕ' and ψ' is not zero:

$$\overline{\phi'\psi'}(x_i, t) = \frac{1}{\Delta t} \int_t^{t+\Delta t} \phi'(x_i, t) \cdot \psi'(x_i, t) dt \neq 0 \quad (1.56)$$

If we apply the Reynolds average to the mass balance conservation equation, it is relatively easy to show that the following equation results:

$$\frac{\partial \bar{\rho}}{\partial t} + \nabla \cdot (\bar{\rho} \bar{u} + \overline{\rho' u'}) = 0 \quad (1.57)$$

1.5.2 Favre averages

The previous Equation (1.57) contains the unclosed velocity and density correlation $\overline{\rho' u'}$, which needs explicit modeling. Reynolds averaging for variable density flows introduces many other unclosed correlations between any quantity ϕ and density fluctuations $\overline{\rho' \phi'}$. In order to partially overcome this problem, the Favre (or mass weighted) average $\tilde{\phi}$ is introduced:

$$\tilde{\phi}(x_i, t) = \phi(x_i, t) + \phi''(x_i, t) \quad (1.58)$$

The mean quantity $\tilde{\phi}$ is defined as:

$$\tilde{\phi}(x_i, t) = \frac{\overline{\rho\phi}}{\bar{\rho}} \quad (1.59)$$

The fluctuation ϕ'' has the following properties:

$$\begin{aligned} \tilde{\phi}''(x_i, t) &= \frac{\overline{\rho(\phi - \tilde{\phi})}}{\bar{\rho}} = 0 \\ \overline{\rho\phi}''(x_i, t) &= 0 \\ \overline{\phi}''(x_i, t) &= -\frac{\overline{\rho'\phi'}}{\bar{\rho}} \neq 0 \end{aligned} \quad (1.60)$$

1.6 RANS simulations for turbulent combustion

With Favre averages for variable density flows, the RANS (Reynolds Averaged Navier Stokes) form of conservation equations can be derived as following.

Mass conservation equation

$$\frac{\partial \bar{\rho}}{\partial t} + \nabla \cdot (\bar{\rho} \tilde{\mathbf{u}}) = 0 \quad (1.61)$$

Momentum conservation equation

$$\frac{\partial}{\partial t} (\bar{\rho} \tilde{\mathbf{u}}) + \nabla \cdot (\bar{\rho} \tilde{\mathbf{u}} \tilde{\mathbf{u}}) = -\nabla \bar{p} + \nabla \cdot \underline{\underline{\tau}} + \nabla \cdot (\bar{\rho} \tilde{\mathbf{u}} \tilde{\mathbf{u}}'') + \bar{\rho} \tilde{\mathbf{f}} \quad (1.62)$$

Species

$$\frac{\partial}{\partial t} (\bar{\rho} \tilde{\omega}_k) + \nabla \cdot (\bar{\rho} \tilde{\mathbf{u}} \tilde{\omega}_k) = \nabla \cdot (\overline{\rho \cdot \Gamma_{k,mix} \nabla \omega_k}) + \bar{\Omega}_k - \nabla \cdot (\bar{\rho} \tilde{\mathbf{u}} \tilde{\omega}_k'') \quad k = 1, \dots, N_s \quad (1.63)$$

Energy

$$\frac{\partial}{\partial t} (\bar{\rho} \tilde{H}_s) + \nabla \cdot (\bar{\rho} \tilde{\mathbf{u}} \tilde{H}_s) = \bar{Q}_R + \frac{D\bar{p}}{Dt} + \nabla \cdot (\overline{\lambda \nabla T}) + \bar{Q}_{diss} + \bar{Q} - \nabla \cdot \left(\overline{\rho \sum_{k=1}^{N_s} \hat{H}_{s,k} \omega_k \vec{V}_k} \right) - \nabla \cdot (\bar{\rho} \tilde{\mathbf{u}} \tilde{H}_s'') \quad (1.64)$$

$$\text{where: } \frac{\overline{Dp}}{Dt} = \frac{\partial \bar{p}}{\partial t} + \overline{\tilde{u} \nabla p} = \frac{\partial \bar{p}}{\partial t} + \tilde{u} \nabla \bar{p} + \overline{\tilde{u}'' \nabla p}$$

In Equation (1.64) the terms related to the sensible enthalpies and to the external volume forces $\overline{f_k}$ are neglected for simplicity.

It is seen that the Favre average makes the turbulent compressible flow equations simpler, with their form resembling those of incompressible flows. The equations (1.61), (1.62), (1.63) and (1.64) are now formally identical to the classical Reynolds averaged equations for constant density flows. However we can recognize some additional unknown terms: the so-called Reynolds stress tensor $\nabla(\overline{\rho \tilde{u}'' \tilde{u}''})$ and the species and enthalpy turbulent fluxes $\nabla(\overline{\rho \tilde{u}'' \omega_k''})$ and $\nabla(\overline{\rho \tilde{u}'' H_s''})$ respectively. Despite the simplifications that Favre average is able to introduce, the density fluctuations or compressibility effects must still be resolved; only mathematical simplifications can be achieved though Favre averages. These quantities represent the process of turbulent diffusion and require the introduction of additional equations matching the same number of unknowns must be provided. This is the process known as the *turbulence closure* or *turbulence modeling*.

The Favre averaging introduces another important issue, which represent one of the most important problems in the numerical modeling of turbulent reacting flows: the formation rate $\overline{\tilde{\Omega}_k}$ of species k needs to be closed using an appropriate “*combustion model*”, which accounts for the effects of turbulence on the chemical reactions.

In the next Chapter the problem of closure of mean formation rate will be presented and discussed more deeply. In the next section we briefly discuss the most used approaches for the modeling of species and enthalpy turbulent fluxes. Then a short presentation of closure problem of Reynolds stresses in the conservation momentum equation will be presented.

1.6.1 Species and enthalpy turbulent fluxes

The species and enthalpy turbulent fluxes are usually modeled using a classical gradient assumption:

$$\overline{\rho \tilde{u}'' \omega_k''} = -\frac{\mu_t}{Sc_{t,k}} \nabla \tilde{\omega}_k \quad k = 1, \dots, N_s \quad (1.65)$$

$$\nabla(\overline{\rho \tilde{u}'' \hat{H}_s''}) = -\frac{\mu_t}{\sigma_t} \nabla \tilde{H}_s \quad (1.66)$$

where μ_t is the turbulent viscosity (which will be defined in the next section), $Sc_{t,k}$ the turbulent Schmidt number for species k and σ_t a constant which is usually assumed equal to 0.85. The gradient assumption is largely used but it could be not appropriate in some turbulent flows, for which counter-gradient turbulent transport are observed.

1.6.2 Reynolds stresses

The turbulent Reynolds stresses are usually described using the turbulence viscosity assumption proposed by Boussinesq. In particular it is assumed that the Reynolds stresses have the same form of the viscous tensor retained for Newtonian fluids:

$$\overline{\rho \tilde{u}'' \tilde{u}''} = \overline{\rho} \widetilde{\tilde{u}'' \tilde{u}''} = \mu_t \tilde{\underline{\underline{\tau}}} + \frac{2}{3} \overline{\rho} \kappa \quad (1.67)$$

In this expression μ_t is the turbulent dynamic viscosity and δ_{ij} is the Kronecker symbol. The last term has been added to recover the right expression for turbulent kinetic energy κ :

$$\kappa = \frac{1}{2} \widetilde{\tilde{u}'' \tilde{u}''} \quad (1.68)$$

The closure problem is now shifted to evaluation of turbulent viscosity μ_t . Three main approaches have been proposed: algebraic expressions which do not require any additional balance equation, one-equation closure and two-equation closure.

The simplest approach is due to Prandtl, who, in analogy with the kinetic theory of gases, evaluated the turbulent viscosity as follows:

$$\mu_t = \overline{\rho} l_{mix}^2 \left| \tilde{\underline{\underline{S}}} \right| \quad (1.69)$$

where l_{mix} is the so-called “mixing length”, analogous to the mean free path of gaseous molecules, and $\tilde{\underline{\underline{S}}}$ is the mean stress tensor, defined as:

$$\tilde{\underline{\underline{S}}} = \frac{1}{2} \left(\frac{\partial \tilde{u}_i}{\partial x_j} - \frac{\partial \tilde{u}_j}{\partial x_i} \right) \quad (1.70)$$

Various empirical relations have been proposed to model l_{mix} , but they strongly depend on the flow geometry and cannot be easily generalized.

A more general formulation can be obtained relating the turbulent viscosity to other quantities characteristic of the turbulence, such as the turbulent kinetic energy κ . The Prandtl-Kolmogorov model in particular is an example of one equation model:

$$\mu_t = \bar{\rho} C_\mu l_{mix} \sqrt{\kappa} \quad (1.71)$$

where C_μ is a model constant (generally chosen as $C_\mu = 0.09$) and l_{mix} is a characteristic length, which depends once again on the flow geometry and whose origin is experimental.

More accurate and general models can be obtained using the two equation approaches, which take into account not only the kinetic energy κ , but also the turbulent dissipation rate ε . In this case, some additional differential equations need to be solved. In the κ - ε model, initially due to Jones and Launder [68], the turbulent viscosity is modeled according to the following expression:

$$\mu_t = \bar{\rho} C_\mu \frac{\kappa^2}{\varepsilon} \quad (1.72)$$

where C_μ is a constant of proportionality. In order to evaluate μ_t , besides the Navier-Stokes and the continuity equations, two additional transport equations for κ and ε are needed. The transport equation for the kinetic energy can be obtained analytically from the Favre averaged Navier-Stokes equations after some algebra:

$$\frac{\partial}{\partial t}(\bar{\rho}\kappa) + \nabla(\bar{\rho}\tilde{u}\kappa) = \nabla \left[\left(\mu + \frac{\mu_t}{\sigma_\kappa} \right) \nabla \kappa \right] + P_\kappa - \bar{\rho}\varepsilon \quad (1.73)$$

On the contrary, the transport equation for the turbulent dissipation rate ε in the standard κ - ε model is empirically derived, thus resulting in the following equation:

$$\frac{\partial}{\partial t}(\bar{\rho}\varepsilon) + \nabla(\bar{\rho}\tilde{u}\varepsilon) = \nabla \left[\left(\mu + \frac{\mu_t}{\sigma_\varepsilon} \right) \nabla \varepsilon \right] + \frac{\varepsilon}{k} (C_{1\varepsilon} P_k - C_{2\varepsilon} \bar{\rho}\varepsilon) \quad (1.74)$$

The source term in the turbulent kinetic energy and dissipation rate equations has the following expression, in which the Reynolds stresses are determined using the Boussinesq expression (1.67):

$$P_k = \overline{\rho} \widetilde{u^* u^*} \nabla \widetilde{u} \quad (1.75)$$

The standard values of the closure constants were proposed by Launder and Spalding [78]: $C_{\mu} = 0.09$, $\sigma_k = 1.0$, $\sigma_{\varepsilon} = 1.3$, $C_{1\varepsilon} = 1.44$ and $C_{2\varepsilon} = 1.92$. The standard κ - ε model is usually of acceptable accuracy for simple flows, but it can be quite inaccurate for complex flows. For example it cannot capture the stabilizing/destabilizing influence of swirling motions and buoyancy forces. Even for a simple round jet the constants need to be adjusted. For example $C_{2\varepsilon} = 1.83$ for axisymmetric round jet is usually recommended than the standard value of 1.92. In Chapter 3 further investigation about the role of κ - ε model for the prediction of turbulent jet will be outlined.

Since the first formulation of this model, several modifications have been proposed to overcome the limitations in the computation of particular kinds of flows.

For example the RNG κ - ε model was derived using a rigorous statistical technique (called Renormalization Group Theory). The analytical derivation results in a model with constants different from those in the standard κ - ε model and additional terms and functions in the transport equations for κ and ε . A more comprehensive description of RNG theory and its application to turbulence can be found in [30]. The RNG model is similar in form to the standard κ - ε model, but includes the some important modifications: there is an additional term in its ε equation that significantly improves the accuracy for rapidly strained flows; the effect of swirl on turbulence is included, enhancing accuracy for swirling flows; the RNG theory provides an analytical formula for turbulent Prandtl numbers, while the standard κ - ε model uses user-specified, constant values. Moreover, while the standard κ - ε model is a high-Reynolds-number model, the RNG theory provides an analytically-derived differential formula for effective viscosity that accounts for low-Reynolds-number effects. These features make the RNG κ - ε model more accurate and reliable for a wider class of flows than the standard κ - ε model.

Another modification of the κ - ε is the so called “*realizable* κ - ε ”, which employs a different formulation for the turbulent viscosity and a different transport equation for ε (derived from an exact equation for the transport of the mean-square vorticity fluctuation) [122]. The term “*realizable*” means that the model satisfies certain mathematical constraints on the Reynolds stresses, consistent with the physics of turbulent flows. Neither the standard κ - ε model nor the RNG κ - ε model is realizable. The realizable κ - ε is able to predict more accurately the spreading rate of round and planar jets and to provide better results especially with flows involving rotation, separation and recirculation.

The most classical turbulence model is the Reynolds Stress equation Model (RSM), which is based on a second moment closure and avoids resorting to the Boussinesq hypothesis. When the flow fields are characterized by complex strain fields or significant body forces, the individual Reynolds stresses are poorly represented by the Boussinesq hypothesis (1.67), even if the turbulent kinetic energy is computed to reasonable accuracy. The main idea behind the RSM consists in solving the additional transport equations for all the components of the Reynolds stress tensor. The exact transport equation for the transport of the kinematic Reynolds stresses has been reported in many texts. In Cartesian coordinate the equation take the following form:

$$\frac{\partial}{\partial t}(\overline{\rho u_i u_j}) + \frac{\partial}{\partial x_k}(\overline{\rho u_k u_i u_j}) = P_{ij} + D_{ij} - E_{ij} + \Pi_{ij} + \Omega_{ij} \quad (1.76)$$

Equation (1.76) describes six partial differential equations: one for the transport of each of the six independent Reynolds stresses (the Reynolds stress tensor is symmetric). If this equation is compared to the exact transport Equation (1.73) for the turbulent kinetic energy, two new physical processes appear in the Reynolds stress equations: the pressure-strain correlation term Π_{ij} (whose effects on the kinetic energy can be shown to be zero) and the rotation term Ω_{ij} . On the contrary The production P_{ij} , the diffusion D_{ij} and dissipation E_{ij} terms are present in the turbulent kinetic energy too. In the equations (1.76) some terms need to be modeled. In particular the numerical models are needed for the diffusion term D_{ij} , the dissipation rate E_{ij} and the pressure-strain correlation Π_{ij} . The remaining terms are present in a closed form and therefore they do not need any modeling. Launder *et al.* [77] and Rodi [115] give comprehensive details of the most general models. The RSM approach accounts for the effects of streamline curvature, swirl, rotation and rapid changes in the strain rate more rigorously than the two equation models, and it is therefore more suitable for the modeling of complex flows involving such phenomena. However the closure modeling of unclosed terms in the Equations (1.76) (in particular the pressure strain term) can strongly affect the accuracy of the results, and should be considered carefully. RSM are clearly quite complex, but is generally accepted that they are the simplest type of model with the potential to describe all the mean flow properties and Reynolds stresses without case-by-case adjustments.

1.7 Conclusions

In this Chapter the conservation equations of mass, momentum, species and energy for reacting turbulent flows were briefly presented. The main approaches for the modeling of turbulence were shortly outlined, providing a first introduction to the so called problem of

turbulence closure. The attention was focused on the RANS approach, which is the method used in the present thesis for the modeling of turbulent flames. In the RANS computations, the equations governing turbulent, reacting flows are averaged in order to make feasible their numerical solution, but this averaging leads to the introduction of additional unknown terms which need to be modeled (or closed). Turbulent combustion modeling is generally focused on the closure of species chemical reaction rates, which will be the subject of the next Chapter. At the present the RANS approach is practically a forced choice if the time required for the simulation is a critical parameter. However, since computer power is rapidly increasing, the application of more accurate methods is becoming more affordable. RANS computations will be probably replaced in the next years by Large Eddy Simulation, which is becoming more and more popular in the academic community.

2 Modeling of combustion in turbulent flows

The study of turbulent reacting flows is of paramount importance in many industrial applications, but their numerical modeling is one of the main issues in chemical reaction engineering. The main difficulties are related to the closure of the chemical source term in the Reynolds-averaged scalar transport equations. Due to the highly non-linear character of chemical source terms, simplified approaches must be taken into account in order to correctly manage the interactions between turbulence and kinetics. In the past decades, several authors proposed different models and methods to properly describe the effects of turbulent fluctuations on chemical reactions and vice-versa. Some important solutions have been formulated for reactions which are very fast if compared to the turbulence characteristic times or for reactions which are very slow with respect to the mixing times, but for intermediate cases, for which the times of chemistry and mixing are similar, the interactions are very strong and the modeling issues becomes more complex. No definitive solutions have been proposed, which can be used for practical systems in reasonably small computation times.

2.1 Introduction

In this chapter the most important models for turbulent reacting flows will be briefly summarized, mainly focusing on the approaches that were adopted in the present thesis. As known, the description of the turbulence-chemistry interactions represents one of the most difficult tasks in turbulent combustion. Since the chemical reactions occur over the scales of molecular mixing and are characterized by a strongly non-linear behavior (especially with respect to the temperature), the effects of turbulence on the chemistry of chemical species need to be accurately modeled. Several models have been formulated to couple turbulence and chemistry in the appropriate way when

RANS equations are adopted for the numerical modeling of a turbulent flame. The different approaches can be grouped in two families [107]: the *Reaction Rates Approach* (RRA) and the *Primitive Variables Approach* (PVA). In the first case it is necessary to model only the reaction term in the transport equations, but a transport equation for all the species must be solved; for example, the *Eddy Dissipation* (ED) [88] and the *Eddy Dissipation Concept* (EDC) models [86, 87] belong to this group. An alternative methodology is the Primitive Variable Approach which solves the transport equations only for a small number of primitive variables which govern the temperature and species concentrations. This is the approach followed for example by the *Steady Laminar Flamelet* (SLF) model [100, 101] or the *Unsteady Laminar Flamelet* (SLF) model [99, 104].

2.2 Interactions between turbulence and chemistry

The Reynolds averaged scalar transport equations for chemical species (1.63) contain a chemical source term of the form (see Equations (1.48) and (1.49)):

$$\bar{\dot{\Omega}}_k = W_k \sum_{j=1}^{N_R} (v_{kj}^r - v_{kj}^f) \bar{r}_j = W_k \sum_{j=1}^{N_R} (v_{kj}^r - v_{kj}^f) \left[\overline{K_j^f \prod_{k=1}^{N_S} (c_k)^{v_{kj}^f}} - \overline{K_j^r \prod_{k=1}^{N_S} (c_k)^{v_{kj}^r}} \right] \quad \text{for } k = 1, \dots, N_S \quad (2.1)$$

This source term is highly non-linear with respect to concentrations and temperature. The chemical source term is unclosed at the level of the first-order moments, which means that it cannot be expressed in terms of mean concentrations and temperature (thus neglecting the effects of turbulent fluctuations). Moreover, since in the Arrhenius law the temperature is present as an exponential function, the chemical source term will be unclosed at any finite level of moments. The closure problem of chemical source term occurs even for relatively simple isothermal reactions, but becomes more and more important for turbulent combustion, where large temperature fluctuations can arise.

The effects of turbulence on the formation rate of each chemical species are strongly dependent on the characteristic times of the chemistry governing the evolution of such species. These chemical times can be defined in terms of the eigenvalues of the Jacobian matrix of formation rates [47]. For example, for an isothermal system, the Jacobian matrix is a $N_S \times N_S$ square matrix given by:

$$J_{ij} = \frac{\partial \dot{\Omega}_i}{\partial c_j} \quad \text{for } i, j = 1, \dots, N_S \quad (2.2)$$

where $\dot{\Omega}_i$ is the formation rate of species i and c_j the molar concentration of species j . For non-linear reaction rates the Jacobian matrix depends explicitly on the concentrations and kinetic parameters appearing in the Arrhenius law (1.50). As a consequence the eigenvalues of \underline{J} will also depend on c_j , which means that the characteristic chemical times are function of the local composition at each time. If the eigenvalues are μ_j , the chemical times are defined as:

$$\tau_{c,j} = \frac{1}{|\mu_j|} \quad \text{for } j = 1, \dots, N_s \quad (2.3)$$

If an eigenvalue is large, the corresponding chemical time scale is small; this is the case of *fast chemistry*. On the contrary, when the time scale is large, the definition of *slow chemistry* is commonly adopted.

Figure 1 shows the characteristic time scales of chemical species in a typical, turbulent reacting system. The characteristic chemical times can easily range over more than ten orders of magnitude, from $10^{-9}s$ (fast chemistry) to 10^2s (slow chemistry). The chemical time scales must be considered in relation to the flow time scales occurring in turbulent reacting flows. These flow time scales range from the Kolmogorov time scale τ_K , through the turbulent micromixing time scale τ_{mix} , up to the mean residence time τ_R . Usually the range of flow time scales (depending on the Reynolds number) is not more than four or five orders of magnitude, even in turbulent flames. By taking into account the flow time scales, the chemical times can be divided into three regimes: *slow chemistry* (for which the chemical times are larger than τ_{mix}); *fast chemistry* (chemical time smaller than τ_K) and *finite rate chemistry* in the between. The ratio between the micromixing time scale and the chemical time scale $\tau_{c,j}$ of species j is defined as the Damköhler number:

$$Da_j = \frac{\tau_{mix}}{\tau_{c,j}} \quad \text{for } j = 1, \dots, N_s \quad (2.4)$$

Fast reactions correspond to a large Damköhler number, while slow reactions to a small value. Closure models for the chemical source terms must account for the values of the chemical time scales relative to the time scales of the flow, or, equivalently, must be a function of the Damköhler number.

For example, the characteristic time of CO is usually very small and therefore the assumption of fast chemistry is justified and appropriate. This allows to adopt simplified closure approaches (like the Eddy Dissipation Model, for example), which consider the formation rates of

chemical species controlled by the turbulent mixing. In other words, the chemistry is so fast with respect to the turbulent mixing, that reactions occur instantaneously when the reactants mix together. The combustion is said to be mixing-limited and the complex, chemical kinetic schemes can be safely neglected. On the contrary, the formation of NO_x is governed by very slow reactions, with large activation energies. In this case the reactions rates are controlled by the chemistry, because turbulent mixing can be considered infinitely fast with respect the slow chemical reactions.

Polycyclic Aromatic Hydrocarbons (PAHs) and soot have characteristic times which are in the same range of the flow times (see Figure 1). In this case the (partial) decoupling between chemistry and fluid-dynamics (which can be applied for fast or slow chemistry) is not possible. The effects of turbulent fluctuations on the formation rates are not easy to understand and describe. As a consequence, for example, the flamelet model, which is largely used for industrial applications, cannot be adopted to get reliable and accurate predictions of soot formation.

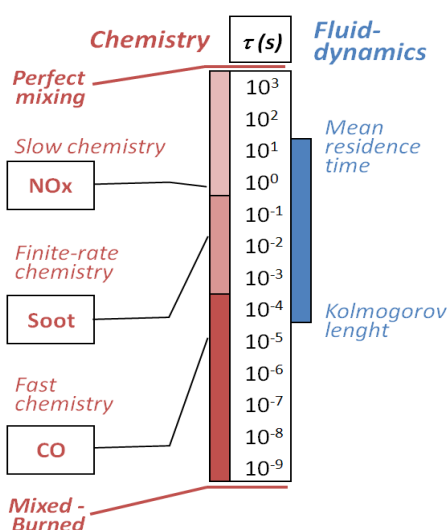


Figure 1. Comparison between chemical time scales and fluid flow time scales in turbulent reacting systems.

2.2.1 Oscillating Perfectly Stirred Reactor

In order to better understand the problem of interactions between turbulence and chemistry and how the turbulent fluctuations affect the formation rates of specific chemical species, a Perfectly Stirred Reactor (PSR) can be conveniently considered. Let us to refer to a PSR fed for example with a mixture of propane and air; the equivalence ratio of this inlet mixture is assumed equal to 2 (in order to enhance the formation of PAHs and soot). The effects of turbulent fluctuations can be “simulated” by forcing the reactor temperature to oscillate about the mean value \bar{T} ; the imposed oscillation is assumed to be for simplicity a sinusoidal function with frequency f and semi-amplitude ΔT , while the residence time is kept fixed (see Figure 2). Of

course, temperature oscillations are expected to induce oscillations in the products concentrations at the exit. From the response of each chemical species, the effects of temperature oscillations on the chemical formation rates can be analyzed and better understood. In particular, the responses of specific chemical species are expected to be different, according to the characteristic times of their chemistry.

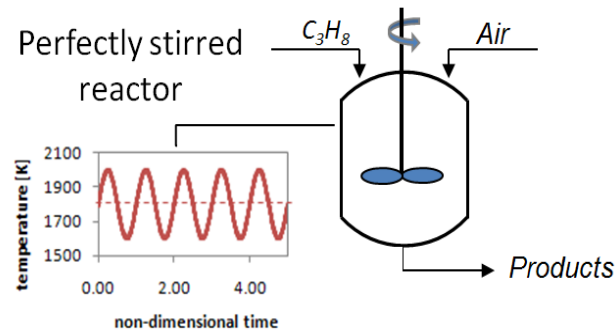


Figure 2. Oscillating perfectly stirred reactor fed with propane and air. The reactor temperature oscillates according to a sinusoidal function, while the residence time is kept fixed.

In Figure 3 the concentrations of CO, CO₂, PAHs and soot at the exit of the PSR are reported versus a non dimensional time t' (simply defined as the ratio between the time and the period of forced oscillations of temperature field); the mean temperature \bar{T} is equal to 1800K and the semi-amplitude of imposed oscillations is 360K (which corresponds to the 20% of \bar{T}). The response of CO to the temperature fluctuations seems to follow the imposed oscillations of the reactor temperature. This result is not so unexpected, since the characteristic time of CO chemistry is very small (see Figure 1). The red line is the composition corresponding to the steady state conditions, i.e. for a fixed reactor temperature equal to the mean value. The response of CO₂ is more complex, probably because this species is involved in equilibrium reactions, strongly dependent on the temperature. Therefore the sensitivity of this species with respect to the temperature is expected to be large. PAHs and soot responses are more strongly affected by the temperature oscillations: the induced oscillations are highly asymmetric and do not follow the sinusoidal shape of the reactor temperature.

Since the reactions governing the formation of chemical species are non linear, we expect a difference between the mean value of composition at the exit ($\bar{\psi}$), which accounts for the temperature oscillations, and the value corresponding to the mean temperature of the reactor (ψ_{steady}), which will be indicated in the following as the steady state value for simplicity:

$$\tilde{\psi} = \frac{1}{\tau} \int_0^{\tau} \psi(t) dt \quad (2.5)$$

$$\psi_{steady} = \psi(\bar{T}) \quad (2.6)$$

where the variable ψ is used to indicate the composition (concentration or molar fraction). Only if the reaction rate were a linear function of the temperature, the difference between $\tilde{\psi}$ and ψ_{steady} would be zero. In Figure 4 the mean and the steady state values of concentrations at the exit versus the reactor temperature are reported (the species are the same considered in Figure 4). As expected, for CO and CO₂ the differences between $\tilde{\psi}$ and ψ_{steady} are small. On the contrary, for PAHs and soot the results are more complex to describe and explain. PAHs concentration shows a maximum at ~1600K when steady state conditions are assumed; if the temperature oscillations are introduced, the mean value becomes smaller than the steady state value in the range ~1400-1700K and larger for temperature in the range ~1700-2100K. Moreover the mean profiles do not present any

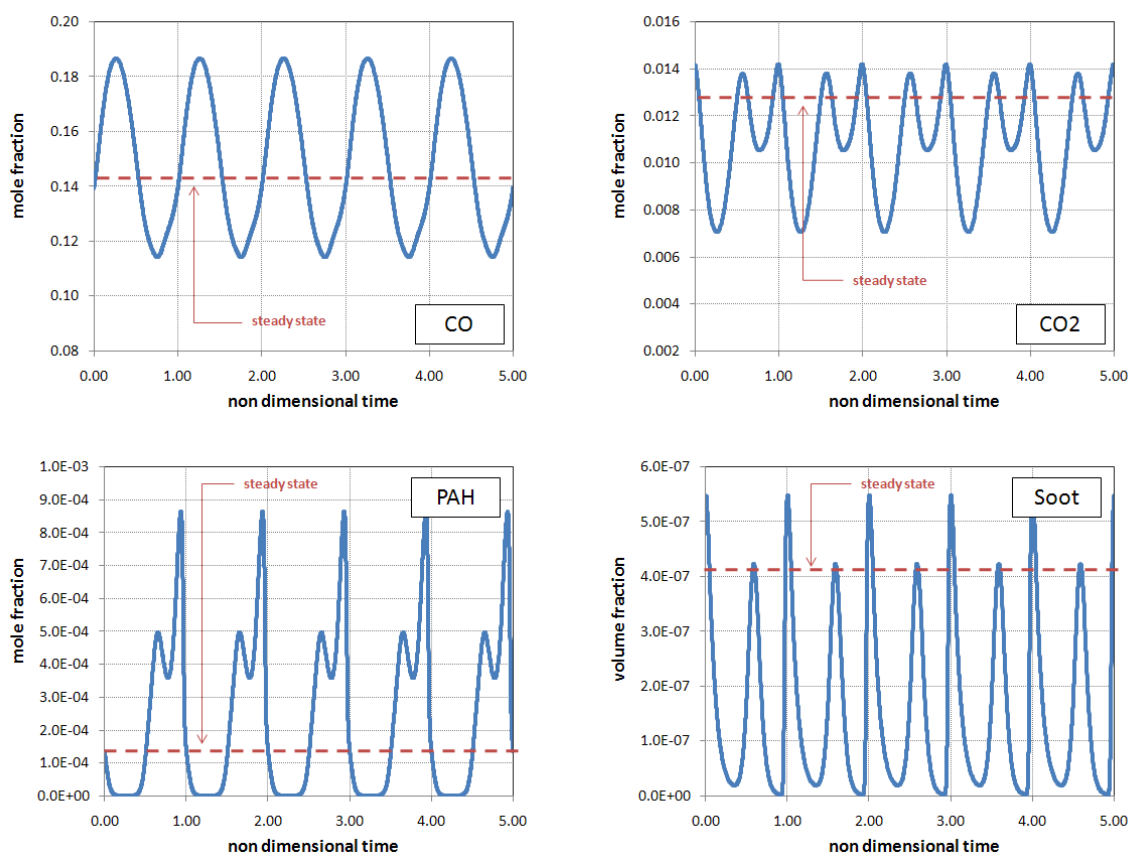


Figure 3. Responses of CO, CO₂, PAH and soot to the imposed temperature oscillations in a perfectly stirred reactor. The mean temperature is 1800K, the semi-amplitude of oscillations is 360K and the frequency 100 Hz.

maximum. The differences between $\tilde{\psi}$ and ψ_{steady} cannot be neglected, especially at mean temperatures around 1700K. More complex is the result for soot. Also in this case, there is a maximum in the curve obtained in steady state conditions (~ 1750 K). The corresponding mean values (which account for temperature oscillations) do not seem to be strongly affected by the value of mean temperature. As a consequence, for mean temperatures smaller than ~ 1600 K or larger than ~ 1950 K the mean concentration results to be larger than the steady state value; on the contrary, between ~ 1600 K and ~ 1950 K the temperature oscillations reduce the mean concentration below the corresponding steady state value. Particularly interesting is the range 1300-1500K: while in steady state conditions there is no soot formation, if the temperature oscillates the soot concentration becomes non negligible. As a consequence, if fluctuations were ignored in calculating the formation rates, the error would be very large and one would arrive to completely wrong conclusions about the soot formation.

In Figure 5 the response of soot is reported also for mean temperatures of 1500K and 2100K respectively. It is interesting to observe that, when the mean temperature is 1500K or 1800K, two minima exist in a single period of oscillation, whilst at 2100K only one minimum is present. The explanation is relatively simple if we refer to Figure 4: the soot concentration has a

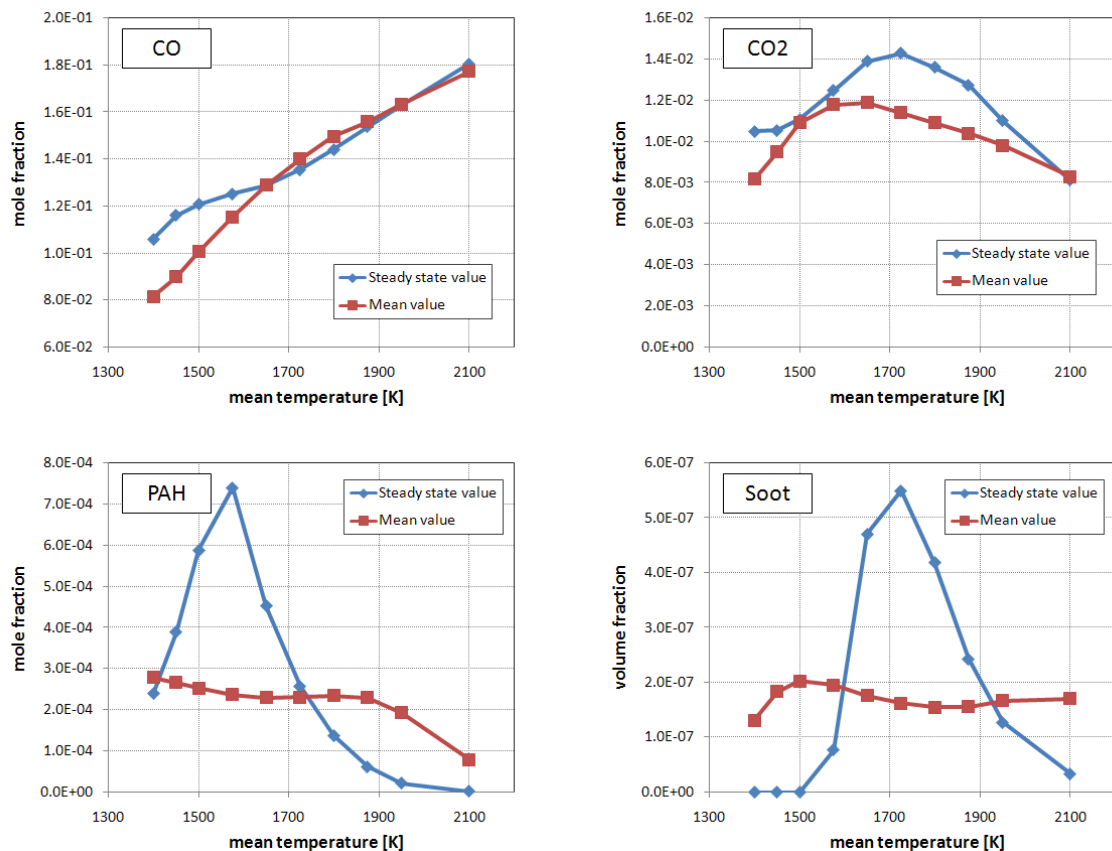


Figure 4. Comparison between steady state and mean compositions of CO, CO₂, PAH and soot at the exit of an oscillating perfectly stirred reactor. The operating conditions are the same reported in Figure 3.

maximum at $\sim 1750\text{K}$, so, if the temperature oscillations are centered in 1500K and 1800K , the two regions where the soot formation tends to zero are crossed by the instantaneous reactor temperature, while at 2100K only the region around the maximum is crossed.

The same analysis can be extended to nitrogen oxides (NO_x), whose chemistry is very slow. It is convenient to change the composition of the inlet mixture, in order to create the conditions which lead to a large amount of NO_x in the reactor. For this purpose the new equivalence ratio is fixed equal to 0.50. The NO response is reported at two different mean temperatures (respectively 1800K and 2100K) in Figure 6. It is evident that the induced oscillations are highly asymmetrical above the steady state value, especially at 2100K . The larger is the activation energy of chemical reactions, the larger are the effects of oscillations (and therefore the non symmetric behavior). The behavior of NO oscillations is very similar for both the temperatures under investigation. The comparison between the mean and steady state values is reported in Figure 7. The mean value is always larger than the steady state value, for every mean temperature. This result can be easily explained, since the NO_x have a monotonic behavior with respect to the temperature, while PAHs and soot do not.

From this simple analysis it is evident that, unless the chemistry of a specific species is very fast, the temperature oscillations strongly affect the mean formation rates. The difference between the mean value and the value corresponding to the mean value of temperature is particularly large for nitrogen oxides. However the effects of oscillations are more complex to describe for PAHs and soot, whose chemistry is not as slow as for the NO_x . The characteristic times of PAHs and soot are in the same range of flow times and therefore it is not so unexpected that the interactions between turbulence and chemistry are more intense and complex.

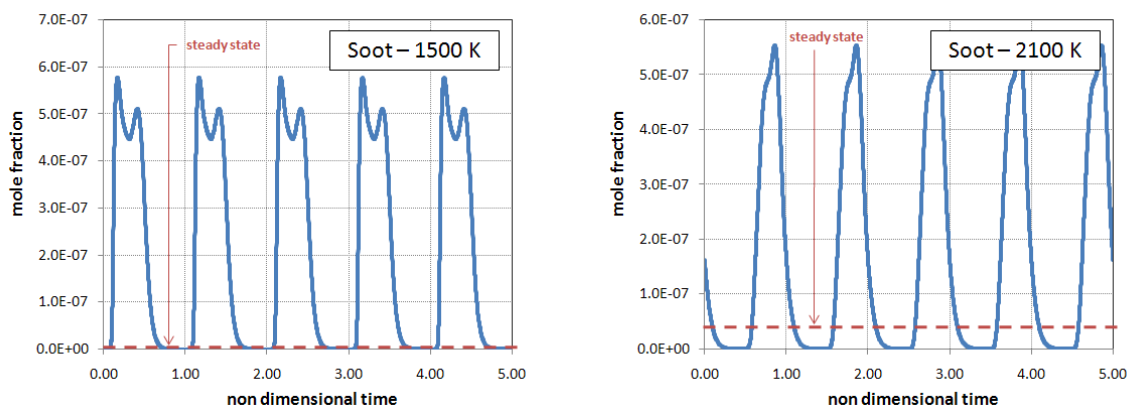


Figure 5. Response of soot to the imposed temperature oscillations in a perfectly stirred reactor at the mean temperatures of 1500K and 2100K . The semi-amplitude of oscillations is 20% of the mean value of temperature and the frequency 100 Hz.

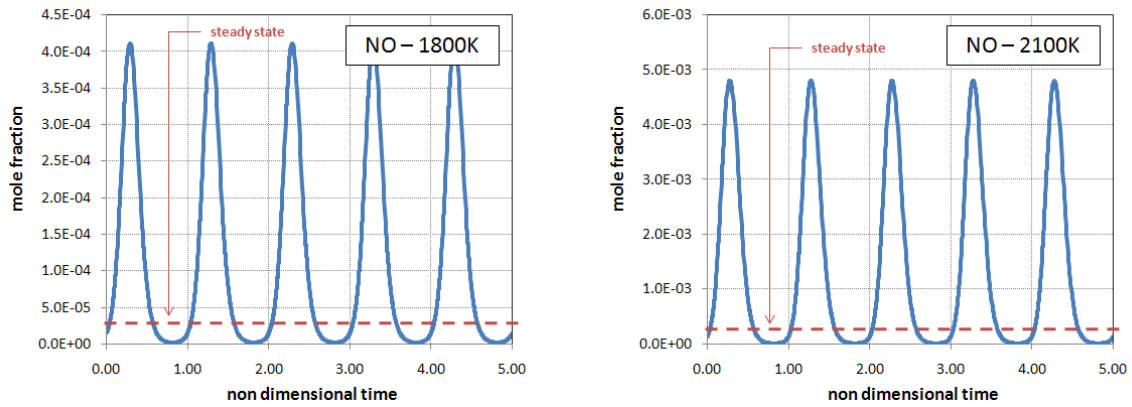


Figure 6. Response of NO to the imposed temperature oscillations in a perfectly stirred reactor at the mean temperatures of 1800K and 2100K. The semi-amplitude of oscillations is 20% of the mean value of temperature and the frequency 100 Hz.

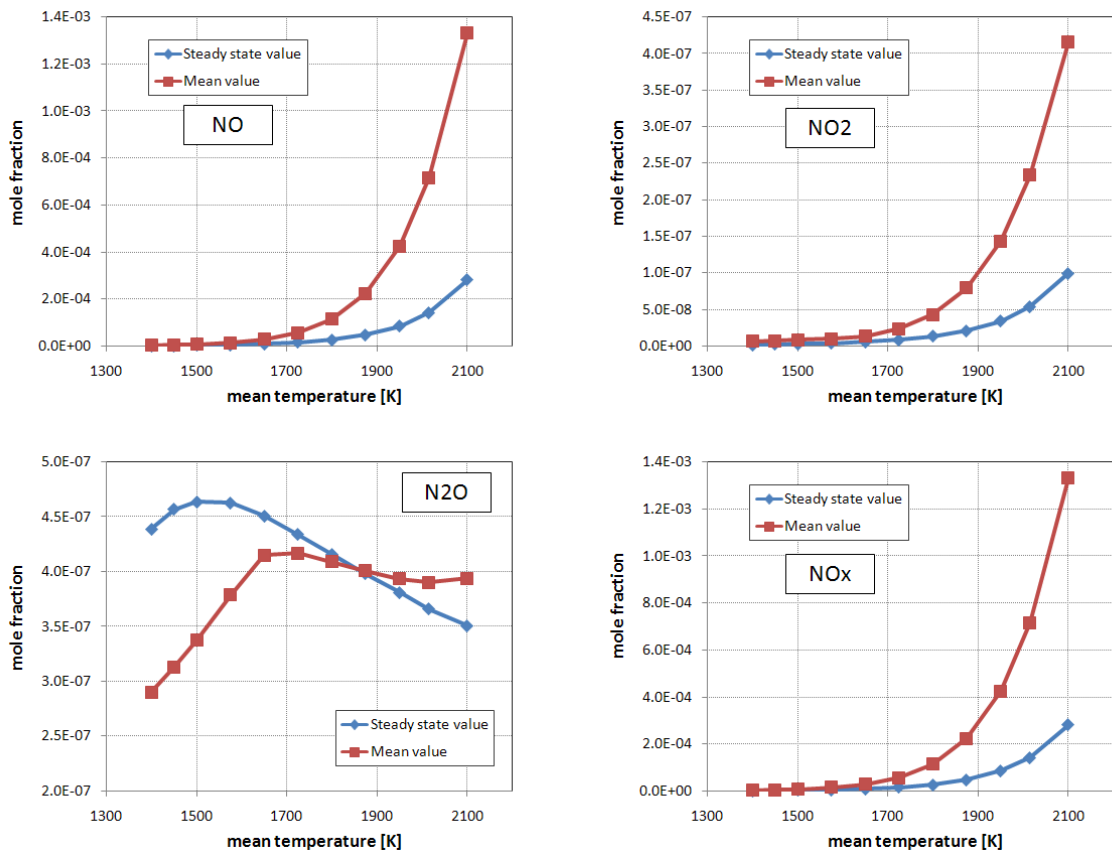


Figure 7. Comparison between steady state and mean compositions of nitrogen oxides at the exit of an oscillating perfectly stirred reactor. The operating conditions are the same reported in Figure 3.

2.3 Series expansion closure

The closure problem reduces to finding a general method for modeling the mean chemical source term only through known variables, i.e. variables which are tracked by the CFD code.

The simplest approach for closing the mean reaction rate is based on series expansions. This is the most direct and most natural approach, but it is very difficult to apply to large and detailed schemes, and it is able to illustrate the difficulties arising from the non-linear character of chemical sources [107]. Let us consider a simple irreversible reaction between the fuel (F) and the oxidizer (O):



The reaction rate can be simply expressed from the Arrhenius law as:

$$\dot{\Omega}_F = -A \cdot \rho^2 T^\beta \omega_F \omega_O e^{-\frac{T_{act}}{T}} \quad (2.8)$$

where A is the factor frequency and T_{act} is the activation temperature. This chemical source term is unclosed at the level of the first order moments. Moreover, due to the exponential linearity in T , the chemical source term will be unclosed at any finite level of moments. The corresponding mean average, which is used in the RANS equations, cannot be expressed as a simple function of mean mass fractions and temperature, because it is highly non linear. The first simple idea is to expand the mean reaction rate as a Taylor series around the mean values of mass fractions and temperature. Even if the reaction is very simple, this expansion leads to a very complex result:

$$\overline{\dot{\Omega}_F} = -A \cdot \overline{\rho^2} \overline{T}^\beta \overline{\omega}_F \overline{\omega}_O e^{-\frac{T_{act}}{\overline{T}}} \left[\begin{aligned} &1 + \frac{\overline{\omega}_F \overline{\omega}_O}{\overline{\omega}_F \overline{\omega}_O} + (P_1 + Q_1) \left(\frac{\overline{\omega}_F \overline{T}^n}{\overline{\omega}_F \overline{T}} + \frac{\overline{\omega}_O \overline{T}^n}{\overline{\omega}_O \overline{T}} \right) \\ &+ (P_2 + Q_2 + P_1 Q_1) \left(\frac{\overline{\omega}_F \overline{T}^{n^2}}{\overline{\omega}_F \overline{T}^2} + \frac{\overline{\omega}_O \overline{T}^{n^2}}{\overline{\omega}_O \overline{T}^2} \right) + \dots \end{aligned} \right] \quad (2.9)$$

where P_n and Q_n are given by:

$$P_n = \sum_{k=1}^n (-1)^{n-k} \frac{(n-1)!}{(n-k)! [(n-k)!]^2 k} \left(\frac{T_{act}}{\overline{T}} \right)^k \quad (2.10)$$

$$Q_n = \frac{b(b+1)\dots(b+n-1)}{n!} \quad (2.11)$$

This equation is characterized by many difficulties. First of all, because of the non-linearities, if only a few terms of the expansion are taken into account, large truncation errors can arise. Moreover, new quantities such as the covariances $\widetilde{\omega_f \omega_o}$ and $\widetilde{\omega_j T^n}$ have to be closed, using for example additional transport equations or simplified approaches. For more realistic and detailed kinetic schemes the expressions corresponding to the Equation (2.9) are more complex and require many additional variables to be transported or modeled. Therefore the computational cost can become very large. It is clear that this kind of approach cannot be followed for realistic kinetic schemes. As a consequence the closure problem reduces to finding general methods for modeling higher-order moments of the composition PDF that are valid over a wide range of chemical time scale.

2.4 Eddy Dissipation model.

When the chemical reactions are fast if compared to the turbulent mixing process, instead of closing the chemical source term using the Taylor's series expansion as described above, a different approach can be followed, as suggested the first time by Spalding [125]. The idea behind this model is that chemistry does not play any explicit role, while turbulence controls the reaction rate. In fact most fuels are fast burning, and the overall reaction rate is controlled by turbulent mixing. In non-premixed flames, turbulence slowly convects/mixes fuel and oxidizer into the reaction zones where they burn quickly. In such cases, the combustion is mixing-limited, and the complex and often unknown, chemical kinetic rates can be safely ignored. This intuitive concept is called the Eddy Break Up (EBU) model. If we consider the simple reaction $F + sO \longrightarrow (1+s)P$, the corresponding turbulent reaction rate can be expressed as:

$$\bar{\dot{\Omega}}_P = C_{EBU} \frac{\bar{\rho}}{\tau_{mix}} \sqrt{\widetilde{\omega_p^2}} \quad (2.12)$$

where C_{EBU} is the Eddy Break Up constant, which needs to be tuned for a particular problem. The turbulent mixing time τ_{mix} can be assumed to be inversely proportional to the specific turbulent dissipation rate \mathcal{E}/κ and therefore the Equation (2.12) can be replaced by the following:

$$\bar{\Omega}_P = C_{EBU} \bar{\rho} \frac{\varepsilon}{\kappa} \sqrt{\bar{\omega}_P'^2} \quad (2.13)$$

A modification of this model is the Eddy Dissipation (ED) model, proposed by Magnussen and Hjertager [88], where the mean reaction rate is related to the mean concentrations instead of variance. In this case the mean reaction rate is taken by the minimum value between three different rates:

$$\bar{\Omega}_F = A \bar{\rho} \frac{1}{\tau_{mix}} \min\left(\tilde{\omega}_F, \frac{\tilde{\omega}_O}{s}, B \frac{\tilde{\omega}_P}{1+s}\right) = A \bar{\rho} \frac{\varepsilon}{\kappa} \min\left(\tilde{\omega}_F, \frac{\tilde{\omega}_O}{s}, B \frac{\tilde{\omega}_P}{1+s}\right) \quad (2.14)$$

where A and B are two model constants. In this expression the reaction rate is limited by the deficient mean species. This is acceptable if the reactions are very fast compared to the turbulent time scales. Generally speaking, this model is too simple to correctly predict the thermal and compositional fields for turbulent non-premixed flames, but can be useful as the first guess solution for the application of more detailed combustion models. One of the main deficiencies of this approach is that it cannot be extended to multiple reactions, and therefore it is not able to manage detailed kinetic schemes (for example for the prediction of pollutant species).

2.5 Eddy Dissipation Concept model.

An extension of the Eddy Dissipation model to incorporate finite rate chemistry in turbulent flames is due to Magnussen, and it is called the Eddy Dissipation Concept (EDC) model [86, 87]. This method is based on a detailed description of the dissipation of turbulent eddies. In a turbulent environment, combustion takes place where there is a molecular mixing, i.e. at small turbulence scales. According to the EDC model, the chemical reactions occur only in small scale micro-mixed turbulent structures known as fine structures. All the reactions of the gas-phase components are assumed to take place within this reaction space that represents the smallest turbulence scales where all turbulent energy is dissipated into heat. As a consequence all reactions in the surrounding fluid are neglected. This assumption is the main simplification, but its validity has been proven in many practical applications.

The fine structures are treated as a perfectly stirred reactors (PSR) with a residence time τ^* and mass fractions ω_k^* . Their volume fraction γ_λ is a function of turbulent properties; the reactions proceed in the fine structures, according to a detailed kinetic scheme, for a time equal to a residence time τ^* and an effective volume V^* :

$$\tau^* = 0.41 \left(\frac{\nu}{\varepsilon} \right)^{1/2} \quad \gamma_\lambda = 2.13 \left(\frac{\nu \varepsilon}{\kappa^2} \right)^{1/4} \quad V^* = \gamma_\lambda \cdot V \quad (2.15)$$

Based on the mass transfer between the fine structures and their surroundings, the mean reaction net mass transfer rate of a species k between the fine structures and the surrounding fluid can be expressed as:

$$\bar{\dot{\Omega}}_k = \frac{\bar{\rho} \gamma_\lambda^2}{\tau^* (1 - \gamma_\lambda^3)} (\tilde{\omega}_k^* - \tilde{\omega}_k^0) \quad \text{for } k = 1, \dots, N_s \quad (2.16)$$

where ρ is the density and ν the laminar kinematic viscosity. The basic assumption is that chemical reactions are quenched if the characteristic chemical times for limiting species are longer than τ^* . The correction factor χ designates the fraction of the fine structures that is heated sufficiently and may react. This factor χ accounts for finite rate chemistry effects when the fast chemistry assumption is used. By treating the reacting fine structures locally as a well stirred reactor that transfers mass and energy only to the surrounding fluid, every chemical kinetic mechanism can be linked with the EDC combustion model. The reaction rates of all species are calculated on a mass and enthalpy balance for the fine structure reactor. The chemical reactions and mass transport can be described by the following algebraic equations for species conservation and total enthalpy:

$$\frac{\rho^*}{\tau^* (1 - \gamma_\lambda^3)} (\tilde{\omega}_k^* - \tilde{\omega}_k^0) = \dot{\Omega}_k^* \quad \text{for } k = 1, \dots, N_s \quad (2.17)$$

$$\frac{\rho^*}{\tau^* (1 - \gamma_\lambda^3)} \sum_{k=1}^{N_s} (\tilde{\omega}_k^* \hat{H}_k^* - \tilde{\omega}_k^0 \hat{H}_k^0) = \dot{Q}^* \quad (2.18)$$

where \dot{Q}^* is the net power per volume that is transferred between the fine structures and the surroundings by other mechanisms, such as radiation. From the last two Equations (2.17) and (2.18) it is possible to calculate the mass fractions $\tilde{\omega}_k^*$ and the enthalpy \hat{H}_k^* in the fine structures as a function of the known quantities $\tilde{\omega}_k^0$ and \hat{H}_k^0 . Then the mean reaction rates of all species can be calculated by using either the mass transfer rate expressed by (2.16) or the chemical reaction rate (2.17) in the fine structures.

The EDC model can incorporate detailed chemical mechanisms into turbulent reacting flows and can be used when the assumption of fast chemistry is invalid. However, typical mechanisms are invariably stiff and their numerical integration is computationally costly. Since the

chemical reaction rates in the fine structures are functions of all the mass fractions and the temperature, a set of nonlinear, coupled, algebraic equations must be solved.

2.6 Steady Laminar Flamelet Model

The mixture fraction is one of the most important quantities for describing non premixed combustion. In a two-feed system with equal diffusivities for all species, the local stoichiometry can be conveniently formed into a mixture fraction variable using elemental mass fractions. The elemental mass fraction Z_i for the element i is defined as:

$$Z_i = \sum_{k=1}^{N_S} \mu_{ik} \omega_k \quad i = 1, 2, \dots, N_E \quad (2.19)$$

where μ_{ik} is the mass ratio of the element i in species k , N_S is the total number of species and N_E is the total number of elements. In chemical reactions the individual species mass fractions are not conserved due to production and consumption, but the elemental mass fractions are conserved, because they can be changed only by mixing. Therefore the elemental mass fractions variables are useful quantities for describing the non-premixed combustion properties. In particular the individual element conservation property results in the following:

$$\sum_{k=1}^{N_S} \mu_{ik} \dot{\Omega}_k = 0 \quad i = 1, 2, \dots, N_E \quad (2.20)$$

If the species equations (1.34) are multiplied by μ_{ik} and summed over all the species and if we assume equal diffusivities Γ for every species, the following equation can be obtained (in Cartesian coordinates):

$$\frac{\partial}{\partial t}(\rho Z_k) + \frac{\partial}{\partial x_i}(\rho u_i Z_k) = \frac{\partial}{\partial x_i} \left(\rho \Gamma \frac{\partial Z_k}{\partial x_i} \right) \quad (2.21)$$

If we consider a two-stream problem having an inlet of fuel stream and a second inlet with an oxidizer stream, the elemental mass fractions can be normalized, such that all the conserved scalars are linearly related with identical boundary conditions. This variable is called mixture fraction and is defined in this case as:

$$Z = \frac{Z_k - Z_{k,O}}{Z_{k,F} - Z_{k,O}} \quad (2.22)$$

where the subscript F refers to the fuel stream and the subscript O to the oxidizer stream. It is easy to demonstrate that the conservation equation for the mixture fraction is the same as the elemental mass fraction. Therefore the mixture fraction is a conserved scalar, whose transport equation is governed by simple convection and diffusion terms, without a source term:

$$\frac{\partial}{\partial t}(\rho Z) + \frac{\partial}{\partial x_i}(\rho u_i Z) = \frac{\partial}{\partial x_i} \left(\rho \Gamma \frac{\partial Z}{\partial x_i} \right) \quad (2.23)$$

The transport equation for the Favre mixture fraction can be obtained from Equation (2.23) reported above:

$$\frac{\partial}{\partial t}(\bar{\rho} \tilde{Z}) + \frac{\partial}{\partial x_i}(\bar{\rho} \tilde{u}_i \tilde{Z}) = \frac{\partial}{\partial x_i} \left(\frac{\mu_t}{\sigma_t} \frac{\partial \tilde{Z}}{\partial x_i} \right) \quad (2.24)$$

Usually a transport equation for the variance of the mixture fraction is needed for the application of presumed PDF methods or for estimating the magnitude of effects of turbulent motions on the chemical formation rates:

$$\frac{\partial}{\partial t}(\bar{\rho} \tilde{Z}^2) + \frac{\partial}{\partial x_i}(\bar{\rho} \tilde{u}_i \tilde{Z}^2) = \frac{\partial}{\partial x_i} \left(\frac{\mu_t}{\sigma_t} \frac{\partial \tilde{Z}^2}{\partial x_i} \right) + C_G \frac{\mu_t}{Sc_t} \left(\frac{\partial \tilde{Z}}{\partial x_i} \right)^2 - C_D \bar{\rho} \frac{\tilde{\epsilon}}{\tilde{\kappa}} \tilde{Z}^2 \quad (2.25)$$

where the last two terms are the generation and the dissipation term respectively. The constant C_D appearing in the dissipation term can be derived by turbulent spectral analysis and is usually set equal to 2; the constant C_G is usually assumed to be equal to 2.86.

The molecular diffusivity in Equations (2.24) and (2.25) is much smaller than the turbulent diffusivity and has therefore been neglected in the equations reported above. Therefore the assumption of equal diffusivities appears to be reasonable.

If the system is not adiabatic, an enthalpy balance equation must be solved:

$$\frac{\partial}{\partial t}(\bar{\rho} \hat{C}_p \tilde{H}) + \frac{\partial}{\partial x_i}(\bar{\rho} \hat{C}_p \tilde{u}_i \tilde{H}) = \frac{\partial}{\partial x_i} \left(\frac{\mu_t}{\sigma_t} \frac{\partial \tilde{H}}{\partial x_i} \right) + \bar{Q}_h \quad (2.26)$$

where \hat{C}_p is the specific heat of the mixture, and \bar{Q}_h is a generic source term that can account for the non-adiabatic behavior of the system (for example radiation heat losses, heat exchange with walls and with a second phase if present, etc.).

The main idea behind presumed PDF approach consists in evaluating the temperature and the composition fields from the temperature and composition corresponding to each value of mean mixture fraction \tilde{Z} , mixture fraction variance $\widetilde{Z'^2}$ and enthalpy \widetilde{H} for a non-adiabatic system. If the enthalpy losses are negligible the average value of the scalar ϕ can be evaluated by the following integral:

$$\tilde{\phi} = \int_0^1 P(Z) \cdot \phi(Z) \cdot dZ \quad (2.27)$$

where $P(Z)$ is the mixture fraction PDF and $\phi(Z)$ is the relationship that links the mixture fraction and the scalar concentration or temperature. If the system is not adiabatic, the joint composition-enthalpy PDF should be used. However, in order to simplify the problem, it is assumed that enthalpy fluctuations are independent on the enthalpy level, so that heat losses do not affect the turbulent enthalpy fluctuations. As a consequence the PDF of the mixture fraction is used to compute the mean values according to the following integral:

$$\tilde{\phi} = \int_0^1 P(Z) \cdot \phi(Z, \widetilde{H}) \cdot dZ \quad (2.28)$$

Several presumed shapes of PDF have been employed for the mixture fraction, in particular the double-delta PDF, the clipped Gaussian PDF and the β -PDF. The double delta PDF represents the distribution as a summation of two delta functions, corresponding to two partially mixed and reacting environments:

$$P(Z) = \begin{cases} 0.50 & Z = \tilde{Z} - \sqrt{\widetilde{Z'^2}} \\ 0.50 & Z = \tilde{Z} + \sqrt{\widetilde{Z'^2}} \\ 0 & elsewhere \end{cases} \quad (2.29)$$

The clipped Gaussian PDF and the β -PDF are more accurate distributions. The clipped Gaussian PDF is based upon the clipping of a Gaussian function, so that the probability is finite only in the allowable region of mixture fraction:

$$P(Z) = \alpha_1 \cdot \delta(Z) + (1 - \alpha_1 - \alpha_2) \frac{G(Z)}{I_G} + \alpha_2 \cdot \delta(1 - Z) \quad (2.30)$$

where $\delta(Z - Z_0)$ is the Dirac delta function centered in $Z = Z_0$; the variable I_G is defined as:

$$I_G = \int_0^1 G(Z) dZ \quad (2.31)$$

while the free parameters α_1 , α_2 are function of the mean \tilde{Z} and the variance $\widetilde{Z'^2}$ of the mixture fraction. Some additional details can be found in Appendix A.

The β -PDF is the most used approach for modeling the mixture fraction PDF, which is described by the following function:

$$p_Z(Z) = \frac{Z^{a-1} (1-Z)^{b-1}}{\int_0^1 Z^{a-1} (1-Z)^{b-1} dZ} \quad (2.32)$$

The β -PDF contains two parameters that can be expressed through the mixture fraction mean and variance by:

$$a = \tilde{Z} \left[\frac{\tilde{Z}(1-\tilde{Z})}{\widetilde{Z'^2}} - 1 \right] \quad (2.33)$$

$$b = (1 - \tilde{Z}) \left[\frac{\tilde{Z}(1-\tilde{Z})}{\widetilde{Z'^2}} - 1 \right] \quad (2.34)$$

The β -PDF is widely used in many codes to approximate the mixture fraction PDF for binary mixing. This choice is motivated by the fact that in many of the canonical turbulent mixing configurations the experimentally observed mixture fraction PDF is well approximated by a β -PDF.

Thus if transport equations for (2.24) and (2.25) are solved, then the presumed PDF will be known at every point in the flow domain. It is evident that the basic assumption consists in assuming that the instantaneous thermo-chemical state of the fluid is related to a conserved scalar

quantity known as the mixture fraction. In this way the species transport equations can be reduced to the transport equations for the mixture fraction \tilde{Z} and one for its variance \tilde{Z}^2 and, if the system is not adiabatic, to an additional equation for the enthalpy.

The temperature and thermo-chemical variables are extracted from a flamelets library, in which the temperature and composition corresponding to each value of mean mixture fraction \tilde{Z} , mixture fraction variance \tilde{Z}^2 and enthalpy \tilde{H} are stored. The mean values of scalars in each computational cell are calculated by interpolation between the neighboring stored values. In this way the turbulence chemistry interactions are pre-processed and calculations do not need to be repeated at each iteration, thus resulting in a relevant saving of computational resources. The detailed chemistry treatment is included in the function $\phi(Z, \hat{H})$, which can be evaluated with different options, as reported in the following.

2.6.1 *Mixed-Burned approach*

The simplest approach is the so-called “*mixed-burned*” or “*flame sheet*” approximation. Such approach assumes that the reactions are infinitely fast and irreversible. In this case no kinetic information is needed and the composition can be computed directly from the reaction stoichiometry, since reactants and products cannot coexist. This approach cannot be used for detailed kinetic schemes and is usually too poor to give satisfactory results, even for the simplest cases.

2.6.2 *Equilibrium approach*

A slightly more accurate approach is the so called “*equilibrium*” assumption. By minimizing the Gibbs free energy of the gas mixture for each assigned value of mixture fraction, variance and enthalpy (for non-adiabatic systems), it is possible to evaluate the temperature and composition of the mixture in equilibrium conditions. Also in this case it is not necessary to have any kinetic data, because the system is considered at equilibrium conditions; only the species present in the system have to be specified. This is a simple reaction model, which is largely used by commercial codes for the numerical prediction of turbulent non-premixed flames. The parameterization is based only by the mixture fraction and its variance if there is no heat loss. In case of non-adiabatic flames, the parameterization must be performed in terms of \tilde{Z} , \tilde{Z}^2 and \tilde{H} . Due to the fast chemistry assumption, this model is not able to give correct prediction of chemical species whose chemistry is slow if compared to the characteristic turbulence times. This is especially true for soot particles and nitrogen oxides.

2.6.3 Flamelets approach

In most cases the non-equilibrium effects must be taken into account to correctly describe a non premixed flame. In such situation the finite rate chemistry need to be considered trough an appropriate approach, as the Steady Laminar Flamelet Model (SLF), which considers a turbulent flame as an ensemble of discrete laminar flames. The SLF model is able to take into account the stretching of the flame (mainly due to the turbulent strain), whose main effects are strong deviations from equilibrium conditions. In particular, the reaction rate is nearly zero at low temperatures and it becomes significant only near the stoichiometric surface defined by the stoichiometric mixture fraction value Z_{st} . As a consequence the reaction is confined in a thin reaction zone, whose thickness is smaller than the Kolmogorov scale.

With few simplifications, the governing equations for species and temperature in one-dimensional laminar diffusion flames can be written in mixture fraction space as [105]:

$$\frac{1}{2} \rho \chi \frac{1}{Le_i} \frac{\partial^2 \omega_i}{\partial Z^2} + \dot{\Omega}_i - \frac{1}{2} \frac{\partial \omega_i}{\partial Z} \left[\rho \chi \frac{1}{Le_i^2} \frac{\partial Le_i}{\partial Z} - \frac{1}{2} \left(1 - \frac{1}{Le_i} \right) \left(\frac{\partial \rho \chi}{\partial Z} + \rho \chi \frac{\hat{C}_p}{\lambda} \frac{\partial}{\partial Z} \left(\frac{\lambda}{\hat{C}_p} \right) \right) \right] = 0 \quad (2.35)$$

$$\frac{1}{2} \rho \hat{C}_p \chi \frac{\partial^2 T}{\partial Z^2} - \sum_{i=1}^{N_s} \hat{H}_i \dot{\Omega}_i + \frac{\rho \chi}{2} \frac{\partial T}{\partial Z} \left[\frac{\partial \hat{C}_p}{\partial Z} + \sum_{i=1}^{N_s} \frac{1}{Le_i} \hat{C}_{p,i} \frac{\partial \omega_i}{\partial Z} \right] + \dot{Q}_{rad} = 0 \quad (2.36)$$

The last term in the equation (2.36) quantifies the heat loss by radiation from the diffusion flame, usually modeled with an optically thin radiation model. In both equations (2.35) and (2.36) Le_i is the Lewis number of species i , defined as the ration between thermal and molecular diffusivities:

$$Le_i = \frac{\lambda}{\rho \hat{C}_p \Gamma_i} \quad (2.37)$$

The scalar dissipation rate χ in the laminar flamelet equation is a function of Z and is usually modeled as:

$$\chi = \chi_{st} \cdot f(Z) \quad (2.38)$$

where χ_{st} is the scalar dissipation rate corresponding to the stoichiometric mixture fraction and $f(Z)$ is a model function which can be derived from the one-dimensional counter-flow diffusion flame layer model:

$$f(Z) = \exp\left(-2\left[\operatorname{erf}^{-1}(2Z-1)\right]^2\right) \quad (2.39)$$

While the mixture fraction and its variance are determined from the transport equations (2.24) and (2.25), the mean scalar dissipation rate at stoichiometric conditions can be evaluated by the following expression:

$$\tilde{\chi}_{st} = C_\phi \frac{\mathcal{E}}{\kappa} \widetilde{Z}^2 \quad (2.40)$$

Its variance is usually assumed to be constant, or, more commonly, is set to zero, in order to simplify the application of the joint PDF for the calculation of average values of scalars (temperature and composition). When χ_{st} decreases, chemistry tends to reach equilibrium conditions; on the contrary, when χ_{st} exceeds a critical value, the flamelet is quenched.

The average value of each scalar can be then evaluated from the joint PDF of mixture fraction, scalar dissipation rate and enthalpy:

$$\tilde{\phi} = \int_0^1 \int_0^\infty \int_{-\infty}^\infty P(Z, \chi_{st}, \hat{H}) \cdot \phi(Z, \chi_{st}, \hat{H}) \cdot dZ \cdot d\chi_{st} \cdot d\hat{H} \quad (2.41)$$

If mixture fraction, scalar dissipation rate and enthalpy are considered to be statistically independent (uncorrelated), the joint-PDF reported above can be simplified as the product of three marginal PDFs, assuming a functional form for each of them:

$$\tilde{\phi} = \int_0^1 \int_0^\infty \int_{-\infty}^\infty P(Z) P(\chi_{st}) P(\hat{H}) \cdot \phi(Z, \chi_{st}, \hat{H}) \cdot dZ \cdot d\chi_{st} \cdot d\hat{H} \quad (2.42)$$

Usually a β -PDF is used for the mixture fraction, a log-normal PDF for the scalar dissipation rate and a Dirac delta distribution for the enthalpy.

Also in this case it is convenient to store the flamelet calculations in a look-up table, where the temperature and composition of the system is related to the mean mixture fraction, mixture fraction variance, scalar dissipation rate and enthalpy if necessary. Following this approach, the chemistry is pre-computed and the thermo-chemical state of the mixture can be read from the look-up table, once the mixture fraction, mixture fraction variance, scalar dissipation rate and enthalpy have been computed by the CFD code. It is necessary to point out that the SLF is not able to predict

large non-equilibrium effect caused by aerodynamic straining. The reaction is assumed to respond instantaneously to the strain, relaxing to equilibrium as the strain relaxes.

2.7 Unsteady Laminar Flamelet Model

The steady laminar flamelet approach models local chemical non-equilibrium due to the straining effect of turbulence. In many combustors the strain is small at the outlet and the steady flamelet model predicts all species, including slow-forming species like NOx, to be near equilibrium, which is often inaccurate. The cause of this inaccuracy is the disparity between the flamelet time-scale, which is the inverse of the scalar dissipation, and the slow-forming species time-scale, which is the residence time since the species started accumulating after mixing in the combustor. The Unsteady Laminar Flamelet Model (ULF) can predict slow-forming species, such as gaseous pollutants or product yields in liquid reactors, more accurately than the steady laminar flamelet model. Computationally expensive chemical kinetics are reduced to one dimension and the model is significantly faster than EDC or PDF (see next Paragraph). To account for the unsteady effects, the one-dimensional laminar diffusion flame equations becomes [99, 104]:

$$\rho \frac{\partial \omega_i}{\partial t} = \frac{1}{2} \rho \chi \frac{1}{Le_i} \frac{\partial^2 \omega_i}{\partial Z^2} + \dot{\Omega}_i - \frac{1}{2} \frac{\partial \omega_i}{\partial Z} \left[\rho \chi \frac{1}{Le_i^2} \frac{\partial Le_i}{\partial Z} - \frac{1}{2} \left(1 - \frac{1}{Le_i} \right) \left(\frac{\partial \rho \chi}{\partial Z} + \rho \chi \frac{\hat{C}_p}{\lambda} \frac{\partial}{\partial Z} \left(\frac{\lambda}{\hat{C}_p} \right) \right) \right] \quad (2.43)$$

$$\rho \hat{C}_p \frac{\partial T}{\partial t} = \frac{1}{2} \rho \hat{C}_p \chi \frac{\partial^2 T}{\partial Z^2} - \sum_{i=1}^{N_s} \hat{H}_i \dot{\Omega}_i + \frac{\rho \chi}{2} \frac{\partial T}{\partial Z} \left[\frac{\partial \hat{C}_p}{\partial Z} + \sum_{i=1}^{N_s} \frac{1}{Le_i} \hat{C}_{p,i} \frac{\partial \omega_i}{\partial Z} \right] + \dot{Q}_{rad} \quad (2.44)$$

The main difference with respect to the SLF equations is the accumulation term on the left-hand side. The time-dependent formulation is able to incorporate processes that occur at a time scale different than the diffusion time scale in mixture fraction. The time dependent formulation facilitates to incorporate processes that occur at a different time scale than the diffusion time scale in the mixture fraction.

The scalar dissipation at stoichiometric mixture fraction (χ_{st}) is required by the flamelet species equation. Depending on the functional dependency of scalar dissipation in time, different unsteady phenomena taking place at that particular time scale can be captured. Usually it is calculated from the steady-state field at each time step as a probability-weighted volume integral. The unsteady laminar flamelet model can be used to predict slow-forming intermediate and product species which are not in chemical equilibrium. Typical examples of slow-forming species are gas-phase pollutants like NOx, and product compounds in liquid reactors. By reducing the chemistry

computation to one dimension, detailed kinetics with multiple species and stiff reactions can be economically simulated in complex 3D geometries.

2.8 Reaction Time Flamelet Model

Both the SLFM and ULFM models account for the heat loss effects through an optically-thin radiation model, as the formulation reported in Equations (2.36) and (2.44) do not allow parameterizing the heat loss effects at the subgrid scale level. The heat loss effects are particularly important on the emissions of many pollutant species, especially nitrogen oxides and soot. The Reaction Time Flamelet Model (RTFM) is a subgrid scale reaction model formulated with a NO formation reaction time scale and a heat loss parameter for accurately accounting for the unresolved scales [38]. The following equations are solved to parameterize the state space in the RTFM model:

$$\rho \frac{\partial \omega_i}{\partial t_{NO}} = \frac{1}{2} \rho \chi \frac{\partial^2 \omega_i}{\partial Z^2} + \dot{\Omega}_i \quad (2.45)$$

$$\rho \hat{C}_p \frac{\partial T}{\partial t_{NO}} = \frac{1}{2} \rho \hat{C}_p \chi \frac{\partial^2 T}{\partial Z^2} - \sum_{i=1}^{NS} \hat{H}_i \dot{\Omega}_i + \gamma \dot{Q}_{rad} \quad (2.46)$$

where t_{NO} is the NO formation time scale and γ is the normalized heat loss parameter, which is defined as:

$$\gamma = \frac{\hat{H}_a - \hat{H}}{\hat{H}_a - \hat{H}_{f,a}^0} \quad (2.47)$$

In the expression reported above, the enthalpies \hat{H} , \hat{H}_a and $\hat{H}_{f,a}^0$ are evaluated as:

$$H = \sum_{k=1}^{N_s} \omega_k \Delta H_f^0 + \sum_{k=1}^{N_s} \omega_k \int_{T_{ref}}^T C_{p,k} dT \quad (2.48)$$

$$H_a = \sum_{k=1}^{N_s} \omega_k \Delta H_f^0 + \sum_{k=1}^{N_s} \omega_k \int_{T_{ref}}^{T_{ad}} C_{p,k} dT \quad (2.49)$$

$$H_{f,a}^0 = \sum_{k=1}^{N_s} \omega_{k,a} \Delta H_f^0 \quad (2.50)$$

where T_a and $\omega_{k,a}$ are the temperature and composition corresponding to adiabatic conditions respectively. The solutions of the above equations are parameterized by (Z, t_{NO}, γ) .

The real challenge in solving the RTFM equations arises in specifying the scalar dissipation profiles with respect to time. Different time dependent phenomena can be captured by modeling this term.

2.9 Transported Probability Density Function

As reported in the previous sections, the Favre-averaged species equations leads to unknown terms for the turbulent scalar flux and the mean reaction rate. The turbulent scalar flux can be modeled with reasonable accuracy by gradient diffusion (treating turbulent convection as enhanced diffusion). However the mean reaction rate, which is invariably highly non-linear, is very difficult to model. The EDC and flamelets model in some cases cannot be able to correctly describe a turbulent flame. An alternative to Favre-averaging the species and energy equations is to derive a transport equation for their single-point, joint Probability Density Function (PDF). In other words the PDF approach trays to calculate the shape of the joint scalar PDF from its transport equation. PDF represents a very general statistical description for turbulent reacting flows and it is applicable to premixed, non premixed and partially premixed combustion. The joint composition PDF of the scalar involved in the reacting system is defined as the probability of the scalar ϕ_i of laying within the range ψ_i and $\psi_i + d\psi_i$:

$$f_\phi(\bar{\Psi}; x, t) = P[\psi_i < \phi_i(x, t) < \psi_i + d\psi_i] \quad (2.51)$$

The advantage of such formulation is that the chemical source term can be treated exactly by means of the joint composition PDF:

$$\widetilde{\dot{\Omega}}_i = \int_0^{+\infty} \dot{\Omega}_i \cdot f_\phi(\bar{\Psi}; x, t) \cdot d\bar{\Psi} \quad (2.52)$$

The closure problem is then solved if we find an appropriate form of the joint composition PDF, or if we are able to compute it.

The transport equation for the joint PDF of velocities and scalars can be derived from the Navier-Stokes equations and the convection-diffusion equation [108]:

$$\frac{\partial}{\partial t}(\rho f_\phi) + \frac{\partial}{\partial x_i}(\rho u_i f_\phi) + \frac{\partial}{\partial \psi_k}(\rho S_k f_\phi) = -\frac{\partial}{\partial x_i} \left[\rho \langle u_i'' | \bar{\psi} \rangle f_\phi \right] + \frac{\partial}{\partial \psi_k} \left[\rho \left\langle \frac{1}{\rho} \frac{\partial J_{i,k}}{\partial x_i} \middle| \bar{\psi} \right\rangle f_\phi \right] \quad (2.53)$$

where f_ϕ is Favre joint-PDF of composition, $\bar{\psi}$ is the composition space vector, u_i'' is the fluid velocity fluctuation vector and $J_{i,k}$ the molecular diffusion flux vector. The notation $\langle \dots \rangle$ denotes expectations, and $\langle A|B \rangle$ is the conditional probability of event A , given the event B occurs.

The PDF, denoted by f_ϕ , can be considered to be proportional to the fraction of the time that the fluid spends at each species and temperature state. The PDF f_ϕ has N_S+1 dimensions for the N_S species and temperature spaces. From the PDF, any thermo-chemical moment (e.g., mean or RMS temperature, mean reaction rate) can be calculated. It is possible to solve the transport equation for the joint composition PDF of each scalar closing exactly the chemical source terms with no assumptions on the functional form of the PDF.

In Equation (2.53), the terms on the left-hand side are closed, while those on the right-hand side are not and require modeling. The terms on the left-hand side represent the accumulation, the convective transport in the physical space (due to the mean velocity field) and in the composition space (due to the chemical reactions) respectively and can be evaluated exactly. The terms on the right-hand side, representing the transport in the composition space due to the molecular diffusion, and in the physical space due to the fluctuations of velocity, need to be closed.

The principal strength of the PDF transport approach is that the highly-non-linear reaction term is completely closed and requires no modeling. The two terms on the right-hand side represent the PDF change due to scalar convection by turbulence (turbulent scalar flux), and molecular mixing/diffusion, respectively. The turbulent scalar flux term is unclosed, and is usually modeled by the gradient-diffusion assumption:

$$\rho \langle u_i'' | \bar{\psi} \rangle f_\phi = -\frac{\mu_t}{\rho \cdot Sc_t} \frac{\partial f_\phi}{\partial x_i} \quad (2.54)$$

where μ_t is the turbulent viscosity and Sc_t is the turbulent Schmidt number. A turbulence model is required for composition PDF transport simulations, and this determines μ_t .

The term which describes the micromixing can be closed using different models proposed in the last decades [39]. For example according to the IEM approach:

$$\left\langle \frac{1}{\rho} \frac{\partial J_{i,k}}{\partial x_i} \middle| \bar{\psi} \right\rangle f_\phi = -\frac{1}{2\tau_{mix}} (\psi - \langle \phi \rangle) f_\phi \quad (2.55)$$

where τ_{mix} is the micro-mixing time scale. The correct description of mixing through a numerical model is critical because combustion occurs at the smallest molecular scales when reactants and heat diffuse together. Modeling mixing in PDF methods is not straightforward, and is the weakest point in the PDF transport approach.

The PDF has N_S+1 dimensions and the solution of its transport equation by conventional finite-difference or finite-volume schemes is not tractable. Instead, a Monte Carlo method is used, which is ideal for high-dimensional equations since the computational cost increases just linearly with the number of dimensions. The disadvantage is that statistical errors are introduced, and these must be carefully controlled.

To solve the modeled PDF transport equation, an analogy is made with a Stochastic Differential Equation (SDE) which has identical solutions. The Monte Carlo algorithm involves notional particles which move randomly through physical space due to particle convection, and also through composition space due to molecular mixing and reaction. The particles have mass and, on average, the sum of the particle masses in a cell equals the cell mass (cell density times cell volume).

Transported PDF codes are usually more CPU intensive than other approaches, for example moment and presumed PDF closures, and not always are tractable for engineering applications. In fact Monte Carlo methods are usually employed for solving the PDF transport equations. Therefore the PDF is treated indirectly by tracking a finite but very large number of notional particles through the computational domain. Of course the computational cost becomes large very fast if the number of scalars is large. In most applications a reaction look-up table is used to store pre-computed changes due to chemical reactions. Current research efforts are focused on smart tabulation schemes capable of handling larger numbers of chemical species.

2.10 Conclusions

The so called chemical-source-term closure problem in turbulent reacting flows is introduced. The main issues related to the strong interactions between turbulent fluctuations and formation of chemical species are presented from a Chemical-Reaction-Engineering (CRE) point of view through numerical investigations performed on an oscillating perfectly stirred reactor. The response of chemical species to the imposed fluctuations of temperature appeared to be strongly affected by the characteristic chemical times. In particular the formation of nitrogen oxides, whose

chemistry is very slow, resulted affected by the turbulent fluctuations in a simple way. The response of PAHs and soot was more complex, because the characteristic times of chemistry are in the same range of characteristic mixing times; as a consequence the interactions between the chemistry and turbulence are complex and very difficult to describe.

The most widely used methods for closing the chemical source term in the Reynolds-Averaged scalar transport equations were briefly summarized.

3 NO_x predictions in turbulent non premixed flames

In this chapter an effective methodology for the prediction of NO_x in turbulent non premixed flames by using computational fluid dynamics (CFD) and detailed chemical kinetics is presented and discussed. The proposed approach is based on the general concept of “Reactor Network Analysis” and can be successfully applied even in complex geometries, which are very usual in industrial cases. In order to show the validity and the accuracy of such methodology several turbulent non premixed flames are numerically investigated.

3.1 Introduction

Turbulent non premixed flames are largely used in many practical combustion devices to convert chemical energy into work, due to the high efficiency, large heat releases and safety reasons. However diffusion flames produce more pollutant species (in particular nitrogen oxides and soot) than premixed flames. Since combustion devices need to respect always more stringent limitations concerning the emissions of pollutants, the design of new burners relying on non premixed flames cannot neglect the issues related to the formation of such pollutant species. This explains the increasing demand for computational tools capable of characterizing the combustion systems in a reliable, accurate way, also in terms of pollutant species. However, even with the continuous increase of computer power and speed, the direct coupling of detailed kinetics, which is usually required to obtain accurate predictions of most pollutants, and complex CFD is not possible (especially when considering the typical dimensions of the computational grids used for complex geometries and industrial applications). The computational cost significantly increases with the number of cells (N_C) of the computational grid and also with the second or third power of the number of reacting species (N_S). Moreover, the turbulent flow of most practical combustion devices leads to and involves strong interactions between fluid mixing and chemical reactions. The direct

use of detailed chemistry in turbulent calculations appears a very difficult task. In most cases, reliable, accurate predictions of pollutant emissions from turbulent flames require simplified approaches, specifically conceived for each class of pollutant species.

If the main interest is the analysis of combustion systems in terms of emissions of pollutant species whose characteristic times are large, like nitrogen oxides, it is possible to follow the approach proposed in this thesis, based on a post-processing procedure. Pollutant species only marginally affect the main combustion process and consequently do not significantly influence the overall temperature and flow fields. Consequently it is feasible to evaluate the structure of the flame with simplified kinetic schemes first and then post-process the CFD results with by using a post-processing technique which uses a detailed kinetic scheme. This is the methodology applied in the present thesis, through a newly-conceived numerical tool, the so-called Kinetic Post-Processor (KinPP). The KinPP model, which can be applied for evaluating industrial burner performances, is able to accurately predict the formation of different pollutants, such as NO_x, CO and can be extended, with appropriate modifications, to other by-products.

3.2 The Kinetic Post-Processor (KinPP)

The general concept of “Reactor Network Analysis” (RNA) has already been employed by various authors to post-process CFD results and evaluate the formation of pollutants, using detailed kinetic mechanisms for various applications by using a different level of description and various numerical methodologies [42, 43, 98, 124]. The Kinetic Post-Processor (KinPP) is based on the same methodology and, as previously mentioned, operates by assuming the temperature and flow fields to be those predicted by a CFD code and solves the overall system of mass balance equations in a complex reaction network with detailed kinetic schemes. Even with new generation computers, the direct coupling of detailed kinetics and complex CFD remains a very difficult and expensive task, especially when considering the number of grid points usually required by industrial applications. For example, when referring to 10^5 - 10^6 grid cells and 100-200 reacting species, the dimensions of the overall system of mass balance equations become larger than 10^7 - 10^8 .

The kinetic post-processing procedure applies two major simplifications which make this numerical approach feasible and advantageous over the direct coupling of a detailed kinetic scheme inside the CFD code:

- i. The first feature is the transformation of the original computational grid into a reactor network. Knowledge of the thermo fluid dynamic field, as evaluated by the CFD code, allows several adjacent and very similar cells to be lumped or grouped into single equivalent reactors. In other words the solution of the CFD code

provides the detailed flow, composition and temperature fields, and this information allows critical and non-critical zones in the overall reacting system to be identified. The description detail can be reduced in several regions without significantly affecting the results. The grouping or clustering of several kinetically similar cells into a single lumped reactor reduces the dimensions of the overall system;

- ii. a second way of making the numerical computations more stable and viable is to define an average and fixed temperature inside the different reactors. The fixed temperature inside these reactors reduces the extreme non-linearity of the system which is mainly related to the reaction rates and to the coupling between mass and energy balances.

3.2.1 Grouping of cells and grid sensitivity

The temperature, composition and fluid dynamic fields obtained through the CFD code allow the identification of the critical zones in the combustion chamber, i.e. the specific regions where large temperature and/or composition gradients are present. It is convenient to retain the original detail of the CFD grid in these zones. However, large volumes of the system are less critical from a kinetic point of view, in particular cold and/or non-reactive zones. As a consequence, the detail of the grid can be locally reduced by clustering and combining several cells into a single equivalent reactor. Of course, the lumped cell volume is simply the sum of the volumes of the grouped cells. The original grid size is thus transformed into a network of several reactors where the links between the different reactors simply combine and reflect the original flow field as evaluated by the CFD code. This allows the total number of equivalent reactors to be

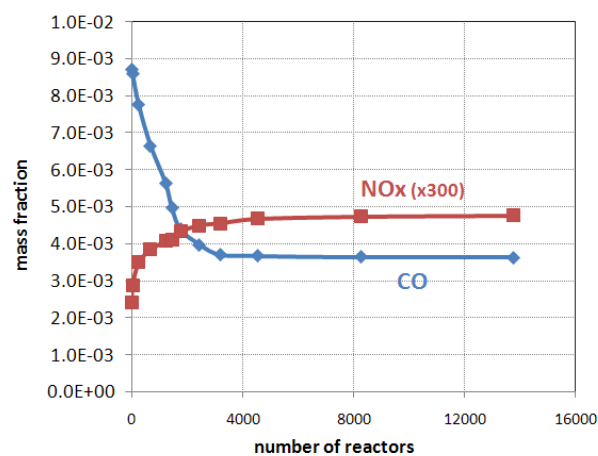


Figure 8. Predicted CO and NO emissions in the exhaust gases as a function of the number of reactors used in kinetic post-processing procedure.

reduced and makes it feasible to handle the mass balance equations by using detailed kinetic schemes with a large number of species. The original 10^5 - 10^6 cells can be conveniently grouped into 10^3 - 10^4 equivalent reactors, maintaining a more than reasonable description of the flame structure and the reacting system.

The mesh-coarsening algorithm was designed in order to prevent possible dangerous situations such as the creation of geometrical irregularities and/or non-smooth transition between zones with very different volumes. The interlinking flows are evaluated on the basis of the convective rates exchanged between the cells belonging to the different reactors. The mass diffusion coefficients for the coarse mesh are calculated in agreement with the original diffusive flow rates. Temperature and initial compositions in the equivalent reactors are the volume averaged values of the combined cells. Different clustering levels are sequentially adopted and calculations are iteratively performed by increasing the number of cells up to the final convergence, i.e. up to the point where a further increase in the reactor network dimensions makes no significant difference in the final solution. The accuracy and convergence of the solution together with the effect of the coarsening of the mesh need to be monitored and these points are analyzed later in this work when numerical procedure is discussed. Figure 8 shows the typical effect of clustering on NO_x and CO predictions in the exhaust gases for a flame fed with syngas (which will be described in the following). The original number of computational cells in the CFD simulation was ~ 30000 . From Figure 8 it is possible to observe that for a number of equivalent reactors larger than ~ 5000 the predicted CO and NO_x emissions are not affected by the clustering. This allows to have a reliable prediction of pollutant emissions without using the original number of computational cells adopted in the CFD calculations. In Figure 9 the NO mass fraction maps in the same flame are

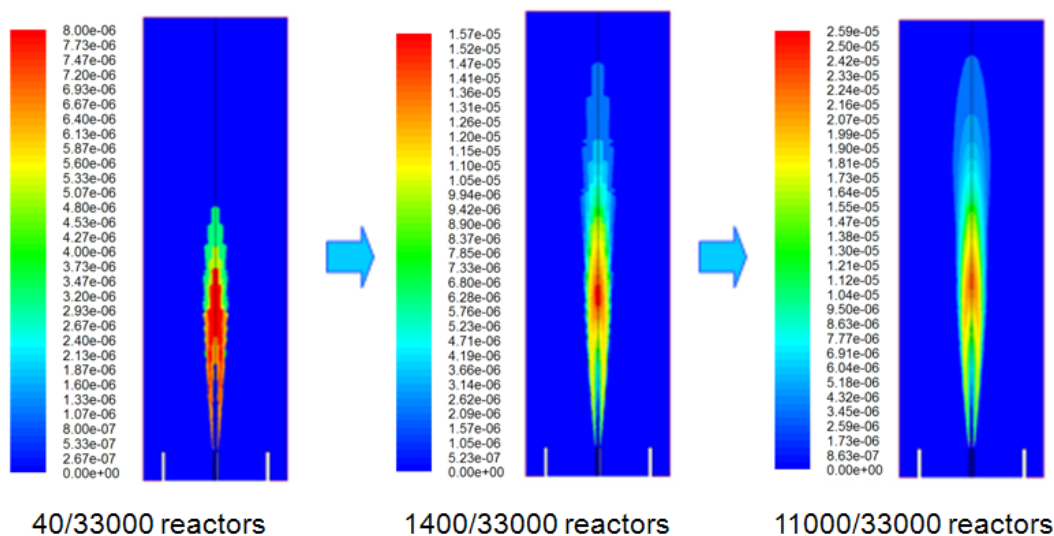


Figure 9. NO mass fraction map as a function of the number of reactors used in the post-processing procedure by the KinPP.

reported as a function of the clustering degree, in order to better visualize the effects of clustering on the numerical predictions. The results obtained on a coarse reactor network can be conveniently used as the starting point for the application of post-processing procedure on a network with a larger number of reactors.

3.2.2 Reaction rate evaluation

As already reported, the KinPP uses the temperature field as obtained by the CFD computations. A fixed average temperature is assumed in each equivalent reactor and the rates of all the reactions involved in the kinetic scheme are evaluated. In turbulent combustion conditions, these reaction rates cannot simply be calculated as a function of the mean temperature and composition, mainly due to the highly non-linear dependence of reaction rates on temperature. Temperature dependence of rate constants is usually described via the modified Arrhenius equation:

$$k(T) = A \cdot T^\beta \cdot \exp\left(-\frac{E_{att}}{RT}\right) \quad (3.1)$$

Consequently, during turbulent combustions, temperature fluctuations in particular have a significant effect on the average rates of reactions with high activation energy. This effect is very important for the reactions involved in NOx formation and needs to be taken into account [86]. The average fluid dynamic temperature \bar{T} is different from the equivalent average temperature from a kinetic point of view, \bar{T}_k . In other words, the average rate value (which accounts for temperature fluctuations over the time) is very different from the reaction rate calculated at the mean temperature \bar{T} :

$$\bar{k} = \frac{\int_0^\tau k(T(t)) dt}{\tau} \neq k(\bar{T}) \quad (3.2)$$

This difference obviously increases for large temperature fluctuations and for reactions with high activation energies. To tackle this problem with reasonable computational efforts, the Taylor expansion of the reaction rate around \bar{T} is used in the post-processing procedure:

$$k(T) = k(\bar{T}) + \sum_{n=1}^{\infty} \frac{1}{n!} \cdot \left. \frac{\partial^n k}{\partial T^n} \right|_{\bar{T}} \cdot T^n \quad (3.3)$$

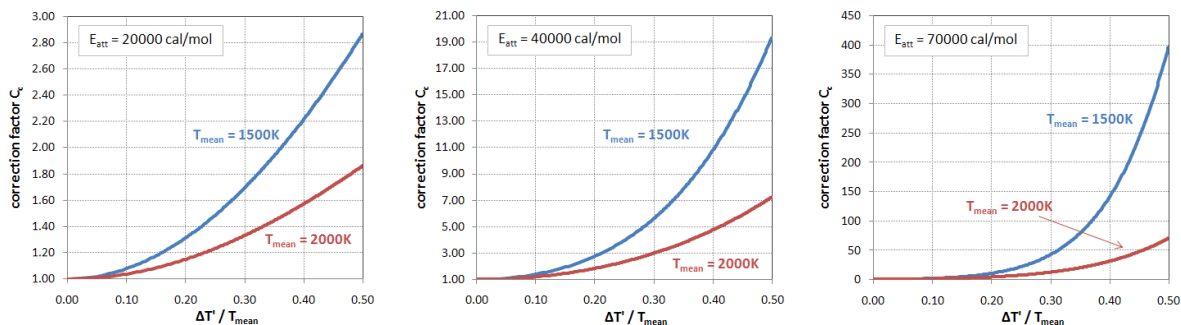


Figure 10. Correction coefficient of the rate constants versus the intensity of temperature fluctuations at average temperatures of 1500 and 2000K. Continuous lines refer to series truncated at the eighth order. (a) activation energy = 20,000 cal/mol; (b) activation energy=40,000 cal/mol; (c) activation energy=70,000 cal/mol.

A few mathematical arrangements allow the following to be deduced:

$$\bar{k} = k(\bar{T}) \cdot \left(1 + \frac{\beta^2 R^2 - \beta R^2 + 2ERT\bar{T}^{-1} \cdot (\beta - 1) + E^2\bar{T}^{-2}}{4R^2} \cdot \left(\frac{T'}{\bar{T}} \right)^2 + \dots \right) = k(\bar{T}) \cdot C_C = k(\bar{T}_K) \quad (3.4)$$

where C_C is a correction coefficient due to the temperature fluctuations. Because of the high fluctuations and slow convergence, the series expansion needs to account for up to the eighth order terms. Of course, C_C value changes for the various reactions due to the different activation energies.

Figure 10 shows the values of the correction coefficient as a function of temperature fluctuations respectively for three different activation energies (20000, 40000 and 70000 cal/mol) at average temperatures of 1500 and 2000 K, and assuming a sinusoidal fluctuation $T'(t) = T'_0 \cdot \sin(t)$. As expected, this coefficient is higher at 1500 K and increases with the activation energy. These figures also show the results obtained with different truncation orders; C_C coefficient estimation converges when accounting the first 3-4 terms of the series (up to the eighth order). These results have been proved to be fully consistent with those obtained through rigorous computation:

$$k(\bar{T}) \cdot C_C = \frac{\int_0^\tau k(\bar{T} + T'_0 \sin(t)) dt}{\tau} = k(T_K) \quad (3.5)$$

where T_K is defined as the equivalent kinetic temperature. The correction coefficients calculated using this approach also agree with those predicted by the double-delta function [45] or by the more accurate but computationally more expensive β -PDF model [47], as reported in Figure 11. It

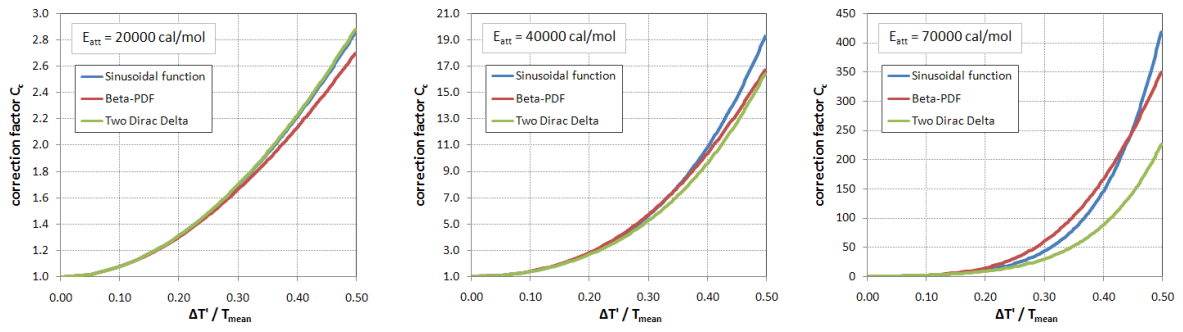


Figure 11. Correction coefficient of the rate constants versus the intensity of temperature fluctuations. The correction coefficients are calculated using the sinusoidal function approach proposed in this thesis, a Beta-PDF and a 2 Dirac delta approach. The mean temperature is assumed equal to 1500K.

is evident that for reactions with low activation energy the differences between the three approaches above mentioned are very small and they seem to be practically equivalent. However, when the activation energy becomes larger, the correction coefficient estimated through the double-delta function is smaller than the correction coefficients predicted by the sinusoidal function approach or by the β -PDF. Since nitrogen oxides chemistry is governed by slow reaction (i.e. with high activation energy), the correction coefficient for such reactions can reach very large values and must be carefully evaluated.

To further clarify the physical meaning of these corrections, we should point out that the equivalent average kinetic temperature T_K becomes 2630 K instead of the average temperature $\bar{T} = 2000\text{K}$, when assuming the higher activation energy and $\Delta T'/\bar{T} = 0.50$. Similarly, T_K would become 2030 K when the average temperature is 1500K. Figure 12 (panel a) shows the kinetic temperatures for three reactions with different activation temperatures as a function of the temperature fluctuation, when the average temperature is 1500K. As expected, the kinetic temperature is always larger than the mean temperature and clearly increases with the fluctuations of temperature. Larger activation energies lead to larger kinetic temperatures for the same

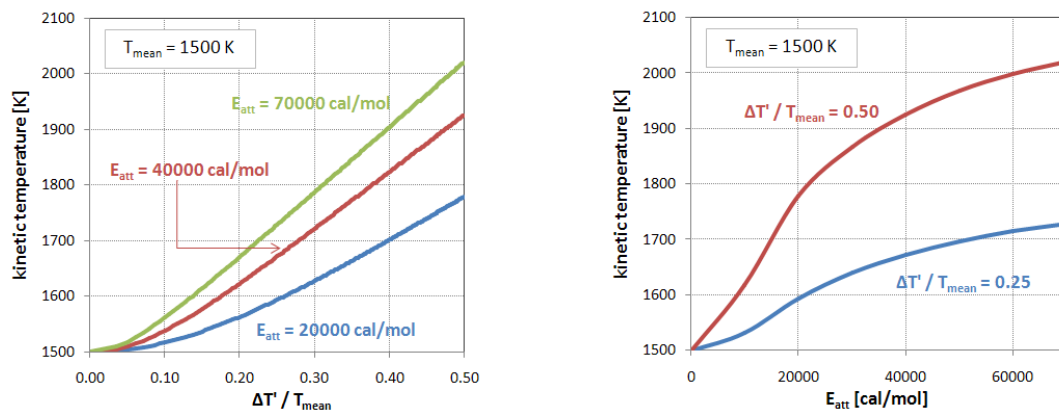


Figure 12. (a) Average kinetic temperature versus the intensity of temperature fluctuations; (b) average kinetic temperature versus the intensity of energy activation. The mean temperature is equal to 1500K.

temperature fluctuation. In panel b of Figure 12 the kinetic temperature is reported as a function of the activation energy for two different values of fluctuation intensity. The curves increase monotonically with the activation energy; of course the kinetic temperature is larger when the fluctuations are larger.

The evaluation of the correction coefficient requires the temperature variance. If not directly available from the CFD simulation, the temperature variance calculation is based on an approximate form of the variance transport equation obtained assuming equal production and dissipation of variance [45, 12]:

$$\widetilde{T}^{\prime 2} = \frac{C_G \cdot \mu_t \cdot (\nabla \widetilde{T})^2}{C_D \cdot \bar{\rho} \cdot \frac{\tilde{\epsilon}}{\bar{\kappa}}} \quad C_G = 2.86, C_D = 2.0 \quad (3.6)$$

A more accurate approach, which was extensively used in this thesis, consists in solving a transport equation for the temperature variance, which is analogous to the transport equation for the variance of mixture fraction:

$$\frac{\partial}{\partial t} (\bar{\rho} \widetilde{T}^{\prime 2}) + \frac{\partial}{\partial x_i} (\bar{\rho} \tilde{u}_i \widetilde{T}^{\prime 2}) = \frac{\partial}{\partial x_i} \left(\frac{\mu_t}{\sigma_T} \frac{\partial \widetilde{T}^{\prime 2}}{\partial x_i} \right) + C_G \mu_t \left(\frac{\partial T}{\partial x_i} \right)^2 - C_D \bar{\rho} \frac{\tilde{\epsilon}}{\bar{\kappa}} \widetilde{T}^{\prime 2} \quad (3.7)$$

where the constants C_G and C_D are the same reported in Equation (3.6) and $\sigma_T = 0.85$ [45].

The proposed approach neglects the effects of composition fluctuations on the average reaction rate, but takes into account only the effects of temperature fluctuations. Such approach is justified, because in most cases the weight of composition fluctuations on the mean reaction rate is very small if compared to the temperature fluctuations. As an example, let us consider a simple second order reaction with respect to the concentration, whose reaction rate is:

$$\dot{r} = AT^\beta \exp\left(-\frac{E_{att}}{RT}\right) \cdot C^2 \quad (3.8)$$

where C is the concentration of a generic species. The sensitivity of this reaction rate to the temperature or concentration fluctuations can be easily estimated. If we consider the dimensionless perturbations δ_T for the temperature and δ_C for the concentration, the ratio between the reaction rate calculated at the perturbed values of T and C and the reaction rate evaluated at the unperturbed values can be considered a measure of this sensitivity:

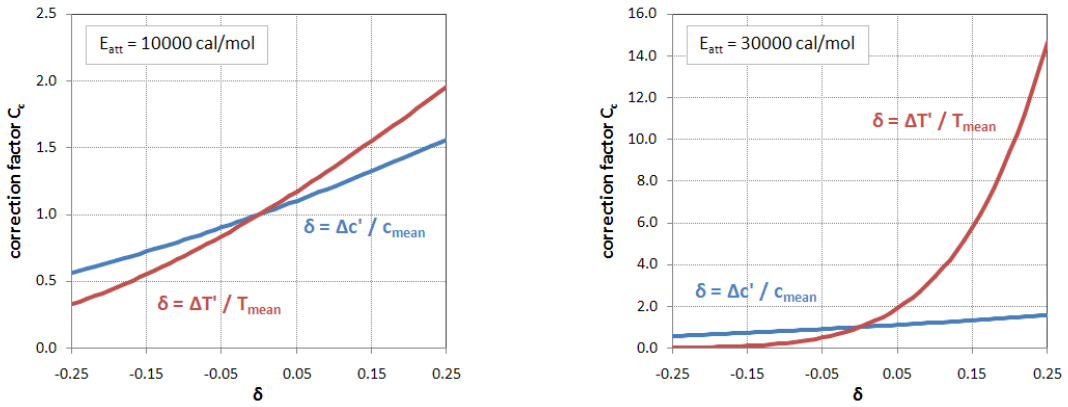


Figure 13. Effects of temperature and concentration oscillation on a second order reaction. The ratio between the reaction rate calculated at $T(\delta) = T_{\text{mean}}(1+\delta)$ or $c(\delta) = c_{\text{mean}}(1+\delta)$ is plotted versus δ for two different activation energies.

$$\frac{\dot{r}(T(1+\delta_T), C(1+\delta_C))}{\dot{r}(T, C)} = (1+\delta_T)^\beta \exp\left(\frac{E_{\text{att}}}{RT} \left(\frac{\delta_T}{1+\delta_T}\right)\right) (1+\delta_C)^2 \quad (3.9)$$

This ratio was plotted in Figure 13 versus the perturbation values imposed on temperature and concentration. It is clear that the reaction rate is more sensitive to the temperature fluctuations, especially for large activation energies. The concentration oscillations are therefore expected to play a minor role on the average reaction rate.

In order to better understand these aspects, the temperature of a perfectly stirred reactor, fed with methane and air in stoichiometric amounts, can be externally forced to follow harmonic oscillations (to simulate the turbulent fluctuations). The corresponding NO mass fraction profiles versus the time are reported in Figure 14, at two different mean temperatures (respectively 1500K and 2000K). The NO profiles oscillate around a mean value, which is reported as a blue, dotted line. The NO mass fraction corresponding to the mean temperature \bar{T} , which does not take into account the fluctuations of temperature and composition, is reported as the green, dotted line. The difference with the mean value is very large, especially for the temperature of 1500K. If only the temperature fluctuations are considered through the proposed approach (see Equation (3.4)), the “corrected value” reported as the red line is obtained. The difference between the exact mean value and the corrected value is due to the composition oscillations.

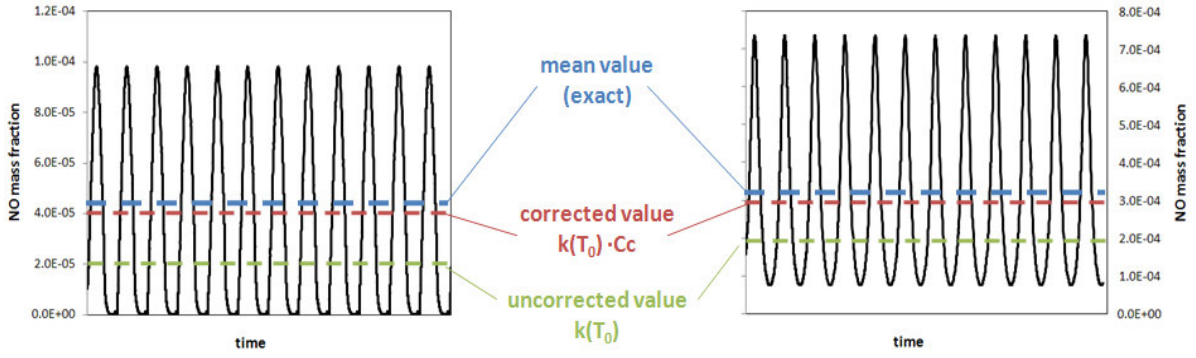


Figure 14. NO mole fraction versus the time in an oscillating perfectly stirred reactor fed with ethylene and air in stoichiometric proportions. (a) Reactor mean temperature equal to 1500K; (b) reactor mean temperature equal to 2000K.

3.2.3 Mass balance equations

CFD results are used to define the overall system by describing the mass balance equations of all the chemical species involved in the detailed kinetic scheme as well as providing the initial composition guess.

For all the equivalent reactors, the steady mass balance of each species (ω_k) accounts for convection, diffusion and chemical reaction terms:

$$\dot{m}_c \cdot \omega_{c,k}^{in} - \dot{m}_c \cdot \omega_{c,k}^{out} + \sum_{n=1}^{N_{F,c}} [\vec{j}_{c,n,k} \cdot S_{c,n}] + V_c \cdot \bar{\dot{\Omega}}_{k,c} = 0 \quad k = 1 \dots N_S, \quad c = 1 \dots N_C \quad (3.10)$$

where \dot{m}_c is the total convective flow pertaining to the reactor c .

The mass diffusion term is the sum of all the contributions pertaining to the adjacent reactors and is computed in the following form:

$$\vec{j}_k = -\frac{\mu_t}{Sc_t} \cdot \nabla \omega_k \quad (3.11)$$

where Sc_t is the turbulent Schmidt number and μ_t the turbulent viscosity. Laminar diffusion is neglected because it is usually overwhelmed by turbulent transport, at least for high Reynolds numbers. $S_{p,c}$ is the surface between the n surface of reactor c and $N_{F,c}$ the number of faces of reactor c . The mean formation rate $\bar{\dot{\Omega}}_{k,c}$ of species k in reactor c is calculated by taking into account the equivalent kinetic temperature:

$$\bar{\Omega}_{k,c} = W_k \sum_{j=1}^{N_R} (v_{kj}^r - v_{kj}^f) \bar{r}_{j,c} \quad \text{for } k = 1, \dots, N_S, c = 1, \dots, N_C \quad (3.12)$$

$$\bar{r}_{j,c} = \bar{K}_{j,c}^f \prod_{k=1}^{NS} (\tilde{c}_k)^{v_{kj}^f} - \bar{K}_{j,c}^r \prod_{k=1}^{NS} (\tilde{c}_k)^{v_{kj}^r} \quad \text{for } j = 1, \dots, N_R, c = 1, \dots, N_C \quad (3.13)$$

where the forward $\bar{K}_{j,c}^f$ and reverse $\bar{K}_{j,c}^r$ mean kinetic constants are evaluated according to the expressions (1.50) and (1.51) respectively, but using the kinetic temperature $T_{K,c}$ instead of the mean temperature. The effective volume V^* available for chemical reactions is evaluated according to the EDC model [87], as reported in Equation (2.15).

3.2.4 Numerical method and control of convergence

After the clustering procedure, the dimension of the overall system, which is now conveniently reduced, becomes $N_C \times N_S$ (N_C is the total number of lumped reactors). As an example, Figure 15 shows a typical Boolean structure of the whole matrix system for a simple structured 2D grid as well as the structure of the single block.

The global Newton or modified Newton methods are not robust enough to solve the system using CFD results as a first-guess. It is therefore convenient to approach a better estimate of the solution by iteratively solving the sequence of individual reactors with successive substitutions. Each reactor is solved by using a local Newton method with the possible use of a ‘false transient’ method (time stepping) to improve the initial guess or to approach the solution. Only when the residuals of all the equations reach sufficiently low values, can a modified global Newton method be applied to the whole system. Otherwise the previous procedure is iterated to further improve the residuals.

The Newton method involves the solution of a linear system of the Jacobian coefficient

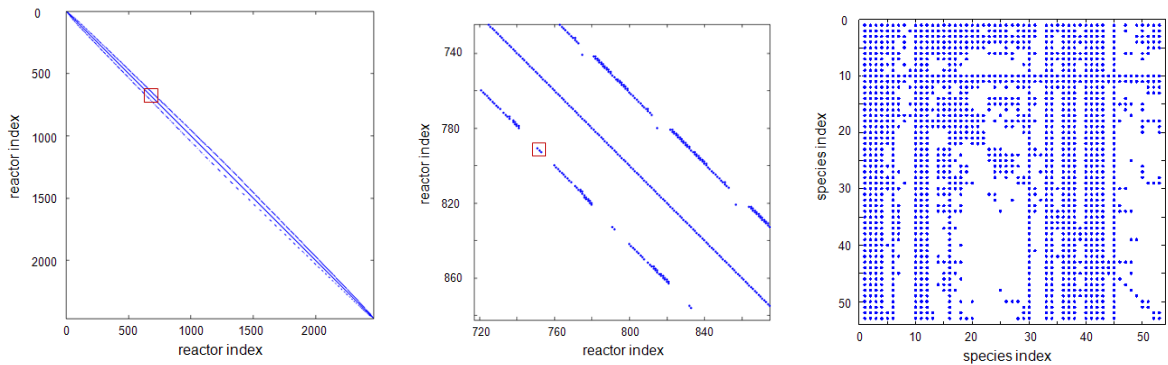


Figure 15. (a) Example of a Boolean structure of the whole matrix system for a simple structured 2D computational mesh. (b) Zoom of the diagonal region (square in panel a). (c) Zoom of the single block structure (square in panel b).

matrix. In order to increase the computational efficiency, special attention is devoted to the evaluation of the sparse Jacobian coefficients. The derivatives of rate equations are evaluated analytically rather than numerically.

The bottleneck of this very large system comes both in memory allocation and in CPU time when a Gauss factorization method is applied to the whole system. Thus, Gauss factorization is applied only to the main diagonal blocks, while an iterative method is applied to the other terms. This approach saves the memory allocation and makes the solution of this overall system viable. In this case too, if the global Newton method does not converge, a ‘false transient’ method is applied to ensure a better approach to the solution of the whole system. The global Newton method not only increases efficiency but, more importantly, ensures the complete convergence to the solution. In fact, it is necessary to speed up the convergence procedure, very slow in the case of direct substitutions. Moreover, it has to be clearly underlined that high attention is required in the convergence check. In fact, in the case of direct substitution, convergence is generally controlled by the typical normalized error sum of squares:

$$E = \sum_{i=1}^{N_V} \left(\frac{\phi_i^{(n)} - \phi_i^{(n-1)}}{\phi_i^{(n)}} \right)^2 \quad (3.14)$$

where $N_V = N_S \times N_C$ is the total number of variables ϕ (mass fractions) and the suffix (n) refers to the iteration. The request that E has to be less than a fixed minimum (ϵ) is a necessary but not sufficient condition. A small E value may just be the result of convergence difficulties rather than

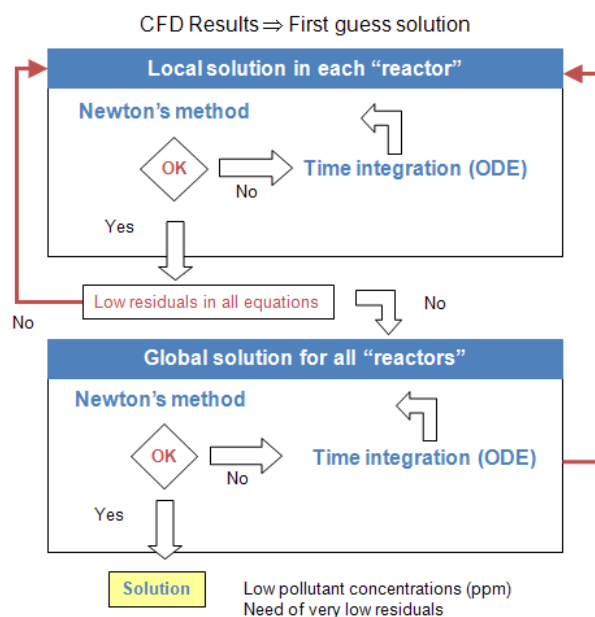


Figure 16. Numerical procedure to solve the mass balances for the reactor network resulting from the clustering procedure.

the numerical solution. The `KinPP` complete numerical procedure is shown schematically in Figure 16.

In order to demonstrate the validity of this approach, three different syngas turbulent jet flames are used as typical test cases. The main results are reported in the following.

3.3 Experimental data

The kinetic post-processing procedure was applied to three different turbulent non-premixed flames fed with syngas. All flames consist of a central fuel jet surrounded by a co-flowing air stream. The geometry of the nozzle and the composition of the fuels are reported in Table 1.

The first two flames (Flame A and B) are described by Barlow *et al.* [7, 8] and were experimentally investigated in the framework of the International Workshop on Measurements and Computation of Turbulent Non-premixed Flames. The composition measurements were made at Sandia National Laboratories, Livermore, California; velocity measurements were obtained at ETH Zurich, Switzerland [46]. The flames are unconfined and the fuel composition is 40% CO, 30% H₂, 30% N₂ (%Vol). The burner has a central duct constructed from straight tubing with squared-off ends with an internal diameter of 4.58 mm for Flame A and 7.72 mm for Flame B. The thick wall of the tubing (~0.88 mm) creates a small recirculation zone that aids the flame stabilization. The computational grid was refined in this zone to better resolve the details of the near-nozzle flow. The central fuel jet mixes with the co-flow air stream, resulting in a turbulent unconfined diffusion flame. The jet fuel velocity is ~76 m/s for Flame A and 45 m/s for Flame B, the co-flow air is ~0.70 m/s velocity and both the streams are at a temperature of 292K; the resulting Reynolds number is ~16700. Experimental results include axial and radial profiles of mean and root mean square (rms) values of temperatures and major species concentrations as well as velocity statistics and Reynolds stresses. Radial profiles of nitric oxide and OH radical concentration are also available at different locations.

The third flame (Flame C) was experimentally investigated by Drake *et al.* [40]. The fuel is fed in a central tube (3.2 mm internal diameter and 1.6 mm wall thickness), centered in a 15cm x 15cm square test section 1m long, with flat pyrex windows on the four sides. The fuel molar composition, very similar to the composition of Flames A and B, is 39.7% CO, 29.9% H₂, 29.7% N₂ and 0.70% CH₄. Ammonia was added in different amounts up to 1.64%; in the absence of ammonia, methane was not included in the fuel mixture. The average fuel flow velocity was 54.6 m/s with a resulting Reynolds number of ~8500; the inlet flow air velocity was 2.4 m/s. The inlet temperature of both the streams is ~300K. Several radial profiles of velocity, temperature and

species concentrations are available at different distances from the fuel inlet. The NO concentration was experimentally analyzed only at a distance of ~ 100 diameters downstream of the nozzle.

Flame	Nozzle ID [mm]	U_{jet} [m/s]	Re_{jet}	Ref.	Fuel composition [% vol]				
					CO	H ₂	N ₂	CH ₄	NH ₃
A	4.58	76.0	16700	[7, 8]	40	30	30	-	-
B	7.72	45.0	16700	[7, 8]	40	30	30	-	-
C	3.20	54.6	8500	[40]	39.7	29.9	29.7	0.7	0-1.64

Table 1. Main data about the turbulent, non-premixed flames fed with syngas

3.4 Flame modeling

The flames were simulated with the commercial CFD code FLUENT 6.2 [45]. A 2D steady-state simulation of the physical domain was considered due to the axial symmetry of the system. The simulations were conducted with a two-dimensional, conformal grid with ~ 33000 rectangular cells for Flames A and B and ~ 38000 cells for Flame C. The grid points are not evenly spaced, but are more dense near the axis of the system (in radial direction) and near the nozzle of the burner (in the axial direction), in order to improve the prediction of the spreading rate of the jet, which affects the shape of the flame. The width and the length of the grid were chosen in order to avoid any effect of boundaries on the flame, which can be considered unconfined, as it was in the experimental work. For the spatial resolution the Second-Order Upwind Scheme was adopted. The segregated implicit solver was used with the SIMPLE procedure for pressure-velocity coupling. PRESTO! (PREssure Staggering Options) algorithm was used for pressure interpolation [45].

Turbulence was modeled via the RANS approach [107, 109]. The flames under consideration are simple jet diffusion flame, in which the central jet spreads due to the turbulent diffusion, allowing the fuel to mix with the surrounding oxidizer and react. No swirl motion is introduced and no bluff-body is employed to stabilize the flame. As a consequence, the fluid dynamics of the system is quite simple and no recirculation zones or other complex flow patterns arise. Therefore the standard κ - ϵ model seems to be a good choice for modeling the turbulence, without resorting to more complex, expensive models. However it is well recognized that the standard κ - ϵ model poorly predicts the velocity field in axisymmetric round jets: in particular it tends to overestimate the spreading rate (or equivalently the decay rate) [138]. Also for the flames under investigation the standard κ - ϵ model over-predicts the diffusion of the central jet and predicts the axial velocity on the centerline lower than the one actually measured. In order to avoid such

inaccuracies, several possible approaches were compared, as extensively reported in the Paragraph 3.6.

As far as modeling turbulence-chemistry interactions is concerned, several approaches were considered. The attention in particular was focused on the following models, which are widely used by the combustion community for simulating turbulent non-premixed flames: the Eddy Dissipation Model (ED), the Eddy Dissipation Concept Model (EDC) and the Steady Laminar Flamelet Model (SLFM).

3.5 Kinetic schemes

The reactions adopted for the ED simulation are very simple and correspond to the complete oxidation of syngas ($\text{CO} + 0.5\text{O}_2 \Rightarrow \text{CO}_2$, $\text{H}_2 + 0.5\text{O}_2 \Rightarrow \text{H}_2\text{O}$). The kinetic scheme used in the EDC and SLF simulations, however, is more accurate and consists of 12 chemical species and 32 chemical reactions [48]. The steady flamelets library was obtained using the FLUENT package and stored in look-up tables describing the dependence of the flamelets on the scalar dissipation rate and the mixture fraction. This kinetic model can significantly improve the predictions of the temperature and compositional fields but it is unable to characterize the flame in terms of pollutant formation. A library of 20 different Laminar Flamelets with different strain rates of up to about 1000 s^{-1} was used in the CFD calculations.

The Kinetic Post-Processor is applied with a more detailed kinetic scheme, which permits the prediction of the nitrogen chemistry and NO_x formation in the flame [113]. As already mentioned, the detailed schemes of hydrocarbon combustion are usually large and computationally expensive in terms of their direct application in the CFD computations, especially when considering complex geometries and when the focus is on pollutants formation.

3.6 Preliminary analysis

3.6.1 Effect of turbulence models

The Flames A and B investigated in this work showed a strong dependence on the turbulence model employed in the CFD code. It is well known that the CFD simulations of axisymmetric turbulent jets require particular attention, because the most common turbulence model used in RANS simulations, the standard κ - ε model, tends to give a poor prediction of the velocity field (round jet anomaly). This model is able to correctly predict the decay and the spreading rate of a planar jet, but the predictions for an axisymmetric jet are not so accurate; in particular the decay rate tends to be largely over-predicted [138]. All flames investigated in this work are affected by this problem: the result is that the axial velocity is lower than that

experimentally measured and therefore the diffusion of the central jet is over-predicted. To overcome these difficulties, which obviously result in a poor prediction of the velocity field, but also of the thermal field, it is possible to follow different approaches, which are briefly summarized in the following.

- i. The simplest methodology consists in applying a correction to the empirical parameters in the transport equation for the dissipation rate of turbulent kinetic energy ε (Equation (1.74)). The last two terms of this equation represents the production and dissipation terms respectively. The default values of constants $C_{1\varepsilon}$ and $C_{2\varepsilon}$ in these two terms were experimentally obtained on turbulent shear flows with air and water. In order to obtain a faster decay of the turbulent kinetic energy ε , the value of $C_{1\varepsilon}$ (which refers to the production term) can be slightly increased or the value of $C_{2\varepsilon}$ (which refers the dissipation term) can be slightly decreased . In the first case the constant value is modified from 1.44 to 1.60 [35, 66]; in the second case the constant $C_{2\varepsilon}$ is decreased from 1.92 to 1.83 [40]. The main effect of this modification is an increase of the turbulent dissipation rate, a decrease of the turbulent kinetic energy, leading to lower turbulent diffusivity. The modification of constants $C_{1\varepsilon}$ and $C_{2\varepsilon}$ is a quite common practice to achieve a better description of turbulent axisymmetric jets, but the conclusions about the effects of such modifications cannot be generalized and must be limited to the case under investigation.
- ii. An alternative approach to the modification of the constants $C_{1\varepsilon}$ and $C_{2\varepsilon}$ was proposed by Pope [60] who suggested the addition of a source term in the transport equation for the dissipation rate of turbulent kinetic energy, to take into account the effect of vortex stretching on the scalar dissipation and therefore on effective viscosity. The resulting modified e equation proposed by Pope is the following:

$$\frac{D\bar{\rho}\tilde{\varepsilon}}{Dt} = \frac{\partial}{\partial x_i} \left[\left(\mu + \frac{\mu_t}{\sigma_\varepsilon} \right) \frac{\partial \tilde{\varepsilon}}{\partial x_i} \right] + C_{1\varepsilon} \frac{\tilde{\varepsilon}}{\tilde{\kappa}} G_k - C_{2\varepsilon} \bar{\rho} \frac{\tilde{\varepsilon}^2}{\tilde{\kappa}} + C_{3\varepsilon} \bar{\rho} \frac{\tilde{\varepsilon}^2}{\tilde{\kappa}} \quad (3.15)$$

The value of the constant proposed by Pope is $C_{3\varepsilon}=0.79$, while the standard values of $C_{1\varepsilon}$ and $C_{2\varepsilon}$ are employed. In Equation (3.15) φ is the non-dimensional measure of vortex stretching, which is defined as follows:

$$\varphi = \omega_j \omega_{jk} S_{ki} \quad (3.16)$$

where:

$$\begin{aligned}\omega_{ij} &= \frac{1}{2} \frac{\tilde{\kappa}}{\tilde{\varepsilon}} \left(\frac{\partial u_i}{\partial x_j} - \frac{\partial u_j}{\partial x_i} \right) \\ s_{ij} &= \frac{1}{2} \frac{\tilde{\kappa}}{\tilde{\varepsilon}} \left(\frac{\partial u_i}{\partial x_j} + \frac{\partial u_j}{\partial x_i} \right)\end{aligned}\quad (3.17)$$

In the case of axisymmetric flows without swirl, the vortex stretching invariant becomes:

$$\varphi = \frac{1}{4} \left(\frac{\tilde{\kappa}}{\tilde{\varepsilon}} \right)^3 \left(\frac{\partial \tilde{u}_x}{\partial r} - \frac{\partial \tilde{u}_r}{\partial x} \right)^2 \frac{\tilde{u}_r}{r} \quad (3.18)$$

where \tilde{u}_x and \tilde{u}_r are the axial and radial component of velocity respectively and x and r the axial and radial coordinates. The modified Equation (3.15) has been implemented in FLUENT by adding the Pope's source term via User Defined Functions to the usual transport equation for ε .

- iii. The third approach simply consists in considering a different turbulence model, which is able to overcome the deficiencies of standard κ - ε in the round jet simulations. For example, the realizable κ - ε model proposed by Shih *et al.* [122] was intended to address the inaccuracies of traditional κ - ε models by adopting a new eddy-viscosity formula and a new model equation for dissipation based on the dynamic equation of the mean-square vorticity fluctuation. This model has been extensively validated for a wide range of flows, including rotating homogeneous shear flows, free flows including jets and mixing layers, channel and boundary layer flows, and separated flows. In most cases the performances of the model have been found to be substantially better than that of the standard κ - ε model. Especially important is the fact that the realizable κ - ε model, according to its authors [122], should be able to resolve the round-jet anomaly and correctly predict the spreading rate for axisymmetric jets.

The approaches briefly summarized above were compared without considering the effect of radiative heat transfer using the same grid and the same boundary conditions. In order to have a more complete analysis, also the Reynolds Stress Model (RSM) [45] was considered, without any

modification In Figure 17 the temperature profiles calculated using the different approaches for solving the round jet anomaly are reported along the axis and along two different radial locations and compared with the experimental data. It is well evident that the standard κ - ε model tends to overestimate the decay rate, as suggested by the peak temperature which is too close to the fuel inlet. However the simulations employing the modified κ - ε model show a too large decrease in the decay rate with respect to the standard model. This results in a temperature profile which is everywhere higher than the experimental one, both for the peak temperature and in the tail of the flame (here the temperature profile shows a very poor agreement with experimental measurements). The κ - ε realizable model seems able to give a better prediction, and its behavior is clearly between the standard κ - ε and the modified κ - ε . However also in this case the peak temperature is a little bit too close to the fuel inlet and the tail of the flame is hotter (but not so much as for the modified κ - ε). The best agreement with the experimental data has been obtained using the *RSM* without any modification. However the results obtained by using this model are very close to those obtained with the κ - ε realizable model, which is computationally less expensive. The axial profiles for the mixture fraction and CO₂ mass fraction (reported in Figure 18) obviously confirm the observations reported above. Therefore, the κ - ε realizable model was chosen to perform the numerical simulation reported in this Chapter.

3.6.2 Grid Sensitivity

The calculations proposed in this chapter were performed on a structured non uniform 2D-axisymmetric mesh, which is very fine in the region close to the fuel inlet and which consists of ~30,000 computational cells.

To investigate the sensitivity of the solution with respect to the employed grid, the simulations have been repeated on different grids: in particular a finer structured mesh and a non-structured mesh with triangular cells were considered for this comparison.

Figure 19 shows the temperature, mixture fraction and main species profiles as obtained using the base grid and a structured grid consisting in about 90,000 cells. Also in this case no important differences can be observed. Similar results have been obtained for the triangular mesh (not here reported).

3.6.3 Effect of different kinetic mechanisms

Two different kinetic mechanisms have been used and compared to construct the flamelet libraries: the kinetic scheme previously described (CRECK scheme) [48] and the GRI 3.0 kinetic mechanism [58]. The non-adiabatic flamelet library has been calculated using the PrePDF

application available in FLUENT [45]; the strain rates considered are from 0.001 Hz to 200 Hz; moreover the equilibrium flamelet was taken into account.

In Figure 20 the results obtained using these two different kinetic schemes are reported for the temperature, mixture fraction, H₂O and CO₂ mass fraction profiles along the axis. It is evident that the differences are negligible, both for the temperature and the main chemical species.

3.6.4 Effect of Radiative Heat transfer

The radiative heat transfer, as also reported in [10], is not important in this flame due to the relatively low temperatures and the absence of soot. The Discrete Ordinates model available in FLUENT [45] has been applied to better investigate the effects of radiation on the temperature profile. The results reported in Figure 21 confirm the previous considerations: the main differences when the radiation model is taken into account consists in a lower peak temperature (~30K), which is closer to the fuel inlet, and a lower temperature in the tail of the flame. The differences in the mixture fraction profile and for the main species in the combustion process are negligible.

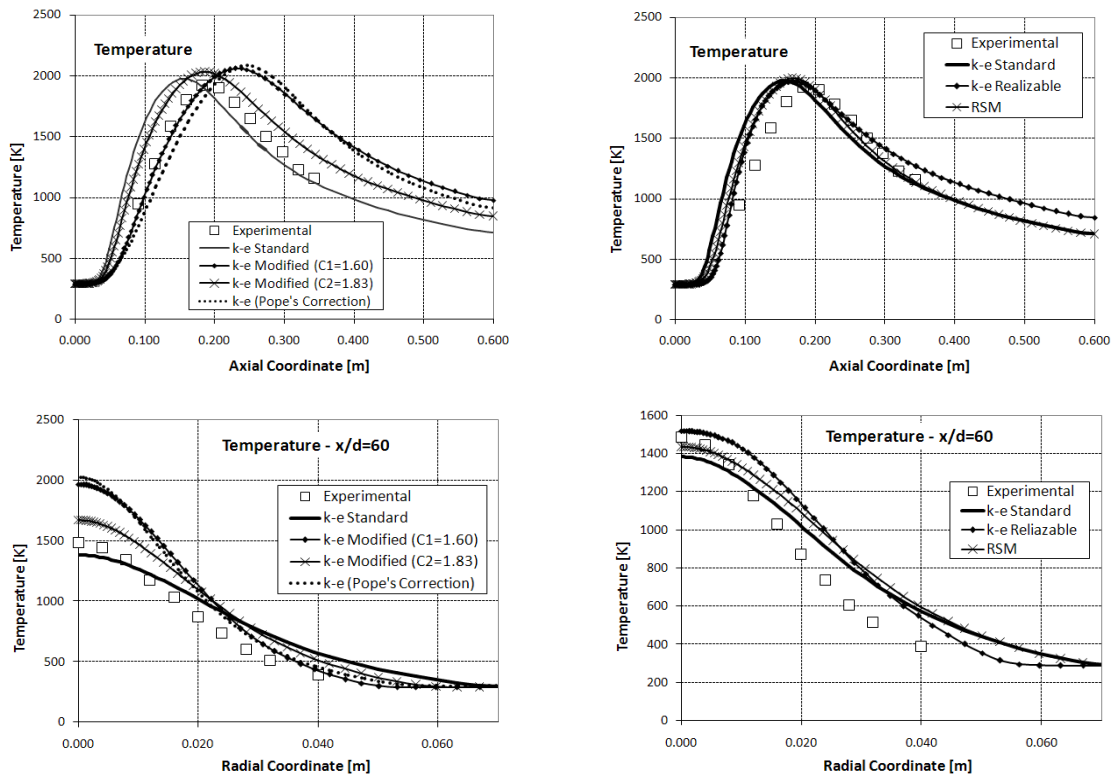


Figure 17. Comparison between the different turbulence models investigated: temperature profile along the axis and in radial direction at $x/d=60$.

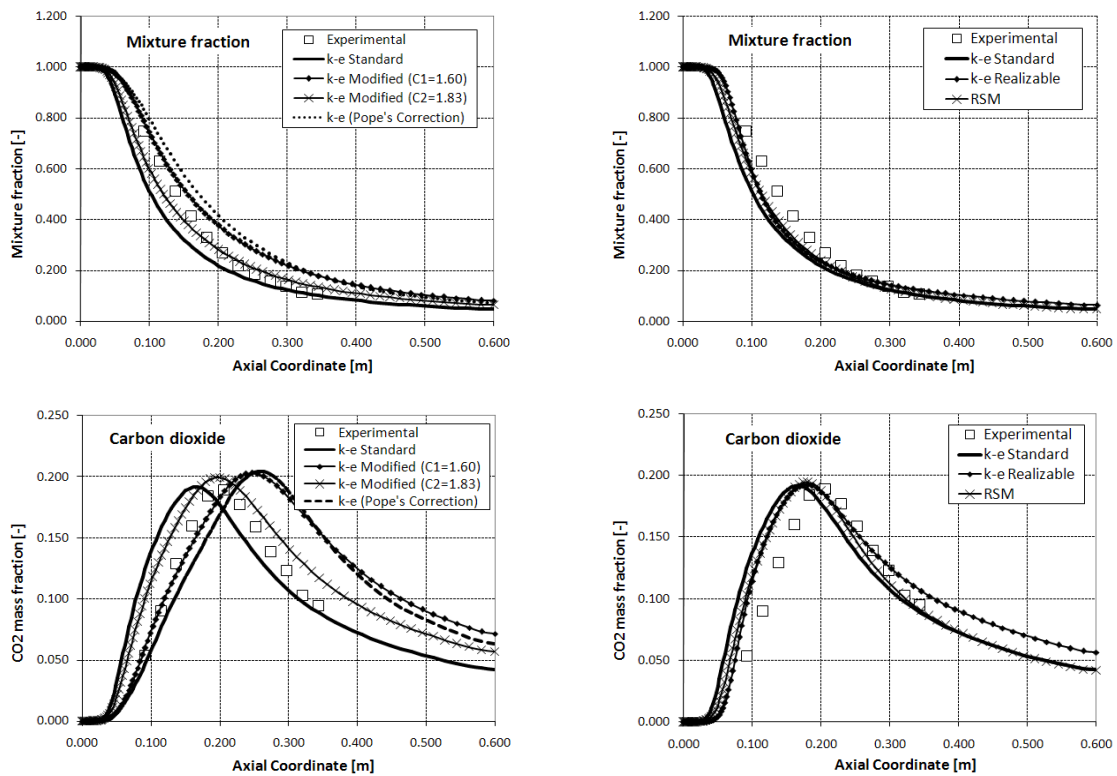


Figure 18. Comparison between the different turbulence models investigated: mixture fraction and carbon dioxide mass fraction profiles along the axis.

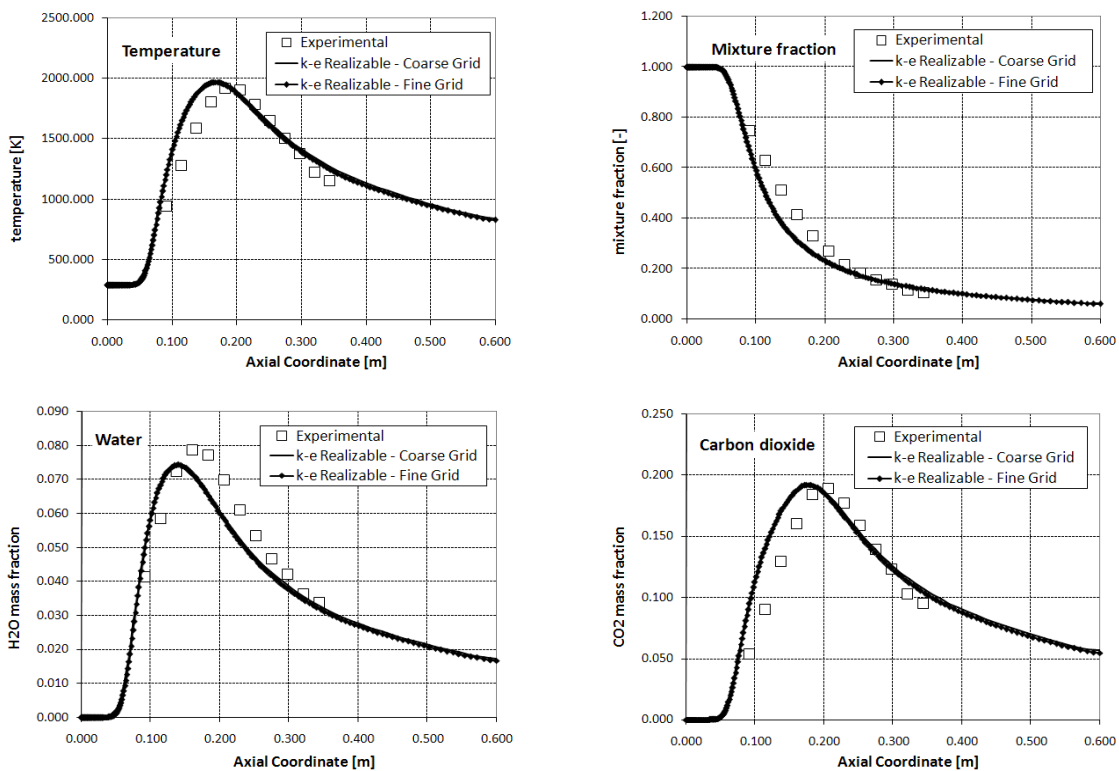


Figure 19. Comparison between the different structured mesh: coarse mesh (~30000 cells) and fine mesh (~90000 cells). Profiles of temperature, mixture fraction, H₂O and CO₂ mass fraction along the axis

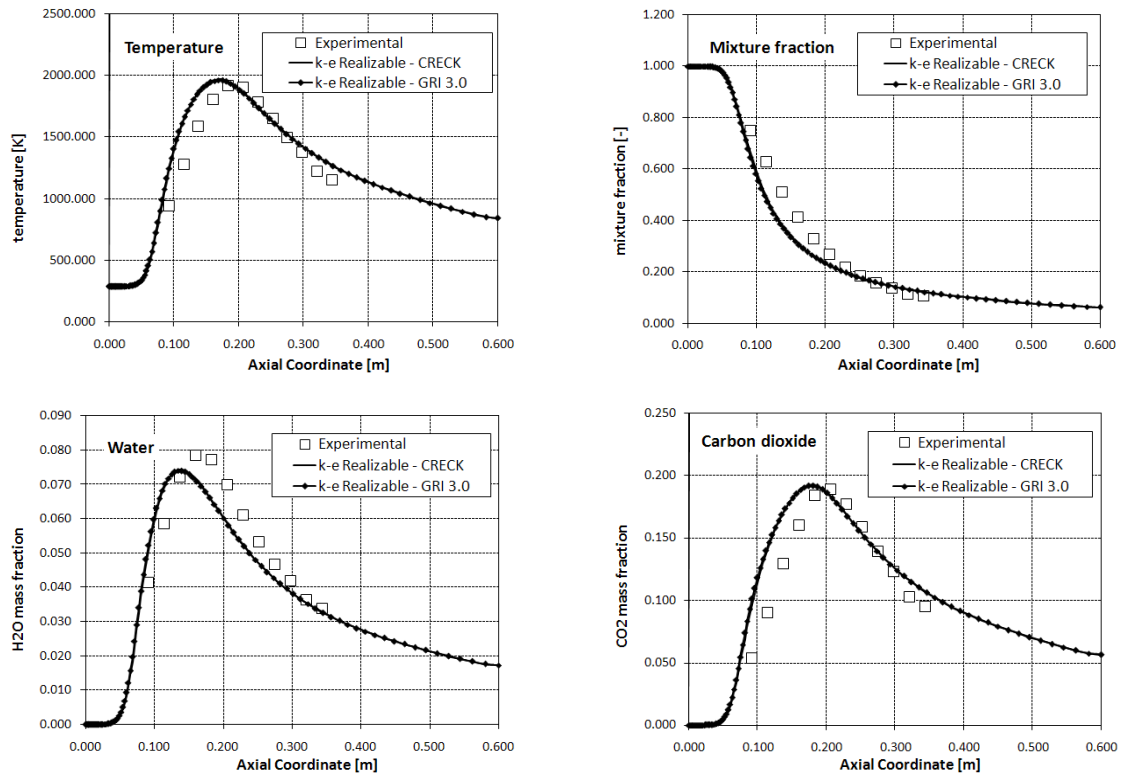


Figure 20. Comparison between the CRECK kinetic scheme [7] and the GRI 3.0 kinetic scheme [58].

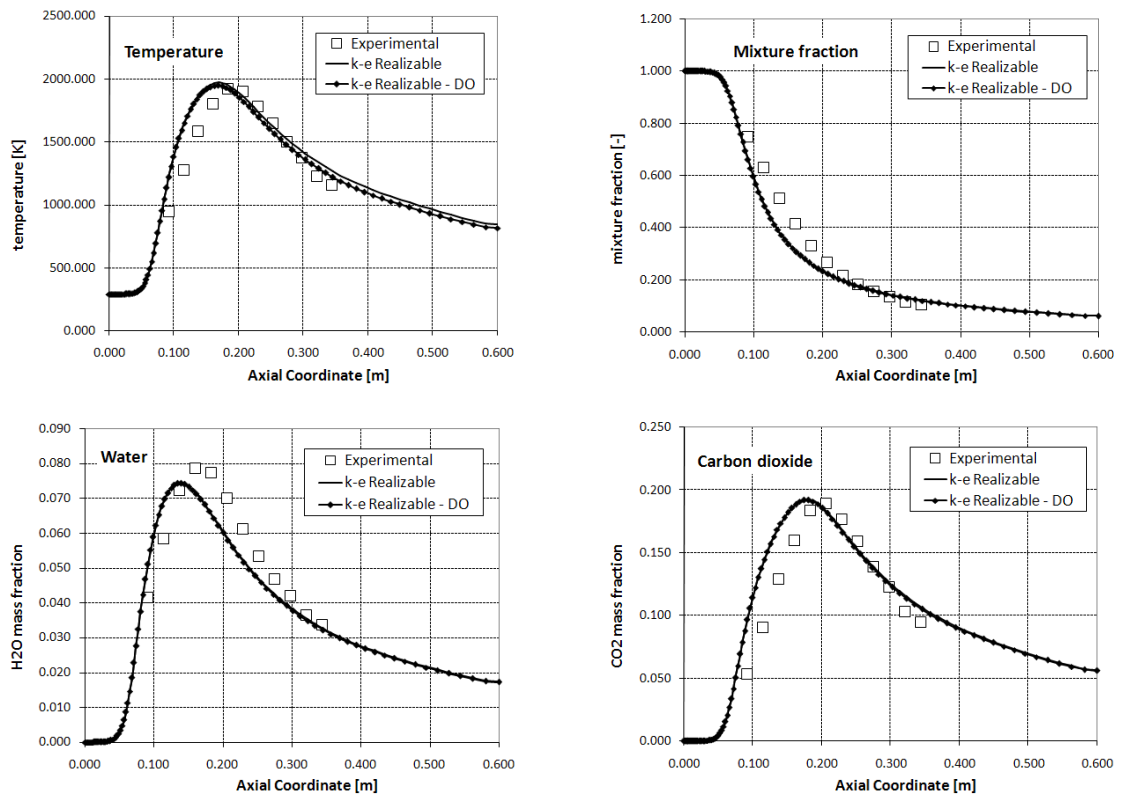


Figure 21. Effects of radiative heat transfer on temperature, mixture fraction and H_2O and CO_2 mass fraction profiles.

3.7 NO_x predictions in Flames A and B

3.7.1 CFD results

Figure 22 shows the temperature fields of flame A and B obtained using the EDC model. Panel a shows a comparison with experimental measurements of temperature along the axis of symmetry. The comparison is satisfactory for both flames and shows that the maximum temperature for the larger flame B is shifted downwards by ~ 150 mm due to the difference in the diameter of the nozzles used for the two flames. In fact by using the nozzle diameter to scale the axial profiles of the two flames, it is possible to obtain very similar temperature profiles (Figure 22) and also major species concentration profiles (not here reported) [8]. It is interesting to note that the scaling by nozzle diameter does not work for OH and NO, which are more heavily influenced by the local fluid-dynamics and residence times. This makes them useful for the evaluation of turbulent combustion models. As a consequence of the similarity between the two flames, the discussion will focus on Flame A, and only OH and NO will be discussed for Flame B.

A comparison between experimental and predicted axial velocity profiles in radial direction for Flame A at several axial locations ($x/d = 20, 40$ and 60) is shown in Figure 23a. The velocity predictions are satisfactory and the above-mentioned κ - ϵ realizable model results in improved predictions that more closely match the dataset. However it is still clear that the CFD simulation slightly overestimates the jet decay rate. In Figure 23b the radial profiles of turbulent kinetic energy

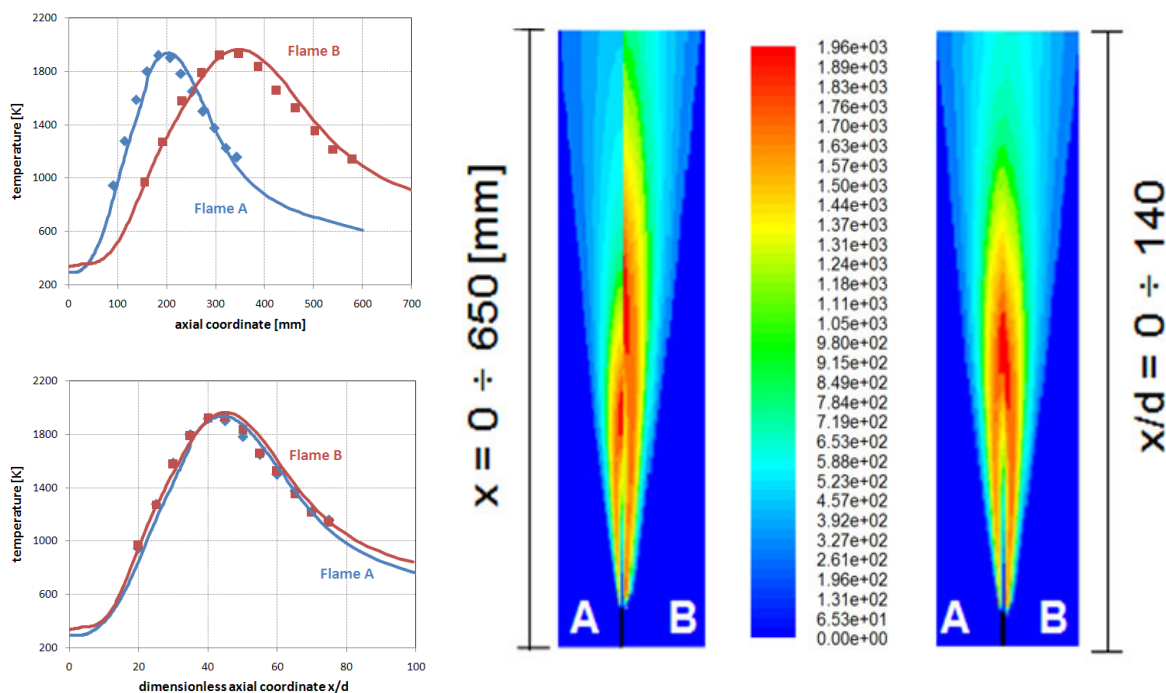


Figure 22. Temperature profiles along the axis: comparison between experimental measurements [7, 8] and numerical calculations (a) in physical space and (b) in the dimensionless axial coordinate. Predicted contours of temperature in physical space and in dimensionless axial coordinate (c). The results refer to the EDC simulation.

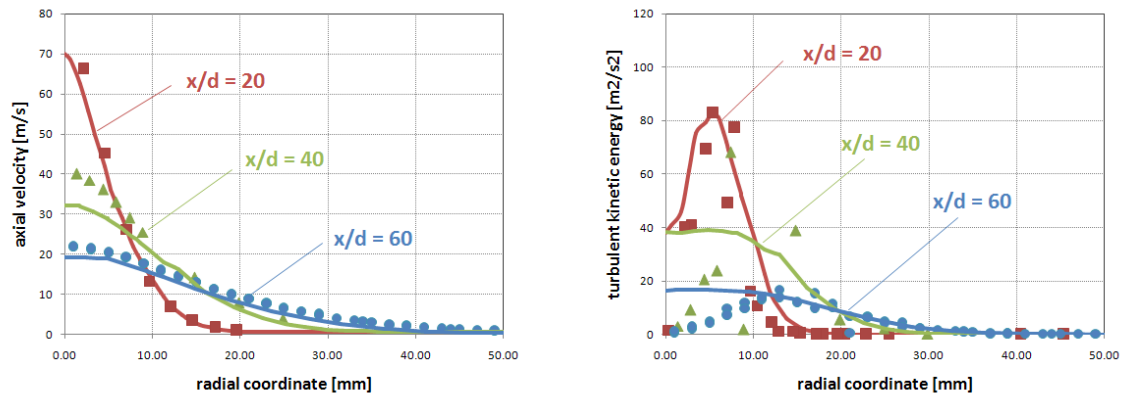


Figure 23. Flame A: comparison between numerical results and experimental measurements in radial direction at several axial locations. (a) Axial velocity; (b) turbulent kinetic energy.

are compared with the experimental measurements at the same axial locations. The agreement seems satisfactory, especially for location close to fuel nozzle.

Figure 24 shows a comparison between the experimental (Flame A) and computed profiles of temperature and mass fractions of major species for the three different turbulent combustion models. The ED model, coupled with the simplified kinetic mechanism mentioned in Paragraph 3.5, gives unsatisfactory predictions, both for the temperature and compositional fields. The best agreement with experimental measurements is obtained for the EDC model: the temperature and compositional profiles can be considered very satisfactory. The shape of CO_2 and H_2O profiles is similar to the one of the temperature; CO_2 is generally slightly over-estimated while H_2O and CO are predicted more precisely. SLF model overestimates the axial temperature profile, especially in the post-flame zone ($x/d > 40$) and this fact represent a serious problem for the correct prediction of pollutant species with the KinPP .

Hewson and Kerstein [61] studied Flame A using a RANS approach and overpredicted the temperature in the flame tail by 50-150 K. According to their work, there are two possible reasons responsible for temperature overprediction in this flame: neglect of radiative heat losses and underprediction of the dissipation rate. They estimated that radiation is not expected to play a major role in this flame, because the time scales for radiative heat losses are long relative to the flame evolution time. Thermal radiation, which is taken into account in this work using the Discrete Ordinates model [45], affects the peak temperature only by about 30-40 K.

A sensitivity analysis on the SLF simulations confirmed that the predicted temperature profile is mostly affected by the turbulence model used, while is nearly insensitive to the grid and the numerical schemes or to the kinetic mechanism used to generate the flamelet library. In fact, different turbulence models affect the jet penetration but also the scalar dissipation rate and thus turbulent mixing. Higher mixing rates noticeably shorten the flame, as already discussed elsewhere [61]. In fact, better temperature profiles in the flame tail can be obtained adopting SLF with RSM

or the standard k- ϵ turbulence models, but the consequence is the overestimation of the temperature close to the nozzle. A further discussion on SLF modeling goes beyond the scope of this work, which is focused on the NO_x chemistry in syngas flames.

It is evident that any model overestimations of the flame temperature affect the prediction of pollutant species with the KinPP.

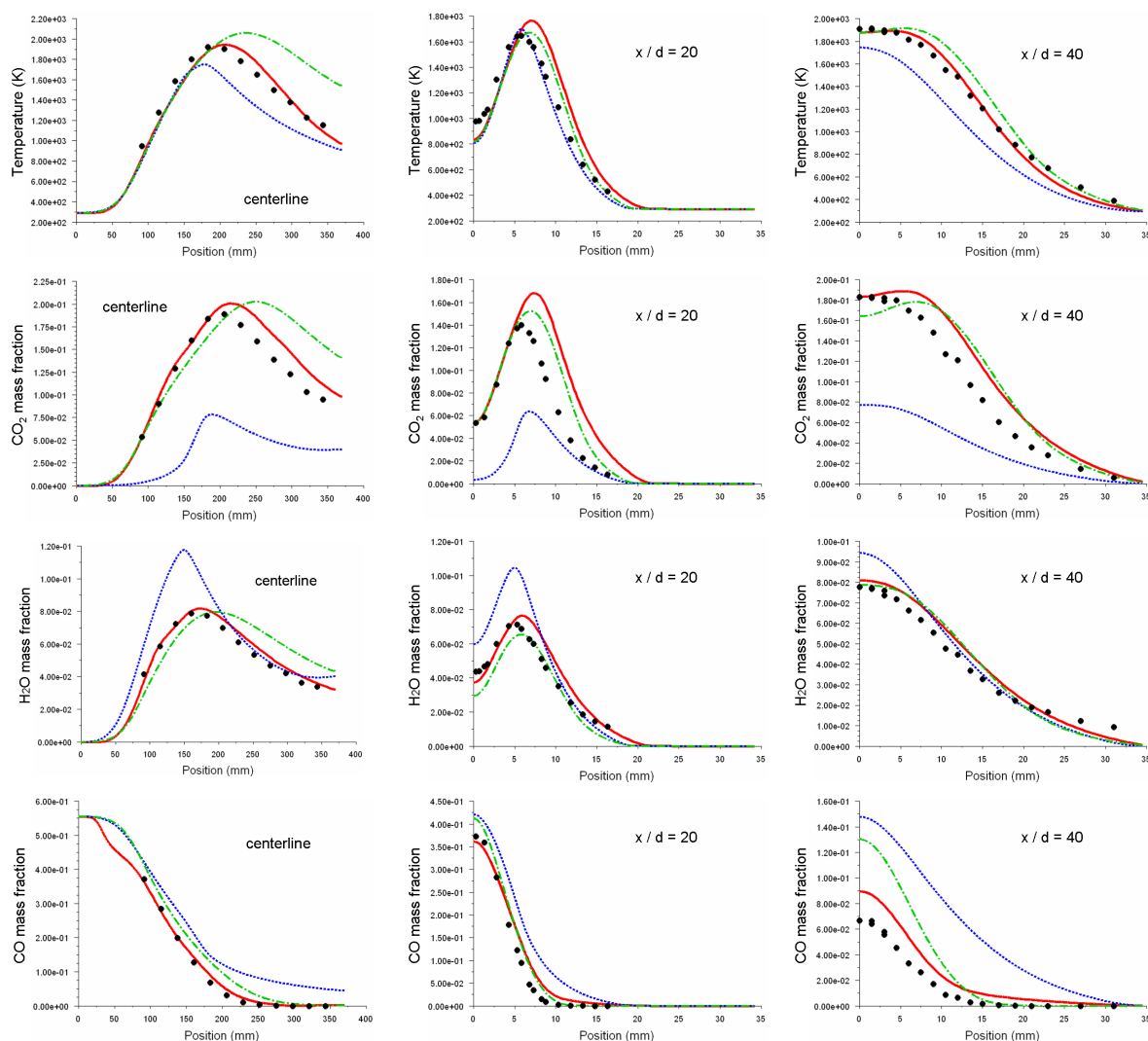


Figure 24. Flame A: temperature and mass fraction profiles along the axis and at several distances from the burner surface in radial direction (d is the internal diameter of the nozzle, x is the axial distance from the nozzle outlet): --- EDC model, --- ED model, --- SLF model.

3.7.2 KinPP results

Moving from these fields obtained with the EDC model for Flame A and B, the Kinetic Post-Processor is applied with the detailed kinetic scheme to predict NO_x formation in the flame also. The predicted NO_x species maps are reported in Figure 25 for flame A. The significant role played by N₂O in the flame front and formation of NO₂ in the post-flame zone can be observed.

Two main NO_x-forming reaction paths are relevant in these syngas flames: thermal NO and the nitrous oxide mechanism (N₂O). The NO formation through nitrous oxide is initiated by the third order reaction $N_2 + O + M = N_2O + M$ which is followed by several N₂O reactions with O, OH and H radicals, ultimately leading to the formation of NO and N₂. The selectivity of this process is ruled by the local temperature and composition of the flame. The NO_x is formed mostly via the N₂O mechanism and, to a limited extent, through the thermal mechanism (about 25% for Flame A). The significant role played by the nitrous oxide mechanism in syngas combustion is a consequence of the significantly enhanced production of O radicals [128].

The thermal mechanism is initiated and controlled by the so called Zeldovich mechanism through $O + N_2 = NO + N$, which is followed by $N + O_2 = NO + O$ and $N + OH = NO + H$.

Figure 26 shows a comparison of NO measurements and predictions along the axis of the flame and the effect of temperature fluctuations on NO formation. The effect of temperature fluctuations is relevant especially for Flame B where the thermal mechanism accounts for about half of the NO formed.

The agreement on these absolute values is satisfactory, even though there are some discrepancies. The shape of the radial NO profile in flame is correctly reproduced at the various distances from the burner surface and is in very good agreement with measurement results at $x/d > 30$, as reported in Figure 27. NO concentration is, however, slightly overestimated close to the nozzle.

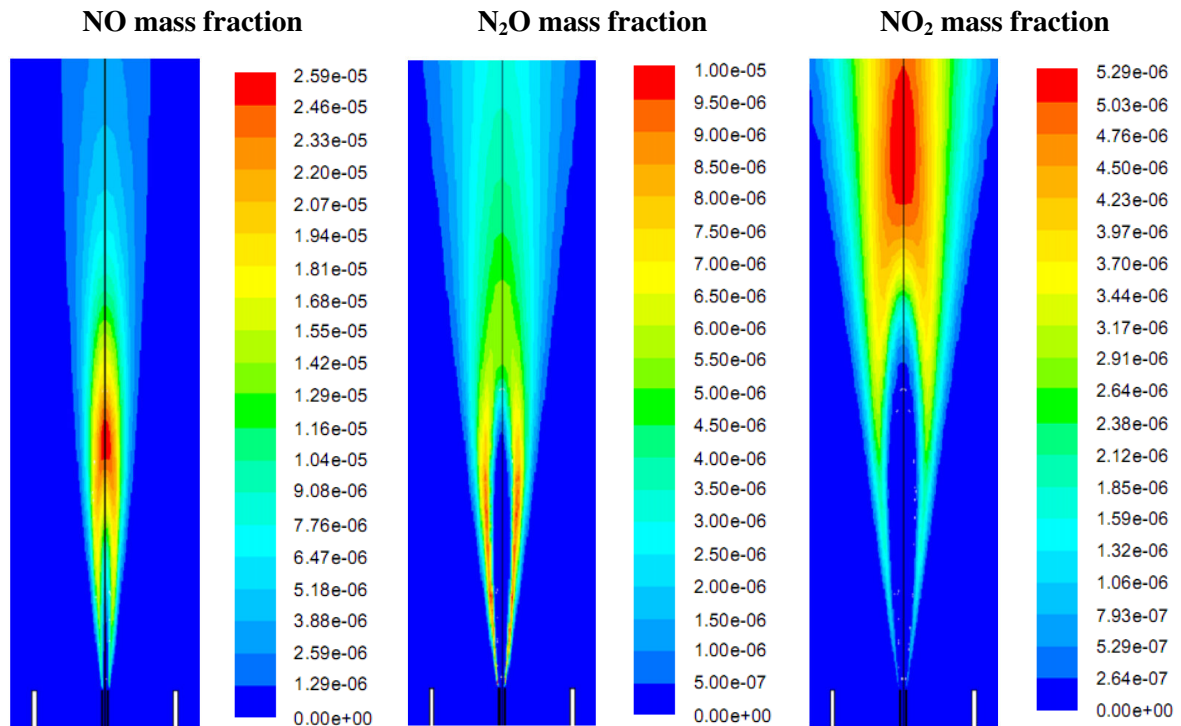


Figure 25. Flame A: predicted contours of NO_x mass fractions. The results refer to the post-processing procedure applied to the CFD predictions obtained using the EDC model.

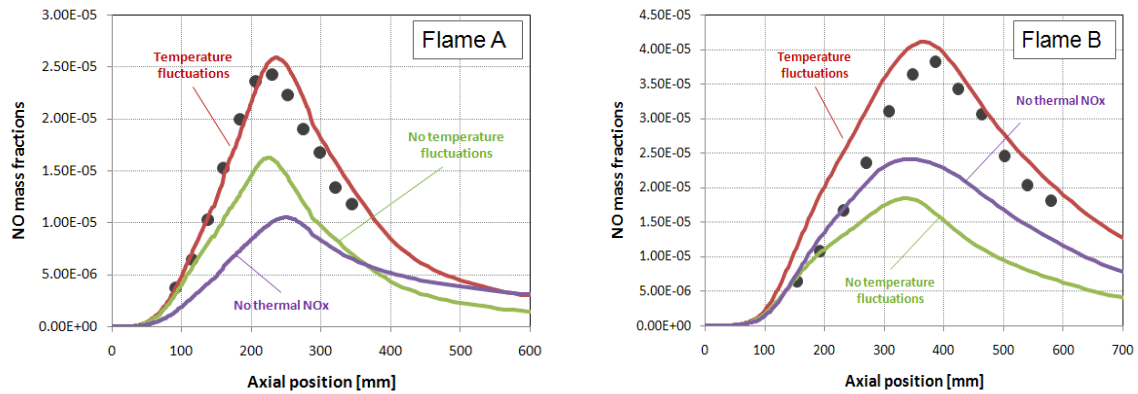


Figure 26. *Flames A and B: comparison between experimental measurements of NO mass fraction [7, 8] and numerical results obtained from the KinPP. The red lines were obtained considering the effects of temperature fluctuation on reaction rates; the green lines neglecting the temperature fluctuations; the purple lines were calculated neglecting the thermal mechanism.*

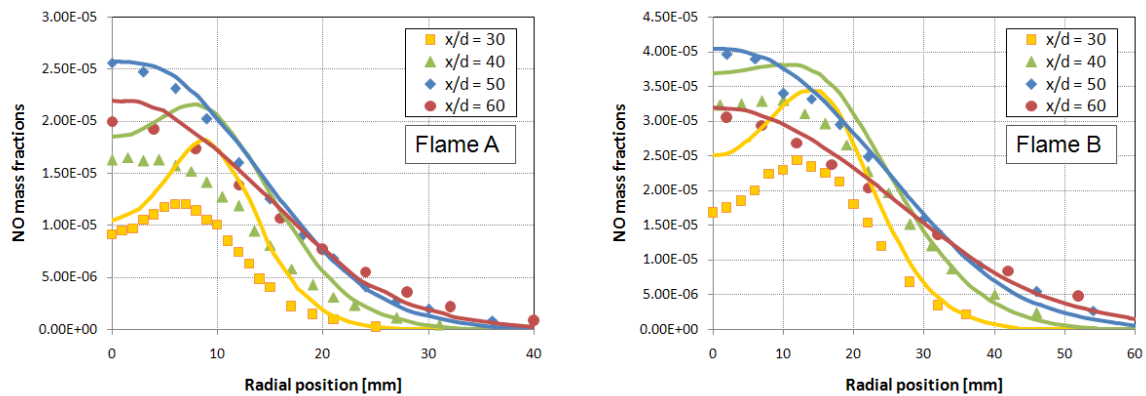


Figure 27. *Flames A and B: comparison between numerical predictions and experimental measurements [7, 8] of NO mass fraction in radial direction at several axial locations.*

The importance of temperature fluctuations on the formation of nitrogen oxides can be better understood from the results reported in Figure 28. The NO and NO₂ mass fraction maps are compared with the predictions obtained without considering the correction due to the temperature fluctuations for the evaluation of mean reaction rates (which means that the correction coefficient C_C was assumed equal to 1). It is evident that if the effects of temperature fluctuations are neglected, the NO_x are largely underestimated.

The interactions between turbulence and NO_x chemistry are more important for Flame B, where the fluctuations of temperature are more intense and the NO_x thermal mechanism plays a significant role. As a result, the temperature fluctuations have a greater impact on NO_x emissions, as shown in Figure 29, which compares NO_x instantaneous measurements and predictions at different axial locations. The measurements of Figure 29 are single-shot NO measurements [8] and are shown in scatter plot as a function of the mixture fraction at different axial locations of Flame B. The mixture fraction is calculated here from the local composition using the Bilger formula [15].

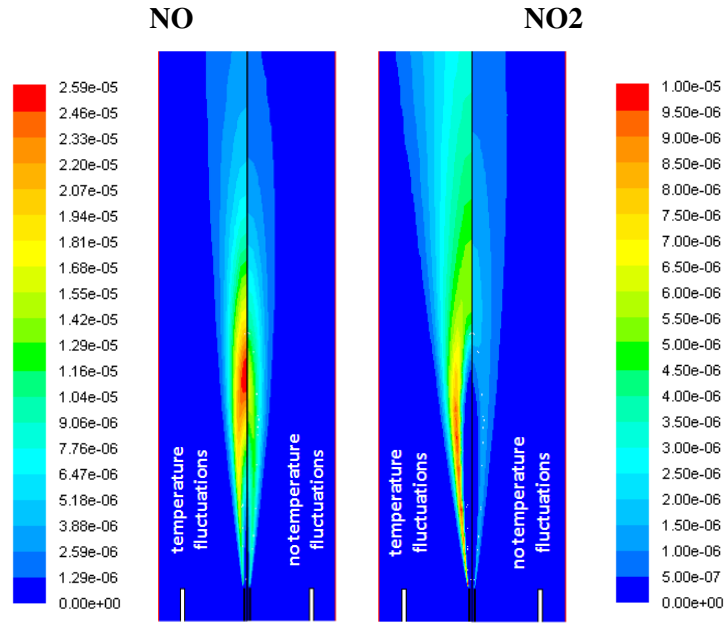


Figure 28. Flame A: predicted contours of NOx mass fractions. Comparison between results obtained taking into account the temperature fluctuations for estimating the reaction rates and results obtained neglecting the effects of temperature fluctuations.

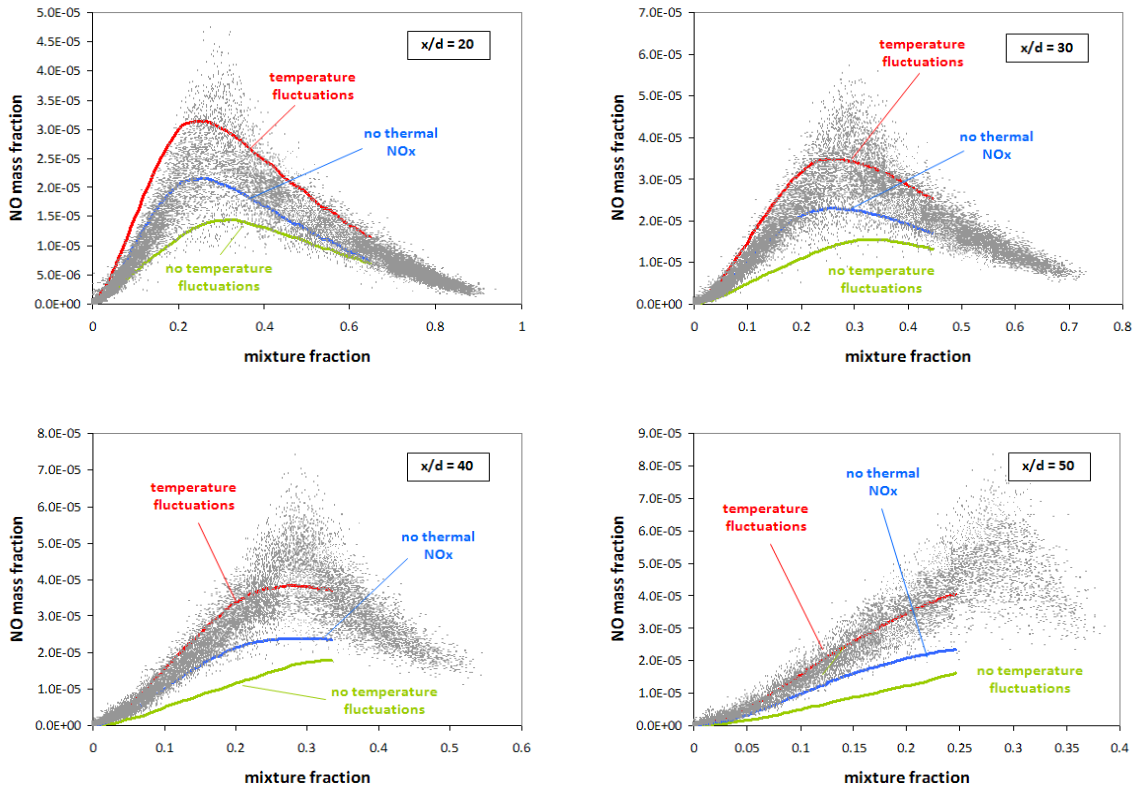


Figure 29. Flame B: NO mass fraction at different distances from the nozzle. Comparison between singles hot measurements (symbols) [7, 8] and average model results (lines). The red lines are the result of the KinPP with the correction for taking into account the fluctuations of temperature on reaction rates; the green lines were obtained from the KinPP neglecting the temperature fluctuation effects on the reaction rates; the blue lines refer to the predicted results calculated without considering the thermal NOx mechanism.

NO predictions, obtained using the Kinetic Post-Processor, are compared with the scatter plot measurements of NO using a red line. It is quite evident that the predicted NO mass fraction is in good agreement with the average NO at high x/d while close to the nozzle NO tends to be overestimated. It is interesting to note that the predicted NO profile obtained when suppressing the effect of temperature fluctuations ($C_C=1$, green line) lies at the lower boundary of the scatter plot, especially close to the fuel inlet.

Figure 30 shows the comparison between single-shot OH measurements [8] and predictions obtained directly in the CFD calculation (with the EDC turbulent combustion model) (green line) and using the KinPP (red line). The agreement between measurements and model predictions is satisfactory. The difference between the two models (KinPP and EDC) is due to the correction coefficients C_C , which are introduced in the KinPP to account for the effect of temperature fluctuations. It is quite evident that the effect is less relevant than in the case of NO shown in Figure 29, as a consequence of the lower apparent activation energy of OH radicals formation process.

As reported by Barlow *et al.* [10], a realistic target for the agreement between NO_x measurements and predictions is $\pm 15\%$, due in part to uncertainties regarding measurements,

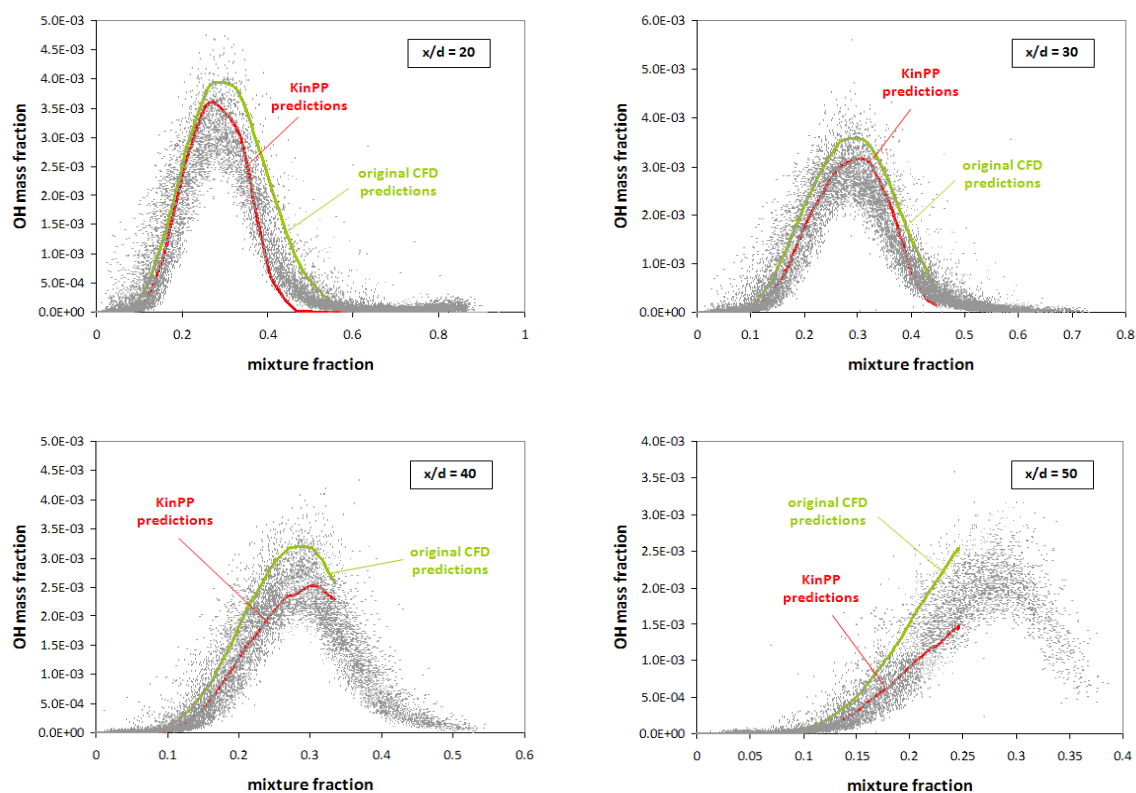


Figure 30. Flame B: OH mass fraction at different distances from the nozzle. Comparison between singles hot measurements (symbols) [7, 8] and average model results (lines). The red lines are the result of the KinPP with the correction for taking into account the fluctuations of temperature on reaction rates; the green lines were obtained from the KinPP neglecting the temperature fluctuation effects on the reaction rates.

boundary conditions and model assumptions. Measurements were not taken very close to the nozzle because of considerations of spatial resolution, and better resolution is expected for larger x/d ratios, especially for the smaller flame.

In Figure 31 the effects of clustering degree on the predicted maximum NO and N₂O mass fractions in the flame are reported as a function of the number of equivalent reactors employed in the kinetic post-processing procedure. It seems evident that 7000-10,000 reactors are enough for obtaining a reasonable estimation of NOx emissions from the flame, without reaching the original number of CFD cells (in this case more than 30,000).

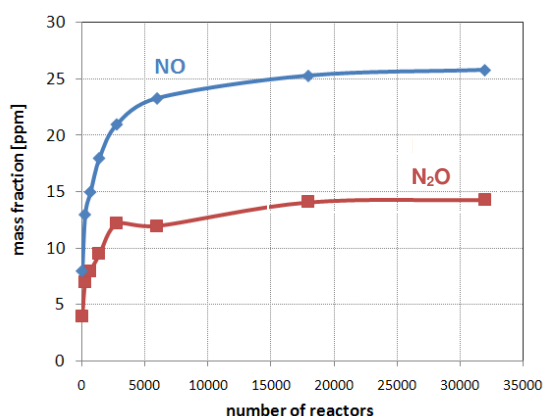


Figure 31. Predicted maximum NO and N₂O mass fractions in the flame as a function of the number of reactors used in kinetic post-processing procedure (Flame A).

3.8 NOx predictions in Flame C

3.8.1 CFD results

Flame C was simulated by using the κ - ϵ realizable model, which showed on Flames A and B more accurate predictions for the turbulent round jet with respect to the standard κ - ϵ model. The three different models for the description of turbulent combustion (ED, EDC and SLF), already adopted for the previous Flames, were applied and compared in terms of velocity, temperature and main species.

Unfortunately no data on the velocity field were available for this flame. Figure 32 compares the predicted and measured radial profiles of temperature, H₂O, CO₂ and CO, in greater detail. These data refer to the flame without ammonia; the velocity, temperature and composition profiles of the main species are not affected by the small added amounts of ammonia and methane. The thermal field is properly predicted by the EDC and SLF models at different axial locations, but the ED model gives unsatisfactory agreement especially at larger distances from the fuel inlet section. Comparisons between experimental and predicted values for main species are slightly less satisfactory than for the previous flames. The CO₂ mole fraction profiles tend to be overestimated

by the EDC and SLF models. The ED model, which makes use of a simplified kinetics, does not represent the CO/CO₂ conversion correctly. CO, on the other hand, is generally underestimated at distances of more than 20 diameters from the fuel inlet.

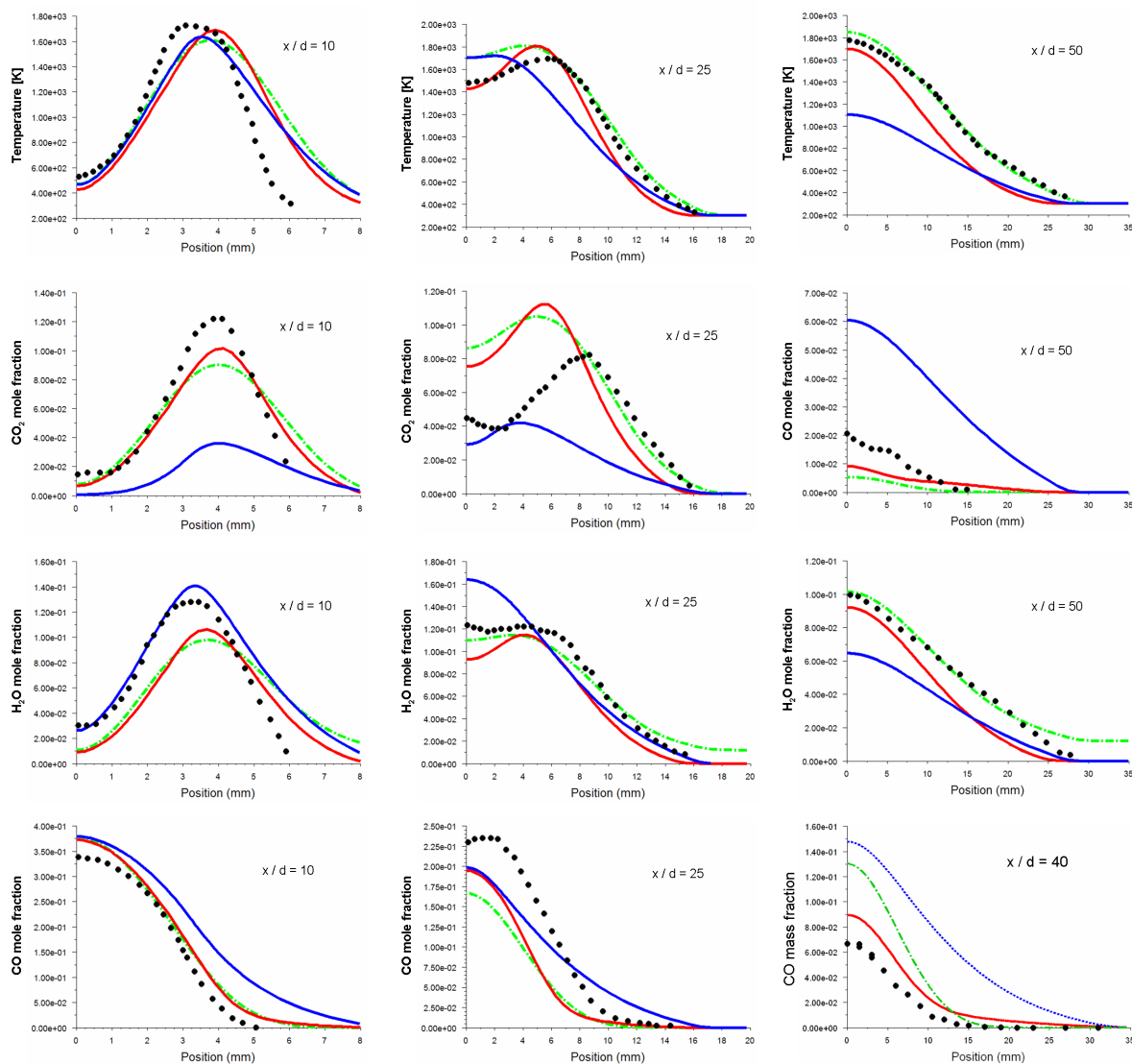


Figure 32. Flame C: temperature and mass fraction profiles along the axis and at several distances from the burner surface in radial direction (d is the internal diameter of the nozzle, x is the axial distance from the nozzle outlet) with 0.80% of total amount of added NH_3 : --- EDC model, -- ED model, - - SLF model.

3.8.2 KinPP results

The KinPP was applied to the CFD results obtained by using the EDC model, which shows the best agreement with the experimental data. The NO and NO₂ mass fraction maps are reported in Figure 33, together with the temperature field used to derive these predictions.

In Figure 34 the calculated temperature and NO mass fraction profiles in radial direction at $x/d=100$ are compared with the experimental measurements. The results show a satisfactory agreement. In particular the peak value and the shape of the curves seem to be well caught. In Figure 35 the calculated radial profiles of NO at the axial location $x/d=100$ are reported for different amounts of added ammonia in the fuel stream. As expected, the larger is the amount of NH_3 in the syngas, the larger is the amount of NO in the flame.

Figure 36a compares the predicted and experimental peak values of NO (corresponding to the axial location $x/d=100$), for various amounts of added NH_3 [40]. The agreement is very satisfactory, even though the predicted results tend to slightly underestimate NO formation with larger amounts of added NH_3 . This agreement is quite clearly confirmed by the comparisons reported in Figure 36b in which total NO (and $\text{NO}_x = \text{NO} + \text{NO}_2$) formation is related to the NH_3 feed. It is clear that the predicted results are very close to the experimental measurements and therefore not only is the adopted kinetic scheme capable of correctly describing NOx formation and NH_3 consumption, but the CFD simulation of the flame was properly grasped. The difference between NOx and NO is mainly due to the successive formation of NO_2 when the temperature is decreasing, as reported in Figure 37.

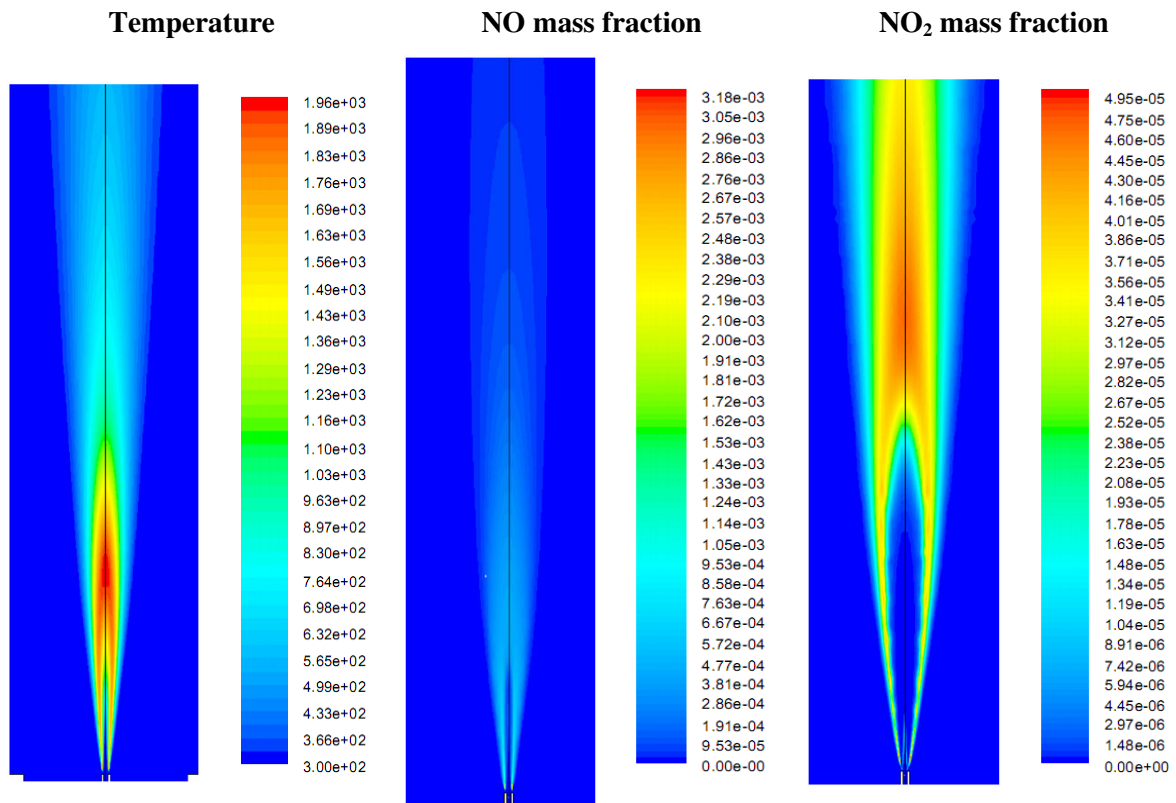


Figure 33. Flame C: predicted contours of temperature and NOx mass fractions. The results refer to the post-processing procedure applied to the CFD predictions obtained using the EDC model.

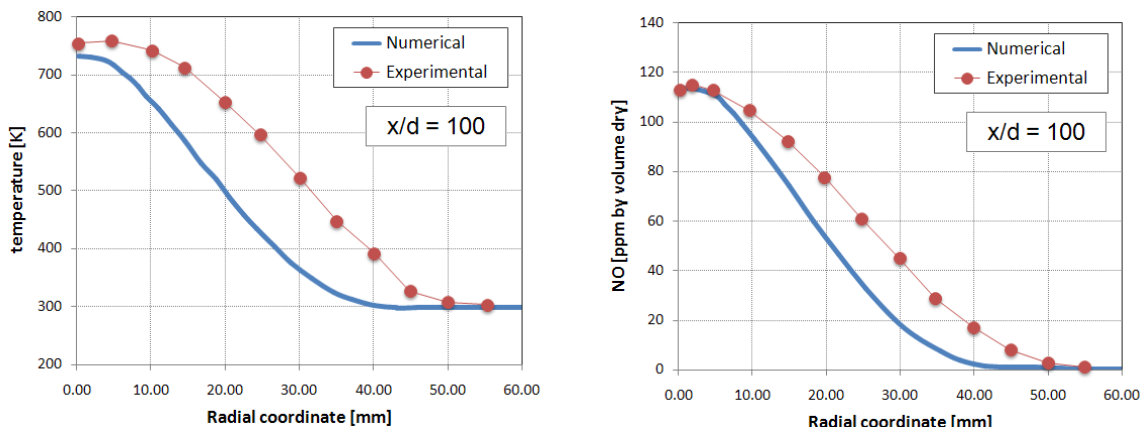


Figure 34. Flame C: comparison of experimental measurements and predictions in radial direction at $x/d=100$ with 0.80% of total amount of added NH_3 . (a) Mean temperature; (b) NO mole fraction.

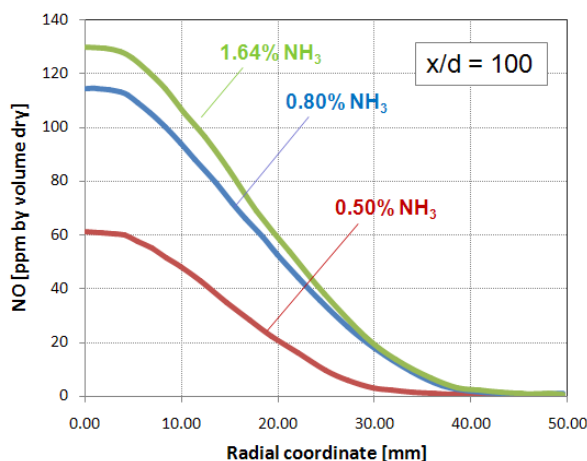


Figure 35. Flame C: comparison between predicted NO mole fraction profiles in radial direction at $x/d=100$ for different total amounts of added NH_3 .

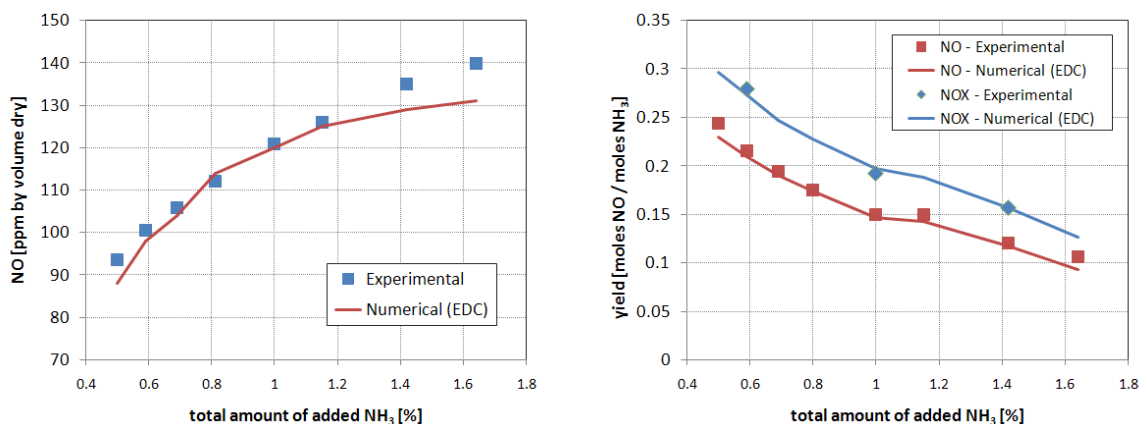


Figure 36. Flame C: (a) comparison of measurements and predictions of the molar yield of NO from NH_3 . The NO flux has been obtained by integration over the cross section at $x/d=100$; (b) radially integrated values of NO at $x/d=100$ divided by the amount of inflow NH_3 .

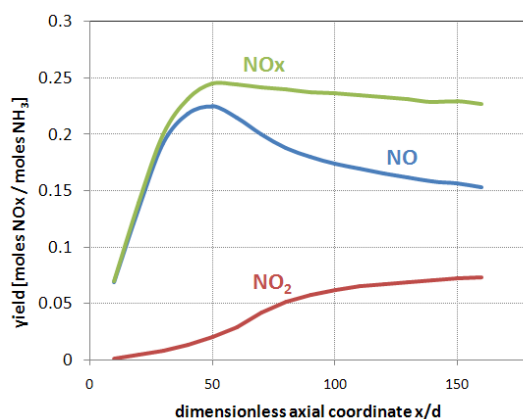


Figure 37. Flame C: radially integrated values of NO, NO₂ and NO_x at $x/d=100$ divided by the amount of inflow NH₃ versus axial position (0.80% of added NH₃).

3.9 Conclusions

Detailed kinetic schemes are usually too large and computationally expensive for their direct application in the CFD codes for the numerical simulation of turbulent flames, especially in the case of large 3D grids needed by industrial applications. For this reason three different flames have been here analyzed with a newly conceived, effective numerical tool: the Kinetic Post-Processor (KinPP). Since pollutant species only marginally affect the main structure of the flame (i.e. temperature and flow field), the CFD results obtained with simple kinetic schemes can be post-processed using large, detailed kinetic schemes, able to accurately predict also the formation of different pollutants, such as NO_x, CO, SO_x and other by-products.

A good prediction of the flame structures is obviously a necessary condition for the correct application of the KPP. The reliability of the KPP results in terms of pollutant predictions is strongly dependent on the completeness and consistency of the original CFD simulation. Therefore the choice of the most appropriate turbulent combustion model is of paramount importance for the application of the post-processing procedure. In particular the numerical results presented in this Chapter show that the EDC (Eddy Dissipation Concept) model is able to give satisfactory results when coupled to the usual κ - ϵ turbulence model (with the correction for the axis-symmetric jets); the agreement with experimental data, both in terms of temperature and main species concentrations, appears to be very good. Unfortunately the EDC model is computationally very expensive. On the contrary, the SLF (Steady Laminar Flamelet) model has a reduced computational cost and in general is able to accurately predict the temperature field of turbulent flames. However, the application of this model to the turbulent flames investigated in this work is not fully satisfactory: the flame temperature is over-predicted, in particular in the tail of the flame.

As a consequence the `KinPP` was applied to the CFD results obtained with the EDC model. The results of the NO formation and reduction are promising, and the agreement between computations and experiments is satisfactory. The successful prediction of flame structures and NO_x formation in these flames supports the proposed approach for the kinetic post-processor.

The `KinPP` code already is a very useful tool for the optimal design of new burners with a particular attention to pollutants formation. Prediction of soot formation in turbulent diffusion flames will be the natural extension and application of this tool. A further step in the study was to investigate the detailed effects of the chemical mechanisms. This detailed knowledge will be useful in developing improved combustion devices, such as low-NO wood stoves and waste incinerators.

4 Soot modeling in turbulent non premixed flames

In this chapter an effective methodology for predicting the formation of soot in turbulent non premixed flames is proposed and discussed. The attention is particularly focused on the correct modeling of interactions between turbulence and soot chemistry, which are taken into account through several approaches.

4.1 Introduction

The problem of soot formation in combustion devices is gaining rising importance due to its negative effects on human health and for the increasingly stringent limitations concerning the emissions of pollutants from combustion devices. Moreover, soot formation significantly influences thermal radiation which controls the burning regime in pool fires under most practical fire scenarios. In fact, soot usually dominates the radiative absorption coefficient [2] and controls the heat feedback to the liquid fuel. Furthermore, the soot formed in the flames affects the radiation heat transfer in furnaces and various practical applications [1].

The formation and oxidation of soot particles are highly complex processes, involving a large number of both homogeneous and heterogeneous chemical reactions and additional physical processes such as coagulation. All these processes can be described with a high degree of accuracy and reliability by using the most sophisticated soot models available in literature. However these models are expensive in terms of CPU time, even for simulations of laminar flames. In the numerical modeling of turbulent flames, the detailed soot models should be used together with other models necessary to describe reacting turbulent flow, leading to a very high CPU-time even for simple flames. Such detailed models could be used to help identify the conditions that reduce soot formation, but for predictions of soot particles in turbulent non premixed flames of practical interest, it is often necessary to use simplified models to keep CPU-time at an acceptable level.

Such simplified models consider only the phenomena essential for obtaining sufficiently accurate predictions of soot concentrations and reliable CFD calculations of radiative heat transfer [74].

Specific approaches are used to model soot formation. In fact, if the thermal field and most chemical species can be successfully modeled using non-equilibrium chemistry through flamelet libraries and presumed probability distribution functions (PDF), the same approach is not able to describe soot formation, due to its comparatively slow chemistry and because the soot volume fraction cannot be simply related to the mixture fraction [72]. As reported in Brookes and Moss [21], the soot is closely correlated with the mixture fraction only in a limited temperature range, corresponding to the soot peak values. On the contrary, at lower soot volume fractions the temperature PDF is broader and in some cases can also show bimodality. This behavior is due to the competition between the growth processes and the oxidation processes, which occur at different positions in the flame (especially at different mixture fraction locations) and therefore at different temperatures. The dependence of soot on the mixture fraction is even more complex: from one hand the nucleation and growth rates show a weak correlation with the mixture fraction, but, on the contrary, the oxidation rate is strongly correlated to the mixture fraction through the OH radical. In order to partially overcome these difficulties, individual balance equations must be introduced and solved for soot properties. In this way it is possible to take into account the interactions between turbulence and chemistry with a higher level of detail.

Despite intensive research over the last decades, neither universal theory, nor models have been developed for soot predictions that are applicable to different fuels and a wide range of flow conditions. If the soot formation in laminar diffusion flames can be predicted with reasonable accuracy, this is usually more difficult in turbulent diffusion flames. In general, in order to achieve a satisfactory agreement with the experimental data the modeling constants have to be adjusted for the particular problem under investigation. The main approaches proposed by in the last two decades are briefly summarized in the following.

Kollmann *et al.* [75] applied a PDF-transport model to simulate the reacting turbulent flow in a sooting ethylene diffusion flame. An additional transport equation for soot mass fraction was introduced and solved using a source term simply expressed as a function of temperature and mixture fraction.

Bai *et al.* [4] expressed the chemical source terms (growth and oxidation) in the transport equation for soot volume fraction using a flamelet library generated with a detailed kinetic scheme and normalized by the local soot volume fraction to account for the surface dependence of growth and oxidation processes. The agreement between numerical predictions and experimental measurements in terms of soot emissions was good, but the temperature was largely over predicted.

A similar approach has been used by Roditcheva and Bai [116] for the prediction of soot formation in methane/air turbulent jet flames. The difference in this case is the introduction of a second transport equation for soot particle number density.

Kronenburg *et al.* [76] predicted soot concentration in turbulent methane-air jet flames using the Conditional Moment Closure. Using this approach the closure of the soot oxidation terms is more accurate if compared to the traditional flamelet-based approaches: in fact it is well known that the laminar flamelet theory currently does not allow accurate closure of the oxidation terms in soot transport equations.

The unsteady flamelet model was used by Pitsch *et al.* [106] to describe chemistry-turbulence interactions and predict soot formation in a turbulent non-premixed jet-flame fed with ethylene. The transport equations for the soot particle number density is introduced in the flamelet library and solved using the method of statistical moments.

Wen *et al.* [136] predicted the soot formation in a turbulent kerosene/air flame comparing a conventional acetylene-based nucleation model with a polyaromatic hydrocarbon (PAH)-based nucleation model. The soot formation was modeled using two transport equations for soot particle number density and volume fraction and semi-empirical models related to the mean values of temperature and concentrations of soot precursors. The same approach was used by Ma *et al.* [85] to investigate the effects of different soot inception, growth, coagulation and oxidation source terms in two turbulent ethylene/air jet flames. The best agreement with measurements was obtained assuming the soot growth rate proportional to the square root of the surface area. A new soot inception submodel based on the naphthalene formation rate was proposed and applied.

Zucca *et al.* [142] simulated the soot formation in turbulent diffusion flames by coupling kinetics and fluid dynamics computations with the solution of the population balance equation via the Direct Quadrature Method of Moments (DQMOM). Semi-empirical models were used to model the soot formation and evolution, but the effects of turbulence on the soot reaction rates were not taken into account: all soot formation rates correspond to the averaged values that are directly calculated based on the averaged species concentrations and temperature in the turbulent flame. The main advantage of this approach with respect to the similar method followed by Wen *et al.* [136] consists in removing the hypothesis of a monodispersed soot distribution, and therefore, depending on the number of nodes used in the DQMOM formulation, more accurate descriptions of soot distribution are possible. The agreement with the experimental data is excellent, but it is not clear if the semi-empirical models used for describing soot formation can be extended to different fuels and to different flow conditions. Moreover no indication is given about the importance of turbulent closure of soot source terms.

In order to solve the important problem of the closure of source terms in soot transport equations, some authors proposed the solution of a transport equation for the joint scalar PDF of

mixture fraction and soot properties. Using this approach the correlation between the mixture fraction and the soot properties is automatically accommodated and the competition between mean surface growth and oxidation, which traditional presumed pdf approach can describe only through *ad hoc* scaling, can be better captured. In particular Aksit and Moss [3] proposed a Lagrangian Monte Carlo solution of the joint scalar PDF transport equation for mixture fraction and soot properties in a methane flame, coupled with a semi-empirical model for the description of soot formation. Unfortunately this approach is computationally very expensive and the presumed PDF approach may continue to offer advantages in most practical applications. On the contrary, Lindstedt and Louloudi [81] applied the method of statistical moments in the context of a transported PDF simulation to predict the soot formation in two different ethylene flames. The results show a good agreement with the experimental measurements and highlight the importance of accurate modeling of turbulence-chemistry interactions for the correct predictions of soot formation in turbulent flames.

In the present work the soot volume fraction in two turbulent non-premixed flames fed with ethylene [72] and methane [20] is predicted using a two-equation model. The major species and the temperature field are calculated using the flamelet approach; for this purpose a non-adiabatic flamelet library, depending on the mixture fraction, strain rate and enthalpy defect is built and stored. Two additional transport equations for the soot particle number density and the soot volume fraction are solved in the CFD code. The associated source terms are calculated using a semi-empirical model, able to take into account nucleation, surface growth, coagulation and oxidation phenomena. The effect of soot radiation is taken into account using a simplified approach, which consists in adding a source term related to the radiation from soot to the energy balance equation. Three different approaches for the closure of source terms in the transport equations for soot particle density and soot mass fractions are formulated and compared. The main objective is to demonstrate the importance of correctly describing the effects of turbulent mixing on the formation of soot in turbulent non-premixed flames.

4.2 The soot population balance equation

The formation of soot particles in a reacting system can be modeled through a Population Balance Equation (PBE). Let us define a property vector $\vec{\xi} = (\xi_1, \xi_2, \dots, \xi_n)$, whose elements ξ_i are some properties of the soot particles (for example volume, area, age, fractal dimension, etc.) and are called *internal coordinates* to distinguish them from the usual *external coordinates* of the physical space. The number density function $n(\vec{\xi}; \vec{x}; t)$ can be introduced so that:

$$n(\bar{\xi}; \bar{x}; t) \cdot d\xi_1 d\xi_2 \dots d\xi_n \cdot dV = n(\bar{\xi}; \bar{x}; t) \cdot d\bar{\xi} \cdot dV \quad (4.1)$$

is the expected number of particles in the infinitesimal volume dV , with internal coordinates in the range $[(\xi_1 + d\xi_1); \dots; (\xi_n + d\xi_n)]$. The total number of particles in the system is:

$$N_{tot}(t) = \int_V \int_{\bar{\xi}} n(\bar{\xi}; \bar{x}; t) \cdot dV \cdot d\bar{\xi} \quad (4.2)$$

whilst the total number density is:

$$N(t) = \int_{\bar{\xi}} n(\bar{\xi}; \bar{x}; t) d\bar{\xi} \quad (4.3)$$

In order to obtain the value of $n(\bar{\xi}; \bar{x}; t)$ in any point of the computational domain a population balance equation must be solved. The PBE is a continuity statement written in terms of the number density function and can be derived as a balance equation for a given control volume [91, 141]:

$$\frac{\partial n(\bar{\xi}; \bar{x}; t)}{\partial t} + \nabla_x \cdot [\bar{v} \cdot n(\bar{\xi}; \bar{x}; t)] + \nabla_{\bar{\xi}} \cdot [\bar{g} \cdot n(\bar{\xi}; \bar{x}; t)] = h(\bar{\xi}; \bar{x}; t) \quad (4.4)$$

In the equation reported above the first term on the left side is the accumulation term; the second and third terms represent the convection in the physical and in the state space respectively. The term on the right hand side is a source term, which takes into account several phenomena leading to discrete changes in the population properties (nucleation, growth, coagulation, fragmentation, etc.). Moreover, \bar{v} is the rate of change of external coordinates and \bar{g} is the rate of change of internal coordinates.

In turbulent flows, after applying the usual Favre averaging, the Equation (4.4) can be rewritten more conveniently as:

$$\frac{\partial \tilde{n}(\bar{\xi}; \bar{x}; t)}{\partial t} + \frac{\partial}{\partial x_i} [\langle U_i | \bar{\xi} \rangle \cdot \tilde{n}(\bar{\xi}; \bar{x}; t)] = \frac{\partial}{\partial x_i} \left[\Gamma_i \frac{\partial \tilde{n}(\bar{\xi}; \bar{x}; t)}{\partial x_i} \right] = \tilde{S}(\bar{\xi}; \bar{x}; t) \quad (4.5)$$

where Γ_i is the turbulent diffusion and $\langle U_i | \bar{\xi} \rangle$ is the expected value of the particle velocity conditioned to the property vector $\bar{\xi}$. The source term in the right hand side accounts for all the processes affecting the evolution of the population (i.e. both the convective term in the particle state space and the source terms in Equation (4.4)).

Soot particles are usually small enough to be considered as entrained by the fluid, i.e. the velocity of the dispersed phase is equal to that of the continuous phase. As a consequence, the system can be treated as monophasic and no multiphase modeling is required. Under these conditions the expected value of the particle velocity $\langle U_i | \bar{\xi} \rangle$ is simply equal to the expected value of the fluid velocity.

The property vector $\bar{\xi}$ can have theoretically an arbitrary number of components, but usually only one or two internal coordinates are considered. In particular for soot particles a single internal coordinate is enough to have satisfactory predictions. When the internal coordinate is the size L of the particle, the function $n(\bar{\xi}; \bar{x}; t)$ is called the Particle Size Distribution (PSD). From this PSD any information about the soot properties can be obtained, in particular the volume fraction (or equivalently the mass fraction) and the soot mean particle diameter.

Assuming that the soot particles are small enough for considering the system as monophasic, the population balance equation for the soot particle size distribution becomes:

$$\frac{\partial \tilde{n}(L; \bar{x}; t)}{\partial t} + \frac{\partial}{\partial x_i} [\tilde{u}_i \cdot \tilde{n}(L; \bar{x}; t)] = \frac{\partial}{\partial x_i} \left[\Gamma_i \frac{\partial \tilde{n}(L; \bar{x}; t)}{\partial x_i} \right] = \tilde{S}(L; \bar{x}; t) \quad (4.6)$$

The solution of Equation (4.6) is not trivial. Several procedures have been proposed, but the most commonly employed methods are based on three different approaches that are briefly summarized in the following:

- *Monte Carlo methods*: the number density function is approximated by a very large number of notional particles by a Monte Carlo algorithm; the main drawback is the large computational time needed for calculating the evolution of the particle size distribution;
- *classes methods*: are based on the discretization of the number density function in a number of classes, each of them representing a portion of the population with internal coordinates in a particular range;
- *moments methods*: the solution is obtained by solving a balance equation for a number of moments of the particle size distribution (thus obtaining indirect information on the

distribution itself). In the present thesis the soot formation is predicted using this approach and therefore some additional details are given in the following.

4.2.1 Method of moments

For a generic monodispersed number density function, the moment of order k is defined as:

$$m_k(x;t) = \int_0^\infty \xi^k n(L;\bar{x};t) \cdot dL \quad (4.7)$$

If Equation (4.6) is multiplied by ξ^k and integrated, the following balance equation for the moment of order k is obtained:

$$\frac{\partial \tilde{m}_k(\bar{x};t)}{\partial t} + \frac{\partial}{\partial x_i} [\tilde{u}_i \cdot \tilde{m}_k(\bar{x};t)] = \frac{\partial}{\partial x_i} \left[\Gamma_i \frac{\partial \tilde{m}_k(\bar{x};t)}{\partial x_i} \right] = \tilde{S}_k^m(\bar{x};t) \quad (4.8)$$

The Standard Method of Moments (SSM) solves a set of transport equations for a number of significant moments of the distribution. This approach is feasible only if the source term $S_k^m(\bar{x};t)$ in Equation (4.8) can be written using the moments which are tracked. Unfortunately this is possible only for very simple systems or assuming particular forms of the particle size distribution.

4.3 Modeling of soot formation

The soot formation in turbulent flames is usually modeled using semi-empirical models for describing the main processes of nucleation, growth, coagulation and oxidation of soot particles. The corresponding rate expressions can be written in terms of soot volume fraction f_v (or mass fraction ω_{soot}) and total number density m_0 , assuming a monodispersed distribution. Under such hypothesis the population balance equation can be conveniently solved through the Standard Method of Moments by considering only the moments of order zero m_0 and three m_3 (if particle size is chosen as the internal coordinate), which are directly related to soot particle number density and soot volume fraction. This approach is used for the numerical methodology presented in this Chapter for predicting soot formation in turbulent flames. A more accurate approach, which removes the restrictive hypothesis of monodispersed particle size distribution, based on the Direct Quadrature Method of Moments (DQMOM), is presented and applied in Chapter 5.

Two additional transport equations are solved in a CFD code to predict soot formation and evolution: the first equation accounts for the transport of particle number density m_0 (which is the moment of zero order of the particle size distribution); the second equation describes the transport of the soot volume fraction f_V (which is related to the moment of order three of the particle size distribution). The particles are assumed to be spherical and the size distribution simply represented by an average diameter d_p . In other words, the particle size distribution becomes a simple Dirac delta function, centered on the average diameter. As a consequence:

$$m_3 = \int_0^{\infty} L^3 \cdot n_L(L) dL = \int_0^{\infty} L^3 \cdot \delta(L - d_p) dL = d_p^3 \quad (4.9)$$

From the hypothesis of spherical shape it is relatively easy to obtain the relation between the soot volume fraction f_V and the moment of order three:

$$\omega_{soot} = \frac{\pi}{6} \int_0^{\infty} L^3 \cdot n_L(L) dL = \frac{\pi}{6} m_3 \quad (4.10)$$

Therefore a transport equation for the soot volume fraction is perfectly equivalent to a transport equation for the moment m_3 of the particle size distribution. The relation between the soot volume fraction and the particle diameter is explicitly reported below for convenience:

$$d_p = \sqrt[3]{\frac{6 f_V}{\pi m_0}} \quad (4.11)$$

For numerical convenience two density weighted variables are introduced: ϕ_N for the particle density and ϕ_M for the soot mass fraction [21]:

$$\phi_N = \frac{m_0}{\rho N_{AV}} \quad (4.12)$$

$$\phi_M = \frac{\rho_{soot} f_V}{\rho} \quad (4.13)$$

The transport equations for these variables are given by:

$$\bar{\rho} \frac{\partial \tilde{\phi}_N}{\partial t} + \bar{\rho} \tilde{u}_i \frac{\partial \tilde{\phi}_N}{\partial x_i} = \frac{\partial}{\partial x_i} \left(\Gamma_t \frac{\partial \tilde{\phi}_N}{\partial x_i} \right) + \tilde{S}_{m0} \quad (4.14)$$

$$\bar{\rho} \frac{\partial \tilde{\phi}_M}{\partial t} + \bar{\rho} \tilde{u}_i \frac{\partial \tilde{\phi}_M}{\partial x_i} = \frac{\partial}{\partial x_i} \left(\Gamma_t \frac{\partial \tilde{\phi}_M}{\partial x_i} \right) + \tilde{S}_M \quad (4.15)$$

It is relatively easy to recognize in the variable ϕ_M the soot volume fraction ω_{soot} . The source terms can be written as a sum of different contributions:

$$S_{m0} = S_{m0}^{nucleation} + S_{m0}^{coagulation} \quad (4.16)$$

$$S_M = S_M^{nucleation} + S_M^{growth} + S_M^{oxidation} \quad (4.17)$$

It is assumed that the influence of oxidation on the nucleation of soot particles is small and therefore the oxidation term is not included in the first equation [129].

For turbulent flames the effects of turbulent fluctuations should be taken into account in the evaluation of these source terms. The simplest approach, which has been followed by several authors [85, 136, 142], solves the transport equations and neglects the effects of turbulence. In the present thesis this simplified approach is compared with two different closure models, which accounts for the effect of turbulent fluctuations on the soot source terms.

4.4 Semi-empirical kinetic models

4.4.1 Nucleation Rate

Soot nucleation is described by the so called acetylene-route, which is based on a simple one-step reaction:



The corresponding source terms are expressed in the usual Arrhenius form:

$$S_{m0}^{nucleation} = A_{nucl} \cdot e^{-T_{nucl}/T} \cdot C_{C_2H_2} \quad (4.19)$$

$$S_M^{nucleation} = M_p S_{m0} \quad (4.20)$$

In the expressions reported above A_{nucl} is the frequency factor, T_{nucl} is the activation temperature, C_{C2H2} is the concentration of acetylene and M_p is the molecular weight of soot primary particles. The rate parameters proposed by Liu *et al.* [84] are adopted and summarized in Table 2.

	A	T_u [K]	M_p [kg/kmol]	References
$k_{Nucleation}$	2.857	16103	8400	[84]
k_{Growth}	42000	10064	-	[84]
$k_{Oxidation}$	108500	19778	-	[79, 84]

Table 2. Reaction rate constants for soot formation and oxidation. Constants are in form of Arrhenius expression $k=A \cdot \exp(-T_a/T)$. Units are [K, kmol, m, s].

4.4.2 Growth Rate

According to Frenklach *et al.* [49], the soot particle growth is determined by the addition of acetylene and on the number of active sites on the surface. Assuming a monodispersed spherical particle distribution, the soot specific surface area can be expressed as a function of the soot particle number density m_0 and to the soot volume fraction f_V :

$$A_{soot} = (36\pi)^{1/3} m_0^{1/3} f_V^{2/3} \quad (4.21)$$

The surface growth rate is given by:

$$S_M^{growth} = A_{growth} \cdot e^{-T_{growth}/T} \cdot C_{C2H2} \cdot f(A_{soot}) \quad (4.22)$$

A range of area dependencies have been proposed in the literature; according to the most common approaches the function f is assumed linearly proportional to the soot specific surface area $f(A_{soot}) = A_{soot}$ or to square root surface area $f(A_{soot}) = \sqrt{A_{soot}}$. Although the square-root dependence of the soot surface area does not seem physically correct, it can be related to the surface aging phenomena and active-site surface deactivation [84]. In this work the model proposed by Liu *et al.* [84] is used and is reported in Table 2.

4.4.3 Coagulation Rate

The coagulation rate depends on soot particles density; assuming a monodispersed distribution of spherical particles:

$$S_{m0}^{coagulation} = \beta m_0^2 \quad (4.23)$$

According to Brookes and Moss [21] and Syed *et al.* [129], β is related to the temperature:

$$\beta = \frac{A_{coagulation}}{N_{AV}^2} \sqrt{T} \quad (4.24)$$

where $A_{coagulation}$ is a semi-empirical constant. The value proposed by Brookes and Moss [21] is used in the present work:

$$A_{coagulation} = 2.25 \cdot 10^{15} \frac{m^3}{s \cdot kmol \cdot \sqrt{K}} \quad (4.25)$$

4.4.4 Oxidation Rate

The oxidation rate strongly depends on the hydroxyl radical (OH) and O₂ but also O radical can play an important role. The rate of oxidation is usually assumed proportional to the soot specific surface area:

$$S_M^{oxidation} = \dot{m}_{ox} A_S \quad (4.26)$$

In this work the model of Lee *et al.* [79] is adopted and soot oxidation is described using a one-step reaction:



The soot oxidation term takes the form:

$$\dot{m}_{ox} = A_{ox} \cdot e^{-T_{ox}/T} \frac{P_{O_2}}{\sqrt{T}} \quad (4.28)$$

This model was also used by Liu *et al.* [84], Wen *et al.* [136] and Ma *et al.* [85] and implicitly assumes that soot oxidation in a diffusion flame is controlled by O₂ into the zone of active soot oxidation at temperatures high enough to react with H and form OH, which is recognized as the main oxidizing species in the stoichiometric/lean side of the flame. On the

contrary, O_2 becomes more important as any surviving particles enter oxygen-rich regions where temperature is still high [34].

4.5 Flamelet library and enthalpy defect

Using the laminar flamelet model, the thermochemical state of an adiabatic turbulent flame is completely determined by the mixture fraction Z and the scalar dissipation rate χ_{st} : $\psi = \psi(Z, \chi_{st})$.

The mean value $\tilde{\psi}$ can be obtained using the bivariate PDF $P(Z, \chi_{st})$:

$$\tilde{\psi} = \int_0^1 \int_0^{+\infty} \psi(Z, \chi_{st}) \cdot P(Z, \chi_{st}) \cdot dZ \cdot d\chi_{st} \quad (4.29)$$

A presumed PDF approach is used in the present thesis. According to Bilger [13], the result of integration with respect to the mixture fraction is relatively insensitive to the details of the PDF shape, if it is chosen on physical grounds. Usually a β -PDF or a clipped Gaussian PDF are adopted. As reported by several authors [47, 101, 107], the integration with respect to χ_{st} can be described by a log-normal distribution.

The effect of radiation cannot be disregarded especially in sooting flames, due to the mutual sensitivity between temperature and soot formation which enhances radiation. The coupling between the flamelet library and the radiative heat transfer in the turbulent flames cannot be easily described. As reported in Bray and Peters [18] and in Hossain *et al.* [66], the radiation heat loss in a laminar flamelet can be very different from the radiation heat loss in the real, turbulent flame. In the first case the radiation heat exchange occurs as thin gas radiative emissions to the surroundings within a thin region of high temperature. On the contrary radiation from the turbulent flame is influenced by local properties and global effects arising from properties at distant locations. These effects, which can be very important, can be taken into account only if an equation for the enthalpy, containing the source term due to the radiative heat transfer, is directly solved in the CFD code. Therefore, according to the approach first suggested by Bray and Peters [18], the coupling between the flamelet library and the mean scalar variable in the turbulent flame can be achieved by introducing an additional parameter, which is called the *enthalpy defect*:

$$\phi_H = \hat{H} - \hat{H}_{AD} = \hat{H} - \left[\hat{H}_{OX} + Z \left(\hat{H}_{FUEL} - \hat{H}_{OX} \right) \right] \quad (4.30)$$

where \hat{H} is the actual enthalpy in the turbulent flame and \hat{H}_{OX} and \hat{H}_{FUEL} denote the enthalpy of the oxidizer and the fuel streams respectively. Once the enthalpy defect is introduced, the average value of every state quantity $\tilde{\psi}$ in the laminar flame can be recovered by introducing a proper joint-PDF of Z , χ_{st} and ϕ_H :

$$\tilde{\psi} = \int_{-\infty}^{+\infty} \int_0^1 \int_0^1 \psi(Z, \chi_{st}, \phi_H) \cdot P(Z, \chi_{st}, \phi_H) \cdot dZ \cdot d\chi_{st} \cdot d\phi_H \quad (4.31)$$

A common simplification is based on the assumption of statistical independence:

$$P(Z, \chi_{st}, \phi_H) = P(Z) \cdot P(\chi_{st}) \cdot P(\phi_H) \quad (4.32)$$

The PDF of enthalpy defect is not easily accessible, neither experimentally nor theoretically. Therefore, in absence of information, starting from the consideration that any reasonable account of heat losses represents an improvement with respect to the assumption of an adiabatic flow, the solution proposed by Bray and Peters [18] and adopted by several authors [53, 92] has been used in this thesis. The effects of enthalpy defect fluctuations are completely neglected and therefore the corresponding $P(\phi_H)$ is assumed to be a Dirac delta function centered on the local mean value of the enthalpy defect ϕ_H . The final form of the joint-PDF $P(Z, \chi_{st}, \phi_H)$ becomes:

$$P(Z, \chi_{st}, \phi_H) = P(Z) \cdot P(\chi_{st}) \cdot \delta(\phi_H - \tilde{\phi}_H) \quad (4.33)$$

where $P(Z)$ is a β -PDF (or a Clipped Gaussian PDF) and $P(\chi_{st})$ a log-normal distribution.

The flamelet profiles can be organized in shelves, using the enthalpy defect ϕ_H as a library parameter [92]. Each shelf represents a different value of the enthalpy defect and contains entries referring to different values of scalar dissipation rate χ_{st} , ranging from the equilibrium solution to the extinction plus the inert state. Each of these shelves is completely independent: the number of scalar dissipation rates, the number of points in the mixture fraction space and in the mixture fraction variance space can be different from one shelf to another one. In this way each value of enthalpy defect can be described with a sufficiently large degree of accuracy. The mean enthalpy \tilde{H} , used to obtain the enthalpy defect, is calculated from its conservation equation:

$$\bar{\rho} \frac{\partial \tilde{H}}{\partial t} + \bar{\rho} \tilde{u}_i \frac{\partial \tilde{H}}{\partial x_i} = \frac{\partial}{\partial x_i} \left(\Gamma_i \frac{\partial \tilde{H}}{\partial x_i} \right) + \bar{Q}_{rad} \quad (4.34)$$

The radiation term \bar{Q}_{rad} is calculated using the optically-thin approximation, but more accurate solutions are possible. Once the value of the mean enthalpy is obtained from the equation reported above, the value of the enthalpy defect can be calculated for each grid node. Mean scalar variables are then calculated using the flamelet profiles. Since a limited number of shelves are available in the library, interpolation is required to calculate the mean scalar variables. A linear interpolation is employed, as suggested by Marracino and Lentini [92] and Hossain *et al.* [66]:

$$\tilde{\psi} = \frac{\tilde{\phi} - \phi_m}{\phi_{m-1} - \phi_m} \tilde{\psi}_{m-1} + \frac{\phi_{m-1} - \tilde{\phi}}{\phi_{m-1} - \phi_m} \tilde{\psi}_m \quad (4.35)$$

where m denotes the library shelf index such that the enthalpy defect at a node lies between m and $m-1$ and where $\tilde{\psi}_m$ stands for:

$$\tilde{\psi}_m = \int_0^1 \int_0^1 \psi(Z, \chi_{st}, \phi_m) \cdot P(Z, \chi_{st}) \cdot dZ \cdot d\chi_{st} \quad (4.36)$$

The flamelet library with enthalpy defect can be constructed by modifying the source term in the flamelet equation for the enthalpy or by modifying the available enthalpy. In this work the second approach has been followed. The flamelet equations are solved in the mixture fraction space and the same value of enthalpy defect is enforced at both the fuel and oxidizer sides. If equal diffusivities for all the species are assumed this assumption warrants the enthalpy defect to be uniform across the flamelet thickness [92].

The approach summarized in this section has been successfully implemented by Marracino and Lentini [92], Giordano and Lentini [53] and Hossain *et al.* [66]. However the flames investigated by these authors were characterized by a small amount of soot. On the contrary the formation of soot particles in the flames studied in the present work is large ($f_V \sim 1$ ppm) and therefore the effects of radiation are expected to be very important. As a consequence the temperature and concentration fields are largely affected by the heat loss.

4.6 Radiative heat transfer

The sooting flames studied in this work can be successfully modeled using the optically-thin approximation [21, 76, 82, 84, 92], although this approximation is known to slightly overestimate radiation, because it neglects re-absorption. According to this model, the radiation source term in Equation (4.34) becomes:

$$\tilde{Q}_{rad} = -4\sigma \cdot a \cdot (\tilde{T}^4 - T_{env}^4) \quad (4.37)$$

where T_{env} is the environment temperature which is assumed to be 300 K. In this model only contributions of H_2O , CO_2 , CO , CH_4 and soot are considered, according to the following expression:

$$a = p_{H_2O} a_{p,H_2O} + p_{CO_2} a_{p,CO_2} + p_{CO} a_{p,CO} + f_V a_{fv,soot} \quad (4.38)$$

where p_i is the partial pressure of species i and f_V is the soot volume fraction. Even if H_2O , CO_2 and soot are the most important radiating species in combustion environments, also methane and carbon monoxide were included in the computation

The extinction coefficients for H_2O , CO_2 , CO and CH_4 are derived from calculations performed by the RADCAL software [59]. The following expressions, which are valid in the range between 300K and 2500K, were used to calculate the Plank mean absorption coefficients [9]:

$$a_{p,H_2O} = -0.23093 - \frac{1.1239 \cdot 10^3}{T} + \frac{9.4153 \cdot 10^6}{T^2} - \frac{2.9988 \cdot 10^9}{T^3} + \frac{0.51382 \cdot 10^{12}}{T^4} - \frac{1.8684 \cdot 10^{10}}{T^5} \quad (4.39)$$

$$a_{p,CO_2} = 18.741 - \frac{1.2131 \cdot 10^5}{T} + \frac{2.735 \cdot 10^8}{T^2} - \frac{1.94050 \cdot 10^{11}}{T^3} + \frac{5.6310 \cdot 10^{13}}{T^4} - \frac{5.8169 \cdot 10^{15}}{T^5} \quad (4.40)$$

$$a_{p,CH_4} = 6.6334 - 0.0035686 \cdot T + 1.6682 \cdot 10^{-8} \cdot T^2 + 2.5611 \cdot 10^{-10} \cdot T^3 - 2.6558 \cdot 10^{-14} \cdot T^4 \quad (4.41)$$

$$a_{p,CO} = c_0 + c_1 T + c_2 T^2 + c_3 T^3 + c_4 T^4 \quad (4.42)$$

where the values of coefficients c_i are reported in Table 3.

The extinction coefficient of soot is evaluated according to Sahzin [118]:

$$a_{f_v,soot} = 1232\rho_{soot} \left[1 + 4.8 \cdot 10^{-4} (T - 2000) \right] \quad (4.43)$$

where ρ_{soot} is the soot density (here assumed to be 1800 kg/m^3) and $a_{f_v,soot}$ units are m^{-1} .

	T<750K	T>750K
c_0	4.7869	10.09
c_1	-0.06953	-0.01183
c_2	$2.95775 \cdot 10^{-4}$	$4.7753 \cdot 10^{-6}$
c_3	$-4.25732 \cdot 10^{-7}$	$-5.87209 \cdot 10^{-10}$
c_4	$2.02894 \cdot 10^{-10}$	$-2.5334 \cdot 10^{-14}$

Table 3. Coefficients in Equation (4.42) for the evaluation of the mean Planck absorption coefficient of carbon monoxide.

4.7 Closure of soot source terms

One of the major issues in the modeling of soot formation is the closure of the soot source terms in the conservation equations for soot particle number density m_0 and soot volume fraction f_v . In general the mean source term can be expressed using the proper joint-PDF $P(\xi, \chi_{st}, \phi_H, m_0, f_v)$:

$$\tilde{S} = \int_0^{+\infty} \int_0^{+\infty} \int_{-\infty}^{+\infty} \int_0^1 S(Z, \chi_{st}, \phi_H, m_0, f_v) \cdot P(Z, \chi_{st}, \phi_H, m_0, f_v) \cdot dZ \cdot d\chi_{st} \cdot d\phi_H \cdot dm_0 \cdot df_v \quad (4.44)$$

The form of this joint-PDF is unknown, both experimentally and theoretically, and therefore simplified approaches must be used in order to obtain the closure of the source term.

4.7.1 Mean Properties

The simplest approach consists in evaluating the source term using the mean flame properties and totally ignoring the effects of turbulence [21]. In this case the joint-PDF can be split in the product of five PDFs of a single variable:

$$P(Z, \chi_{st}, \phi_H, m_0, f_v) \cong P(Z) \cdot P(\chi_{st}) \cdot P(\phi_H) \cdot P(m_0) \cdot P(f_v) \quad (4.45)$$

Moreover each PDF simply becomes a Dirac delta function centered on the mean value of each independent variable:

$$P(Z, \chi_{st}, \phi_H, m_0, f_V) \cong \delta(Z - \tilde{Z}) \cdot \delta(\chi_{st} - \tilde{\chi}_{st}) \cdot \delta(\phi_H - \tilde{\phi}_H) \cdot \delta(m_0 - \tilde{m}_0) \cdot P(f_V - \tilde{f}_V) \quad (4.46)$$

4.7.2 Uncorrelated closure

A different solution assumes that mixture fraction and enthalpy defect are completely uncorrelated with soot properties (m_0 and f_V). This solution was adopted by many authors [4, 21, 116] and assumes that the influence of scalar fluctuations in the gas phase are dominant. The joint-PDF can be split in the product of two different PDFs:

$$P(Z, \chi_{st}, \phi_H, m_0, f_V) \cong P(Z, \chi_{st}, \phi_H) \cdot P(m_0, f_V) \quad (4.47)$$

Moreover, the soot properties are also assumed statistically independent:

$$P(Z, \chi_{st}, \phi_H, m_0, f_V) \cong P(Z, \chi_{st}, \phi_H) \cdot P(m_0) \cdot P(f_V) \quad (4.48)$$

The single PDF for the soot volume fraction is unknown. Two Dirac delta functions can be used to obtain the closure. The final form of the joint-PDF is therefore the following:

$$P(Z, \chi_{st}, \phi_H, m_0, f_V) \cong P(Z, \chi_{st}, \phi_H) \cdot \delta(m_0 - \tilde{m}_0) \cdot \delta(f_V - \tilde{f}_V) \quad (4.49)$$

where: $P(Z, \chi_{st}, \phi_H) \cong P(Z) \cdot P(\chi_{st}) \cdot \delta(\phi_H - \tilde{\phi}_H)$.

A very large flamelet library must be constructed and stored using a large number of enthalpy defects. For each ϕ_H about 20 steady flamelets were calculated at different strain rates, from equilibrium conditions ($\chi_{st} = 0$) to the extinction value ($\chi_{st} = \chi_{ext}$) (which is affected by ϕ_H). A finite-difference C++ code and a fully-implicit method, based on the BzzLibraries [25, 26], was used to build the flamelet library adopting detailed chemistry [113]. The integration in the mixture fraction space must be performed in a very accurate way due to the possible presence of singularities of the β -PDF at $Z = 0$ and $Z = 1$. The approach proposed by Liu *et al.* [83] is adopted, as it warrants higher accuracy than traditional methods [80]. The integration in the scalar dissipation rate is easier and was performed following the approach proposed by Lentini [80]. Some additional details about the library construction are reported in Appendix A.

4.7.3 Correlated Closure

The third approach assumes that the soot properties m_0 and f_V are perfectly correlated with the mixture fraction. This approximation can be considered satisfactory in the regions where the soot formation is fast. In this case the soot is associated with a limited temperature range and is therefore closely correlated with the mixture fraction, as experimentally observed by Sivanathu and Faeth [123]. On the contrary if the soot concentration is low, the PDF broadens and in some cases becomes bimodal. The bimodality is associated with the soot growth and oxidation phases, which are characterized by two different temperature ranges.

The soot mean properties can be usually described in the mixture fraction space by functions of constant shape, but different magnitude (depending on the strain rate and enthalpy defect values). This behavior can be successfully exploited in the correlated approach by imposing the profiles of soot particle number density m_0 and soot volume fraction f_V (obtained from a laminar flame calculation, as discussed in the following) on the mean soot properties (obtained from the transport equations in the CFD code). The joint-PDF $P(Z, \chi_{st}, \phi_H, m_0, f_V)$ can successfully be replaced by the PDF $P(Z, \chi_{st}, \phi_H)$. As a consequence the mean soot properties are calculated according to the following expression:

$$\tilde{m}_0 = \int_{-\infty}^{+\infty} \int_0^1 \int_0^1 m_0(Z, \chi_{st}, \phi_H) \cdot P(Z, \chi_{st}, \phi_H) \cdot dZ \cdot d\chi_{st} \cdot d\phi_H \quad (4.50)$$

$$\tilde{f}_V = \int_{-\infty}^{+\infty} \int_0^1 \int_0^1 f_V(Z, \chi_{st}, \phi_H) \cdot P(Z, \chi_{st}, \phi_H) \cdot dZ \cdot d\chi_{st} \cdot d\phi_H \quad (4.51)$$

In order to correctly take into account the dependence of growth and oxidation phenomena on the soot particle specific area A_{soot} , the normalized profiles of soot particle number density $m_0^N(Z, \chi_{st}, \phi_H)$ and soot volume fraction $f_V^N(Z, \chi_{st}, \phi_H)$, obtained from laminar calculations, must be introduced in the expressions reported above. In particular, it is possible to express the soot particle number density and soot volume fraction profiles as a function of the normalized profiles:

$$m_0(Z, \chi_{st}, \phi_H) = \frac{m_0^N(Z, \chi_{st}, \phi_H)}{\tilde{m}_0^N} \tilde{m}_0 \quad (4.52)$$

$$f_V(Z, \chi_{st}, \phi_H) = \frac{f_V^N(Z, \chi_{st}, \phi_H)}{\tilde{f}_V^N} \tilde{f}_V \quad (4.53)$$

Normalized profiles of soot particle number density $m_0^N(Z, \chi_{st}, \phi_H)$ and soot volume fraction $f_V^N(Z, \chi_{st}, \phi_H)$ allow one to calculate the soot mean properties in the turbulent flame:

$$\begin{aligned} \tilde{m}_0 &= \int_{-\infty}^{+\infty} \int_0^1 \int_0^1 \frac{m_0^N(Z, \chi_{st}, \phi_H)}{\tilde{m}_0^N} \cdot \tilde{m}_0 \cdot P(Z, \chi_{st}, \phi_H) \cdot dZ \cdot d\chi_{st} \cdot d\phi_H = \\ &= \frac{\tilde{m}_0}{\tilde{m}_0^N} \int_{-\infty}^{+\infty} \int_0^1 \int_0^1 m_0^N(Z, \chi_{st}, \phi_H) \cdot P(Z, \chi_{st}, \phi_H) \cdot dZ \cdot d\chi_{st} \cdot d\phi_H \end{aligned} \quad (4.54)$$

$$\begin{aligned} \tilde{f}_V &= \int_{-\infty}^{+\infty} \int_0^1 \int_0^1 \frac{f_V^N(Z, \chi_{st}, \phi_H)}{\tilde{f}_V^N} \cdot \tilde{f}_V \cdot P(Z, \chi_{st}, \phi_H) \cdot dZ \cdot d\chi_{st} \cdot d\phi_H = \\ &= \frac{\tilde{f}_V}{\tilde{f}_V^N} \int_{-\infty}^{+\infty} \int_0^1 \int_0^1 f_V^N(Z, \chi_{st}, \phi_H) \cdot P(Z, \chi_{st}, \phi_H) \cdot dZ \cdot d\chi_{st} \cdot d\phi_H \end{aligned} \quad (4.55)$$

Also in this case:

$$P(Z, \chi_{st}, \phi_H) \cong P(Z) \cdot P(\chi_{st}) \cdot \delta(\phi_H - \tilde{\phi}_H) \quad (4.56)$$

The normalized profiles $m_0^N(Z, \chi_{st}, \phi_H)$ and $f_V^N(Z, \chi_{st}, \phi_H)$ are obtained from two additional transport equations for m_0 and f_V , which are included in the laminar flamelet library [105]:

$$\frac{\partial m_0}{\partial t} = -\sqrt{\frac{\chi}{2\Gamma_f}} \left[\frac{\partial}{\partial Z} (\rho m_0 V_{soot}) + \frac{\partial m_0}{\partial Z} \frac{\partial}{\partial Z} \left(\rho \Gamma_f \sqrt{\frac{\chi}{2\Gamma_f}} \right) \right] + S_{m0} \quad (4.57)$$

$$\rho \frac{\partial \phi_M}{\partial t} = -\sqrt{\frac{\chi}{2\Gamma_f}} \left[\frac{\partial}{\partial Z} (\rho \phi_M V_{soot}) + \frac{\partial \phi_M}{\partial Z} \frac{\partial}{\partial Z} \left(\rho \Gamma_f \sqrt{\frac{\chi}{2\Gamma_f}} \right) \right] + S_M \quad (4.58)$$

where ϕ_M is the soot mass fraction which is simply related to the volume fraction by $\phi_M = f_V \rho_{soot} / \rho$. The Equations (4.57) and (4.58) allow the accurate description of differential diffusion effects in the flamelet library for soot particles. The soot diffusion velocity V_{soot} is

computed assuming that only thermophoretic diffusion occurs [50] and neglecting the interaction of soot with other species in the gas phase:

$$V_{soot} = -0.55 \frac{\nu}{T} \sqrt{\frac{\chi}{2D_f}} \frac{\partial T}{\partial \xi} \quad (4.59)$$

where ν is the kinematic viscosity of the gas mixture. The construction of a non-adiabatic flamelet library for the correlated approach, accounting of course for different enthalpy defects, is not trivial, because of the assumption of non-unitary Lewis numbers. A simplified solution is adopted: since only soot particle density and mass fraction are characterized by a non-unity Lewis number, constant enthalpy defects are assumed in the mixture fraction space.

4.8 Kinetic mechanism

Numerical results presented in this Chapter were obtained using the detailed kinetic scheme *C1C30704*, which describes pyrolysis and oxidation reactions of light hydrocarbons [113]. The scheme consists of 69 species involved in 1136 elementary reactions. Thermodynamic data and transport properties are taken from the CHEMKIN Database [71] with improved values for OH and HO₂ formation enthalpy [48]. Reverse rate constants are calculated via forward rates and equilibrium constants.

This detailed kinetic mechanism is the core of a larger scheme, based on a modular and hierarchical structure [137], which has been validated in a wide range of pyrolysis and combustion conditions both with pure fuels and hydrocarbon mixtures up to surrogates of real transportation fuels [110, 111]. This kinetic scheme has been also extended to also include the kinetics of soot formation and oxidation, with the discrete sectional method [55, 114].

4.9 Experimental flames

This work analyses two different turbulent flames, experimentally investigated by Kent and Honnery (Flame A) [72] and Brookes and Moss (Flame B) [21]. For both of them accurate measurements of temperature and soot volume fraction are available. The main data for the flames investigated are summarized in Table 4.

Flame A is a non confined turbulent jet flame, in which ethylene is burned in air at atmospheric pressure; the fuel is injected through a nozzle with a diameter equal to 3 mm at the temperature of 322 K. The fuel mean velocity is ~52 m/s; the resulting Reynolds number is ~14500. The experimentally measured length of the flame is ~460 mm, which corresponds to

~153D (where D is the fuel inlet diameter). Experimental results include axial and radial profiles of temperature and soot volume fraction.

Flame B is a confined turbulent jet flame fed with methane. The fuel is injected in a central tube (4.07 mm internal diameter and 1.6 mm wall thickness). The average fuel flow velocity was 20.3 m/s with a resulting Reynolds number of ~5000. The flame is confined in a Pyrex tube of internal diameter 155 mm. The inlet temperature of fuel and air is ~290K. Axial and radial profiles at different distances from the fuel inlet are available for temperature and soot volume fraction.

	Flame A	Flame B
<i>Fuel</i>	Ethylene	Methane
<i>Fuel Temperature [K]</i>	322K	290K
<i>Nozzle Diameter [mm]</i>	3.00	4.07
<i>Fuel Velocity [m/s]</i>	52	20.3
<i>Reynolds Number</i>	14460	5000
<i>Flame Length</i>	153D	130D
<i>Stoichiometric Mixture Fraction</i>	0.064	0.055
<i>References</i>	[72]	[20]

Table 4. Operating conditions for the two flames investigated

4.10 Construction of the Flamelet Library

About 10 different enthalpy defects, ranging from 0 to -550 kJ/kg (which is the minimum value observed in Flame A) and from 0 to -400 kJ/kg for Flame B, were considered. Each flamelet was solved using about 70 non-equispaced points and a mixture fraction variance space described by 32 non-equispaced points. The resulting flamelet libraries are very large: more than 200 flamelets for Flame A and Flame B were calculated, post-processed and stored.

In Figure 38 and Figure 39 an example extracted from the flamelet library calculations from Flame A and Flame B is reported. The temperature and main species mole fraction profiles are reported at several scalar dissipation rates. As expected the peak temperature tends to become lower when the scalar dissipation rate is increased. The behavior of chemical species is more complex is: for example the OH shows a super-equilibrium concentration when the scalar dissipation rate as an intermediate value between 0.10 and 5 Hz. On the contrary, CO₂ concentration decreases in a monotonic way when the scalar dissipation rate increases.

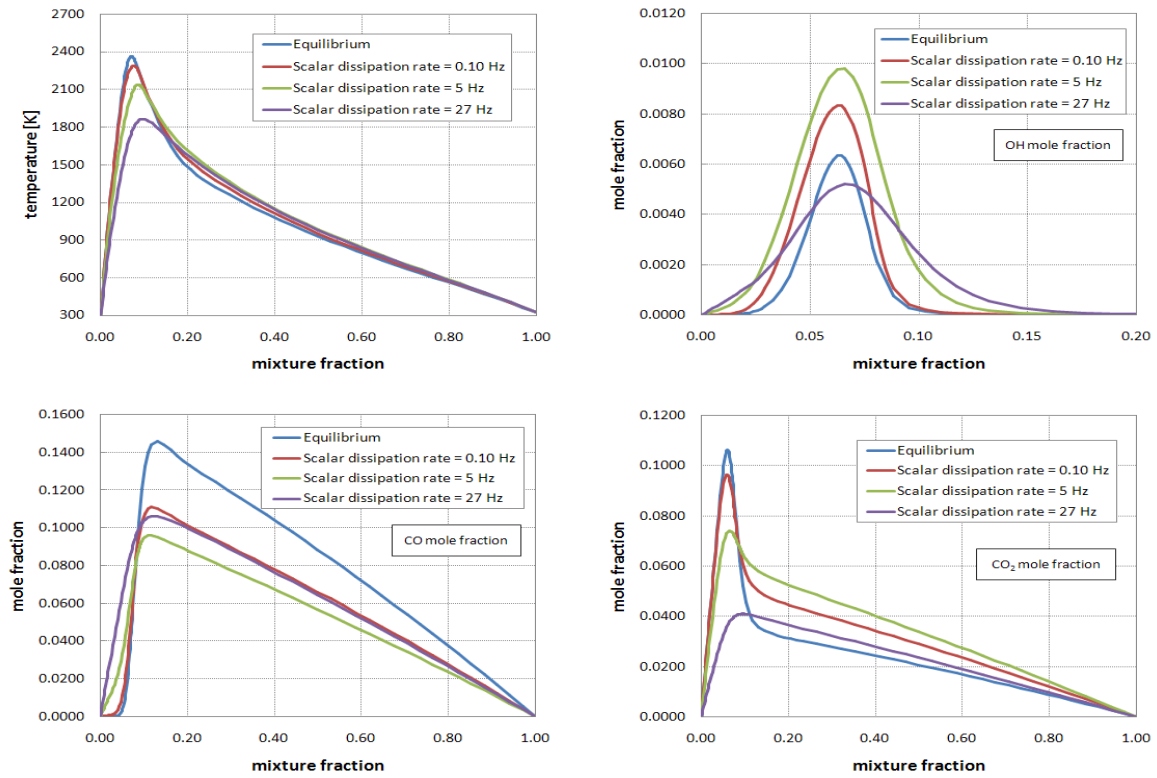


Figure 38. Flame A: temperature and species profiles versus the mixture fraction at different scalar dissipation rate.

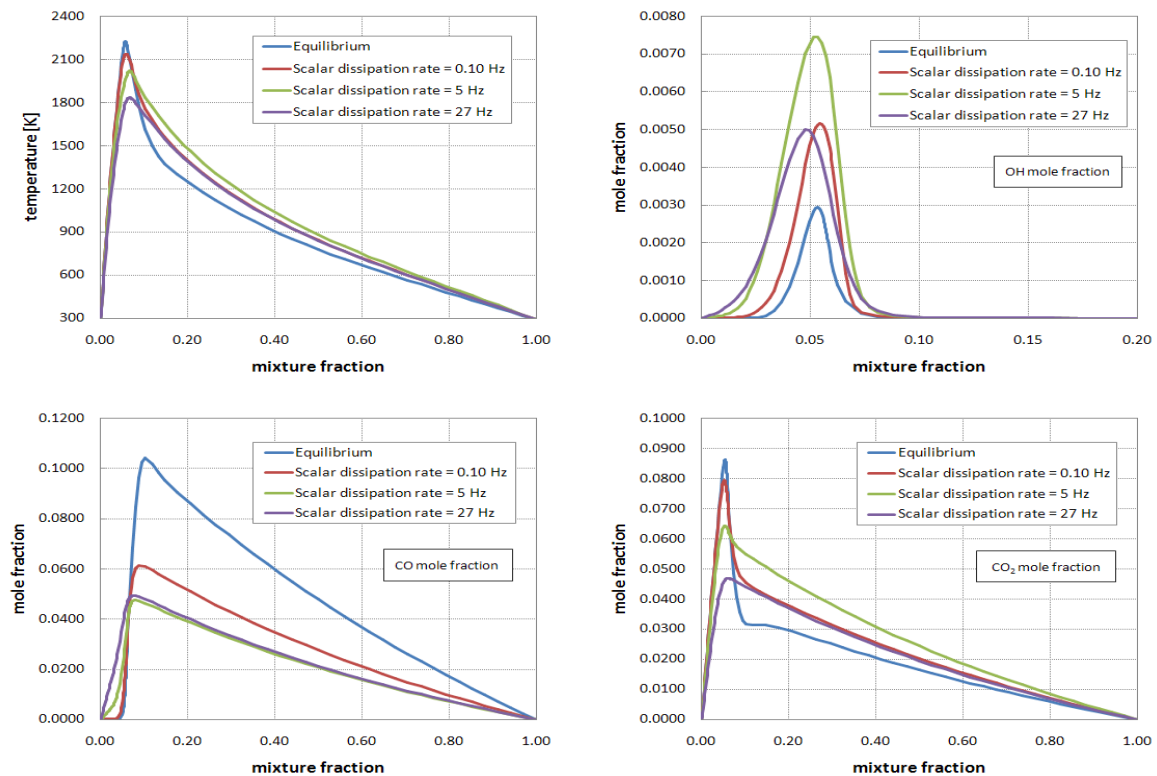


Figure 39. Flame B: temperature and species profiles versus the mixture fraction at different scalar dissipation rate.

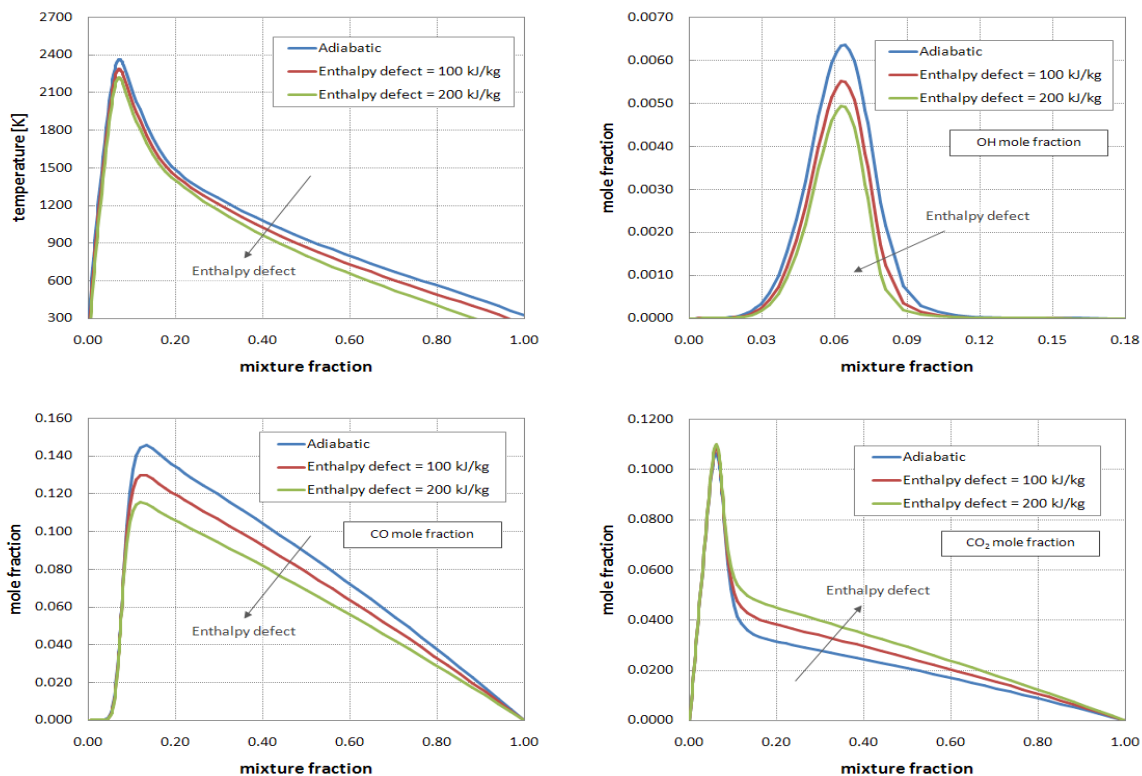


Figure 40. Flame A: temperature and species profiles versus the mixture fraction at different enthalpy defects and equilibrium conditions.

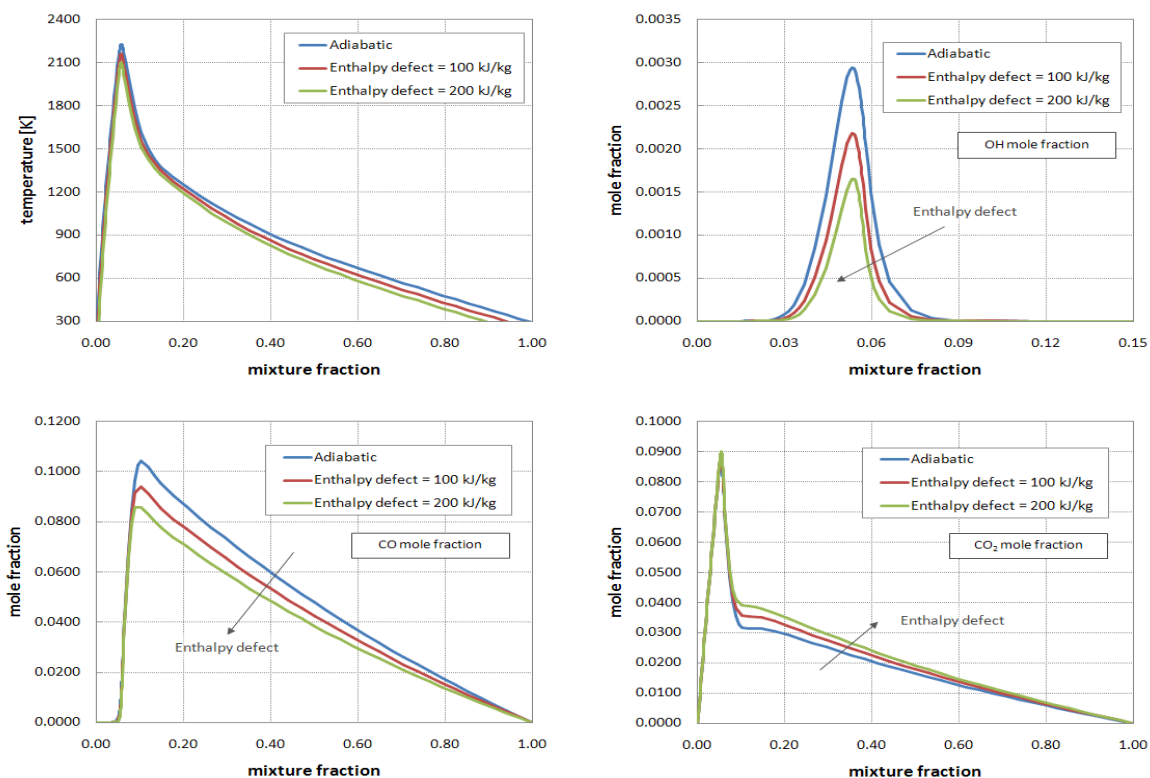


Figure 41. Flame B: temperature and species profiles versus the mixture fraction at different enthalpy defects and equilibrium conditions.

More interesting is to investigate the role of enthalpy defect on the temperature and species profiles, as reported in Figure 40 and Figure 41. As expected, a large enthalpy defect can cause a strong reduction in the temperature peak. For example, when the enthalpy defect is equal to 200 kJ/kg (which can be found in both the flames in the region where the soot amount is large), the peak temperature decreases of 150K with respect to the adiabatic value. The concentration of main species tends to become smaller when the enthalpy defect is large, with the exception of CO₂. The trends are very similar for both the flames.

If the uncorrelated approach is adopted, the soot source terms (nucleation, growth, coagulation and oxidation) must be extracted from the flamelet library in order to obtain the mean source terms which take into account the effects of turbulent fluctuations. In Figure 42 and Figure 43 the soot source terms profiles of nucleation, growth and oxidation are reported versus the mixture fraction at several scalar dissipation rates in adiabatic conditions. Typically the maximum value for soot nucleation and growth does not correspond to the equilibrium conditions, but it is obtained for an intermediate value of scalar dissipation rate. The oxidation rate is located in a very narrow region of the mixture fraction space, near the stoichiometric value.

The soot particle number density and volume fraction profiles in the mixture fraction space must be calculated if the correlated approach is chosen to close the soot source term. In Figure 44 and Figure 45 the soot particle number density and soot volume fraction profiles are reported versus the mixture fraction as calculated through the flamelet equations for Flame A and Flame B respectively. It is pretty evident that the peak values, both of m_o and f_v , are strongly dependent on the scalar dissipation rate. As expected the soot formation tends to decrease when the scalar dissipation rate becomes larger. Flame B, which is fed with ethylene, produce a thicker sooting zone than the Flame A, fed with methane, whilst the peak value is lower. Moreover the differences between the shapes of soot volume fraction profiles for the two Flames are very evident.

If the soot profiles are normalized using the peak values, it is possible to show that the curves corresponding to the normalized profiles tend to collapse on each other, as evident from Figure 46. As a consequence the normalized profiles m_o^N and soot volume fraction f_v^N are relatively independent of the scalar dissipation rate.

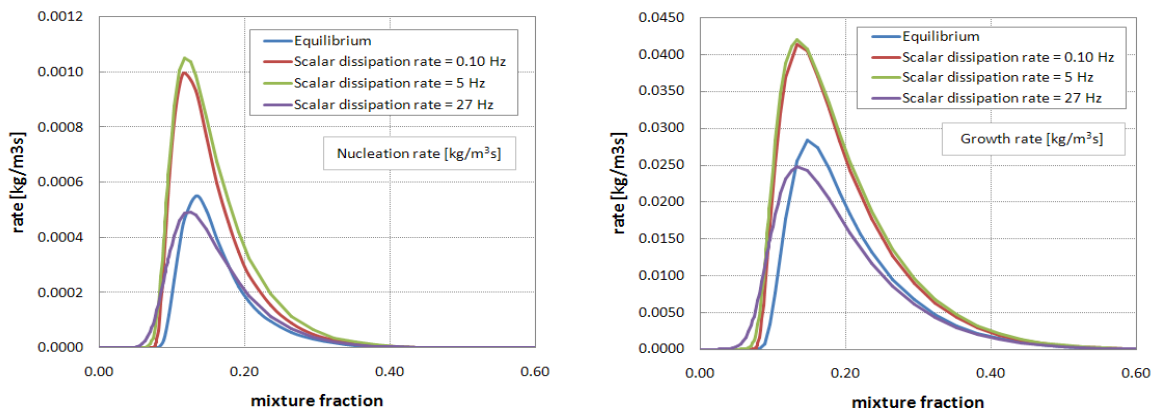


Figure 42. Flame A: profiles of source terms in the soot properties transport equations at adiabatic conditions for different values of scalar dissipation rate: nucleation rate (a); growth rate (b); oxidation rate (c).

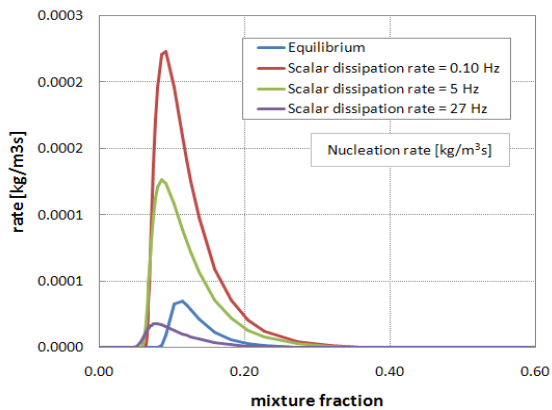
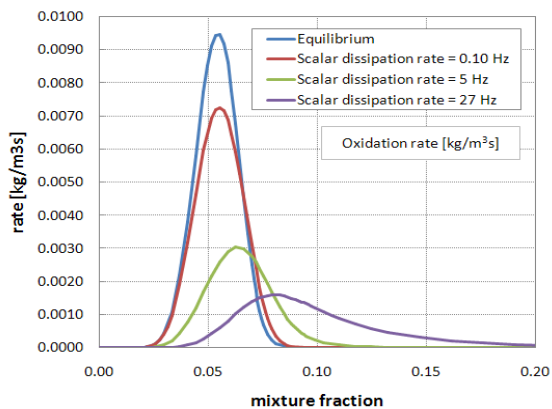
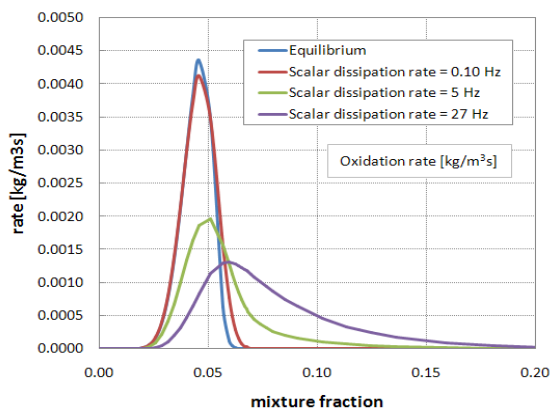


Figure 43. Flame B: profiles of source terms in the soot properties transport equations at adiabatic conditions for different values of scalar dissipation rate: nucleation rate (a); growth rate (b); oxidation rate (c).



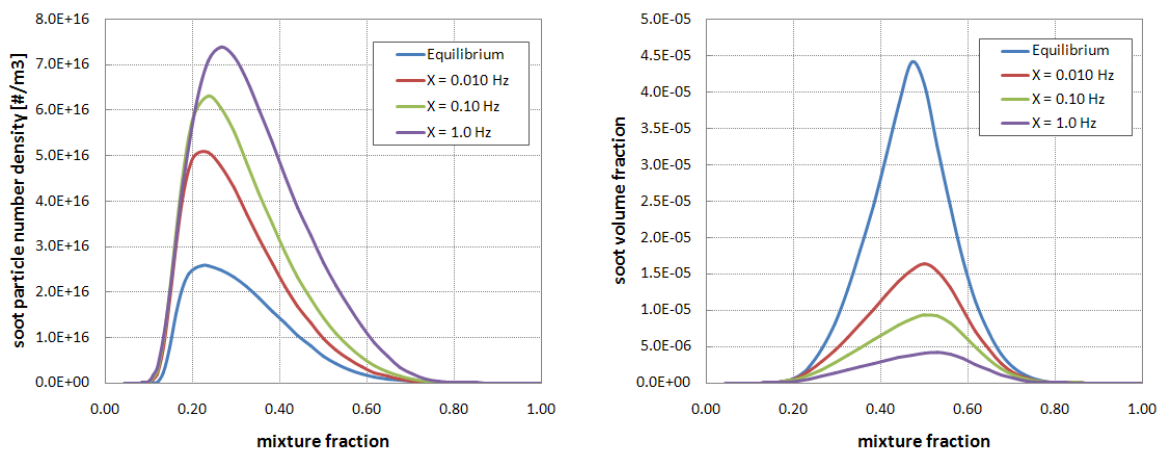


Figure 44. Flame A: soot particle number density (a) and soot volume fraction (b) profiles versus the mixture fraction as predicted by the flamelet calculations at different scalar dissipation rates.

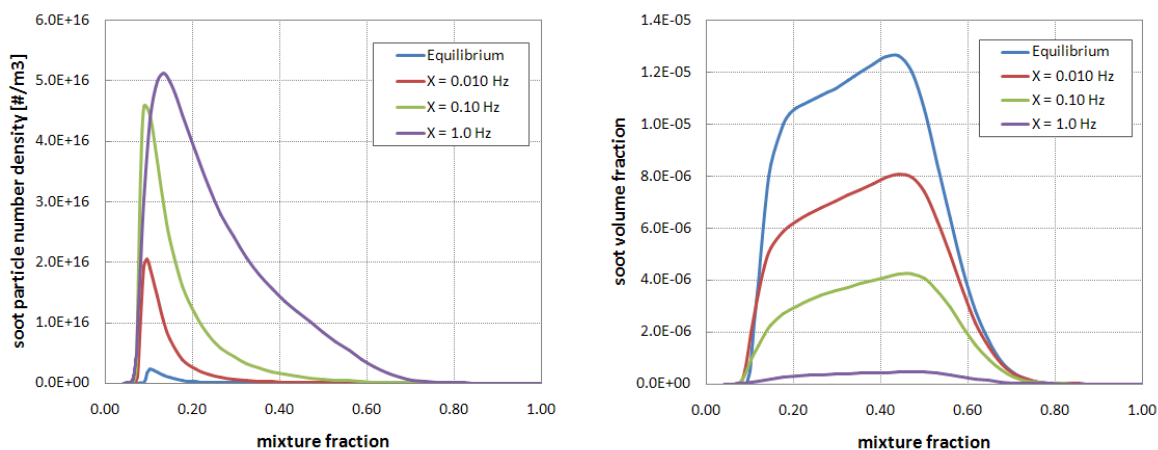


Figure 45. Flame B: soot particle number density (a) and soot volume fraction (b) profiles versus the mixture fraction as predicted by the flamelet calculations at different scalar dissipation rates.

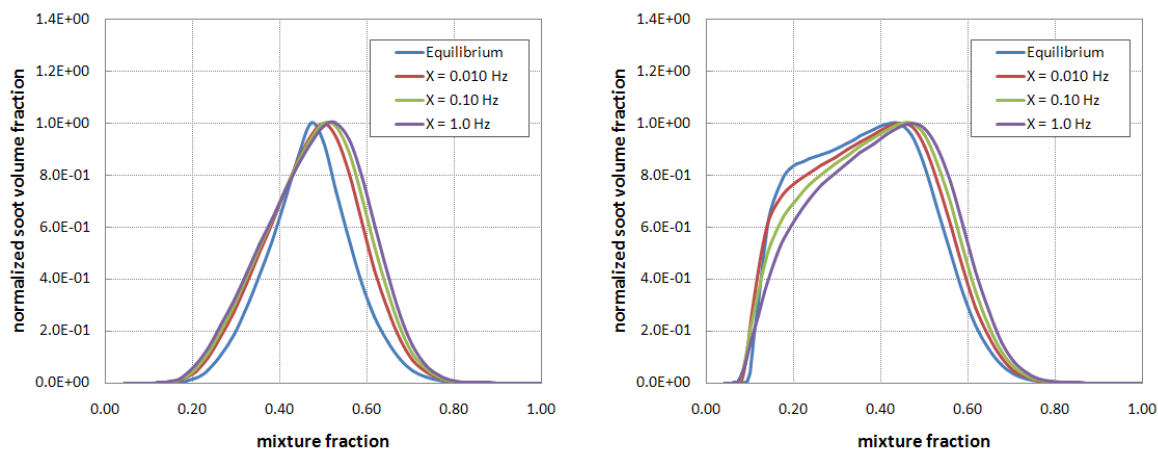


Figure 46. Normalized soot volume fraction profiles versus the mixture fraction as predicted by the flamelet calculations at different scalar dissipation rates: (a) Flame A; (b) Flame B.

4.11 CFD simulation of experimental flames

The flow field solutions are obtained by using the FLUENT 6.3 commercial code [45]. A 2D steady-state RANS simulation of the physical domain was considered due to the axial symmetry of the system. For the Flame A, a structured 60x180 numerical grid was used on a rectangular 75x1000 mm domain, while for the Flame B a structured 80x230 numerical grid was used on a rectangular 77.5x1000 mm domain.

The Favre averaged Navier-Stokes equations together with the κ - ϵ realizable model are employed to calculate the reactive flow. The buoyancy effect has been taken into account in the turbulence model. For the spatial resolution the Second-Order Upwind Scheme was adopted. The segregated implicit solver was used with the SIMPLE procedure for the pressure-velocity coupling. For the pressure interpolation the PRESTO! (PREssure Stagging Options) algorithm was used. The interaction between chemistry and turbulence has been taken into account through the steady laminar flamelet approach [100, 101].

4.12 Combustion regimes

The application of the steady laminar flamelet model is possible only for some particular combustion regimes. The flamelet regime requires the chemical time t_C to be smaller than the smallest turbulence time scale t_K . In this case the flamelet structures are not affected by turbulence. Following the approach proposed by Lentini [80], it is possible to identify a characteristic chemical time, which accounts for the energetically significant reactions:

$$t_C = \frac{Z_{st}^2 (1 - Z_{st})^2}{\chi_{ext}} \quad (4.60)$$

and the following reference length and velocity scales:

$$\hat{l} = (\nu t_C)^{1/2} \quad (4.61)$$

$$\hat{v} = (\nu / t_C)^{1/2} \quad (4.62)$$

In the expressions reported above, χ_{ext} is the extinction scalar dissipation rate (which is assumed to be ~170 Hz for the Flame A and ~27 Hz for the Flame B) and ν is the molecular kinematic viscosity.

Three different turbulent combustion regimes can be easily identified on the plane $\log(\sqrt{\kappa}/\hat{v})$ vs $\log(l_t/\hat{l})$, where l_t is the integral length scale (here assumed equal to $\kappa^{3/2}/\varepsilon$):

- the *flamelet regime*, where turbulence do not affect the flamelet structures;
- the *perturbed flamelet regime*, where the flamelets interact with turbulence;
- the *thickened flame regime* where the chemical time is larger than the largest turbulence time scale and therefore the flamelet structure is completely destroyed by the turbulence.

Figure 47 shows the combustion regimes for the two flames using continuous lines. The curves refer to the axial locations along the flames and the non-dimensional abscissa x/D is used as a coordinate along them. As expected, for both the flames it is evident that the combustion regime is laminar very close to the fuel inlet; however the flamelet regime is reached very soon, at about $x/D = 2$. The same Figure also shows the curves representing the typical slow regime of soot formation. The chemical time for soot formation is estimated according to the following expression:

$$t_{C,soot}(x) = \frac{f_V(x,r) \cdot \rho_{soot}}{S_M(x,r)} \Big|_{r=0} \quad (4.63)$$

This result confirms that soot formation occurs at timescales which are longer compared to the timescales of local mixing of fuel and oxidizer, therefore it cannot be treated as a species which is connected to thin laminar flamelet structures. This precludes the possibility to directly use steady laminar flamelets (which require widely separated timescales and rapidly adjust to local flow conditions) to model soot formation and oxidation.

A different criterion for the validity of the laminar flamelet concept was proposed by Bilger [14] and Peters [101]. Of course also in this approach the flamelet concept requires that the reaction zone be embedded within the smallest scale of turbulence, the Kolmogorov scale l_K , but this condition is expressed by the following criterion:

$$8\varepsilon_q^4 \cdot Ka < 1 \quad (4.64)$$

where ε_q (which is defined as the ratio between the oxidation layer thickness and the diffusion layer thickness in the mixture fraction at extinction) has been estimated to be 0.16 for methane-air flames [119] and Ka is the Karlovitz number, which represents the ratio between the chemical time scale t_C and the Kolmogorov time scale t_K . Therefore, according to this criterion, for a methane-air flame

the flamelet concept can be applied if $Ka < 190$. In Figure 48 the Karlovitz number for the two flames is reported: it is observed that the value for the methane flame is everywhere smaller than 190. Also the more stringent criterion $Ka < 100$, derived from the analysis of premixed flames, is satisfied.

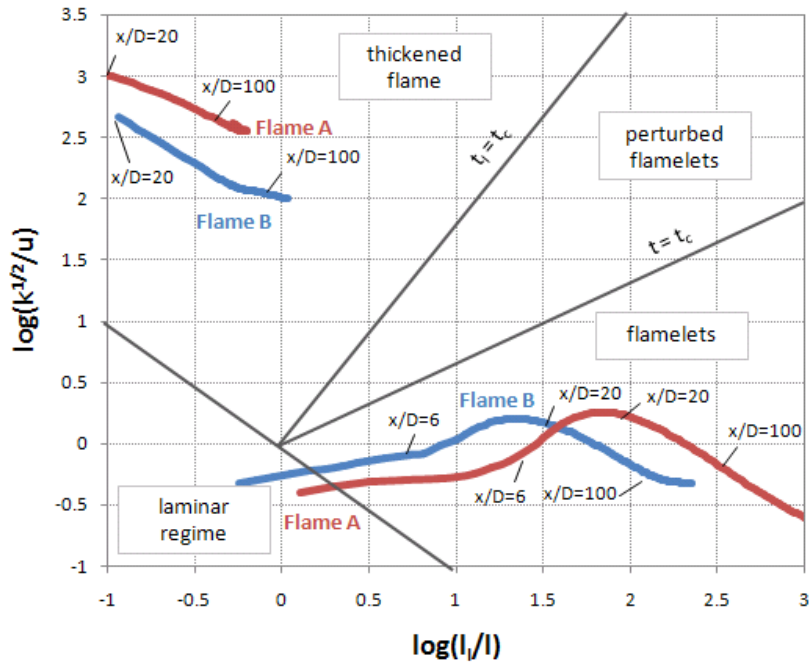


Figure 47. Regimes of turbulent combustion for Flame A [72] and B [21]. Continuous lines represent fast reactions (combustion), dashed lines soot formation (nucleation).

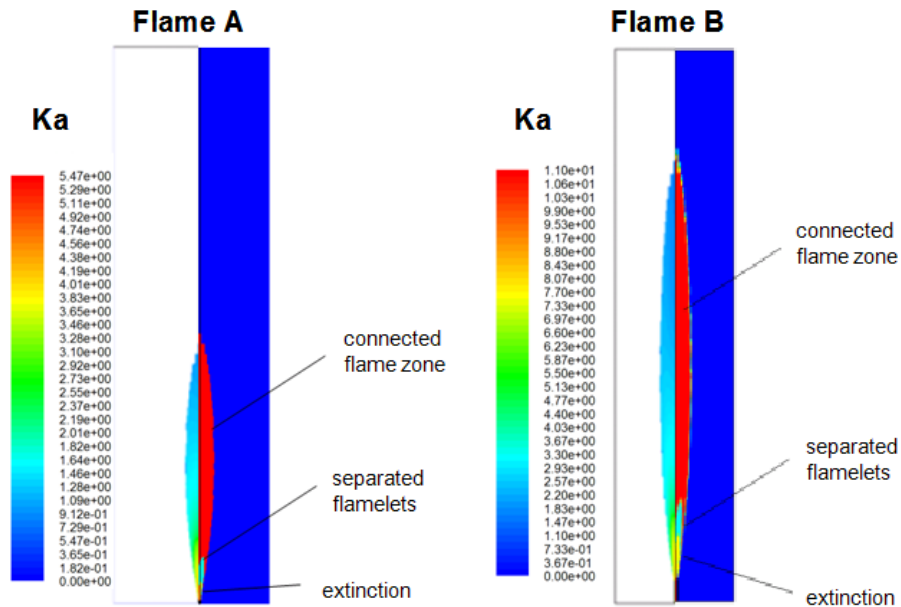


Figure 48. Karlovitz number (left side) and combustion regimes (right side) for turbulent diffusion Flame A [72] and B [21].

4.13 CFD results

4.13.1 Flame A

The temperature and enthalpy defect maps calculated using the uncorrelated approach are reported in Figure 49. The peak temperature is ~1820K, which is in excellent agreement with the experimental measurements. The radiative heat transfer is very important in this flame, mainly due to the large amount of soot. In particular the enthalpy defect has a peak value of ~550 kJ/kg at the axial location of ~400 mm. Since acetylene it's the main soot precursor in the simplified kinetic schemes here adopted for soot predictions, its map is reported in the same Figure.

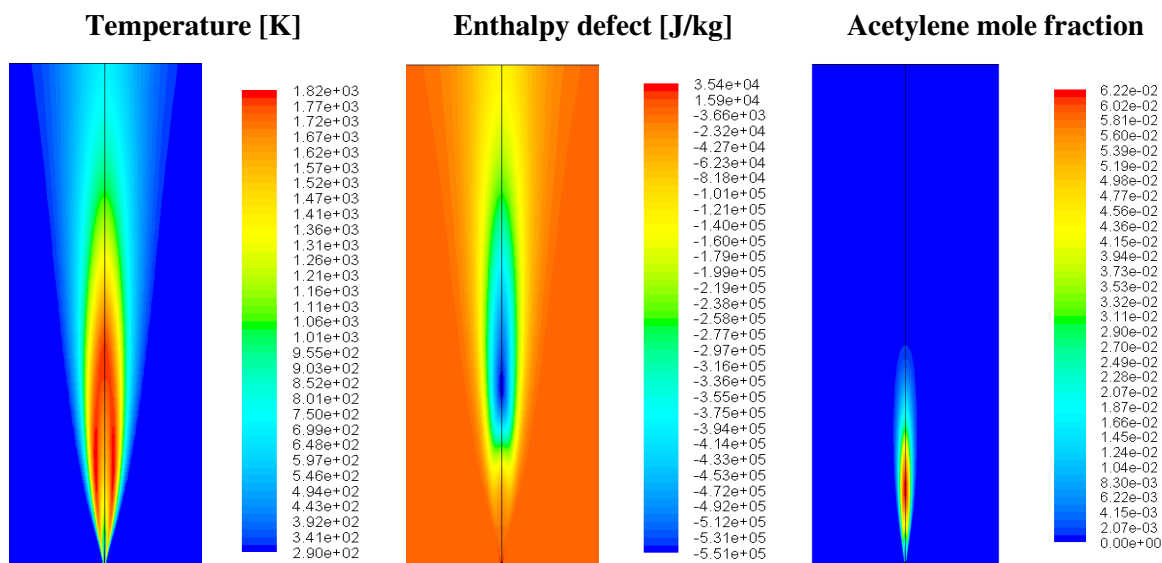


Figure 49. Flame A: temperature, enthalpy defect and acetylene mole fraction contours calculated using the totally uncorrelated closure model.

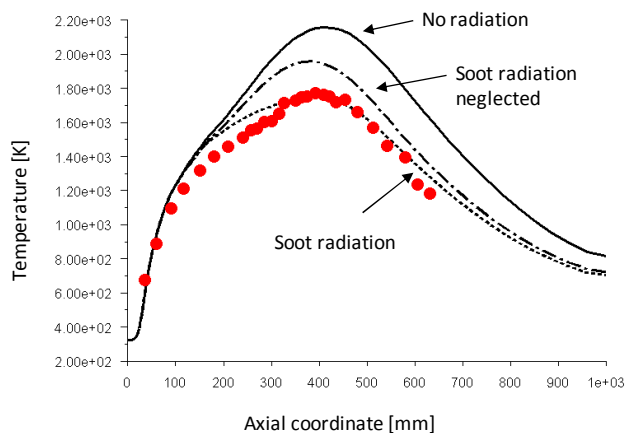


Figure 50. Flame A: comparison between experimental measurements of temperature field and numerical results obtained using the totally uncorrelated closure model.

Figure 50 compares the predicted axial temperature profiles with the experimental measurements. These results refer to the simulation obtained using the totally uncorrelated approach for soot predictions. The predictions of temperature and soot fields obtained using the mean properties and the totally correlated approach are show a similar trend and do not need a discussion. Figure 50 allows to evaluate the effects of both soot and gas radiation: in particular the peak temperature is modified by soot radiation by approximately $\sim 150\text{-}200\text{K}$. Soot radiation acts mainly on the rich side of the flame because soot only exists in the fuel-rich regions; on the lean side, gas radiation is particularly strong in the tail of the flame, where water and carbon dioxide concentrations are higher. The agreement with the experimental measurements can be considered satisfactory, both along the centerline and in the radial directions. Also the peak temperature which appears around $x = 210\text{ mm}$ at an off-axis radial position is well predicted. Only in the range $x = 250 \div 380\text{ mm}$ the temperature is slightly overpredicted and this can lead to an overprediction of soot volume fraction. The same kind of result was also observed by Pitsch *et al.* [106]. No experimental data are available for the mixture fraction; however the stoichiometric value of 0.064 is reached along the centerline in the current calculations at $x = 151D$ (where D is the fuel inlet diameter), which is in quite good agreement with the simulations by Kent and Honnery [72], where $x = 153D$, and with the numerical results by Pitsch *et al.* [106], where $x = 147D$.

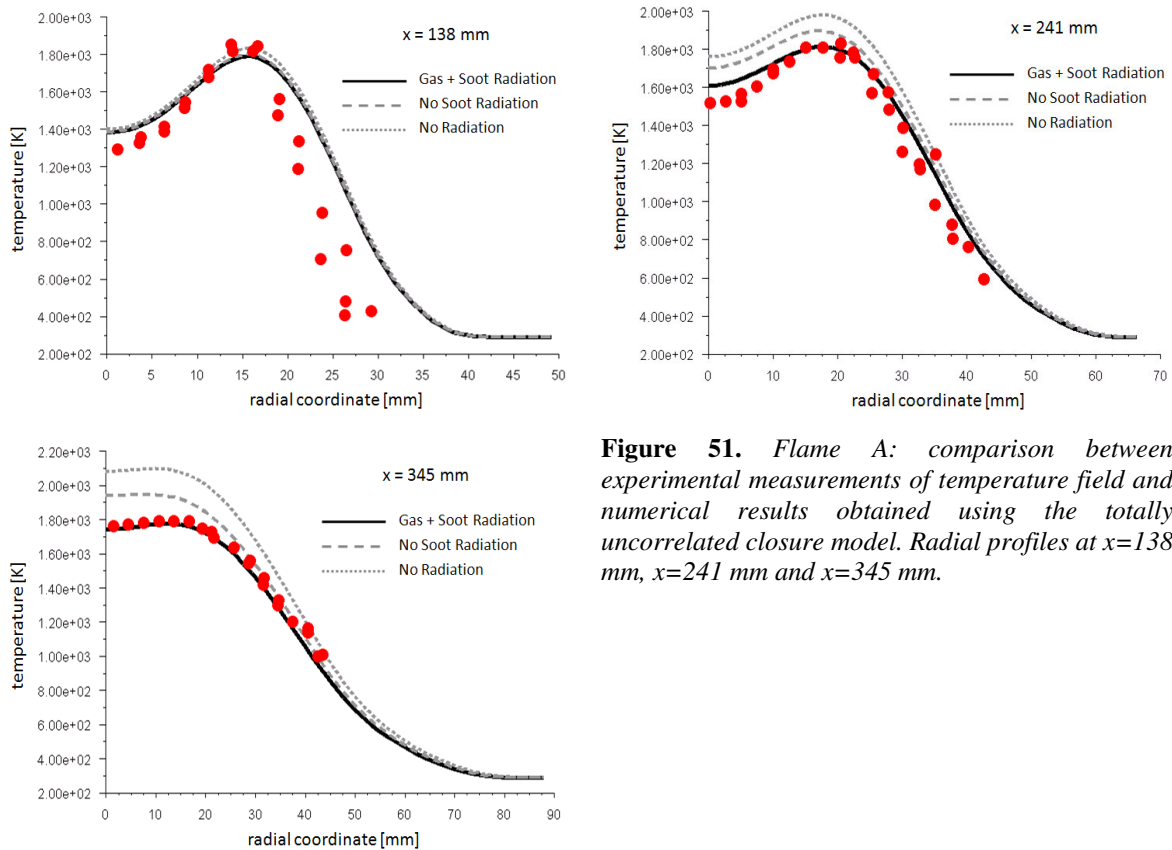


Figure 51. Flame A: comparison between experimental measurements of temperature field and numerical results obtained using the totally uncorrelated closure model. Radial profiles at $x=138\text{ mm}$, $x=241\text{ mm}$ and $x=345\text{ mm}$.

In Figure 51 the temperature profiles are reported along the radial direction at several axial locations and are compared with the experimental measurements. Of course these results mirror the predictions reported in Figure 50. If both gas and soot radiation is taken into account, the agreement with experimental data is very satisfactory.

4.13.2 Flame B

The calculated flame height and flame width are sensitive to the inlet conditions, in particular to the turbulence intensity, which is not available in the experimental data. Following the suggestion proposed by Roditcheva and Bai [116] the inlet turbulence intensity was calculated using $u'/u=0.08$, where u' and u are the rms and mean axial velocity component respectively.

In Figure 52 the temperature, enthalpy defect and acetylene mole fraction maps are reported, as predicted by the uncorrelated approach. Similar results were obtained using the mean properties and the correlated approaches. The radiative losses are not so large as in the previous flame (the peak value is ~ 370 kJ/kg), mainly due to the small amount of soot, but cannot be neglected in the tail of the flame (where the temperature is still high and the concentrations of H_2O and CO_2 are large). The peak value of acetylene concentration is located at ~ 400 mm from the fuel inlet, while the maximum of temperature is found at ~ 500 mm.

Figure 53 compares the predicted axial temperature profiles with the experimental measurements. The importance of radiation for this flame is significant, but less critical than in the case of flame A: in particular without considering the radiation the peak temperature is

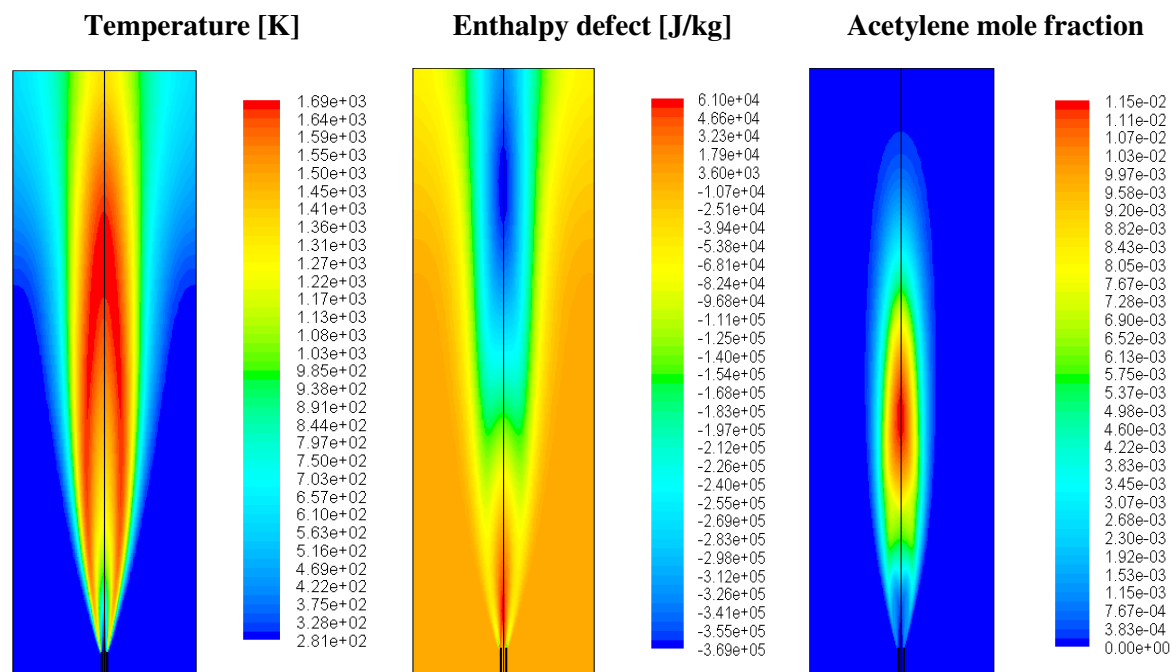


Figure 52. Flame B: temperature, enthalpy defect and acetylene mole fraction contours calculated using the totally uncorrelated closure model.

overpredicted by approximately $\sim 150\text{K}$. The agreement with the experimental measurements can be considered satisfactory, both along the centerline and in the radial directions (see Figure 54), but unfortunately no data are available in the tail of the flame and therefore a complete comparison is not possible. The stoichiometric value of mixture fraction (0.055) is reached along the axial direction at $x/D=135$, in good agreement with the experimental measurements. However, from the comparison between predicted and measured axial and radial profiles of mixture fraction (not reported in this work), the decay rate of the round jet seems to be slightly under-predicted.

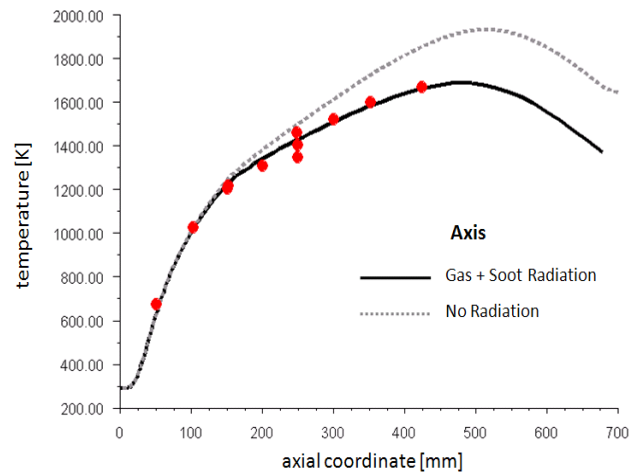


Figure 53. Flame B: comparison between experimental measurements of temperature field and numerical results obtained using the totally uncorrelated closure model.

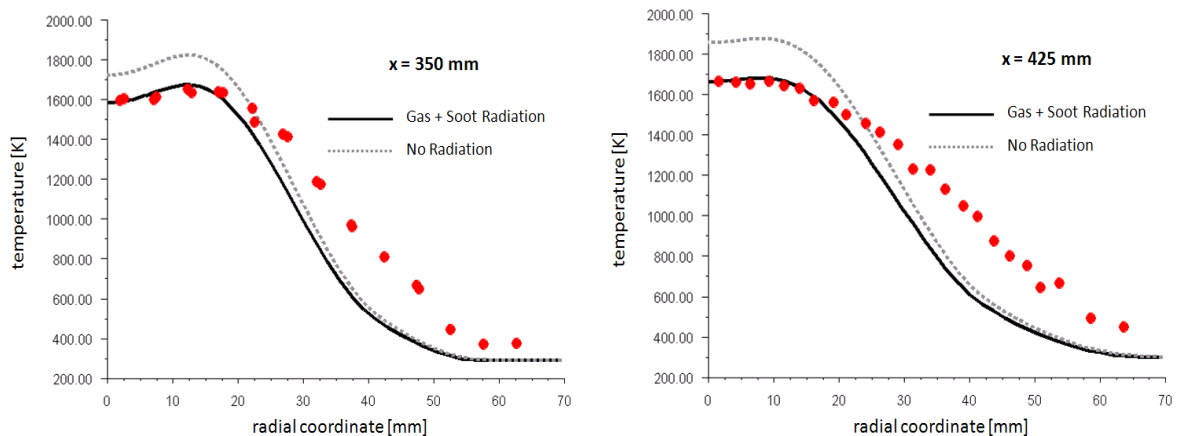


Figure 54. Flame B: comparison between experimental measurements of temperature field and numerical results obtained using the totally uncorrelated closure model. Radial profiles at $x=350\text{ mm}$ and $x=425\text{ mm}$.

4.14 Soot predictions

4.14.1 Flame A

In Figure 55 the predicted soot volume fraction (using the uncorrelated closure) is reported. The peak value and its location are in excellent agreement with the experimental data. The peak value of soot particle number density is located, as expected, in the same location of acetylene concentration peak and is closer to the fuel inlet than the soot volume fraction peak. The soot particle mean diameter is ~ 25 -30 nm in the core of the flame, but tends to increase at larger distances from the fuel nozzle. The oxidation seems to have a minor role in this flame. This is confirmed by the maps reported in Figure 56, which refer to the nucleation, growth and oxidation

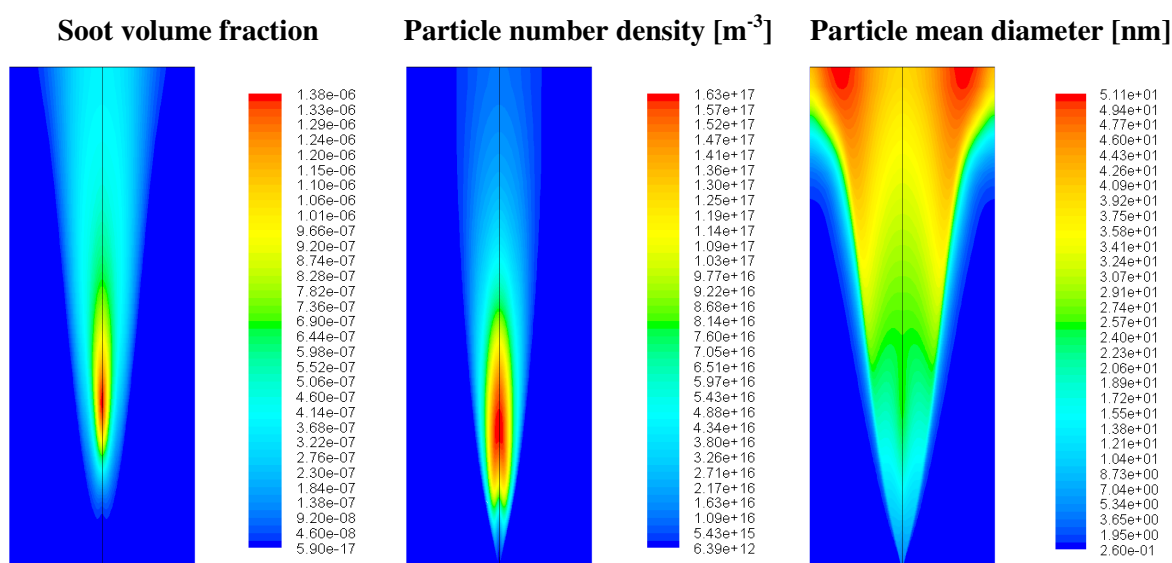


Figure 55. Flame A: soot volume fraction, particle number density and particle mean diameter contours calculated using the totally uncorrelated closure model.

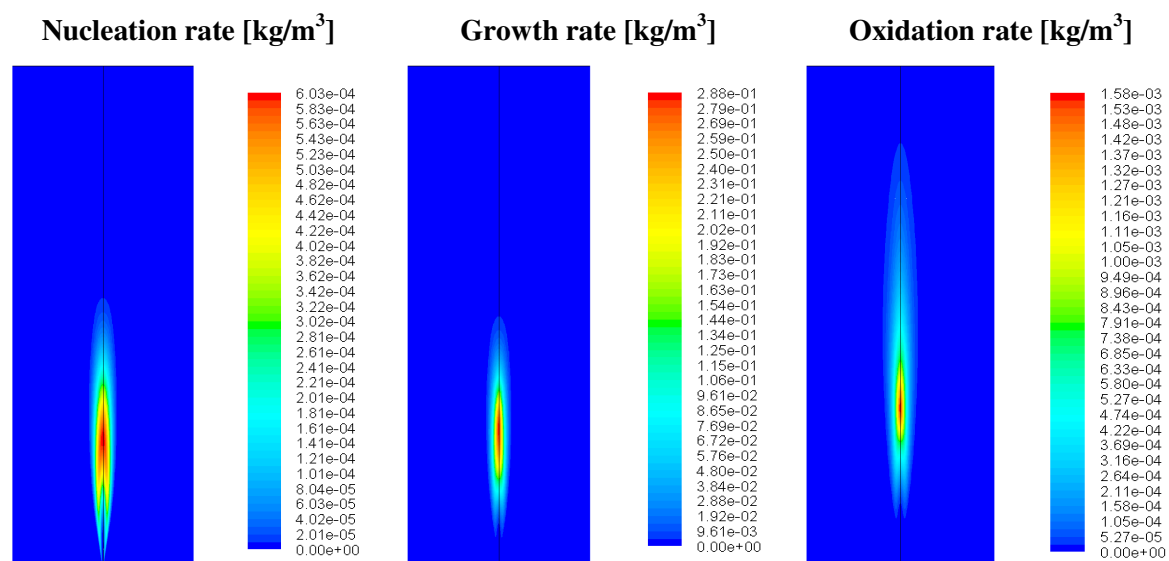


Figure 56. Flame A: nucleation, growth and oxidation rate contours calculated using the totally uncorrelated closure model.

rates. It is evident that the mean value of oxidation rate is about two orders of magnitude lower than the growth rate. Moreover oxidation is not particularly important in the tail of the flame and this explains why the soot particle mean diameter does not have a maximum along the axis.

Figure 57 and Figure 58 show a comparison between the measured soot volume fraction and the model results obtained using the three different approaches for closing the soot production term. When the closure is simply obtained using the mean properties, thus neglecting the effect of turbulent fluctuations, the soot volume fraction is over-predicted and the position of the peak value occurs prior to the experimental data. As a consequence, also the soot radial profiles are overestimated in the initial part of the flame. In particular the calculated maximum value of soot volume fraction along the axis is ~ 2.40 ppm, while the experimental measurement is ~ 1.60 ppm. As expected from the temperature profiles, the soot concentration is especially overestimated in the rich region of the flame. A similar result was also found by Pitsch *et al.* [106], who offered an explanation in terms of a small overprediction in the decay rate of the axial mixture fraction profile. However in the present work this problem in the peak location seems due to the soot source term closure model, which, in the case of the mean properties closure, cannot take into account the turbulent fluctuations. This explanation is confirmed by results obtained using the uncorrelated and correlated closure approaches (reported in the following), which show a better agreement with the experimental measurements in terms of soot peak value location. The overall agreement with the experimental data can be considered reasonable in view of the simplifications related with this approach.

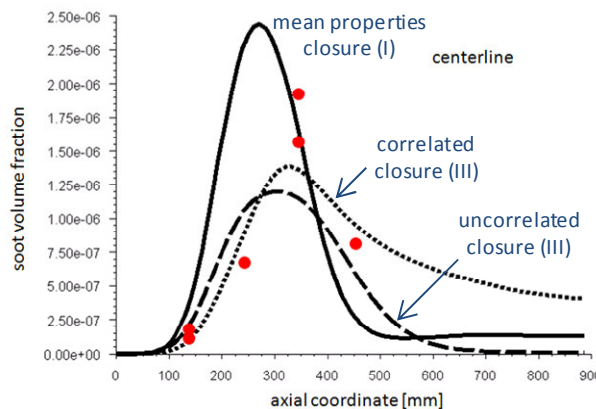


Figure 57. Flame A: comparison between experimental measurements of soot volume fraction and numerical results obtained using different closure models.

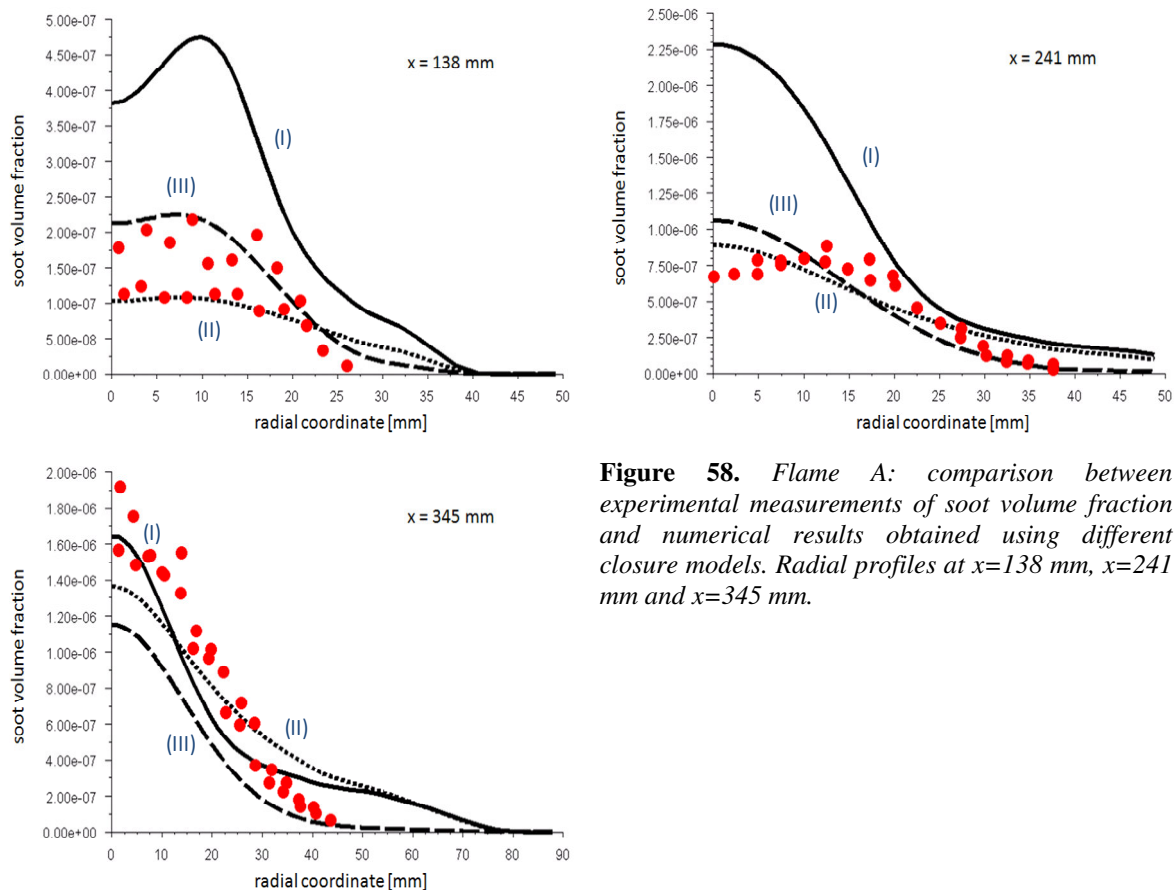


Figure 58. Flame A: comparison between experimental measurements of soot volume fraction and numerical results obtained using different closure models. Radial profiles at $x=138$ mm, $x=241$ mm and $x=345$ mm.

The agreement with the experimental measurements can be improved using the uncorrelated closure. As shown in Figure 57, the shape of the profile in axial direction is well described and the peak location is correctly predicted. The maximum amount of soot is slightly under-predicted, but also along the radial direction the agreement is reasonable.

Finally, the soot volume fraction calculated using the correlated approach is in good agreement with the experimental data, although the maximum value is slightly under-predicted. The radial profiles are also correctly described. Some important differences can be observed by comparing these results with the predictions obtained with the uncorrelated approach, in particular in the tail of the flame. Using the uncorrelated closure the soot volume fraction becomes negligible at ~ 700 mm from the fuel inlet due to the oxidation reactions. Unfortunately no experimental information is available in this zone of the flame and therefore it is not possible to single out the right model.

Figure 59 compares the source terms for nucleation, growth and oxidation of soot particles along the axis of the flame. The nucleation and growth rate are directly related to the acetylene concentration and therefore the shapes of their profiles are very similar. On the contrary the consumption of soot due to the oxidation reactions is particularly strong only in the tail of the flame, where the oxidation rate becomes larger. It is possible to observe some significant

differences between the models, in particular for the oxidation rate. The approach based on mean properties show a small oxidation rate in the first part of the flame with respect to the other models. This behavior clearly explains the shape of the soot volume fraction discussed above. On the contrary the oxidation rate cannot be considered negligible when the uncorrelated approach is used. The main consequence is the reduction of the peak soot volume fraction value, which leads to a better agreement with the experimental data. Moreover the oxidation rate is slightly smaller in the tail of the flame and this explains the slower decrease of soot concentration in this zone. The correlated approach predicts an oxidation rate which is smaller everywhere if compared to the results obtained from the mean properties and uncorrelated closure models. As a consequence a non negligible amount of soot can be also observed in the tail of the flame. The nucleation and growth rates are very similar for the uncorrelated and correlated closure models. Some differences with respect to the mean properties closure model can be observed in the tail of the flame.

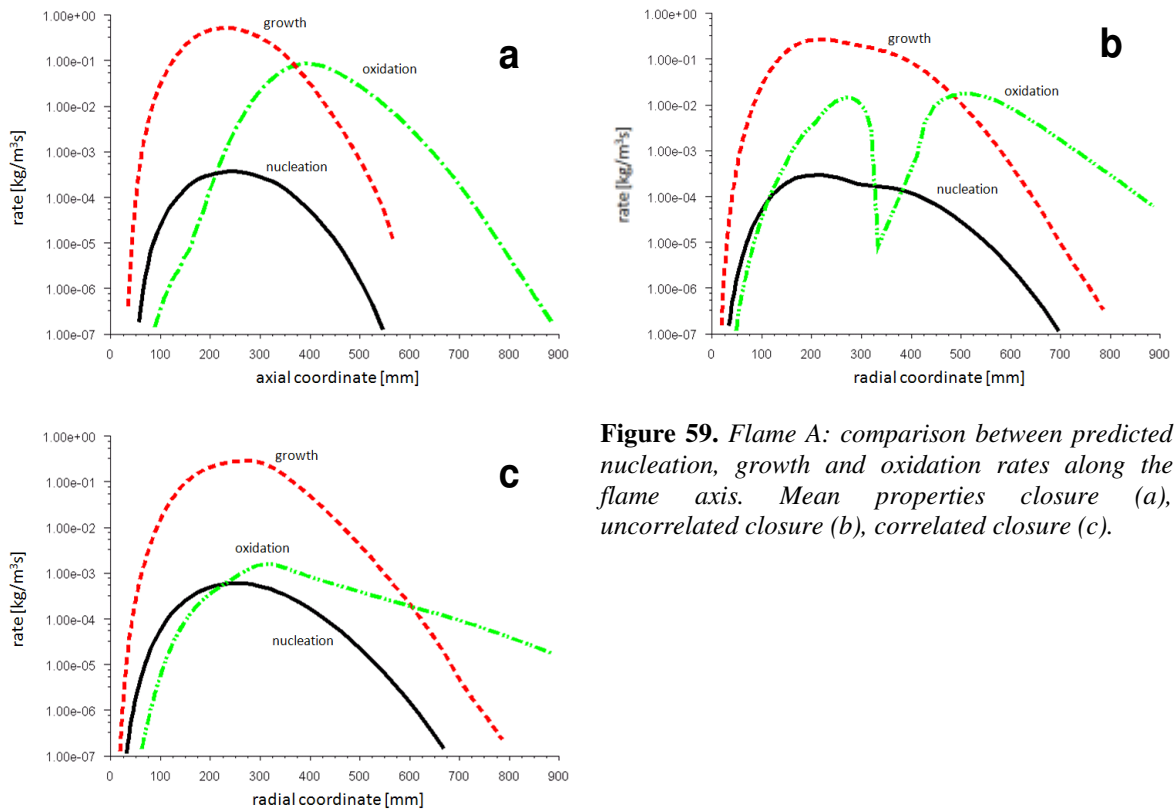


Figure 59. Flame A: comparison between predicted nucleation, growth and oxidation rates along the flame axis. Mean properties closure (a), uncorrelated closure (b), correlated closure (c).

4.14.2 Flame B

In Figure 60 the predicted soot volume fraction profile is reported. The total amount is about one order of magnitude lower than for Flame A and the peak value is located at a larger distance from the fuel nozzle. The soot particle mean diameter shows a maximum value of ~ 20 nm

in the same location of peak temperature. This behavior, which was not observed in the previous flame, can be explained in terms of soot oxidation, which is important for this flame, leading to the reduction of soot particle diameter. This observation is confirmed by the maps of soot nucleation, growth and oxidation, reported in Figure 61. The soot oxidation rate in the tail of the flame is only one order of magnitude lower than the growth rate, while in Flame A the difference was two orders of magnitude of magnitude.

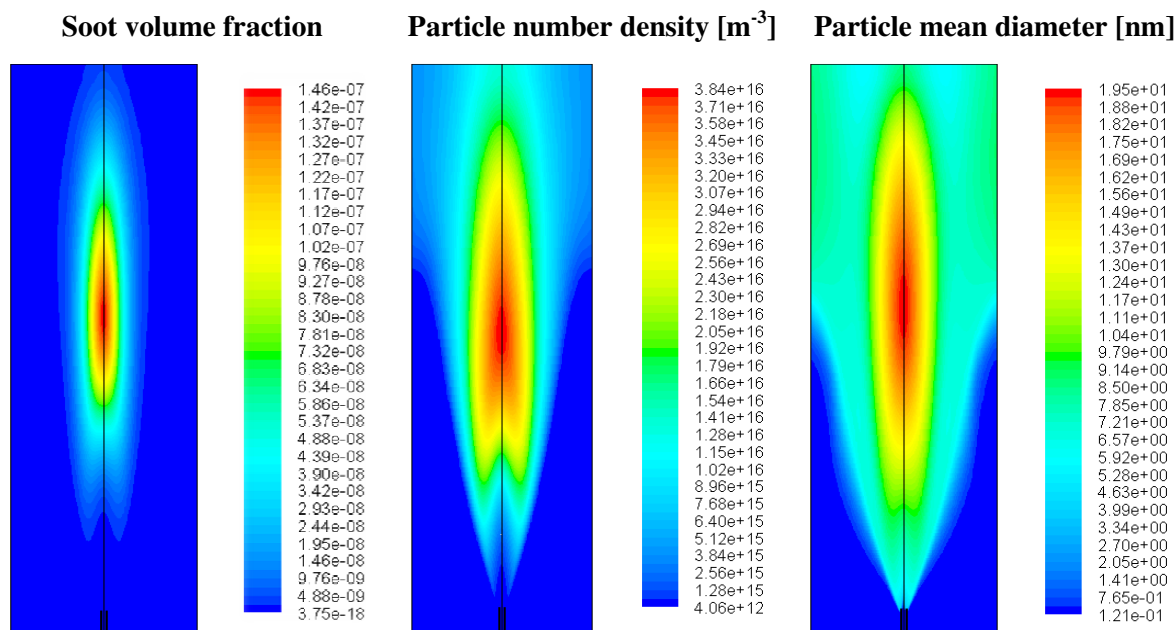


Figure 60. Flame B: soot volume fraction, particle number density and particle mean diameter contours calculated using the totally uncorrelated closure model.

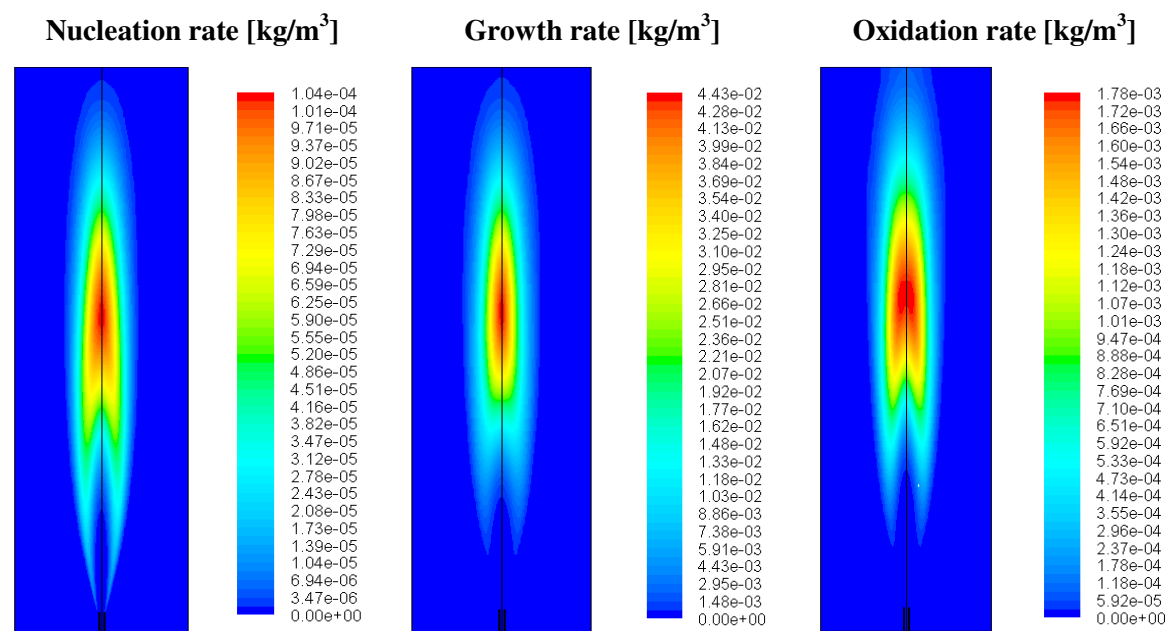


Figure 61. Flame B: nucleation, growth and oxidation rate contours calculated using the totally uncorrelated closure model.

Figure 62 and Figure 63 show the comparison between measured and predicted soot volume fraction. Also in this flame the soot volume fraction is largely over-predicted using the closure simply based on mean properties. The axial position of the soot peak is anticipated by ~ 50 mm. Along the radial direction, not only are the mean values of the predicted results and experimental data different, but also the shape. The experimental profiles show a slow decrease of soot volume from the axis location.

Using the uncorrelated approach the agreement is more accurate along the axis, in particular when compared with the previous results. The peak value better agrees with the experimental location. The agreement for the radial profiles is less accurate: also in this case the shape of these profiles is different from the experimental one. However similar results were also obtained by several authors [21, 116].

The results obtained using the correlated closure are in poor agreement with experimental measurements: the peak value is over-estimated by a factor ~ 2.50 , as for the mean properties closure. However, the peak location is now correctly predicted and the shape of radial profiles seems to be in a better agreement with the experimental data. A possible explanation is related to the oxidation rate, which, in the case of a correlated closure, becomes very small, both along the centerline (as shown in Figure 64) and in radial direction. As a consequence the soot volume fraction is overestimated along the axis, but at the same time the soot consumption is reduced in the radial direction and this explains the better agreement between the predicted and measured shapes.

The uncorrelated closure seems therefore able to give a more reliable prediction of soot formation in this flame. Unfortunately it is important to stress that the reliability of this kind of predictions strongly depends on the sub-models used for describing nucleation, growth, coagulation and oxidation of soot particles. A different set of such sub-models could result in different results and bad predictions.

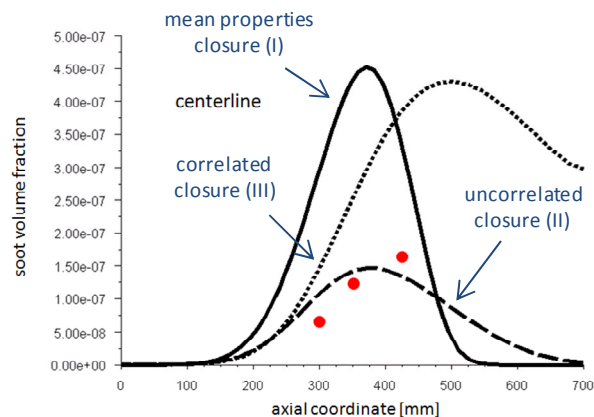


Figure 62. Flame B: comparison between experimental measurements of soot volume fraction and numerical results obtained using different closure models.

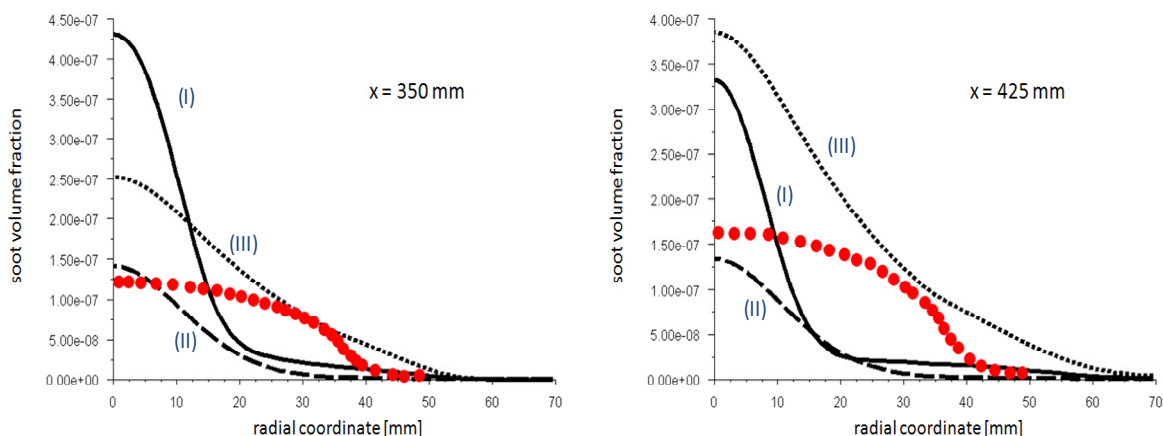


Figure 63. Flame B: comparison between experimental measurements of soot volume fraction and numerical results obtained using different closure models. (I) mean properties closure (continuous line); (II) uncorrelated closure (dashed line); (III) correlated closure (dotted line).

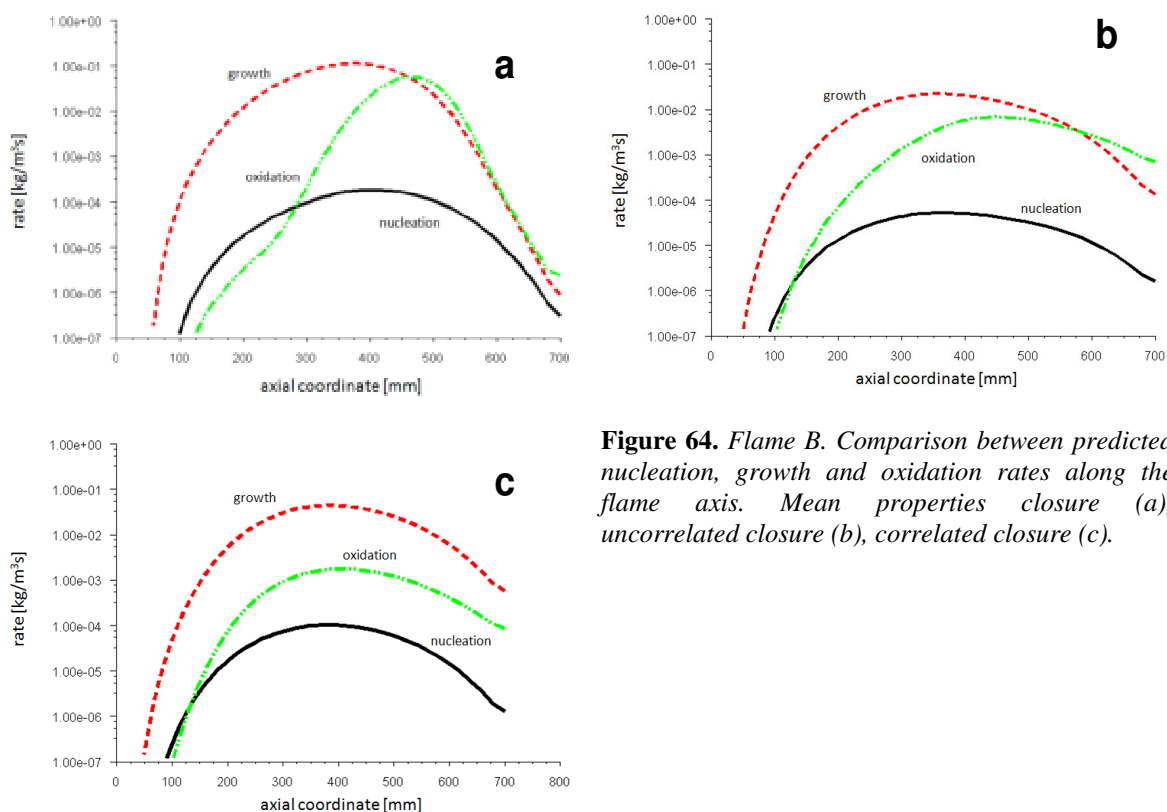


Figure 64. Flame B. Comparison between predicted nucleation, growth and oxidation rates along the flame axis. Mean properties closure (a), uncorrelated closure (b), correlated closure (c).

4.15 Sensitivity analysis to the nucleation rate

The purpose of Figure 65 is to compare several nucleation models, using obviously the same surface growth, coagulation and oxidation models, to investigate the sensitivity of soot properties to nucleation for Flame B. The uncorrelated approach, which showed the best

agreement with the experimental data, was used to close the source terms in the soot transport equations. All nucleation models are based on the acetylene-route:



For most models the corresponding expression for the reaction rate is:

$$S_{m0} = A_{nucl} \cdot e^{-T_{nucl}/T} \cdot C_{C_2H_2} \quad (4.66)$$

Four different values for the rates of nucleation are taken into account in the present work; they are summarized in the Table 5.

	Liu (2003)	Liu (2006)	Brookes (1999)	Wen (2003)
$A_{nucl} [s^{-1}]$	0.004857	2.857	54	54
$T_{nucl} [K]$	7548	16103	21100	21100
$M_p [kg / kmol]$	8400	8400	144	1200
$d_p [nm]$	2.40	2.40	0.65	1.20
<i>References</i>	[82]	[84]	[21]	[136]

Table 5. Constants in the soot models

	Moss (1995)	Syed (1990)
$A_{nucl} \left[\frac{kmol \cdot m^3}{kg^2 s \sqrt{K}} \right]$	$6 \cdot 10^6$	$6.54 \cdot 10^4$
$T_{nucl} [K]$	46100	46100
$M_p [kg / kmol]$	144	144
$d_p [nm]$	0.65	0.65
<i>Reference</i>	[96]	[129]

Table 6. Constants in the soot models

However a slightly different model can also be used [96, 129]:

$$S_{m0} = A_{nucl} \cdot e^{-T_{nucl}/T} \cdot \rho^2 \sqrt{T} \cdot \frac{C_{C2H2}}{C_{TOT}} \quad (4.67)$$

where C_{TOT} is the total concentration. Two different nucleation rates have been compared and they are summarized in the Table 6.

In Figure 65a the nucleation rate of soot particles along the axis is reported for the different nucleation models. The peak values predicted by the six models here adopted can be found in the same locations, as a consequence of the linear dependence on the acetylene concentration. However the predicted values show very large differences: for example, the nucleation rate proposed by Liu *et al.* [84] is about three order of magnitude larger than the corresponding value predicted according to the model proposed by Syed *et al.* [129], along the whole axial direction. This result is expected as a consequence of the large differences in the constants (frequency factor and activation temperature) in the semi-empirical models adopted for modeling the nucleation rate. However, despite the very different nucleation rates, soot volume fraction is largely unaffected, as reported in Figure 65b. Very similar results (not shown) can be observed using the mean properties closure approach. A similar results has been also observed by Ma *et al.* [85] for a turbulent non-premixed ethylene/air flame. The sensitivity of soot formation in this flame to the nucleation models was

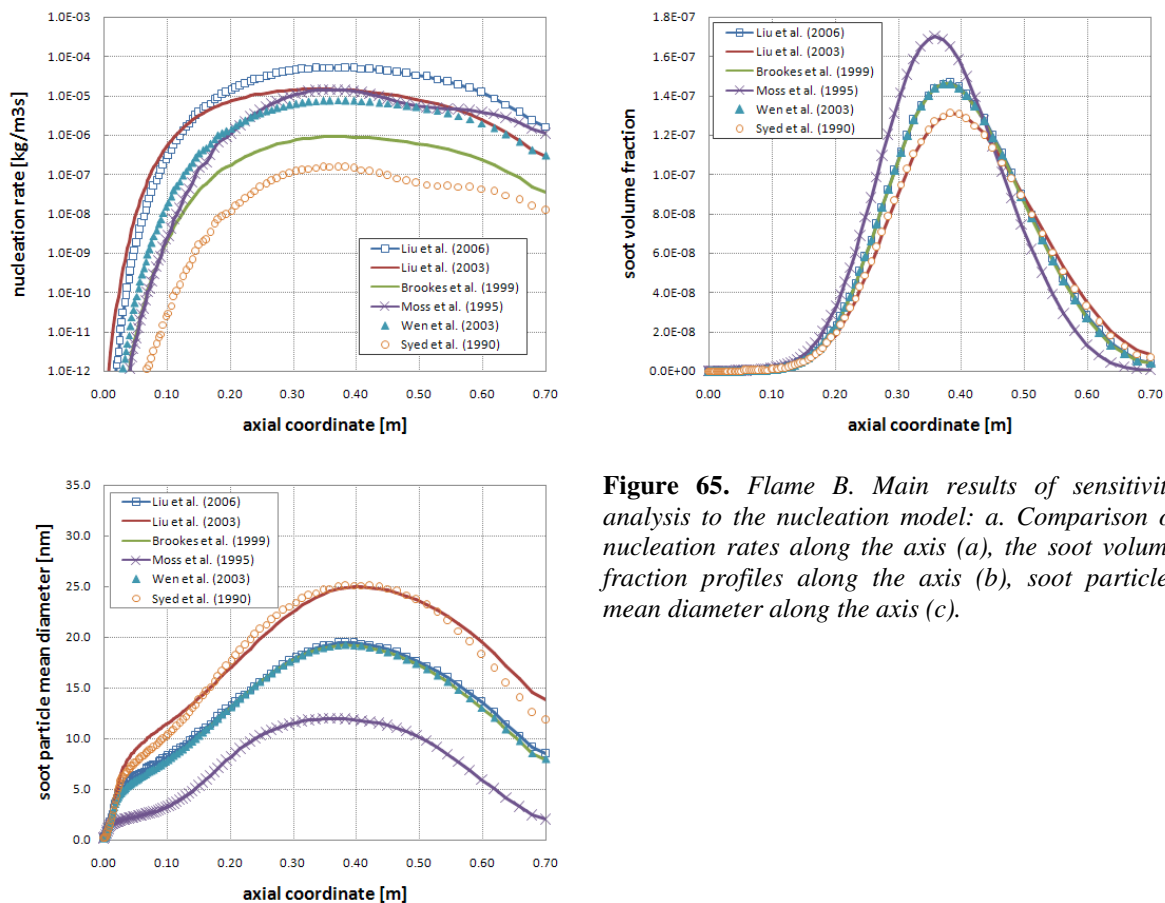


Figure 65. Flame B. Main results of sensitivity analysis to the nucleation model: a. Comparison of nucleation rates along the axis (a), the soot volume fraction profiles along the axis (b), soot particles mean diameter along the axis (c).

found to be negligible if the surface growth rate of soot particles was assumed proportional to the square root of the surface area (as assumed by the model [84] which is used in the present work). On the contrary, if the surface growth rate was assumed to be proportional to the soot surface area or proportional to the soot particle number density the results were completely different and the soot volume fraction in the flame was strongly affected by the nucleation model adopted. A possible explanation of these interesting results is the weaker dependence of the nucleation rate on the soot surface area when the surface growth rate is assumed to be proportional to the square root of the soot surface area. Some differences can be observed in the soot particle mean diameter (Figure 65c): this result is expected, due to the differences in the soot primary particles diameters, which range from 0.62 to 2.4 nm, depending on the nucleation model.

4.16 Conclusions

The principal objective of the analysis presented in this Chapter is to demonstrate the application of a two-equation model for soot predictions in a turbulent non-premixed flame coupled with a steady laminar flamelet model for the description of thermal and gaseous species fields. A simple semi-empirical scheme for the description of soot nucleation, growth, oxidation and coagulation was adopted using three different closure methods for the source terms in the transport equations of soot. Neglecting the effects of turbulent fluctuations of both temperature and composition on the soot source terms results in an overprediction of the soot volume fraction. The perfectly correlated approach gives good results for the ethylene Flame A, which is characterized by a large amount of soot, but it is unsatisfactory for the methane Flame B. The best agreement with experimental data for both flames can be achieved using the totally uncorrelated approach. This activity confirmed that the coupling between the soot production rate and the radiative heat loss must be carefully taken into account to accurately model the formation of soot.

The predicted soot amount in the turbulent flame was found to be relatively insensitive to the semi-empirical model adopted for describing the nucleation process. A deeper sensitivity analysis to the growth, oxidation and coagulation models could be very useful in a future work to investigate the role of individual soot formation rates to determine the optimal parameters for a two-equation soot model that can be used in the simulation of turbulent non-premixed flames.

5 Soot modeling in turbulent non premixed flames - DQMOM

The methodology proposed in the previous Chapter for predicting the formation of soot in turbulent non premixed flames is here extended to non monodispersed soot particle size distributions through the Direct Quadrature Method of Moments. The formation of soot is numerically modeled using semi-empirical kinetic models and the attention is focused on the accurate closure of source terms in the transport equations of soot.

5.1 Introduction

Modeling soot formation in practical combustion systems still remains a non trivial problem, mainly due to the strong interactions between the complex chemistry and the turbulence and the difficulties related to the formulation of reliable and accurate models for describing the inception, growth, coagulation and oxidation of soot particles. A complete decoupling of soot from the gas-phase computations, which can be successfully applied for the prediction of nitrogen oxides [32], cannot be adopted due to the strong effect of soot on thermal radiation. If the thermal field and most chemical species can be successfully modeled using non-equilibrium chemistry through flamelet libraries and presumed probability distribution functions (PDF), the same approach is not able to give good predictions for soot emissions, due to its comparatively slow chemistry and because the soot volume fraction cannot be simply related to the mixture fraction. As clearly demonstrated by Kent and Honnery [72], if a single relationship between the soot volume fraction and the mixture fraction is assumed, the results could be very poor. In order to partially overcome these difficulties, individual balance equations must be introduced and solved for the soot particles: in this way it is possible, through the source terms in these equations (which are strongly dependent on the temperature), to account for the interactions between turbulence and chemistry with a higher level of detail.

In this Chapter the soot volume fraction in turbulent non premixed flames is numerically predicted using the Direct Quadrature Method of Moments for solving the conservation equations of moments related to the soot particle distribution. The same turbulent non-premixed flames fed with ethylene (experimentally investigated by Kent and Honnery [72]) and methane (experimentally investigated by Brookes and Moss [21]) already presented in the previous Chapter are investigated. The major species and the temperature field are calculated using the flamelet approach; for this purpose a non-adiabatic flamelet library, depending on the mixture fraction, strain rate and enthalpy defect is built and stored. Additional transport equations describing the soot particle size distribution are solved in the CFD code. The associated source terms are calculated using a semi-empirical model, able to take into account nucleation, surface growth, coagulation and oxidation phenomena. The effect of soot radiation is taken into account using a simplified approach, adding an additional source term related to the soot volume fraction in the energy balance equation.

Two different approaches for the closure of source terms in the transport equations for soot particle size distribution have been used and compared. For turbulent flames the effects of turbulent fluctuations should be taken into account in the evaluation of the source terms in the population balance equation and consequently in the transport equations for weights and weighted abscissas. The simplest approach, which has been followed by many authors ([85, 136, 142]), solves the transport equations and neglects the effects of turbulence. In the analysis presented in this Chapter this simplified approach is compared with a more appropriate closure model, which accounts for the effect of turbulent fluctuations on the soot source terms (uncorrelated closure).

Results clearly show that the steady flamelet model approach is able to correctly predict the thermal and mixture fraction fields. On the contrary the closure model to take into account the turbulence effects on the soot source terms plays an important role on the prediction of soot amount in the turbulent flame investigated. In particular the best agreement with the experimental data has been obtained using the so-called *uncorrelated model*, which consists in assuming that the mixture fraction and the enthalpy defect are totally uncorrelated with the soot properties. Moreover the soot predictions seem to be strongly dependent on the growth and oxidation models used for the simulation, but on the contrary the nucleation model has a small effect on the soot mass fraction.

5.2 Modeling of Soot Formation using DQMOM

The formation of soot particle in the turbulent, diffusive flames investigated in the present work can be described by the following Population Balance Equation (PBE), already introduced in Chapter 4:

$$\frac{\partial n(L, \bar{x}, t)}{\partial t} + \frac{\partial}{\partial x_i} [u_i \cdot n(L, \bar{x}, t)] = \frac{\partial}{\partial x_i} \left(\Gamma_i \frac{\partial n(L, \bar{x}, t)}{\partial x_i} \right) + S(L, \bar{x}, t) \quad (5.1)$$

where $n(L, \bar{x}, t)$ is the particle size distribution (PSD), L is the internal coordinate (which is assumed to be the soot particle size) and $S(L, \bar{x}, t)$ is the source term, which accounts for different processes (nucleation, growth, coagulation and oxidation) and is therefore the summation of several contributions:

$$S(L, \bar{x}, t) = S_{nucleation} + S_{growth} + S_{aggregation} + S_{oxidation} \quad (5.2)$$

The solution of this PBE inside a CFD code is not trivial and usually is very time consuming if Monte Carlo methods or Classes methods are employed. Among the many approaches introduced in recent years, the method of moments has received particular attention, due to the limited number of scalars which need to be transported in a CFD code. However the Standard Method of Moments can be applied only for very simple systems, involving for example nucleation and molecular growth with linear growth rate. The main issue is related to the so called closure problem: the source term in Equation (4.8) usually requires moments which are not transported in the CFD code. The Quadrature Method of Moments (QMOM) or the Direct Quadrature Method of Moments (DQMOM), which is used in the present work, are two convenient approaches for the solution of this closure problem.

5.2.1 Quadrature Method of Moments

According to QMOM [94, 95], the particle size distribution $n(L, \bar{x}, t)$ is approximated by a linear combination of Dirac delta functions (quadrature approximation):

$$n(L; \bar{x}; t) \approx \sum_{j=1}^N w_j \cdot \delta[L - L_j(\bar{x}, t)] \quad (5.3)$$

where N is the number of nodes used in the quadrature approximation, w_j and L_j are respectively the weight and the local abscissa of node j ; $\delta[L - L_j(\bar{x}, t)]$ is the Dirac delta function centered in L_j .

The moment of order k of the distribution can be easily obtained from the weights and local abscissas:

$$m_k(x;t) = \int_0^\infty n(L,x,t) \cdot L^k dL \approx \sum_{j=1}^N w_j \cdot L_j^k \quad (5.4)$$

Given the first $2N$ moments of the particle size distribution, it is possible to calculate the values of N weights and N abscissas of the quadrature approximation having the same first $2N$ moments. This can be obtained by forcing the moments of quadrature approximation (given by Equation (5.4)) to yield known values of the moments. The resulting $2N \times 2N$ non linear system is very bad conditioned, but can be conveniently solved through the Product-Difference (PD) algorithm [54].

5.2.2 Direct Quadrature Method of Moments

Another approach, which can be extended to multivariate distributions, consists in directly solving the transport equations of weights and local abscissas, as first proposed by Marchisio and Fox [91]. The latter approach is called Direct Quadrature Method of Moments and is based on the solution of the following transport equations:

$$\rho \frac{\partial w_j}{\partial t} + \rho u_i \frac{\partial w_j}{\partial x_i} = \frac{\partial}{\partial x_i} \left(\Gamma_t \frac{\partial w_j}{\partial x_i} \right) + \dot{S}_j^w \quad (5.5)$$

$$\rho \frac{\partial \zeta_j}{\partial t} + \rho u_i \frac{\partial \zeta_j}{\partial x_i} = \frac{\partial}{\partial x_i} \left(\Gamma_t \frac{\partial \zeta_j}{\partial x_i} \right) + \dot{S}_j^\zeta \quad (5.6)$$

where ζ_j are the weighted abscissas, defined as:

$$\zeta_j = w_j \xi_j \quad (5.7)$$

The source terms \dot{S}_j^w and \dot{S}_j^ζ are obviously related to the source term in the population balance equation; the relation can be obtained solving the following linear system:

$$(1-k) \sum_{j=1}^N L_j^k \cdot \dot{S}_j^w + k \sum_{j=1}^N L_j^{k-1} \cdot \dot{S}_j^\zeta = \bar{S}_k + \bar{C}_k \quad (5.8)$$

where \bar{S}_k is the source term for the k^{th} moment:

$$\bar{S}_k = \int_{-\infty}^{+\infty} L^k \cdot S(L; x; t) dL \quad (5.9)$$

and \bar{C}_k is a correction term, due to the quadrature approximation:

$$\bar{C}_k = \Gamma_i \cdot k(k-1) \cdot \sum_{j=1}^N L_j^{k-1} w_j \frac{\partial L_j}{\partial x_i} \frac{\partial L_j}{\partial x_i} \quad (5.10)$$

For example, if $N=2$ in the monovariate case, the following linear system, with rank equal to 4, allows to calculate the source terms in Equations (5.5) and (5.6):

$$\begin{bmatrix} 1 & 1 & 0 & 0 \\ 0 & 0 & 1 & 1 \\ -L_1^2 & -L_2^2 & 2L_1 & 2L_2 \\ -2L_1^3 & -2L_2^3 & 3L_1^2 & 3L_2^2 \end{bmatrix} \cdot \begin{bmatrix} \dot{S}_1^w \\ \dot{S}_2^w \\ \dot{S}_1^\zeta \\ \dot{S}_2^\zeta \end{bmatrix} = \begin{bmatrix} \bar{S}_0 \\ \bar{S}_1 \\ \bar{S}_2 + \bar{C}_2 \\ \bar{S}_3 + \bar{C}_3 \end{bmatrix} \quad (5.11)$$

If the particles are assumed to be spherical, the soot particle diameter is given by the following expression:

$$d_p = \left(\sum_{j=1}^N w_j L_j^3 \right)^{1/3} \quad (5.12)$$

and the soot mass fraction and soot volume fraction can be expressed as:

$$\omega_{soot} = \frac{\pi \rho_{soot}}{6 \rho} \sum_{j=1}^N w_j L_j^3 \quad (5.13)$$

$$f_V = \frac{\pi}{6} \sum_{j=1}^N w_j L_j^3 \quad (5.14)$$

The linear system (5.8) can be solved only if the source terms \bar{S}_k , which result from the summation of several contributions, are known and expressed in terms of weights and local abscissas; we call these approximate expressions by the symbol $\bar{S}_k^{(N)}$. In the following the definition of such source terms due to nucleation, molecular growth and coagulation will be briefly discussed.

5.2.3 Nucleation

Nucleation of new soot particle must be carefully managed, because, when the abscissas of the quadrature approximation are null (as occurs in the regions where there are no particles), the linear system (5.8) becomes singular and cannot be solved. An effective solution of this problem consists in assuming that nucleation produces a uniform distribution of nuclei of size $0 \leq L \leq d_{nucl}$, where d_{nucl} is the maximum size of the nuclei. Using the PD algorithm [54], on which the standard QMOM is based, it is possible to evaluate the N local abscissas corresponding to the uniform distribution of the nuclei. For example:

$$N = 2 \quad \begin{cases} L_1 = 0.2113 \cdot d_{nucl} \\ L_2 = 0.7887 \cdot d_{nucl} \end{cases} \quad (5.15)$$

$$N = 3 \quad \begin{cases} L_1 = 0.1127 \cdot d_{nucl} \\ L_2 = 0.5000 \cdot d_{nucl} \\ L_3 = 0.8873 \cdot d_{nucl} \end{cases} \quad (5.16)$$

If $S_{m0}^{nucleation}$ is the nucleation rate of soot particles (see Equation (4.19)), the source term of moments due to nucleation of this uniform distribution of nuclei is [142]:

$$\bar{S}_k \approx \bar{S}_k^{(N)} = \frac{d_p^k}{k+1} S_{m0}^{nucleation} \quad (5.17)$$

5.2.4 Molecular growth

The source terms of moments due to the molecular growth requires the rate of continuous change of the particle size $G(L)$:

$$\bar{S}_k = k \int_0^\infty L^{k-1} G(L) n(L) dL \quad (5.18)$$

Applying the quadrature approximation (Equation (5.3)), we obtain:

$$\bar{S}_k^{(N)} = k \sum_{j=1}^N w_j L_j^{k-1} G(L_j) \quad (5.19)$$

The use of the expression reported above requires the rate of change of local abscissas $G(L_j)$, which is usually not directly available, but must be derived from source term for soot mass fraction related to the molecular growth. Under the usual assumption of spherical particles, the mass of a single particle and its time derivative can be expressed as:

$$m_p = \rho_{soot} V_p = \rho_{soot} \frac{\pi}{6} d_p^3 \quad (5.20)$$

$$\frac{dm_p}{dt} = \rho_{soot} \frac{\pi}{2} d_p^2 \frac{dd_p}{dt} \quad (5.21)$$

The (5.21) gives the rate of change of the mass of the single soot particle, which can be easily related to the soot growth rate S_M^{growth} (see Equations (4.17) and (4.22)):

$$\frac{dm_p}{dt} = \frac{S_M^{growth}}{m_0} \quad (5.22)$$

Therefore, combining the (5.21) and the (5.22), an expression for the rate of continuous change of the particle size can be obtained:

$$\frac{dd_p}{dt} = \frac{2S_M^{growth}}{\rho_{soot}} \frac{1}{m_0 \pi d_p^2} = \frac{2S_M^{growth}}{\rho_{soot}} \frac{1}{A_{soot}} \quad (5.23)$$

where A_{soot} is the specific soot surface area, defined in (4.21).

The rate of continuous change of the particle size $G(L_j)$ is assumed equal to dd_p/dt and as a consequence the source term due to the molecular growth in the equations of moments becomes:

$$\bar{S}_k^{(N)} = k \sum_{j=1}^N w_j L_j^{k-1} G(L_j) = k \sum_{j=1}^N w_j L_j^{k-1} \frac{2S_M^{oxidation}}{\rho_{soot}} \frac{1}{A_{soot}} \quad (5.24)$$

5.2.5 Coagulation

The coagulation rate is usually defined through the collision radius R_c of the aggregates involved in the collisions, which can be evaluated as [142]:

$$R_c = k_f r_0 \left(\frac{V}{V_0} \right)^{1/D_f} \quad (5.25)$$

where k_f is the fractal pre-factor, which is usually assumed equal to 1, r_0 and V_0 are the radius and the volume of primary particles respectively and D_f the fractal dimension. The quantity in brackets is the number of primary particles in the aggregate. If soot particles are assumed to be spherical, the fractal dimension becomes equal to 3 and the collision radius is simply the radius of the sphere.

The coagulation of two particles of sizes L_1 and L_2 gives rise to the following source term:

$$\begin{aligned} \bar{S}_k = & \frac{1}{2} \int_0^\infty \int_0^\infty (L_1^3 + L_2^3)^{k/3} \beta(R_{c_1}, R_{c_2}) n(L_1) n(L_2) dL_1 dL_2 + \\ & - \int_0^\infty \int_0^\infty L_1^k \beta(R_{c_1}, R_{c_2}) n(L_1) n(L_2) dL_1 dL_2 \end{aligned} \quad (5.26)$$

where $\beta(R_{c_1}, R_{c_2})$ is the frequency (or kernel) of coagulation of two particles with collision radii R_{c_1} and R_{c_2} ; the terms on the right side are the birth and the death rate respectively. Applying the quadrature approximation (5.3), the following source term is obtained:

$$\bar{S}_k^{(N)} = \frac{1}{2} \sum_{i=1}^N \sum_{j=1}^N (L_i^3 + L_j^3)^{k/3} \beta_{ij} w_i w_j - \sum_{i=1}^N \sum_{j=1}^N L_i^k \beta_{ij} w_i w_j \quad (5.27)$$

where: $\beta_{ij} = \beta(R_{c_i}, R_{c_j})$

5.2.6 Oxidation

The oxidation of soot particles can be treated in the same way of surface growth; as a consequence the corresponding source term in the DQMOM equations becomes:

$$\bar{S}_k^{(N)} = k \sum_{j=1}^N w_j L_j^{k-1} G(L_j) = k \sum_{j=1}^N w_j L_j^{k-1} \frac{2S_M^{growth}}{\rho_{soot}} \frac{1}{A_{soot}} \quad (5.28)$$

5.3 Semi-empirical kinetic models

The semi-empirical models for evaluating the nucleation, surface growth and oxidation of soot particles are the same already adopted in the previous Chapter. On the contrary, a more accurate model for describing the coagulation of soot particles is adopted.

5.3.1 Nucleation Rate

Soot nucleation is described by the so called acetylene-route, which is based on a simple one-step reaction:



The corresponding source terms are expressed in the usual Arrhenius form:

$$S_{m0}^{nucleation} = A_{nucl} \exp\left(-\frac{T_{nucl}}{T}\right) \cdot C_{C_2H_2} \quad (5.30)$$

The rate parameters proposed by Liu *et al.* [84] are adopted and summarized in Table 5. In the present thesis it is assumed that nucleation produces a uniform distribution of nuclei of size $0 \leq \theta \leq d_{nucl}$, where d_{nucl} is the maximum size of the nuclei, which is related to the diameter of primary particles d_{pp} through the following expression:

$$d_{nucl} = 4^{1/3} d_{pp} \quad (5.31)$$

5.3.2 Growth Rate

According to Frenklach *et al.* [49] the soot particle growth is determined by the addition of acetylene and on the number of active sites on the surface. The corresponding surface growth rate is given by:

$$S_M^{growth} = A_{growth} \exp\left(-\frac{T_{growth}}{T}\right) \cdot C_{C_2H_2} \cdot f(A_{soot}) \quad (5.32)$$

The soot specific surface area A_{soot} can be expressed as a function of the moment of order two of the particle size distribution:

$$A_{soot} = \pi \cdot m_2 = \pi \sum_{j=1}^N w_j L_j^2 \quad (5.33)$$

A range of area dependencies have been proposed in the literature; according to the most common approaches the function f is assumed linearly proportional to the soot specific surface area A_{soot} or to square root surface area $\sqrt{A_{soot}}$. Although the square-root dependence of the soot surface area does not seem physically correct, it can be related to the surface aging phenomena and active-site surface deactivation [84]. In this work the model proposed by Liu *et al.* [84] is used and is reported in Table 5.

5.3.3 Coagulation Rate

In the present thesis, since the soot particles are assumed to be perfectly spherical, the collision radius (5.25) becomes the soot particle radius. The source terms for the moments of the particle size distribution due to the coagulation can be evaluated through the Equation (5.27). The coagulation kernel β_{ij} depends on the Knudsen number Kn , which is the ratio between the mean free-path of gas molecules and the particle radius. The coagulation kernel is evaluated by the Fuchs interpolation formula [51], which is valid in the transition regime between the free molecule ($Kn \gg 1$) and the continuum regime ($Kn \ll 1$). The complete expression is reported in Table 7.

5.3.4 Oxidation Rate

The oxidation rate strongly depends on the hydroxyl radical (OH) and O_2 but also O radical can play an important role. In this work the model of Lee *et al.* [79] is adopted and soot oxidation is described using a one-step reaction:



The rate of oxidation is usually assumed proportional to the soot specific surface area:

$$\dot{S}_{ox} = \dot{m}_{ox} A_{soot} \quad (5.35)$$

$$\dot{m}_{ox} = A_{ox} \exp\left(-\frac{T_{ox}}{T}\right) \cdot \frac{p_{O_2}}{\sqrt{T}} \quad (5.36)$$

This model was also used by Liu *et al.* [84], Wen *et al.* [136] and Ma *et al.* [85] and implicitly assumes that soot oxidation in a diffusion flame is controlled by O₂ into the zone of active soot oxidation at temperatures high enough to react with H and form OH, which is recognized as the main oxidizing species in the stoichiometric/lean side of the flame. On the contrary, O₂ becomes more important as any surviving particles enter oxygen-rich regions where temperature is still high [34].

Expressions	
Coagulation kernel	$\beta_{ij} = \frac{4\pi(\Gamma_i + \Gamma_j)(R_i + R_j)}{K_{ij}}$
Diffusion coefficient	$\Gamma_i = \frac{k_B T}{6\mu R_i} \left[\frac{5 + 4Kn_i + 6Kn_i^2 + 18Kn_i^3}{5 - Kn_i + (8 + \pi)Kn_i^2} \right]$
Fuch's correction	$K_{ij} = \frac{R_i + R_j}{R_i + R_j + \sqrt{g_i^2 + g_j^2}} + \frac{4(\Gamma_i + \Gamma_j)}{(R_i + R_j)\sqrt{c_i^2 + c_j^2}}$ $c_i = \sqrt{\frac{8k_B T}{\pi m_i}}$ $g_i = \frac{(2R_i + l_i)^3 - (4R_i^2 + l_i^2)^{3/2}}{6R_i l_i} - 2R_i \quad l_i = \frac{8\Gamma_i}{\pi c_i}$
Legend	k_B Boltzmann constant Kn Knudsen number

Table 7. Coagulation kernel

5.4 Flamelet library and enthalpy defect

Using the laminar flamelet model the thermochemical state of an adiabatic turbulent flame is completely determined by the mixture fraction Z and the scalar dissipation rate χ_{st} :

$$\psi = \psi(Z, \chi_{st}) \quad (5.37)$$

The mean value $\bar{\psi}$ can be obtained using the bivariate PDF $P(Z, \chi_{st})$:

$$\tilde{\psi} = \int_0^{+\infty} \int_0^1 \psi(Z, \chi_{st}) \cdot P(Z, \chi_{st}) \cdot dZ \cdot d\chi_{st} \quad (5.38)$$

A presumed PDF approach is used. According to Bilger [13] the result of the integration respect to ξ is relatively insensitive to the PDF shape; usually a β -PDF or a clipped Gaussian PDF are adopted. As reported by many authors ([47, 101, 107]), the integration with respect χ_{st} can be described by a log-normal distribution.

The effect of radiation cannot be disregarded especially in sooting flames, due to the mutual sensitivity between temperature and soot formation which enhances radiation. The radiation heat loss in a laminar flamelet is very different from the radiation heat loss in the turbulent flame [18, 53, 66, 92]. Therefore the coupling between the flamelet library and radiation in a turbulent flame is achieved introducing the *enthalpy defect*:

$$\phi_H = \hat{H} - \hat{H}_{AD} = \hat{H} - \left[\hat{H}_{OX} + Z(\hat{H}_{FUEL} - \hat{H}_{OX}) \right] \quad (5.39)$$

State variables are then expressed as a function of Z , χ_{st} and ϕ_H using a proper joint-pdf:

$$\tilde{\psi} = \int_{-\infty}^{+\infty} \int_0^{+\infty} \int_0^1 \psi(Z, \chi_{st}, \phi_H) \cdot P(Z, \chi_{st}, \phi_H) \cdot dZ \cdot d\chi_{st} \cdot d\phi_H \quad (5.40)$$

A common solution is based on the assumption of statistical independence:

$$P(Z, \chi_{st}, \phi_H) = P(Z)P(\chi_{st})P(\phi_H) \quad (5.41)$$

The PDF of enthalpy defect is calculated following Bray and Peters [18] and Marracino and Lentini [92] completely neglecting the effect of ϕ_H fluctuations. Therefore the final form of the joint-PDF $P(Z, \chi_{st}, \phi_H)$ becomes:

$$P(Z, \chi_{st}, \phi_H) = P(Z)P(\chi_{st})\delta(\phi_H - \tilde{\phi}_H) \quad (5.42)$$

where $P(Z)$ is a β -PDF, $P(\chi_{st})$ a log-normal distribution and $\delta(\phi_H - \tilde{\phi}_H)$ is the Dirac function.

According to Marracino and Lentini [92], the flamelet profiles can be organized in shelves, which represent different values of ϕ_H . The mean enthalpy \tilde{H} , used to obtain the enthalpy defect, is calculated from its conservation equation:

$$\bar{\rho} \frac{\partial \tilde{H}}{\partial t} + \bar{\rho} \tilde{u}_i \frac{\partial \tilde{H}}{\partial x_i} = \frac{\partial}{\partial x_i} \left(\Gamma_t \frac{\partial \tilde{H}}{\partial x_i} \right) + \bar{Q}_{rad} \quad (5.43)$$

The radiation term \bar{Q}_{rad} is calculated using optically-thin approximation, but more accurate solutions are possible. Since a limited number of shelves are available in the library a linear interpolation is employed [66, 92].

5.5 Closure of soot source terms

One of the major issues in the modeling of soot formation is the closure of the soot source terms in the conservation equations for weights and weighted abscissas. In general the mean source term can be expressed using the proper joint-PDF $P(Z, \chi_{st}, \phi_H, w_1, \dots, w_N, \zeta_1, \dots, \zeta_N)$:

$$\begin{aligned} \tilde{S} = & \int_0^{+\infty} \dots \int_0^{+\infty} \int_{-\infty}^{+\infty} \int_0^{+\infty} \int_0^1 S(Z, \chi_{st}, \phi_H, w_1, \dots, w_N, \zeta_1, \dots, \zeta_N) \\ & \cdot P(Z, \chi_{st}, \phi_H, w_1, \dots, w_N, \zeta_1, \dots, \zeta_N) \cdot dZ \cdot d\chi_{st} \cdot d\phi_H \cdot dw_1 \cdot \dots \cdot dw_N \cdot d\zeta_1 \cdot \dots \cdot d\zeta_N \end{aligned} \quad (5.44)$$

The form of this joint-PDF is unknown, both experimentally and theoretically, and therefore simplified approaches must be used in order to obtain the source mean term.

5.5.1 Mean Properties

The simplest approach consists in evaluating the source term using the mean flame properties and totally ignoring the effects of turbulence [21]. In this case the joint-PDF can be split in the product of $3+2N$ PDF's of a single variable:

$$P(Z, \chi_{st}, \phi_H, w_1, \dots, w_N, \zeta_1, \dots, \zeta_N) \approx P(Z)P(\chi_{st})P(\phi_H)P(w_1)\dots P(w_N)P(\zeta_1)\dots P(\zeta_N) \quad (5.45)$$

Moreover each PDF simply becomes a Dirac delta function centered on the mean value of the property:

$$\begin{aligned} P(Z, \chi_{st}, \phi_H, w_1, \dots, w_N, \zeta_1, \dots, \zeta_N) = & \delta(Z - \tilde{Z}) \cdot \delta(\phi_H - \tilde{\phi}_H) \cdot \delta(\chi_{st} - \tilde{\chi}_{st}) \\ & \cdot \delta(w_1 - \tilde{w}_1) \dots \delta(w_N - \tilde{w}_N) \cdot \delta(\zeta_1 - \tilde{\zeta}_1) \dots \delta(\zeta_N - \tilde{\zeta}_N) \end{aligned} \quad (5.46)$$

5.5.2 Uncorrelated closure

A different solution assumes that mixture fraction and enthalpy defect are completely uncorrelated with soot particle size distribution (and therefore with w_j and ζ_j). This solution was adopted by several authors [4, 21, 116] and assumes that the influence of scalar fluctuations in the gas phase are dominant. The joint-PDF can be split in the product of two different PDFs:

$$P(Z, \chi_{st}, \phi_H, w_1, \dots, w_N, \zeta_1, \dots, \zeta_N) \approx P(Z, \chi_{st}, \phi_H) \cdot P(w_1, \dots, w_N, \zeta_1, \dots, \zeta_N) \quad (5.47)$$

Moreover, the soot properties are also assumed statistically independent:

$$P(Z, \chi_{st}, \phi_H, w_1, \dots, w_N, \zeta_1, \dots, \zeta_N) \approx P(Z, \chi_{st}, \phi_H) \cdot P(w_1) \dots \cdot P(w_N) \cdot P(\zeta_1) \dots \cdot P(\zeta_N) \quad (5.48)$$

The single PDFs for the soot properties are unknown. The Dirac delta functions can be used to get the closure. The final form of the joint-PDF is therefore the following:

$$P(Z, \chi_{st}, \phi_H, w_1, \dots, w_N, \zeta_1, \dots, \zeta_N) \approx P(Z, \chi_{st}, \phi_H) \cdot \delta(w_1 - \tilde{w}_1) \dots \cdot \delta(w_N - \tilde{w}_N) \cdot \delta(\zeta_1 - \tilde{\zeta}_1) \dots \cdot \delta(\zeta_N - \tilde{\zeta}_N) \quad (5.49)$$

where: $P(Z, \chi_{st}, \phi_H) \approx P(Z) \cdot P(\chi_{st}) \cdot P(\phi_H)$.

A very large flamelet library must be constructed and stored using a large number of enthalpy defects. For each enthalpy defect ϕ_H about 20 steady flamelets were calculated and at different strain rates, from equilibrium conditions ($\chi_{st} = 0$) to the extinction value $\chi_{st,ext}$, which is affected by ϕ_H . A finite-difference C++ code and a fully-implicit method, based on the BzzLibraries [24], was used to build the flamelet library adopting a detailed chemistry. The integration in the mixture fraction space must be performed in a very accurate way due to the possible presence of singularities of the β -PDF at $Z=0$ and $Z=1$. In the present thesis, the approach proposed by Liu *et al.* [83] is adopted, as it warrants higher accuracy than traditional methods [80]. The integration in the scalar dissipation rate is easier and was performed following approach proposed by Lentini [80].

Additional details about the flamelet library construction are reported in Appendix A.

5.6 Radiative heat transfer

The radiative heat transfer is modeled using the optically-thin approximation, already describe in the previous Chapter (see Paragraph 4.6).

5.7 Kinetic mechanism

Model results presented in this work were obtained using the detailed kinetic scheme *C1C30704* [113] able to describe pyrolysis and oxidation reactions of light hydrocarbons. The scheme consists of 69 species involved in 1136 elementary reactions. Thermodynamic data and transport properties were taken from the CHEMKIN Database [71] with improved values for OH and HO₂ formation enthalpy [48]. Reverse rate constants are calculated via forward rates and equilibrium constants. This detailed kinetic mechanism is the core of a larger scheme, based on a modular and hierarchical structure [137], which has been validated in a wide range of pyrolysis and combustion conditions both with pure fuels and hydrocarbon mixtures up to surrogates of real transportation fuels [110, 111]. This kinetic scheme has been also extended to include also the kinetics of soot formation and oxidation, with the discrete sectional method [55, 114].

5.8 CFD Simulation of Experimental Flames

This work analyses two different turbulent jet flames, experimentally investigated by Kent and Honnery [72] and Brookes and Moss [20]. The main data for the flames investigated were already reported in Paragraph 4.9 and are summarized in Table 4. Flame A is fed with ethylene and is unconfined, while Flame B is fed with methane and is confined in a Pyrex tube.

The flow field solutions are obtained by using the FLUENT 6.3 commercial code [45]. A 2D steady-state simulation of the physical domain was considered due to the axial symmetry of the system. For the Flame A a structured 60 x 180 numerical grid was used on a rectangular 75x1000 mm domain, while For the Flame B a structured 80 x 230 numerical grid was used. The Favre averaged Navier-Stokes equations together with the standard κ - ϵ model are employed to calculate the reactive flow. The buoyancy effects have been taken into account in the turbulence model. For the spatial resolution the Second-Order Upwind Scheme was adopted. The segregated implicit solver was used with the SIMPLE procedure for the pressure-velocity coupling. For the pressure interpolation the PRESTO! (PREssure Staggering Options) algorithm was used. The interaction between chemistry and turbulence has been taken into account trough the flamelet approach [100, 101].

The DQMOM was implemented through user-defined functions in the commercial CFD code FLUENT 6.3 [45], which computes the velocity, temperature and composition fields of the

flame. The additional equations of weights and weighted abscissas are introduced and solved by applying the two different approaches for closing the turbulent source term.

5.9 CFD results

5.9.1 Flame A

Figure 66 compares the predicted axial and radial temperature profiles with the experimental measurements. These results refer to the simulation obtained using the totally uncorrelated approach for soot predictions. The predictions of temperature and composition fields obtained using the mean properties and the totally correlated approach are similar and do not need a discussion. Figure 66 allows evaluating the effect of both soot and gas radiation: in particular the peak temperature is modified by soot radiation by $\sim 150\text{--}200\text{K}$. Soot radiation acts mainly on the rich side of the flame because soot only exists in this part of the flame; on the other side, gas radiation is particularly strong in the second part of the flame, where water and carbon dioxide concentrations are higher. The agreement with the experimental measurements can be considered satisfactory, both along the centerline and in the radial directions.

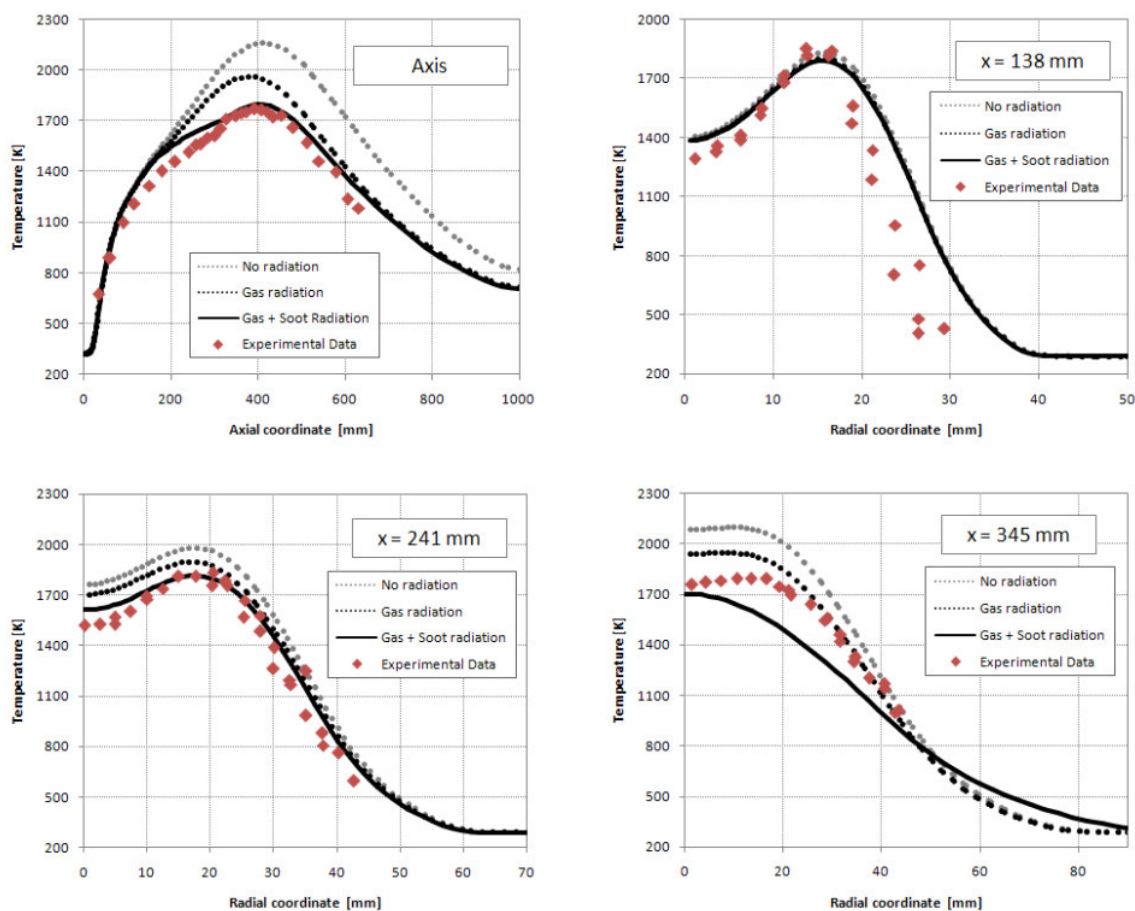


Figure 66. Flame A: comparison between experimental measurements of temperature [72] and numerical predictions along the axis.

5.9.2 Flame B.

Figure 67 compares the predicted axial and radial temperature profiles with the experimental data. The importance of radiation for this flame is significant but less critical than in the case of Flame A: in particular without considering the radiation the peak temperature is over-predicted by $\sim 150\text{K}$. The agreement with the experimental measurements can be considered satisfactory, both along the centerline and in the radial directions, but unfortunately no data are available in the tail of the flame and therefore a complete comparison is not possible.

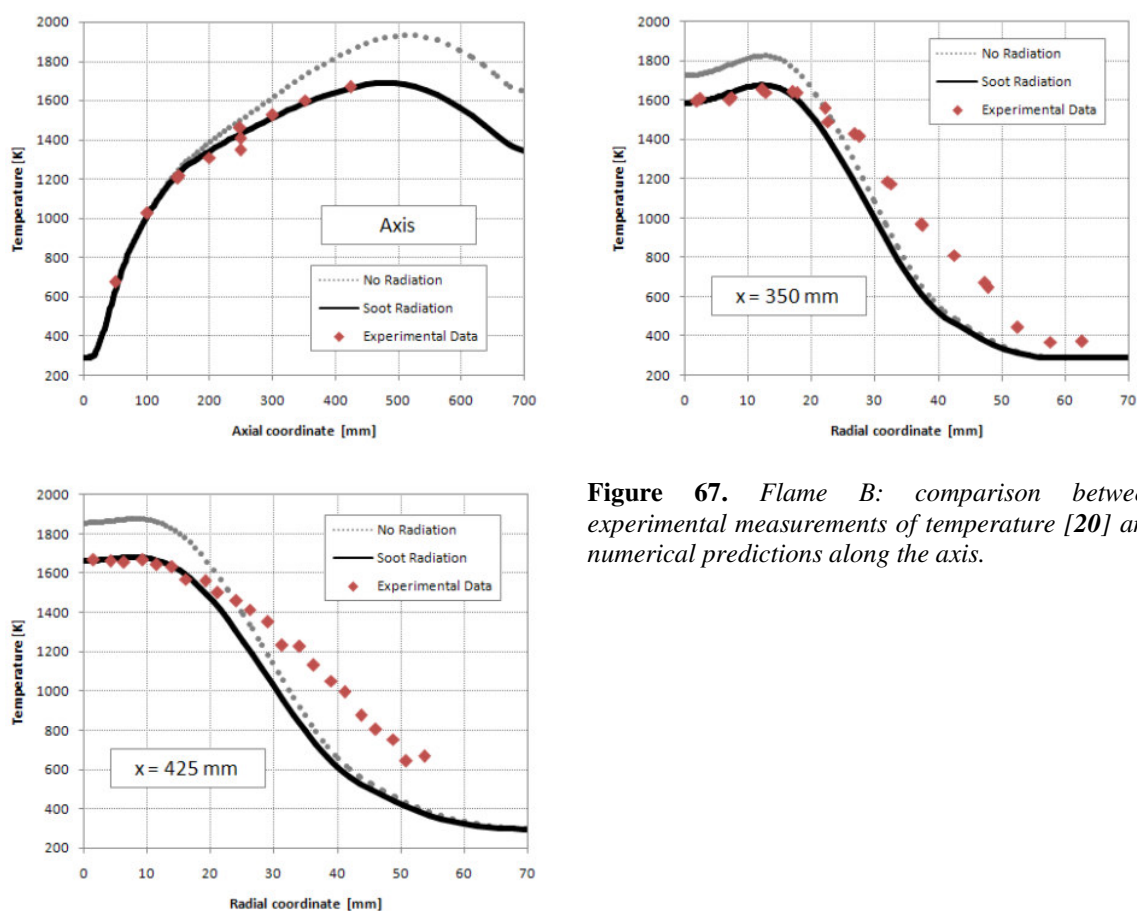


Figure 67. Flame B: comparison between experimental measurements of temperature [20] and numerical predictions along the axis.

5.10 Soot predictions

5.10.1 Flame A.

The predicted soot volume fraction map (obtained using the uncorrelated approach) is reported in Figure 68. The peak value and location are in excellent agreement with the experimental data. Obviously the soot volume fraction is higher in the region where the acetylene concentration is higher, but, due to the molecular growth, the peak value is not exactly in the same location. The soot particle mean diameter d_{32} , calculated as the ratio between the moment of order 3

and the moment of order 2, is reported in the same Figure 68. Four main regions can be easily recognized, as indicated in the map:

- i. the nucleation of new soot particles mainly occurs in the first region; the mean diameter is very small and close to the soot primary particle diameter (1-2 nm);
- ii. in region 2 the growth reactions increase the diameter of soot particles, which reaches a maximum value of 50 nm; in this zone the temperature and the concentration of acetylene are large enough to have a large growth rate;
- iii. in the third region the oxidation rate is large, leading to a reduction of diameter of soot particles;
- iv. in the final region of the flame, where the temperature are low and acetylene concentration is small, the coagulation phenomena occur; as a consequence the mean diameter of soot particles increases up to the value of 55 nm.

Unfortunately no experimental data are available for the particle diameter, but these results are in good agreement with the numerical results obtained by Zucca *et al.* [142] for the same flame, using a different model for description of soot formation.

Figure 69 shows a comparison between the measured soot volume fraction and the numerical results obtained using the two different approaches for closing the soot production term. When the closure is simply obtained using the mean properties, thus neglecting the effect of turbulent fluctuations, the soot volume fraction is slightly overpredicted and the position of the peak value is anticipated. As a consequence, also the soot radial profiles are overestimated in the initial part of the flame. This problem was also found by Pitsch *et al.* [106] who offered an

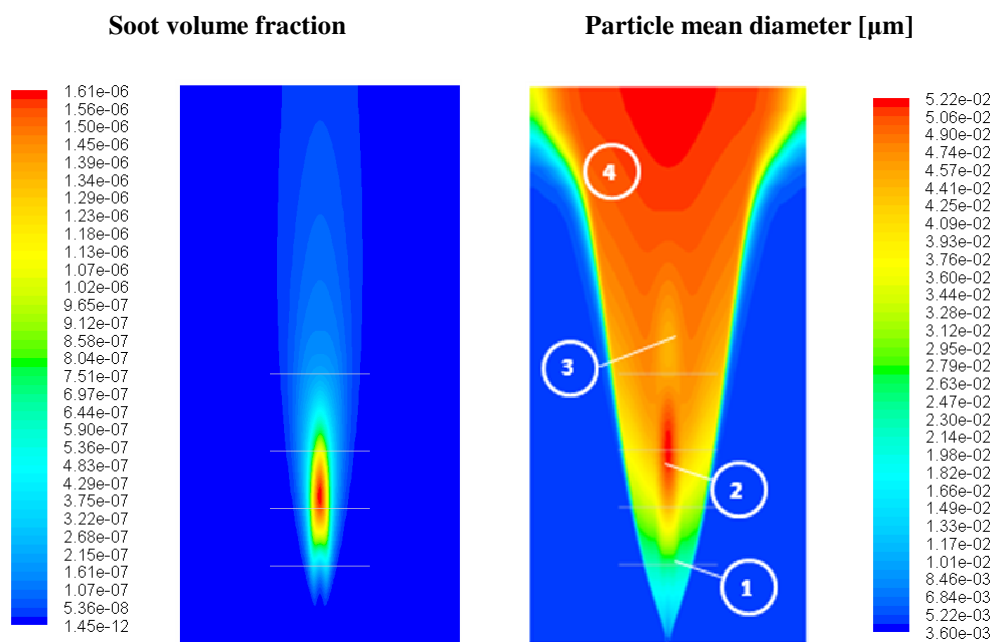


Figure 68. Flame A: soot volume fraction and soot particle mean diameter maps obtained using the uncorrelated approach.

explanation in terms of a small overprediction in the decay rate of the axial mixture fraction profile. However in the present work this problem in the peak location seems due to soot source term closure model, which, in the case of the mean properties closure, cannot take into account the turbulent fluctuations. The overall agreement with the experimental data can be considered reasonable in view of the simplifications related with this approach. The agreement with the experimental measurements can be improved using the uncorrelated closure. As shown in Figure 69 the shape of the profile in axial direction is well described and the peak location is correctly predicted. The maximum amount of soot is slightly under-predicted, but also along the radial direction the agreement is reasonable. Using the uncorrelated closure the soot volume fraction becomes negligible at ~ 700 mm from the fuel inlet due to the oxidation reactions. Unfortunately no experimental information is available in this zone of the flame and therefore it is not possible to single out the right model.

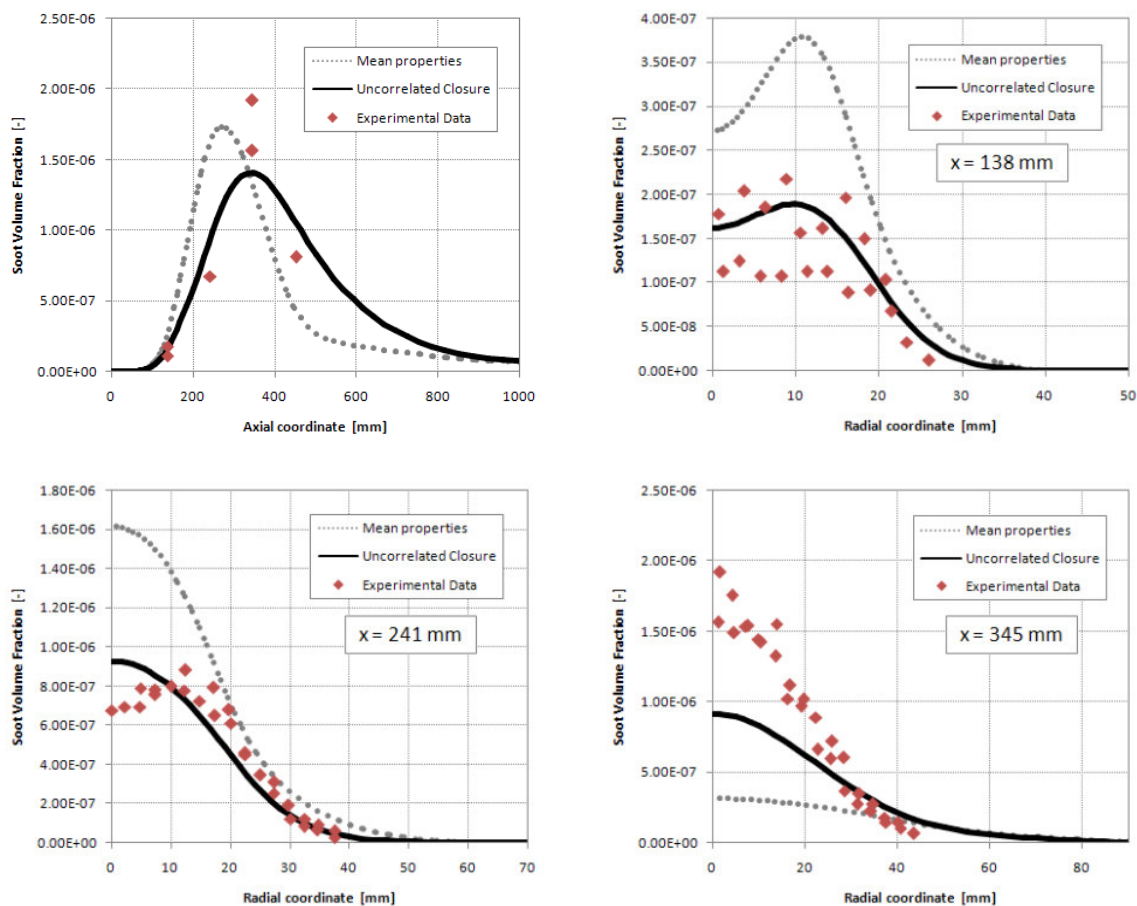


Figure 69. Flame A: comparison between experimental measurements of soot volume fraction and numerical results obtained using different closure models. Mean properties closure (dotted line) and uncorrelated closure (continuous line).

5.10.2 Flame B.

Since the mean temperature and the acetylene concentration in this flame are lower than for Flame A, a smaller amount of soot is expected. This is confirmed by the map of soot volume fraction reported in Figure 70. The peak value is about one order of magnitude smaller (~ 2 ppm in Flame A, ~ 0.2 ppm in this flame). The soot particle mean diameter, reported in the same Figure, does not show a maximum as in the case of Flame A; probably this is due to the growth reactions, which are not so fast and strong as for the ethylene flame.

Figure 71 shows the comparison between measured and predicted soot volume fraction. In this flame the soot volume fraction is largely overpredicted using the closure based on mean properties. The axial position of the soot peak is anticipated by about 50 mm. Along the radial direction not only the mean values of predicted results and experimental data are different, but also the shape: the experimental profiles show a slow decrease of soot volume from the axis location. Using the uncorrelated approach the agreement is more accurate along the axis, in particular when compared with the previous results. The peak value better agrees with the experimental location. The agreement for the radial profiles is less accurate: also in this case the shape of these profiles is different from the experimental one. Similar results were also obtained also by different authors [21, 116].

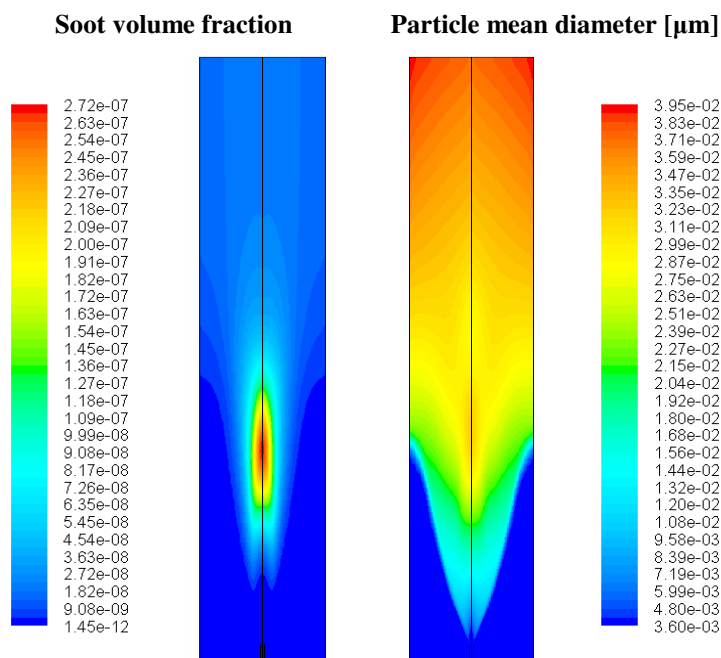


Figure 70. Flame B: soot volume fraction and soot particle mean diameter maps obtained using the uncorrelated approach.

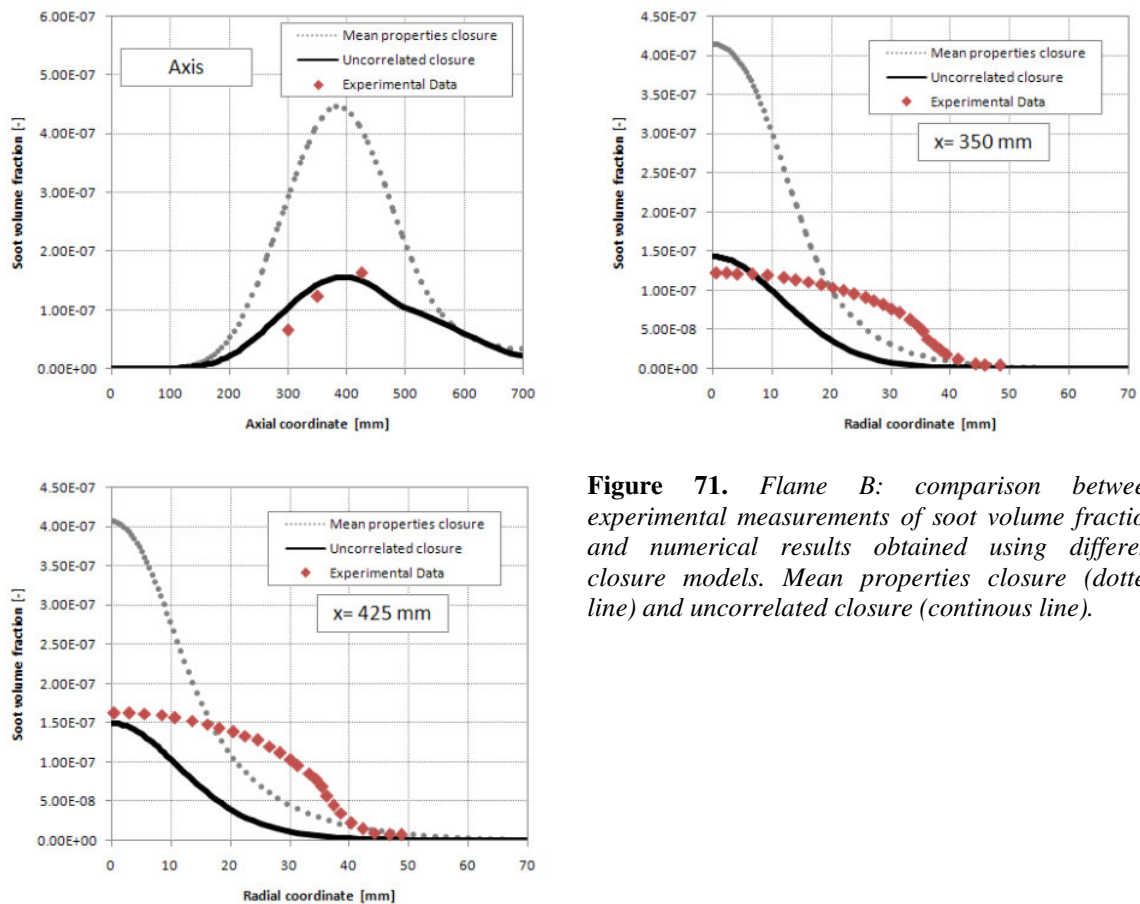


Figure 71. Flame B: comparison between experimental measurements of soot volume fraction and numerical results obtained using different closure models. Mean properties closure (dotted line) and uncorrelated closure (continuous line).

5.11 Sensitivity analysis to the nucleation rate.

The nucleation models employed for the numerical simulation of soot formation in turbulent non premixed flames have usually a small impact on the final prediction of soot volume fraction, as reported by Ma *et al.* [85] and observed in the previous Chapter. In this section a sensitivity analysis to the nucleation models is performed using the DQMOM; the results are reported only for Flame A. The uncorrelated approach, which showed the best agreement with the experimental data, was used to close the source terms in the soot transport equations. All nucleation models for which the sensitivity analysis is conducted are based on the acetylene-route. The tested models are exactly the same introduced in Paragraph 4.15 and therefore they are not here repeated.

Despite the very different nucleation rates (more than three order of magnitude), soot formation is largely unaffected (Figure 72). Similar results (not here shown) can be observed using the mean properties closure approach. However some differences can be observed in the soot particle mean diameter, reported in Figure 73, which can be explained by taking into account the differences in the diameter of primary particles.

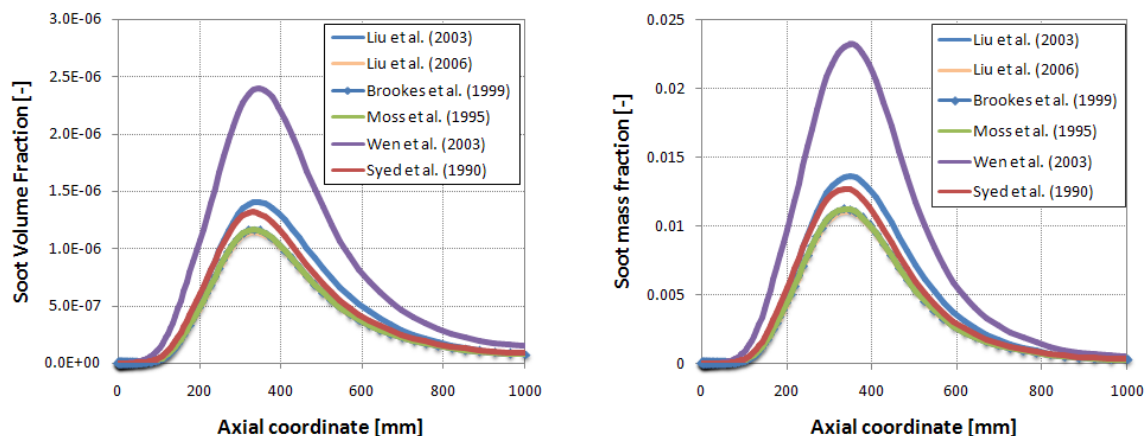


Figure 72. Flame A: main results of sensitivity analysis to the nucleation model. (a) Soot volume fraction profile along the axis; (b) soot mass fraction along the axis.

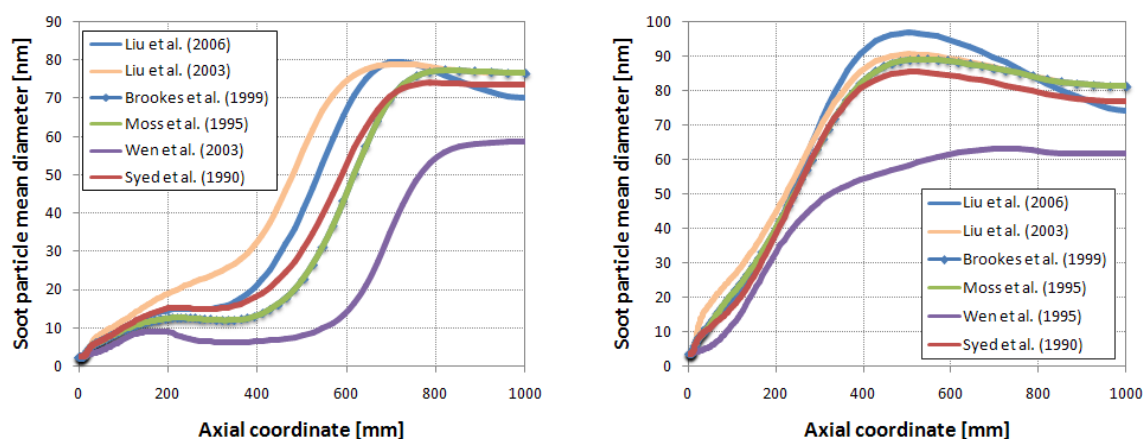


Figure 73. Flame A: main results of sensitivity analysis to the nucleation model. (a) Soot particle mean diameter (d_{10}) along the axis; (b) Soot particle mean diameter (d_{32}) along the axis.

5.12 Conclusions

The principal objective of the analysis presented in this Chapter is to demonstrate the importance of turbulent fluctuations for accurate soot predictions in a turbulent non-premixed flame using a steady laminar flamelet model for the description of thermal and gaseous species field. The description of soot nucleation, growth, oxidation and coagulation is modeled through a semi-empirical model, but the hypothesis of a monodispersed distribution of soot particles (adopted in the previous Chapter) is removed by applying the Direct Quadrature Method of Moments (DQMOM). Two different closure methods for the source terms in the transport equations of soot were formulated and adapted to the DQMOM. Neglecting the effects of turbulent fluctuations of both temperature and composition on the soot source terms results in an overprediction of the soot volume fraction. Results clearly show that the steady flamelet model approach is able to correctly

predict the thermal and mixture fraction fields. On the contrary the closure model to take into account the turbulence effects on the soot source terms plays an important role on the prediction of soot amount in the turbulent flame investigated. In particular the best agreement with the experimental data has been obtained using the so-called *uncorrelated model*, which consists in assuming that the mixture fraction and the enthalpy defect are totally uncorrelated with the soot properties. Moreover this activity confirmed that the coupling between the soot production rate and the radiative heat loss must be carefully taken into account to accurately model the formation of soot. The predicted soot amount in the turbulent flame is relatively insensitive to the semi-empirical model adopted for describing the nucleation process, as clearly showed through a sensitivity analysis.

6 Unsteady counter flow diffusion flames

The formation of pollutant species in turbulent diffusion flames is strongly affected by the coupling between the highly non-linear chemical kinetics with three dimensional, unsteady hydrodynamics. In order to accurately predict non-equilibrium effects in the numerical modeling of pollutant formation (especially PAH and soot), it is necessary to better understand this interdependency of transport and kinetic mechanisms. However the effects of turbulence on soot chemistry cannot be easily investigated on turbulent flames, because of their complexity and the existence of many coupled phenomena. An alternative approach was proposed and applied in this thesis. Unsteady counter flow diffusion flames can be conveniently used to address the effects of hydrodynamic unsteadiness on the pollutant chemistry, because they possess much of the physics of turbulent diffusion flames and exhibit a large range of combustion conditions with respect to steady flames. Thus, these flames give insights into a variety of chemistry-flow field interactions important in turbulent combustion. Opposed counter-flow diffusion flames (CFDF) can be exposed to harmonic oscillations of the strain rate in order to simulate turbulent fluctuations and their effects on the formation of pollutant species. Each chemical species responds to the imposed oscillations according to the characteristic times of its chemistry and this allows to accurately investigate the role of turbulent mixing on the formation of pollutant species.

In this Chapter a mathematical model for simulating unsteady counterflow diffusion flames is briefly presented and applied to several flames fed with methane, propane and ethylene at different global strain rates. In particular, unsteady effects on the formation of PAH and soot are investigated for the methane and propane flames by imposing harmonic oscillations in the strain rate in a large range of frequencies. Numerical results reveal a net increase in the concentration of aromatic species and soot when the strain rate oscillations are imposed on the flame. The response of the flame in terms of soot and PAH concentrations appears strongly dependent on the applied forcing frequency. PAH and soot exhibit specific behaviour according to their characteristic

chemical time scales which are longer than the one of the whole combustion process. The PAH and soot formation is found less sensitive to velocity fluctuations for flames with large initial strain rate. At low frequencies of imposed oscillations the structure of soot profile shows strong deviations from the steady state profile. At large frequencies a decoupling between the soot concentration and the velocity field appears to be evident.

6.1 Introduction

Turbulent non premixed flames are largely used in many practical combustion devices to convert chemical energy into work, due to the high efficiency, large heat releases and safety reasons. However diffusion flames produce more pollutant species (in particular soot) than premixed flames. Since combustion devices need to respect always more stringent limitations concerning the emissions of pollutants, the design of new burners relying on non premixed flames cannot neglect the issues related to the soot formation. Turbulent diffusion flames are difficult to study, due to the complex interactions and the strong coupling between spatial and time scales of fluid dynamics and chemistry. Moreover, the formation of pollutant species can be accurately predicted only if large and detailed kinetic schemes are used, with hundreds of chemical species and thousands of reactions. The direct coupling between detailed kinetics and complex CFD becomes therefore computationally very expensive, especially when considering the typical dimensions of the computational grids used for industrial applications. As a consequence, despite the continuous increase in the speed of computational tools, simplified approaches for the modeling of turbulent flames must be taken into account.

The Steady Laminar Flamelet Model (SLFM) represents one of the most used approaches to numerically predict complex turbulent reacting flows and is largely applied for the simulation of turbulent non premixed flames in different kinds of combustion devices [100, 101, 107, 47]. The main advantage in this approach is related to the small number of variables which need to be transported in the CFD code. A steady flamelet library can be built in a preprocessing step, using the mixture fraction, its variance, the scalar dissipation rate and the enthalpy loss as independent variables; the concentration of every species can be expressed as a function of these independent parameters.

The flamelet approach implicitly assumes that the flamelets respond in a quasi-steady manner to the local strain rate variations in the combustion device. It is pretty evident that in a real combustion device the strain rate can fluctuate around its main value (which is established by the large scale eddies) due to the smaller eddies with characteristic turnover times which are comparable to the characteristic diffusion time (especially for high Reynolds number). In particular, since a turbulent flow consists of eddies with a wide spectrum of lengths and time scales, if the Reynolds

number is sufficiently high it is expected a large range of eddy sizes in which the characteristic eddy turn-over time becomes comparable with the diffusion time in the laminar flamelet [67]. If such conditions are met, the unsteadiness begins to show its effects on the characteristics of laminar flamelets. Moreover, fluctuations of reactants and temperature around their main values can directly affect the structure of the flamelet. The importance of a better understanding of the transient response of flames has been recognized by many authors [6, 41, 60, 93, 139]. In particular the main objective is to understand for which conditions the unsteady effects are important for the flamelets or, in other words, if information obtained in steady state conditions can be extended to unsteady conditions.

From a numerical point of view the introduction of unsteadiness in combustion is a challenge due the strong coupling between the time and spatial scales of convection, diffusion and reaction. As a first step, many authors suggested to perform this kind of investigations by exposing the laminar flames to far-field harmonic oscillations, using a large range of frequencies, from very low to very high values [36, 37, 41, 67]. If the oscillations directly affect the strain rate, some important information can be obtained, due to the induced large variations in the characteristic range of eddy scales. In this contest the most appropriate choice is the counter-flow diffusion flame (CFDF), because such system posses much of the relevant physics postulated for diffusion flamelets. Moreover, it is easy to relate the strain rate of these flames to the scalar dissipation rate of the diffusion flamelets.

The effects of unsteadiness on counter flow diffusion flames were experimentally investigated by several authors [36, 37, 134, 135]; on the contrary a few numerical studies have been performed on the same subject [41, 67, 127]. From both experimental and numerical results, it is evident that the strain rate responds quasi instantaneously to the oscillations imposed on the velocities of fuel and air streams, both at low and large frequencies. However the response of temperature and concentrations of main species is quasi-steady only if the frequencies are sufficiently low. At high frequencies the phase lag between the oscillations and the response of the flame cannot be neglected and then the chemical reactions do not respond immediately to the oscillations in the strain rate and the chemistry and flow field become uncoupled. At intermediate values of oscillation frequency the behavior of the flame response is more complex: in fact, depending on the characteristic time of chemistry for each species, the response can be quasi-steady or can be characterized by a large phase shift. Indeed, it is evident that the assumption of quasi-steady response in some conditions is not appropriate or questionable.

The response of the flame to the externally imposed fluctuations is particular important for pollutant species, whose chemistry is usually slow. In this case the non-equilibrium effects are expected to be very important and the response to the unsteadiness larger and more complicated. Few studies have attempted to clarify how unsteady strain rates affect the production of soot and its

precursors, in particular Polycyclic Aromatic Hydrocarbons (PAH). Xiao *et al.* [139] experimentally studied the response of PAHs concentrations in two different counter flow diffusion flames (fed with methane and propane) to externally imposed harmonic oscillations on the velocity field. From the experimental results it was evident that different classes of PAHs respond in a different way to the oscillation of the strain rate, because of the different chemical times and therefore the different Damköhler numbers. Smallest PAHs continue to respond in a quasi-steady manner to the instantaneous strain rate at higher frequencies whilst largest PAHs do not. At high oscillation frequency the large PAHs do not appreciably respond to the fast strain rate fluctuations; sinusoidal responses, also for large PAHs, can be observed for low or intermediate oscillation frequencies in the instantaneous strain rate. Moreover the response of the largest PAHs to the frequency changes is much damped and the response of the smallest PAHs is less damped. From the quantitative measurements in oscillating counter-flow diffusion flames, performed by Decroix *et al.* [37], strong deviations in soot formation from the corresponding steady value are observed.

In the following the attention will be focused on the effect of unsteady strain rates on the formation of soot and its precursors in several counter flow diffusion flames fed with methane, propane and ethylene. The transport equations governing the dynamic behavior of the flame are numerically solved using a very detailed kinetic scheme and an accurate description of the transport properties. Harmonic oscillations of fuel and oxidizer stream velocities are externally imposed to introduce the unsteadiness in the strain rate. The response of the flame to the variations in the free stream reactant properties is investigated in terms of temperature and species concentration oscillations. However, it is important to stress that the inherent randomness in the turbulent flow may complicate the direct application of the results obtained following this kind of approach to the laminar flamelet regime of turbulent combustion.

6.2 Counter-flow diffusion flames

The counter-flow diffusion flames studied in the present thesis results from impinging separate fuel and oxidizer streams. Two main geometrical configurations are possible, as reported in Figure 74. The axisymmetric geometry consists of two concentric, circular nozzles directed towards each other and produces an axisymmetric flow field with a stagnation plane between the nozzles. The planar geometry consists of two concentric linear nozzles directed towards each other. This configuration produces a 2-D planar flow field with a stagnation line between the two nozzles. Both these opposed flow geometries make an attractive experimental configuration, because the flames are flat, allowing for detailed study of the flame chemistry and structure. The location of the stagnation plane depends on the momentum balance of the two streams and can be evaluated as a

first approximation through the following global balance, which neglects the dependence of velocity field on the temperature:

$$\frac{\rho_F v_F^2}{x_{SP}} = \frac{\rho_O v_O^2}{L - x_{SP}} \quad (6.1)$$

where ρ_F and ρ_O are respectively the density of fuel and oxidizer streams, v_F and v_O their velocities, L is the distance between the nozzles and x_{SP} the stagnation plane distance from the fuel nozzle. From Equation (6.1) the approximate stagnation plane location is:

$$x_{SP} = \frac{\rho_F v_F^2}{\rho_F v_F^2 + \rho_O v_O^2} L \quad (6.2)$$

The flame position usually does not correspond to the stagnation plane, but is located where the composition reaches its stoichiometric value. Since most fuels require more air than fuel by mass, the diffusion flame usually sits on the oxidizer side of the stagnation plane; fuel diffuses through the stagnation plane to establish the flame in a stoichiometric mixture.

Experimentally it is possible to observe three, main regions (see Figure 75), which will be discussed in the next sections. In particular in the blue region, usually called the primary reaction zone, the composition is near the stoichiometric value.

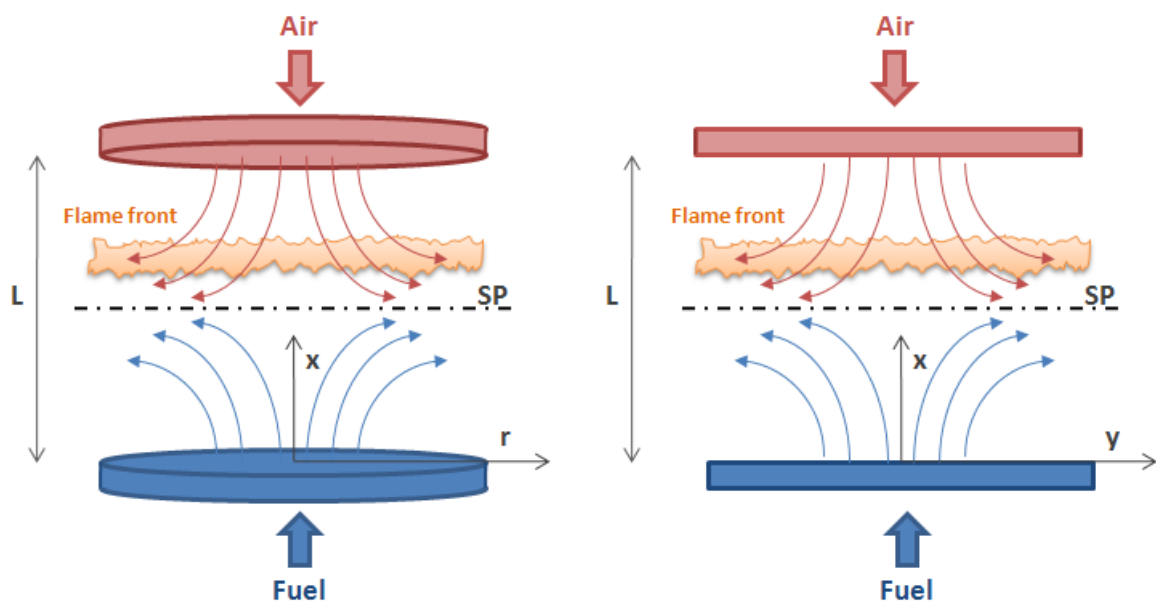


Figure 74. (a) Geometry of the axisymmetric opposed-flow diffusion flame; (b) geometry of the planar opposed-flow diffusion flame. The dashed lines represent the stagnation plane (SP).

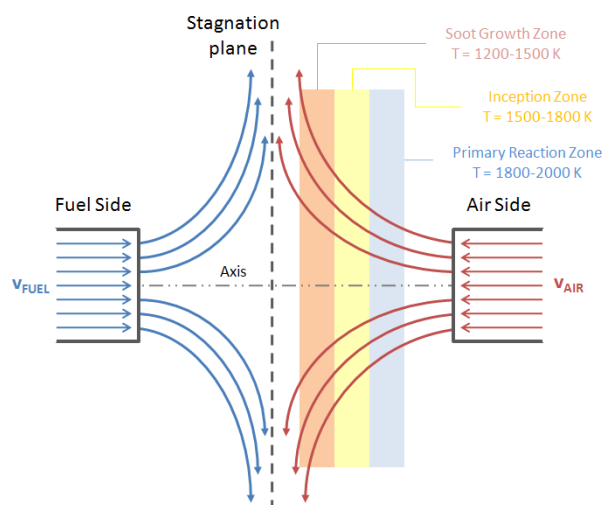


Figure 75. Undiluted hydrocarbon/air counterflow diffusion flame geometry and sooting structure (from Zhang *et al.*[140]).

6.3 Mathematical model of unsteady counter-flow diffusion flames

The numerical solution of the counter flow diffusion flame is obtained by solving the unsteady conservation equations of mass, momentum, energy and species concentrations, reported in the Chapter 1. However, the three-dimensional flow can be reduced mathematically to one dimension by assuming that the tangential velocity varies linearly in the tangential direction, which leads to an important simplification, in which the fluid properties are functions of the axial distance x only. The reduction of the three-dimensional flow is based upon similarity solutions advanced for incompressible flows by von Karman [132], which are not here repeated. The mathematical model used in this thesis is derived from the model that was originally developed by Kee *et al.* [69] for premixed opposed-flow flames. Since the model is based on a finite domain, which corresponds to the region between the fuel and oxidizer nozzles, an eigenvalue must be included in the solution of the equations. Using the assumption that:

- the temperature and mass fractions of all species are function only of the coordinate x normal to the flame;
- the normal velocity u component is a function of x only;
- the tangential velocity v is proportional to the coordinate tangential to the flame (r for axisymmetric geometry or y for planar geometry, see Figure 74);
- the solution is considered along the x axis only;

the resulting system of equations has only time t and the spatial coordinate x as independent variables.

The hypotheses reported above are acceptable only if the distance between the inlet nozzles of fuel and oxidizer streams is smaller than their diameter. In this case it is possible to consider the flame perfectly flat, neglecting the distortion of velocity field (which results in a deep distortion of the front flame).

6.3.1 Governing equations

Since the counter flow diffusion flames investigated in the present work consist of two concentric, circular nozzles directed towards each other, the resulting geometry is axisymmetric. As a consequence, the governing equations are more conveniently written using cylindrical coordinates, exploiting the axisymmetric geometry. The overall model consists of system of differential and algebraic equations, corresponding to the conservation equations and the boundary conditions for the dependent variables (G, F, H, ω_k, T) . The derivation of the following equations and some additional details about the numerical procedure for their solution are reported in Appendix B:

$$\frac{\partial \rho}{\partial t} = 2 \left(G - \frac{\partial F}{\partial x} \right) \quad (6.3)$$

$$\frac{\partial G}{\partial t} = \frac{\partial}{\partial x} \left[\mu \frac{\partial}{\partial x} \left(\frac{G}{\rho} \right) \right] - 2 \frac{\partial}{\partial x} \left(\frac{FG}{\rho} \right) + \frac{3}{\rho} G^2 + H = 0 \quad (6.4)$$

$$\frac{1}{r} \frac{\partial P}{\partial r} = H = \text{const} \quad (6.5)$$

$$\frac{\partial \omega_k}{\partial t} = - \frac{2F}{\rho} \frac{\partial \omega_k}{\partial x} - \frac{1}{\rho} \left[\frac{\partial}{\partial x} (\rho \omega_k V_k) - \dot{\Omega}_k \right] \quad k = 1, \dots, N_s \quad (6.6)$$

$$\frac{\partial T}{\partial t} = - \frac{2F}{\rho} \frac{\partial T}{\partial x} + \frac{1}{\rho \hat{C}_p} \frac{\partial}{\partial x} \left(\lambda \frac{\partial T}{\partial x} \right) - \frac{1}{\hat{C}_p} \sum_{k=1}^{NC} \hat{C}_{p,k} \omega_k V_k \frac{\partial T}{\partial x} - \frac{1}{\rho \hat{C}_p} \sum_{k=1}^{NC} \hat{H}_k \dot{\Omega}_k \quad (6.7)$$

In the equations reported above G and F are respectively:

$$G(x) = -\frac{\rho v}{r} \quad F(x) = \frac{\rho u}{2} \quad (6.8)$$

and H is the uniform pressure curvature, which is an eigenvalue of the problem.

6.3.2 Boundary conditions

The boundary conditions for the fuel (F) and oxidizer (O) streams at the nozzles are:

$$\text{Fuel side } (x=0) \left\{ \begin{array}{l} F = \frac{\rho_F u_F}{2} \\ G = 0 \\ T = T_F \\ \rho u \omega_k + \rho \omega_k V_k = (\rho u \omega_k)_F \end{array} \right. \quad (6.9)$$

$$\text{Air side } (x=L) \left\{ \begin{array}{l} F = \frac{\rho_O u_O}{2} \\ G = 0 \\ T = T_O \\ \rho u \omega_k + \rho \omega_k V_k = (\rho u \omega_k)_O \end{array} \right. \quad (6.10)$$

The boundary conditions for each chemical species specifies the total mass flux (accounting for diffusion and convection), rather than the species mass fraction, as adopted in previous works [41]. If gradients exist at the boundary, these conditions allow diffusion into the nozzle and therefore they warrant a more accurate description.

6.3.3 Initial conditions

Initially the problem for the steady flame is solved: the corresponding solution is the starting point for the application of the harmonic oscillations [41]. Therefore for $t < 0$ the flow is assumed to correspond to the steady solution; at $t = 0$ the oscillations are applied to the inlet velocity of fuel and oxidizer streams. These oscillations induce fluctuations of the strain rate in a quasi-steady manner. In the present work it is assumed that the oscillations of the inlet velocities have the following form:

$$u(t) = u_{steady} \left[1 + A_u \cdot \sin(2\pi f \cdot t) \right] \quad (6.11)$$

where u_{steady} is the steady state value of the inlet velocity and A_u the dimensionless semi-amplitude of the oscillations; f is the frequency of the imposed oscillations.

6.4 Numerical methodology

The overall model consists of a differential system of the conservation equations with boundary and initial conditions for the dependent variables. The attention to the description of soot precursors and PAHs leads to the use of a detailed kinetic mechanism, which includes a large number of components. The resulting system of algebraic and partial differential equations requires particular attention to the numerical aspects of the problem. The partial differential equations are discretized by means of a non uniform spatial grid. Discretization of the differential equations uses conventional finite differencing techniques for non-uniform mesh spacing. Diffusive terms use central differences; for better convergence, convective terms use upwind differencing, based on the sign of the axial convective velocity. The discretized form of equations (6.3)-(6.7) is reported in Appendix B.

The numerical problem corresponds to a large system of differential-algebraic equations (DAE). The structure of this DAE system is a tridiagonal block, due to spatial discretization; most of the equations are devoted to the chemical species involved in the detailed kinetic scheme, with $(NS+4)$ equations for each discretization point, where NS is the number of species in the adopted kinetic scheme. The total number of equations is therefore equal to $(NS+4) \cdot NP$, where NP indicates the number of points using for the numerical discretization in space. For example, if a kinetic scheme with ~ 280 species is used and a spatial grid with ~ 200 points is taken into account, the number of differential-algebraic equations to be solved is equal to $\sim 55,000$.

The complexity of this problem, coupled to the intrinsic stiffness of the DAE systems [121], means that specific attention must be paid to the numerical methods and solver routines. In fact, this problem is quite challenging, not only with regard to the precision required, but also in terms of robustness (due to high gradients and very different characteristic times for the chemistry of each species) and efficiency. We adopted the `BzzMath` numerical library, which is freeware for noncommercial use and can be directly downloaded at the following web site: <http://www.chem.polimi.it/homes/gbuzzi> [25, 26]. The possibility of exploiting the tridiagonal block structure is of crucial importance in drastically reducing CPU time. For this purpose, a specifically developed C++ DAE class of the `BzzMath` library was adopted [26, 89]. Some additional details are reported in Appendix C.

The mathematical model presented above was applied for studying the effects of unsteadiness on PAH formation for three different counter flow diffusion flames fed with methane, neglecting the formation of soot. Then the same methodology was adopted for investigating the

role of unsteadiness on soot chemistry for different counter flow diffusion flames fed with propane. In the next sections the main results are reported and discussed: in Paragraph 6.5 the methane flames are investigated; in Paragraph 6.6 the attention is focused on the propane flame.

6.5 PAH formation in unsteady counter flow diffusion flames

6.5.1 Flames Investigated

The counter flow diffusion flames numerically simulated in this section were experimentally investigated by Xiao *et al.* [139]. The oxidizer and the fuel tubes are 25.4 mm in diameter and have a 12.7 mm separation distance; the inlet temperatures, both of fuel and air streams, are 298K. A controlled oscillation was established in the reactant flow fields by driving two loudspeakers with a sine wave from an amplified signal generator. Three different strain rates were studied; the corresponding operating conditions are reported in Table 8.

	Flame I	Flame II	Flame III
<i>Global Strain Rate [Hz]</i>	23	44	74
<i>Nozzle Diameters [mm]</i>	25.4	25.4	25.4
<i>Distance [mm]</i>	12.7	12.7	12.7
<i>Fuel Velocity [cm/s]</i>	25.71	50.11	75.82
<i>Air Velocity [cm/s]</i>	18.92	38.10	57.25
<i>Flame temperature [K]</i>	2052	2032	2005
<i>Flame front location [mm]</i>	7.49	7.09	6.97
<i>Stagnation plane location [mm]</i>	5.14	5.40	5.57
<i>Fuel diffusive layer thickness [mm]</i>	3.11	2.33	1.94
<i>Air diffusive layer thickness [mm]</i>	2.03	1.49	1.25

Table 8. Operating conditions and main numerical results for the flames fed with methane, experimentally investigated by Xiao *et al.* [139].

6.5.2 Kinetic Scheme

Detailed kinetic models can be effectively used to analyze the combustion of hydrocarbon and the formation of pollutant species such as PAH and soot. For this purpose, in addition to pyrolysis and oxidation reactions that convert and oxidize hydrocarbons, it is also necessary to include several classes of condensation and dealkylation reactions that govern the growth of polycyclic aromatic hydrocarbons and soot. Moreover, the large number of reactions that are required to describe the combustion of large hydrocarbons precludes the possibility to adopt a fully

detailed approach to describe their combustion mechanism. A semi-detailed or lumped approach can be conveniently adopted to reduce the overall complexity of the resulting chemical-kinetic scheme both in terms of equivalent species and lumped or equivalent reactions. In fact, the scheme uses a lumped description of the primary propagation reactions for the large species to smaller species, and then treats the successive reactions of smaller species with a fully detailed chemical-kinetic scheme [56, 113].

The simulations presented in this section were obtained using a reduced scheme, able to account for small- and medium-size PAH formation but neglecting the successive formation of larger PAH and soot. The resulting, adopted kinetic scheme consists of 106 species involved in 2722 reactions.

The thermo-chemical information on the gas phase was obtained primarily from the CHEMKIN thermodynamic database [70, 71]; unavailable thermodynamic data were estimated by group additivity method [11].

6.5.3 *Steady Flame Results*

In this section the numerical results obtained in steady state conditions are reported and discussed. From the velocity profile (reported in Figure 76a) it is evident that the stagnation plane (where the axial velocity is zero) is located on the fuel side. Its location mainly depends on the momentum balance of the two streams and, since most fuels require more air than fuel by mass, the diffusion flame usually sits on the oxidizer side of the stagnation plane; fuel diffuses through the stagnation plane to establish the flame in a stoichiometric mixture. The temperature profiles along the centerline for the three different strain rates are reported in Figure 76b. As expected, the maximum value (the so-called flame temperature) is larger for low strain rates, but the differences are not very large. Moreover, the flame front location moves closer to the fuel nozzle when the strain rate is large. The flame front and stagnation plane locations have some important consequences on the flame structure: oxygen is supplied to the flame by both convection and diffusion, while the fuel is supplied mainly by diffusion. From Figure 76c the differences in the mole fractions of fuel and oxygen in the reaction zone are evident: the fuel is completely decomposed before reaching the flame front; on the contrary the oxygen is able to penetrate deeply in the fuel zone. The heat release profiles along the centerline are reported in Figure 76d. As expected, the maximum is located in the vicinity of the flame front.

Five different characteristic zones can be observed in the counter flow diffusion flames investigated, as reported in Figure 77 (which refers to Flame II). First of all the convective zones immediately close to the fuel and oxidizer nozzles are characterized by temperatures and main reactants concentrations nearly uniform. Two diffusive layers (in which the concentration of fuel and oxygen decreases rapidly from ~95% to ~5% values of the inlet streams) can be observed: their

width is inversely proportional to the strain rate. These diffusive layers are the main responsible of the characteristics of the response of the flame to the externally imposed oscillations. Finally the main reaction zone, which is located between the two diffusive layers, is characterized by a large heat release and high values of temperature. The flame front is roughly centered on this zone. The proposed representation of the flame is very useful to better understand the response of temperature and main species to the externally imposed oscillations. The main numerical results for the three flames investigated are summarized in Table 8.

Following Xiao *et al.* [139], PAHs were grouped in three classes. Class A includes one- and two-rings PAHs, Class B three- and four-rings PAHs and Class C PAHs with more than four rings. Figure 78 shows the mole fraction profiles of three different classes of PAH at different strain rates. As expected the PAHs are located on the fuel side of the flame. It is evident that increasing the strain rate, the peak values and the total amount of each class decrease; as clearly shown in Figure 78, the PAH sensitivity to the flame strain rate varies significantly among different classes. This result is not unexpected, since if the strain rate increases, the residence time is reduced

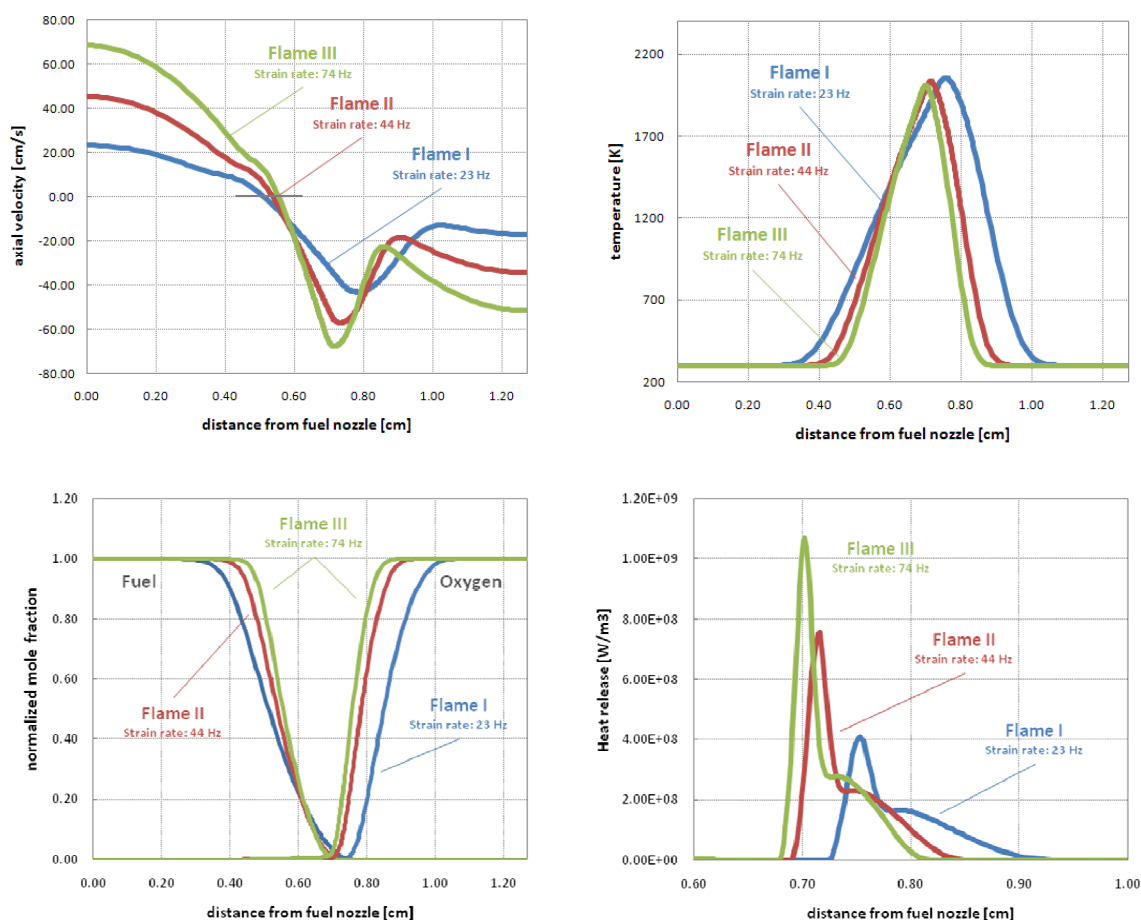


Figure 76. Comparison between the numerical results obtained for the flames fed with methane in steady state conditions: (a) Axial velocity profiles; (b) temperature profiles; (c) normalized (by their free stream values) mole fraction profiles of methane and oxygen; (d) heat release profiles along the centerline. All profiles are reported along the centerline.

and the flame temperature is lower: small PAHs are formed even at low residence times, but the successive formation of larger PAH would require more time.

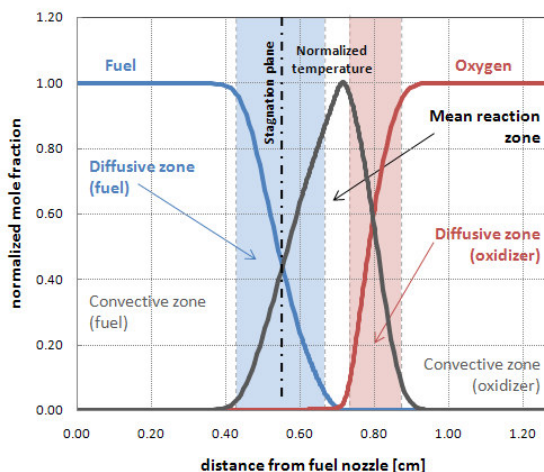


Figure 77. Mole fraction profiles of main reactants normalized by their free stream values and temperature profile normalized by its maximum value (methane flame, GSR=30 Hz).

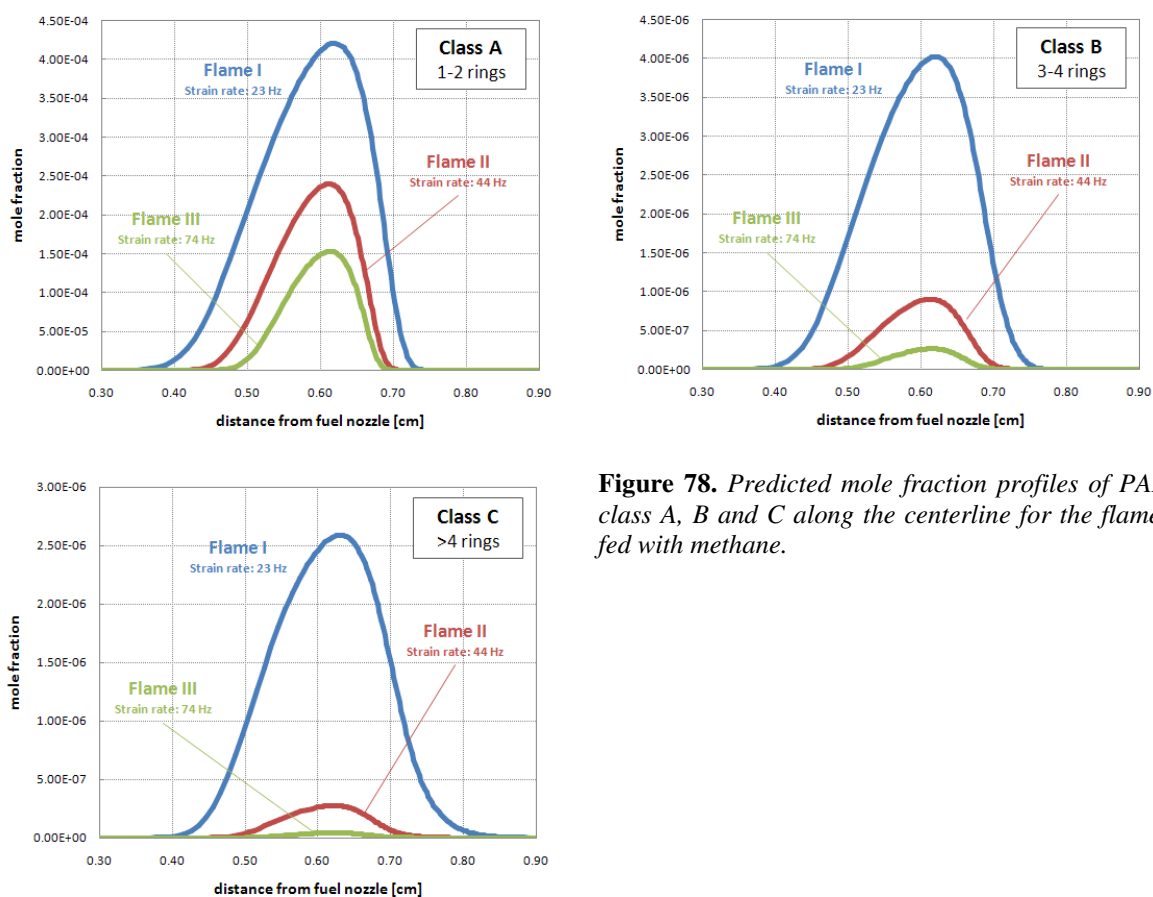


Figure 78. Predicted mole fraction profiles of PAH class A, B and C along the centerline for the flames fed with methane.

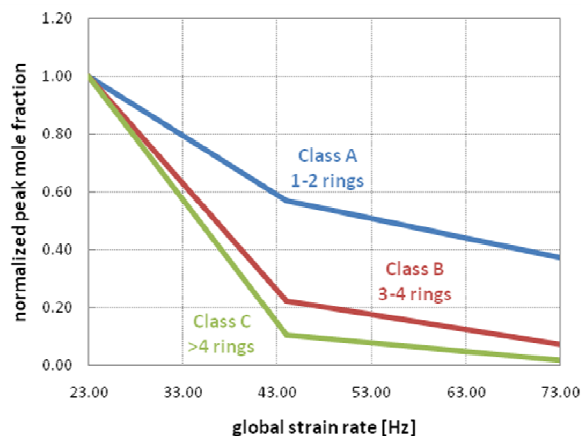


Figure 79. Predicted PAH peak values as a function of strain rate (normalized by the value at the lowest strain rate).

6.5.4 Unsteady Flame Results

Velocity unsteadiness has been introduced as previously explained at the exit of both nozzles, while the free-stream values of reactant concentrations and temperature were held fixed. Initially the system is in its steady state; at $t=0$ the velocities begin to fluctuate according to a sinusoidal function with frequency f and semi-amplitude A_u . In the present work the exit velocities from the fuel and oxidizer nozzles have the same semi-amplitude and oscillate in phase with one another. The position of the stagnation plane, which depends on the stream momenta, oscillates accordingly. In particular, when the inlet velocities increase, the stagnation plane tends to move towards the fuel nozzle. Several values of the frequencies of the imposed oscillations have been considered, ranging from 1Hz to 500Hz; different semi-amplitude oscillation values have been used, from 25% to 75% of the steady value of inlet velocities. In this way a wide range of conditions were taken into account to study the response of the flame.

In Figure 80 the numerical results obtained for Flame II are summarized in terms of temperature and PAH mole fraction peak values. The oscillation semi-amplitude was 50% of the steady value and different oscillation frequencies have been considered (1, 30, 100, 200 Hz). The results are reported as a function of a non dimensional time t' (which is obtained scaling the time t by the period of oscillations). Panel *d* of Figure 80 shows the variation of the maximum temperature induced by the oscillation of velocities of the streams. It is evident from the numerical results that the amplitude of the oscillations decreases when the imposed frequencies are higher. On the contrary the phase lag, which tends to zero for low values of the frequencies, becomes large when the frequencies are higher. The peak mole fraction of the smallest PAHs (Class A) is reported in the Panel b. The results are very similar to the temperature profile: when the frequencies are very large the phase lag between imposed oscillations and flame response is particularly high; on the contrary, when a low frequency is used to produce the oscillations of the fuel and oxidizer streams,

the induced oscillation amplitude of the PAH profiles is very large and the symmetry about the mean value is lost. However the phase lag is small, which indicates a quasi-steady response of the smallest PAHs in these conditions. For Class B and Class C the same observations can be repeated (Panels c and d of Figure 80). Moreover the maximum frequency for which the flame response can be considered quasi-steady becomes higher if compared to the smallest PAHs. These results are in agreement with experimental and numerical investigations performed by several authors [41, 139].

Figure 81 shows the detailed frequency response of the amplitudes of the maximum flame temperature and maximum mole fraction value for the three classes of PAHs. The steady state value of each variable, its mean value (which accounts for the oscillations) and its peak and trough values are reported as a function of the externally imposed frequency; the phase shift is also reported. Of course the results (referring to the same conditions) mirror those shown in Figure 80: in particular the amplitude of oscillations is largely reduced at higher frequencies, while at low frequencies the flame response to the changes in the inlet velocity value can be considered quasi-steady. The amplitude reduction (the difference between maximum and minimum values) occurs

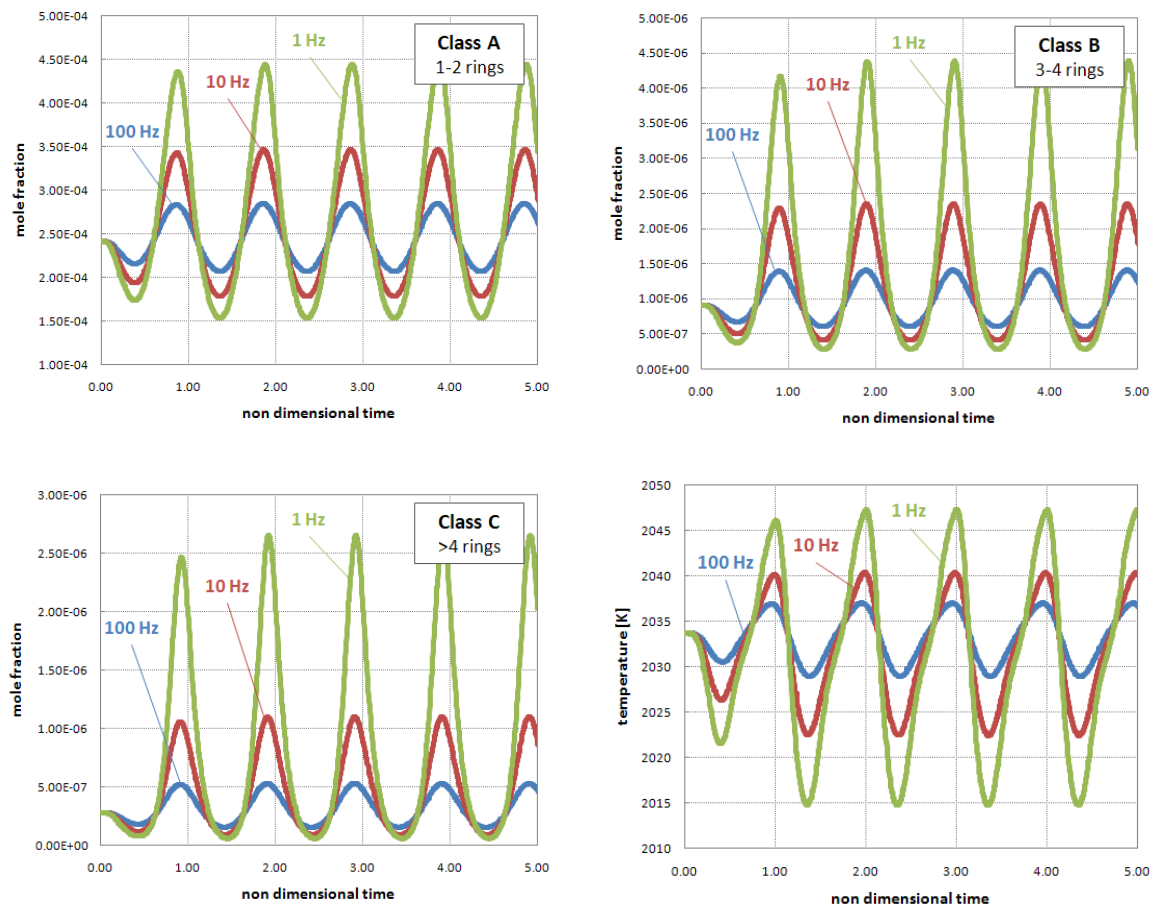


Figure 80. Flame II: peak values for each PAH class and maximum flame temperature at different frequencies, with non dimensional time $t' = \text{time}/\text{period}$. (a) Mole fraction peak value of Class A; (b) mole fraction peak value of Class B; (c) mole fraction peak value of Class C; (d) maximum temperature. The semi-amplitude of velocity oscillations is 50% of the steady value.

asymmetrically about the mean values, with the trough values increasing faster than the reduction of peak values. The non symmetrical behavior is particularly evident for low frequencies and for largest PAH. The phase shift is very small at low frequencies, but becomes large when the frequencies of induced oscillations are high. The most interesting result however is related to the difference between the steady value of each variable and the corresponding mean value, which accounts for the oscillations. It is evident that at low frequencies the mean value can be very large if compared to the steady state value (in particular for the largest PAHs); therefore the oscillations have a strong and non negligible effect on the formation of PAHs. When the frequency is higher the mean values tend to approach the steady value, but the flame response cannot be considered quasi-steady due to the large phase-lag.

The value of the observed amplitudes largely depends on the amplitude of the imposed oscillations in the inlet velocities. From the numerical results obtained at three different values of oscillation semi-amplitude (25%, 50% and 75%), which are reported in Figure 82, it is evident that larger externally imposed amplitudes increase the amplitude of the induced oscillations. Moreover, they lead to a larger asymmetry. On the contrary the phase lag can be considered independent on the amplitude of imposed oscillations.

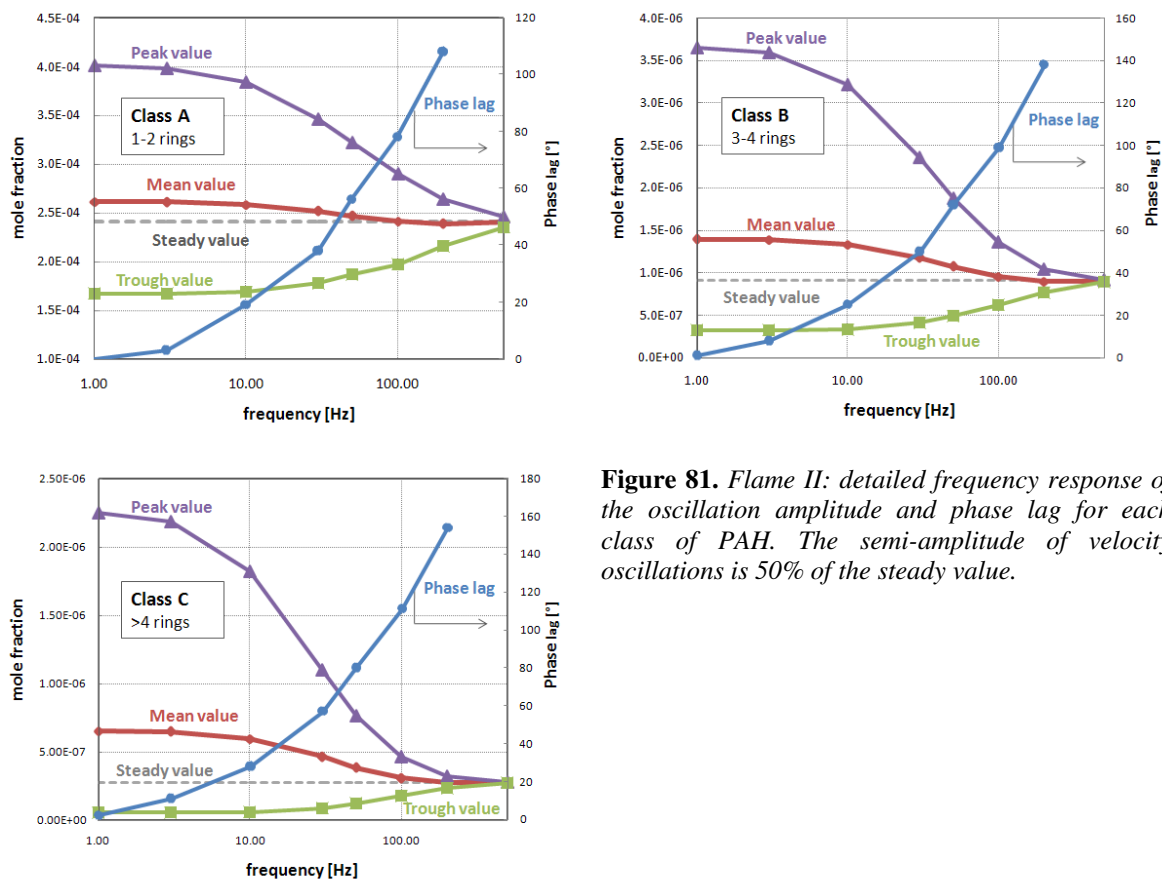


Figure 81. Flame II: detailed frequency response of the oscillation amplitude and phase lag for each class of PAH. The semi-amplitude of velocity oscillations is 50% of the steady value.

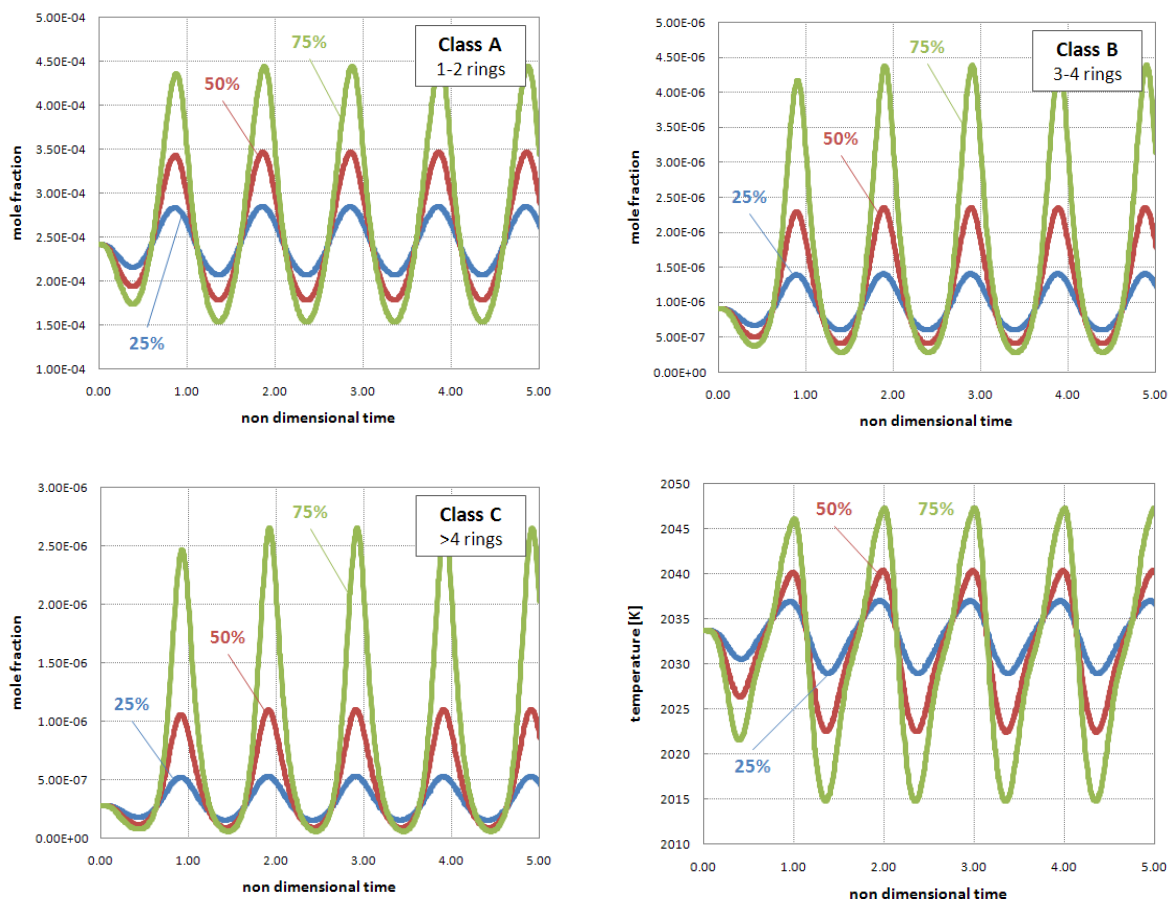


Figure 82. Flame II: peak values for each PAH class and maximum flame temperature at different oscillation semi-amplitude, with non dimensional time $t' = \text{time}/\text{period}$. (a) Mole fraction peak value of Class A; (b) mole fraction peak value of Class B; (c) mole fraction peak value of Class C; (d) maximum temperature. The frequency of velocity oscillations is 10 Hz.

The quasi-steady response at low frequencies can be explained by comparing the diffusion time in the flame structure with the oscillation time: in this case the diffusion time is smaller and therefore the response is quasi instantaneous. At higher frequencies the diffusion times can be larger than the oscillation time and therefore a phase lag can arise between the imposed oscillation and the flame response. The diffusion time is different for every chemical species and each species responds in a different way and the overall response of the flame can be very complex. At low frequencies the flame properties follow the externally imposed oscillations in a quasi-steady manner; however the amplitude of the oscillations are very large and the mean value of each variable can be very different from the corresponding steady-state value. On the contrary at higher frequencies a phase shift can be observed between the forced oscillations and the flame response, but the amplitude of these oscillations is largely reduced and the mean value of all properties asymptotically tends to the steady state value. Egolfopoulos and Campbell [41] offered an explanation of this phenomenon: the imposed oscillations in the hydrodynamic zone of the flame can reach the reaction zone only passing through a diffusion zone adjacent to the front flame.

During this passage the fluctuations are attenuated by diffusion. This is particular true for high frequencies, because in this case the length of this diffusion layer becomes of the same order or larger than the characteristic penetration length and therefore the attenuation effect should significantly influence the structure in the diffusive zone. At the same time, the phase lag can also be similarly explained: the main reaction zone responds with a time shift to the imposed oscillations because those oscillations pass through this diffusive zone. For higher frequencies this diffusive time becomes comparatively larger than the oscillation period and therefore a higher phase lag is shown.

Figure 83 shows the induced oscillations on the temperature and PAH mole fraction peak values for the three different flames investigated. The oscillation frequency and semi-amplitude are respectively 30 Hz and 50% of the steady value. Flame I, whose global strain rate is very low, shows the smallest amplitudes in the induced oscillations; on the contrary, the oscillation amplitude can be very large if the strain rate is large (Flame III). What previously observed allows to explain the results of Figure 81 too. If the global strain rate of the flame is low (Flame I), the diffusive layer

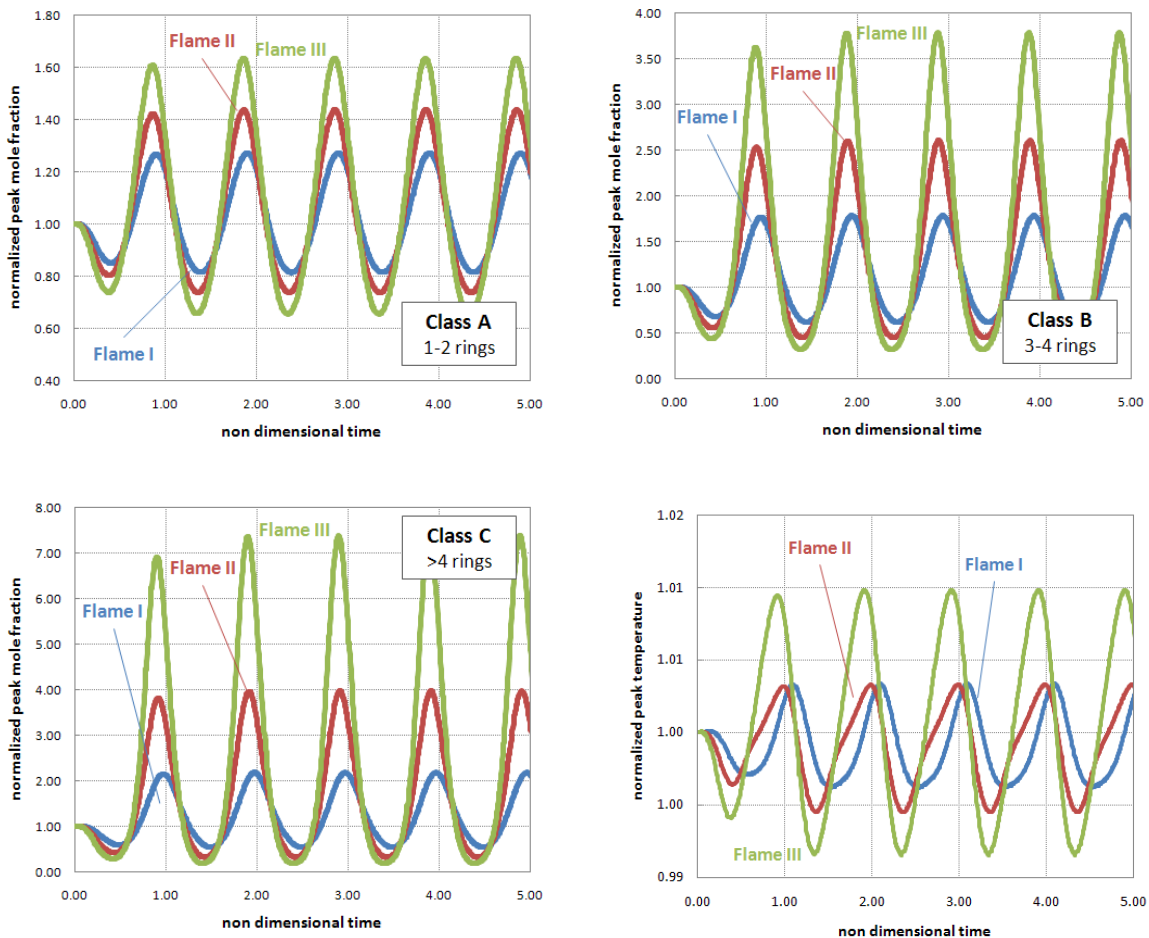


Figure 83. Variation of the maximum flame temperature and peak values for each PAH class at different frequencies, with non dimensional time $t' = \text{time}/\text{period}$. (a) Mole fraction peak value of Class A; (b) mole fraction peak value of Class B; (c) mole fraction peak value of Class C; (d) normalized maximum temperature. The semi-amplitude of velocity oscillations is 50% of the steady value.

thickness (see Table 8) is very large and therefore the oscillations are significantly damped: this is confirmed by the temperature and PAH mole fraction profiles. However, at the same time, the phase lag is larger because the oscillations have to propagate along a thicker diffusive layer. This phenomenon also explains why the temperature and mole fraction profile shapes are more different from a sinusoidal shape (corresponding to the externally imposed oscillations) for low strain rate flames than for high strain rates.

6.5.5 Stokes' number

The diffusion attenuates the oscillations in the reaction zone in a manner which is analogous to the velocity attenuation in Stokes' second problem, as reported by different authors [41, 139]. The introduction of the non-dimensional Stokes' number can be therefore very useful to better understand the frequency response of counter flow diffusion flames and to easily collect and organize the information obtained from the unsteady analysis proposed in this work. The Stokes' parameter is defined as:

$$\eta_K = \sqrt{\frac{\pi \cdot f}{K}} \quad (6.12)$$

where f is the frequency of imposed oscillations and K is the cycle mean strain rate. The Stokes' parameter is a non-dimensional number comparing the characteristic time of imposed oscillations, ($1/f$), with the characteristic time of diffusion phenomena in the flame, which can be approximated as $\sim 1/K$. As a consequence when the Stokes' parameter is low the diffusion time is lower than oscillation time and therefore a small phase-lag is expected between the imposed and induced oscillations. On the contrary, for higher values of Stokes' parameter the diffusion time becomes larger than oscillations time and large phase shifts in the flame response can be observed in the flame. Figure 84 shows the variation of the mole fraction peak value for each PAH class normalized by the corresponding quasi-steady value for each PAH Class against the Stokes' parameter. As expected, the amplitude of the oscillations is very small for large values of Stokes parameter, because of the strong diffusion phenomena which are able to damp the effects of imposed oscillations. The three curves have a similar shape and tend to collapse on each other. In particular it is possible to observe a rapid decrease of oscillations amplitudes for Stokes' number ~ 1 , for the three PAH classes. A similar result is reported in Figure 85, where the three curves refer to the three PAH classes and are plotted for Flame II. Therefore the Stokes' number can be considered a universal parameter able to describe the diffusion-limited frequency response of diffusion flames and therefore and it could be successfully used to summarize the results of the numerical investigations.

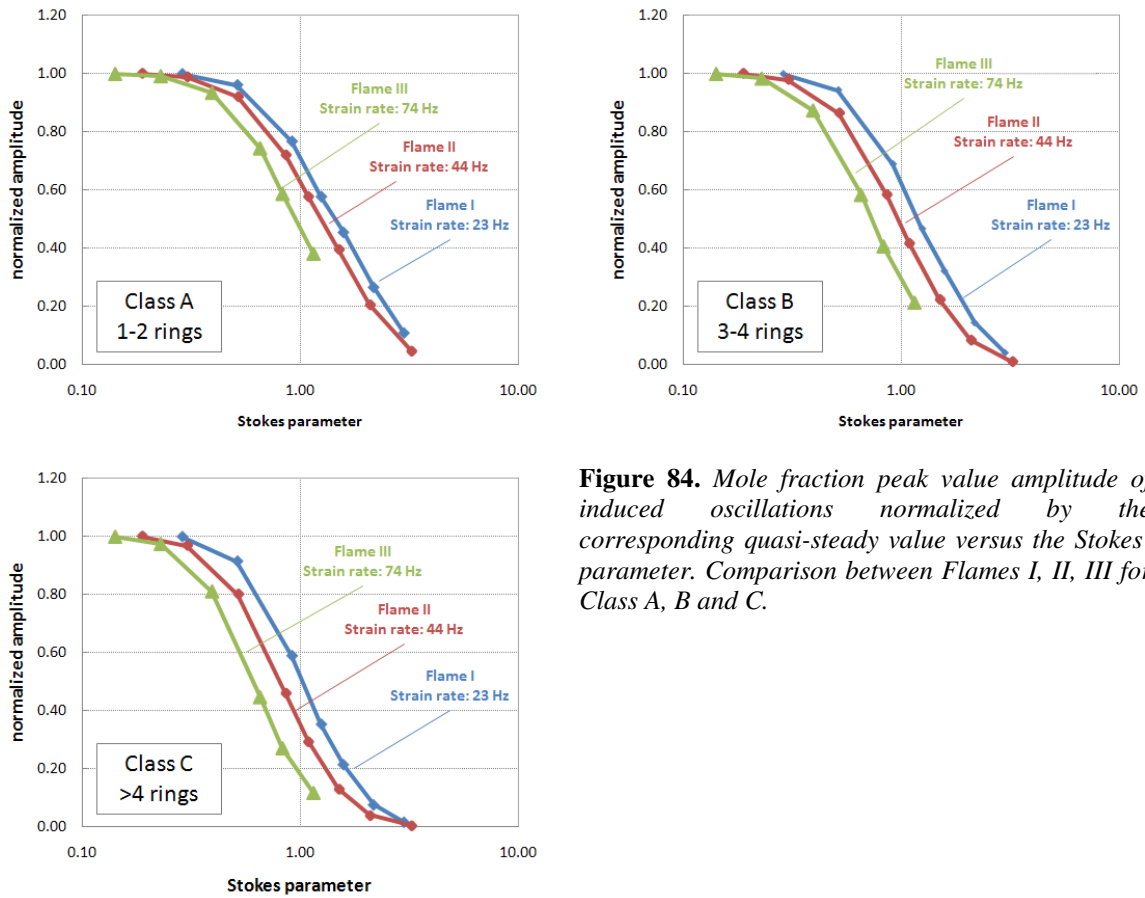


Figure 84. Mole fraction peak value amplitude of induced oscillations normalized by the corresponding quasi-steady value versus the Stokes' parameter. Comparison between Flames I, II, III for Class A, B and C.

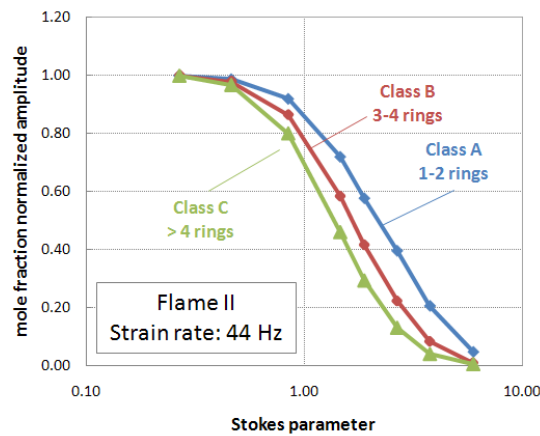


Figure 85. Mole fraction peak value amplitude of induced oscillations normalized by the corresponding quasi-steady value versus the Stokes' number. Comparison between Class A, B, C for Flame II.

6.5.6 Comparison with experimental measurements

Figure 86 shows the peak value of the mole fraction of each PAH class (normalized by the steady value) versus the Stokes' number. The results refer to the Flame II and externally imposed oscillations with semi-amplitude equal to the 70% of the steady value of the inlet velocities. The numerical results are compared with the experimental measurements obtained in the same conditions by Xiao *et al.* [139]. Both experimental and numerical results confirm the large amplitudes of oscillations for Class C, especially for low Stokes' numbers. As expected the ratio between the peak and the steady state values are larger when the Stokes number is small. The amplitude of the oscillations is strongly damped for large Stokes numbers (which mean high values of oscillation frequency). Figure 87 shows the detailed frequency response of Flame II (with externally imposed oscillations of 30Hz with semi-amplitude equal to the 70% of the steady value of the inlet velocities) in terms of peak value mole fraction of each PAH class (normalized by the steady value) versus a non dimensional time. The agreement can be considered satisfactory for the smallest PAH (Class A). On the contrary, the numerical results for larger PAH overestimate the experimental peak values. A possible explanation is suggested by the use in the present work of a reduced kinetic mechanism which accounts for small- and medium-size PAH formation, but neglects the successive formation of larger PAHs and soot. Therefore the largest PAHs in Figure 87 are not involved in successive reactions leading to their consumption and this could cause the overestimation of their concentration. Moreover if the radiative heat transfer (neglected in this work) were taken into account, a better agreement with experimental data would be expected, because of the smoother temperature oscillations. Of course further investigations are necessary to better understand the differences between experimental and numerical results. However the non symmetric behavior of oscillations respect to the steady value is caught by the numerical results.

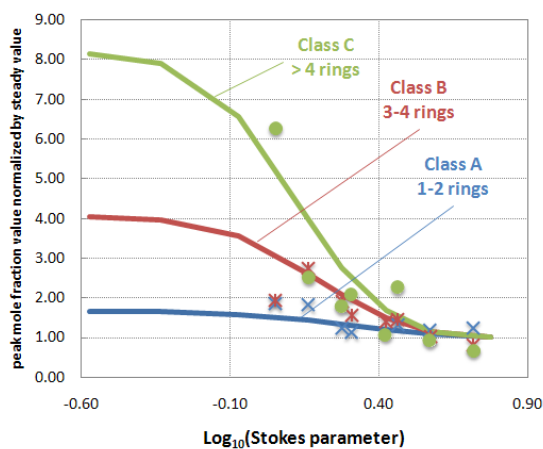


Figure 86. Normalized mole fraction peak values versus the Stokes number compared with experimental measurements [139] (Flame II, oscillation semi-amplitude 70% of the steady state value). The profiles are scaled by the steady state value.

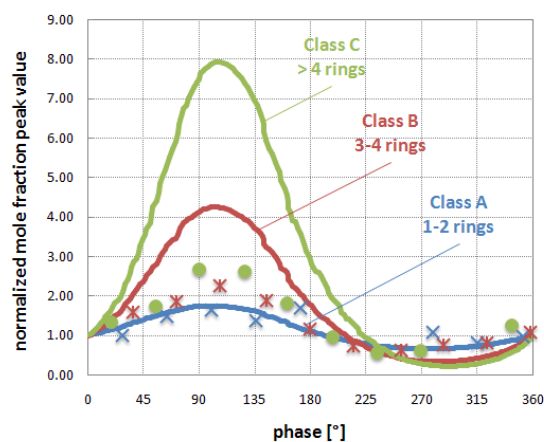


Figure 87. Normalized mole fraction peak values versus the non dimensional time (here expressed in $^{\circ}$) compared with experimental measurements [139] (Flame II, oscillation semi-amplitude 70% of the steady state value). The profiles are scaled by the steady state value.

6.6 Soot formation in unsteady counter flow diffusion flames

6.6.1 Flames Investigated

The counterflow diffusion flames numerically simulated in this section were experimentally investigated by Decroix *et al.* [37] and partially by Xiao *et al.* [139]. The oxidizer and the fuel nozzles are 25.4 mm in diameter and have a 12.7 mm separation distance. The inlet temperatures, both of fuel and air streams, are 294 K. A controlled oscillation was established in the reactant flow fields by driving two loudspeakers with a sine wave from an amplified signal generator. Three different fuels have been investigated (corresponding to different values of C/H ratio): methane, propane and ethylene. For each flame four different global strain rates (GSR) [139] have been considered: 15, 30, 60 and 90 Hz.

6.6.2 Kinetic Scheme

The kinetic scheme briefly described in Paragraph 6.5.2 was extended to soot formation using the discrete sectional method. PAHs larger than 20 C atoms and soot particles are divided into a limited number of classes covering certain mass ranges. Each class is represented by two or three lumped pseudo-species, called BIN, with a given number of carbon and hydrogen atoms. The general features of this approach were already presented and discussed recently [57, 112]. The soot formation process can be described in terms of three major steps: homogeneous nucleation of particles, particle surface reactions and finally particle coagulation. The resulting kinetic scheme involves 253 species in ~14,000 reactions. The general features of this approach were recently presented and discussed [57, 112].

The thermo-chemical information on the gas phase is obtained primarily from the CHEMKIN thermodynamic database [71]. Unavailable thermodynamic data are estimated by the group additivity method.

6.6.3 Steady Flame Results

The flames are located on the oxidizer side of the stagnation plane, as evident from Figure 77. The flame front and stagnation plane locations have some important consequences on the flame structure: oxygen is supplied to the flame by both convection and diffusion, while the fuel is supplied mainly by diffusion. Therefore the fuel is completely decomposed before reaching the flame front. On the contrary the oxygen is able to penetrate deeply in the fuel zone. After inception on the fuel side, soot particles are convected away from the flame toward the stagnation plane. As a consequence soot oxidation is absent. Two diffusive layers (in which the concentration of fuel and oxygen decreases rapidly from ~95% to ~5% values of the inlet streams) can be observed, whose thickness is inversely proportional to the strain rate. These diffusive layers are the main responsible of the characteristics of the flame response to the externally imposed oscillations.

Figure 88 compares the normalized axial profiles of OH and soot of a propane-air flame at the strain rate of 15 Hz with the experimental profiles obtained by Decroix *et al.* [37]. The numerical results correctly predict the location of the flame front (which corresponds to the peak value in the OH profile) and of the soot region, which is located on the fuel side of the flame. The width of the sooty zone is well matched too.

Figure 89 compares the predicted maximum soot volume fraction of the three investigated fuels with the experimental data [37] as a function of the global strain rate. The soot volume fraction decreases with the global strain rate, which is inversely proportional to the characteristic residence time. As evident, the soot volume fraction is a strong function of the fuel type (C/H ratio) and is larger for ethylene (see Figure 90). Moreover, at low strain rates the soot production is more sensitive to the strain rate. The agreement with the experimental measurements can be considered satisfactory for ethylene and propane, even if the numerical results slightly overestimate the peak soot volume fraction. On the contrary the model under-predicts the soot formation of the methane flame for a strain rate equal to 15 Hz (which is the only experimental data available). A partial explanation refers to the uncertainties in the measurements of velocities at low strain rates, which strongly affect the soot production [37].

The thickness of the soot containing region, measured in the axial direction, is reported in Figure 91 and compared with the experimental measurements (which refer to the propane-air flame). Both the numerical and experimental results confirm that the thickness of the soot region is independent of the fuel type, implying that it is only a function of the hydrodynamics. In particular the thickness of the soot region linearly decreases with the square root of the strain rate. At each

strain rate investigated, the width of the soot containing region is almost identical, even if the soot volume fractions from the ethylene and methane flames are very different (more than two or three orders of magnitude). These observations are relatively easy to explain. The propane flames investigated in this section are always balanced, i.e. the momentum of air and fuel stream is the same. As a consequence, for each assigned global strain rate, the stagnation plane and maximum temperature locations are roughly the same for the different fuels. The fluid dynamics of these flames can be considered very similar, even if the fuels are not the same; therefore we expect that the sooting zone location and its main features are not so strongly dependent on the fuel type. On the contrary the total amount of soot is obviously a strong function of the characteristics of fuel and, as expected and confirmed by experimental and numerical results, is larger for fuels with larger C/H ratio.

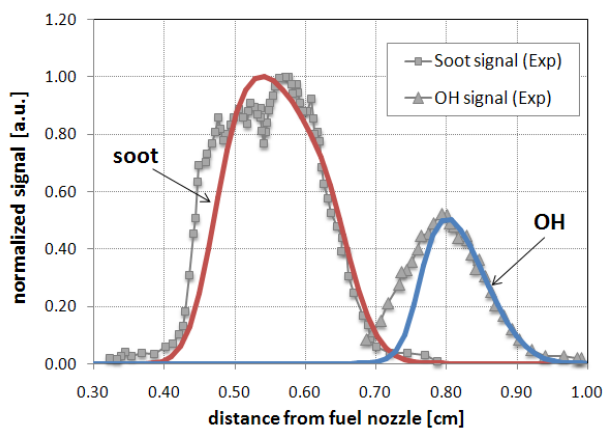


Figure 88. Comparison between predicted and experimental [37] profiles of OH and soot (propane flame, GSR=15 Hz). The profiles are reported in arbitrary units.

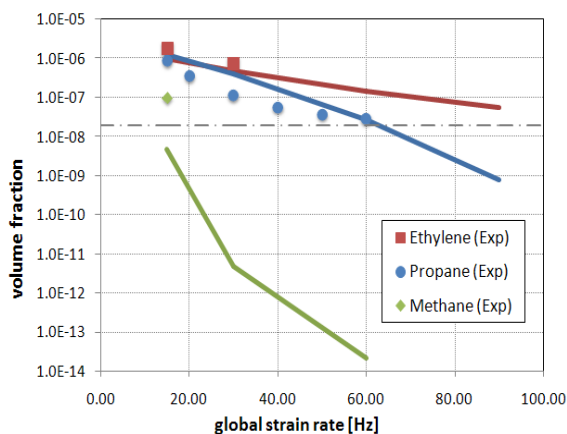


Figure 89. Peak soot volume fraction versus the global strain rate. The lines refer to the numerical results, while the points are the experimental measurements reported in [37]. The dotted line indicates the minimum experimental amount of detectable soot.

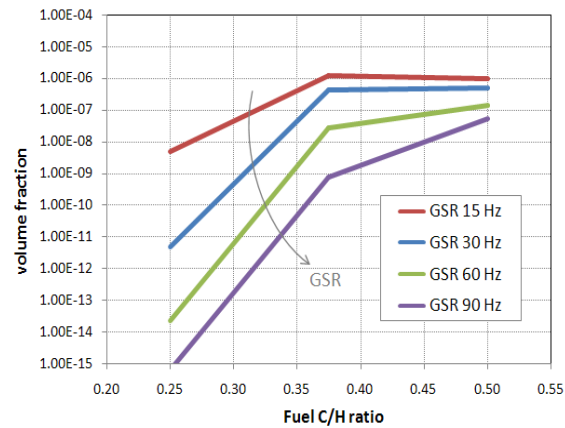


Figure 90. Peak soot volume fraction versus the fuel C/H ratio at different values of GSR for the flames fed with propane.

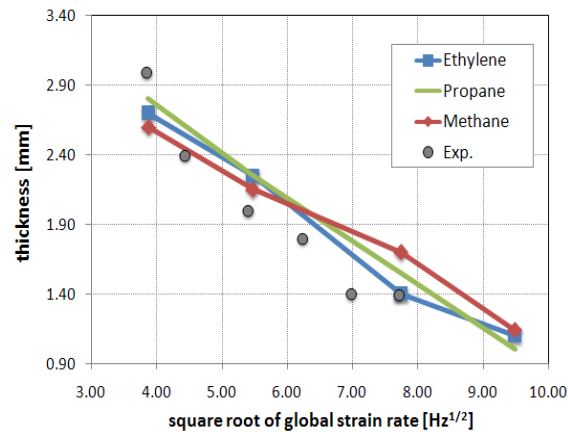


Figure 91. Thickness of the soot region versus the square root of strain rate. The lines refer to the predicted results, while the points are the experimental measurements reported in [37].

6.6.4 Unsteady Flame Results

Velocity unsteadiness was introduced as previously explained at the exit of both nozzles, while the free-stream values of reactant concentrations and temperature were held fixed. Initially the system is in its steady state; at $t=0$ the velocities of fuel and air streams begin to fluctuate according to a sinusoidal function with frequency f and semi-amplitude A_u .

Figure 92 summarizes the numerical results obtained for the flame fed with propane in terms of PAH mole fraction and soot volume fraction peak values. The results are reported as a function of a non dimensional time t' , which is obtained scaling the time t by the period of oscillations. The amplitude of the induced oscillations of PAH and soot is strongly influenced by the frequency of the imposed oscillations. In particular the amplitude of the induced oscillations becomes very large at low frequencies and tends to rapidly decrease when the imposed frequencies

are larger. Moreover the symmetry of the soot volume fraction profile about the mean value is lost at low frequencies. As expected, the phase lag between the imposed oscillations in the velocity field and the induced oscillations in the composition fields tends to zero for low values of the frequencies, but becomes large when the frequencies are higher. However, for the same oscillation frequency, the phase lag is larger for soot than for PAH (see maximum position in Figure 92). Therefore only for very low oscillation frequencies the response of the flame in terms of PAH and soot can be considered quasi-steady. The maximum frequency for which the flame response is quasi-steady becomes larger for PAHs. These results are in agreement with recent experimental and numerical investigations [41, 139].

Figure 93 shows the detailed frequency response of soot to the imposed oscillations. The steady state value, the peak and trough values and the mean value (which accounts for the oscillations) of soot volume fraction are reported as a function of the externally imposed frequency together with the phase shift. Of course these results (which refer to the same conditions) mirror those shown in Figure 92. The amplitude of the oscillations is largely reduced at higher frequencies, while at low frequencies the flame response to the changes in the inlet velocity value can be considered quasi-steady. The amplitude reduction (the difference between maximum and minimum values) occurs asymmetrically about the mean values. This non symmetrical behavior is particularly evident at low frequencies. The main effect of oscillations is an increase in soot production. When the frequency is large the mean values tend to approach the steady value (and therefore the unsteady effects are less important), but the flame response cannot be considered quasi-steady because of the large phase-lag.

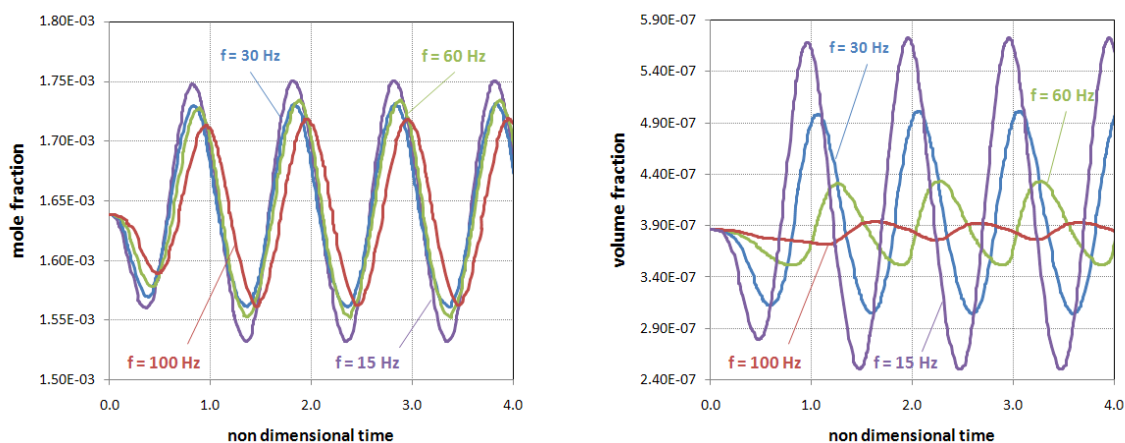


Figure 92. Peak values of PAH mole fraction (a) and soot volume fraction (b) at different oscillation frequencies (propane flame, $GSR=60$ Hz, $A_u=60\%$).

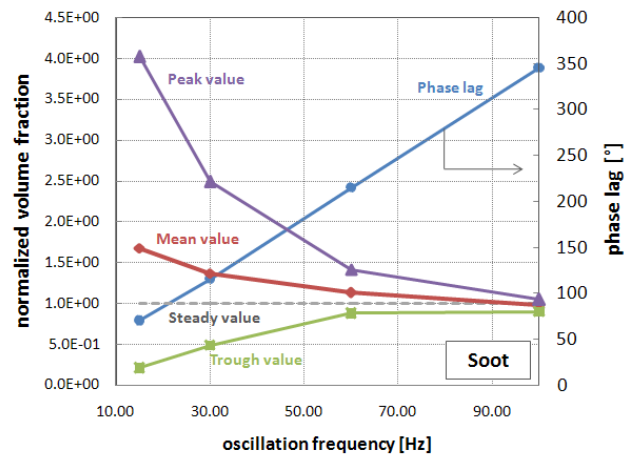


Figure 93. Detailed frequency response of the oscillation amplitude and phase lag of soot (propane flame, $GSR=60$ Hz, $Au=60\%$).

The flame response can be explained by comparing the diffusion time in the flame structure with the oscillation time. At low frequencies the diffusion time is small and therefore the response is quasi-instantaneous. At higher frequencies the diffusion time becomes larger than the oscillation time and therefore a phase lag arises between the imposed and induced oscillations. At low frequencies, even if the flame follows the externally imposed oscillations in a quasi-steady manner, the amplitude of the oscillations is very large and the mean value of each variable can be very different from the corresponding steady-state value. On the contrary, at higher frequencies the amplitude of induced oscillations is largely reduced and the mean value of all properties asymptotically approaches the steady state value. The imposed oscillations in the hydrodynamic zone of the flame can reach the reaction zone only passing through a diffusion zone adjacent to the flame front [41]. During this passage the fluctuations are attenuated by the diffusion, especially at high frequencies, because in this case the thickness of this diffusion layer becomes larger than the characteristic penetration length. Therefore the attenuation effect significantly influences the structure in the diffusive zone. The phase lag can be explained in a similar way: the main reaction zone responds with a time shift to the imposed oscillations because those oscillations pass through this diffusive zone. For higher frequencies this diffusive time becomes comparatively larger than the oscillation period and therefore a higher phase lag occurs. The overall response of the flame can be very complex because the diffusion time is different for every chemical species and therefore each species responds in a different way.

The value of the observed amplitudes largely depends on the amplitude of the imposed oscillations of the inlet velocities. From the numerical results obtained at different values of oscillation semi-amplitude and shown in Figure 94, it is evident that larger externally imposed amplitudes not only increase the amplitude of the induced oscillations, but also lead to a larger

asymmetry about the steady state value. However the phase lag can be considered independent of the imposed oscillation amplitude.

Figure 95 shows the induced oscillations on the PAH mole fraction and soot volume fraction peak values for the propane flame at different steady-state strain rates. The flame corresponding to the lowest global strain rate (30 Hz) shows the smallest amplitudes in the induced oscillations. If the global strain rate of the flame is low, the diffusive layer thickness is large and therefore the oscillations are significantly damped. However, at the same time, the phase lag is larger because the oscillations have to propagate along a thicker diffusive layer. This phenomenon also explains why the profile shapes of PAH and soot oscillations are more different from the imposed sinusoidal shape, especially for soot.

Table 9 summarizes the results obtained from the numerical simulations of the propane-air flame. For each flame the ratio between the mean peak soot volume fraction calculated during the oscillations and the peak value calculated in the same flame in steady state conditions is reported. Soot production, as already observed, becomes insensitive to high frequency oscillations ($\geq 100\text{Hz}$),

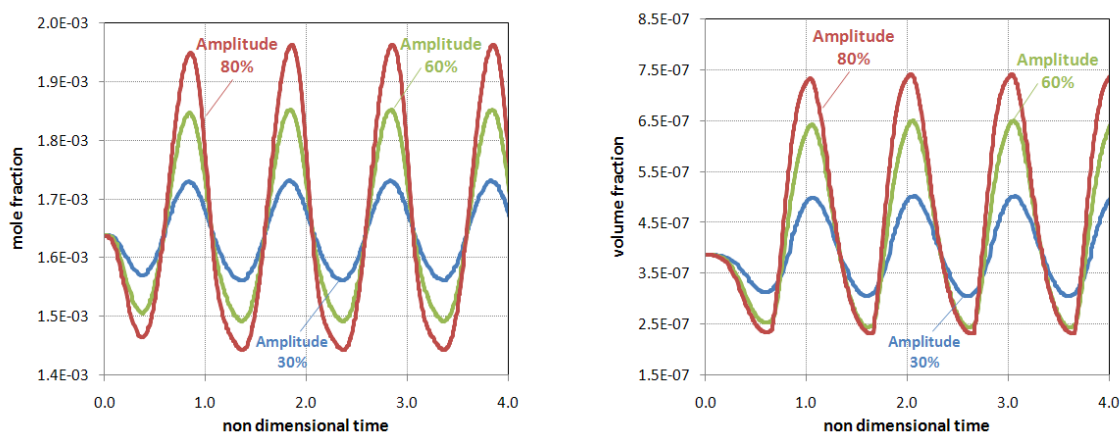


Figure 94. Peak values of PAH mole fraction (a) and soot volume fraction (b) at different amplitudes of oscillations (propane flame, $\text{GSR}=60\text{ Hz}$, $f=30\text{ Hz}$).

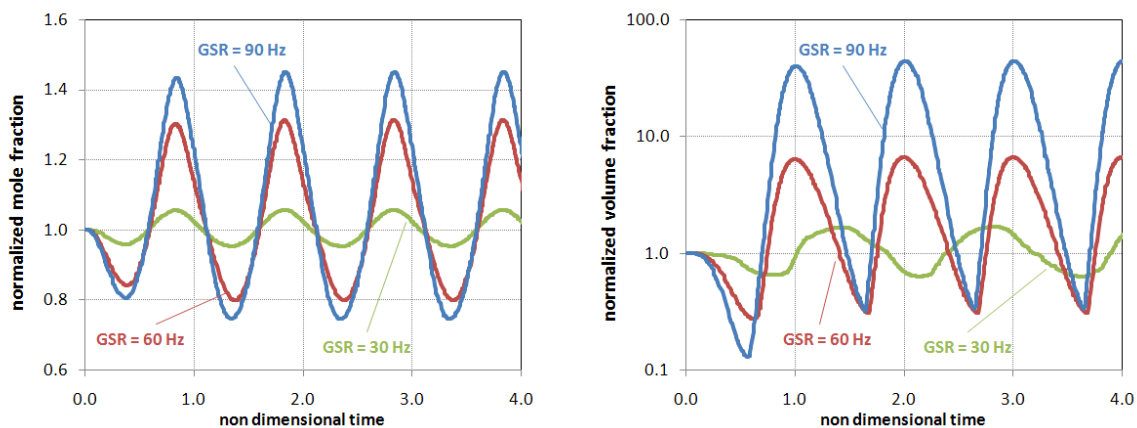


Figure 95. Peak values of (a) PAH mole fraction and (b) soot volume fraction for different global strain rates (propane flame, $A_{ii}=60\%$, $f=30\text{ Hz}$). The lines are normalized by the steady state value.

<i>Frequency</i> (Hz)	<i>SR 30Hz</i>		<i>SR 60Hz</i>		<i>SR 90Hz</i>	
	$A_u=30\%$	$A_u=60\%$	$A_u=30\%$	$A_u=60\%$	$A_u=30\%$	$A_u=60\%$
15	1.04	1.20	1.70	4.13	4.60	36.10
30	1.04	1.17	1.41	2.70	2.50	14.00
60	1.01	1.03	1.12	1.55	1.37	3.30
100	~1.00	~1.00	~1.00	1.02	1.13	1.65

Table 9. Mean of peak soot volume fraction for unsteady propane flames normalized to the peak soot volume fraction for the steady flame.

especially when the strain rate of the flame is low. Low frequency oscillations, in particular 15Hz, significantly increase the soot concentration. Decroix *et al.* [37] and Shaddix *et al.* [120] also discussed the increase of the maximum soot volume fraction in their unsteady flames compared with the corresponding unforced flames for different kinds of fuels. Unfortunately a direct comparison between the numerical simulations performed in this thesis and the experimental measurements obtained by Decroix *et al.* [37] is not possible. In fact, due to the large amplitude of the oscillations used in this experimental work, the inlet velocities approached zero and in some cases reached negative values, indicating the presence of a reversal flow. Such conditions induce strong deformations in the flame structure that cannot be numerically simulated with the 1-D model used in the present thesis. However the main trends are in agreement with the experimental measurements.

The influence of unsteady hydrodynamics on soot chemistry can be further investigated by comparing the soot profiles at different temporal positions. Figure 96 shows the soot volume fraction profiles at four different temporal locations, compared with the corresponding profile obtained in steady state conditions. The four different temporal positions correspond to: maximum velocity (steady + fluctuation component, designated as Max), zero fluctuation and decreasing velocity (0-), minimum velocity (steady – fluctuation component, Min) and zero fluctuation and increasing velocity (0+). Even if the mean value of the soot peak volume fraction is only 2.70 times larger in unsteady conditions (see Table 9), unsteadiness strongly modifies the soot region shape during the oscillations. Hence the unsteady flow field does in fact have a strong impact not only on the maximum and mean soot volume fraction, but also on the whole soot formation process.

Figure 97 shows the profiles (normalized between -1 and 1) of peak temperature, PAH mole fraction and soot volume fraction versus the non dimensional time for the propane flame. As evident, the temperature field is not in phase with the velocity field. For a quasi-instantaneous response, the minimum temperature should correspond to the maximum velocity location (minimum residence time). On the contrary the minimum temperature occurs with a phase shift of $\sim 87^\circ$. Moreover the minimum soot volume fraction should occur at the maximum velocity. On the

contrary this minimum is found between the 0- and Min temporal positions. In particular the calculated phase shift between the minimum soot volume fraction in the oscillation and the maximum velocity is $\sim 118^\circ$. The maximum PAH mole fraction occurs between the Max and 0- locations. As a consequence the phase lag between the maximum PAH and maximum soot concentrations is $\sim 290^\circ$. These numerical results are in good agreement with the experimental measurements performed by Santoianni *et al.* [117] on the same flame and summarized in Table 10.

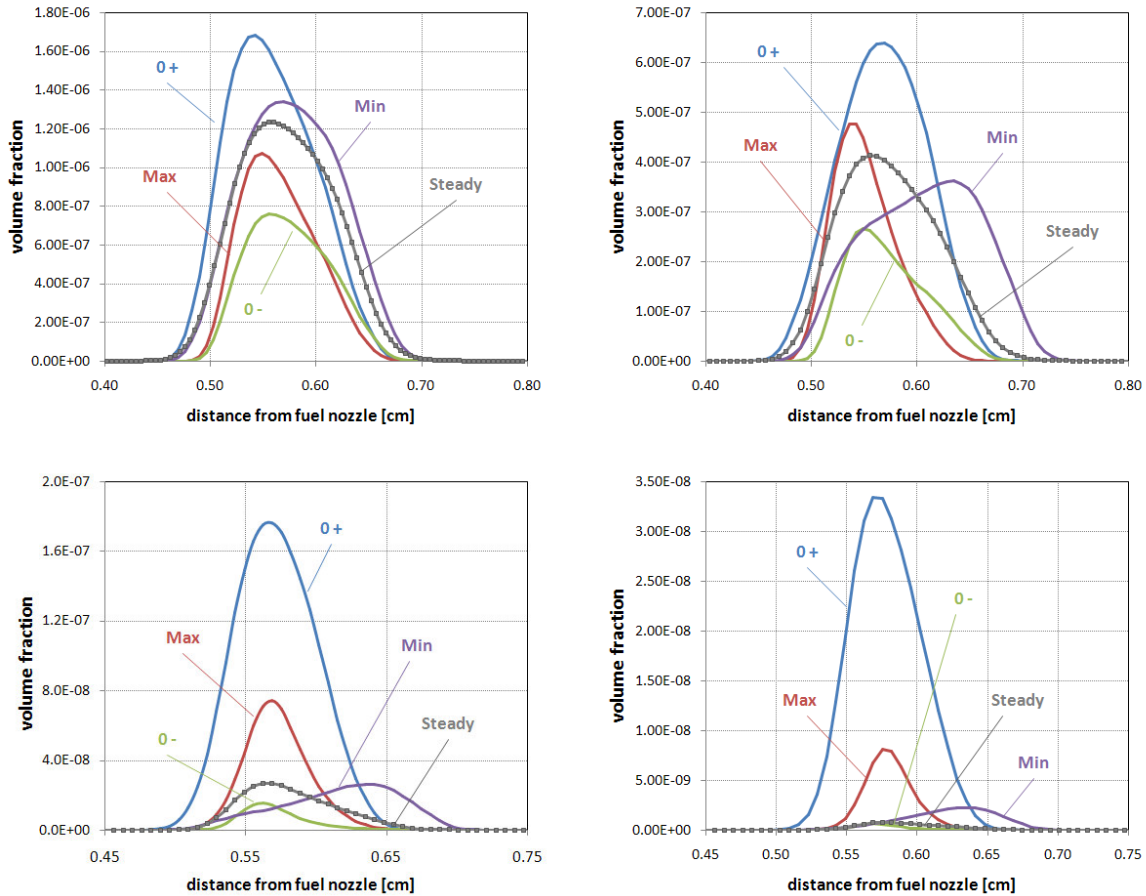


Figure 96. Soot volume fraction profiles in steady-state conditions and at different temporal locations (propane flame, $GSR=60$ Hz, $A_u=60\%$, $f=30$ Hz).

Phase lag	Exp.	Num.
Max velocity – Min temp.	$\sim 90^\circ$	$\sim 87^\circ$
Max velocity – Min Soot	$\sim 125^\circ$	$\sim 118^\circ$
Max PAH – Max Soot	$\sim 270^\circ$	$\sim 290^\circ$

Table 10. Experimental [117] and numerical phase shifts (propane flame, $A_u=60\%$, $f=25$ Hz).

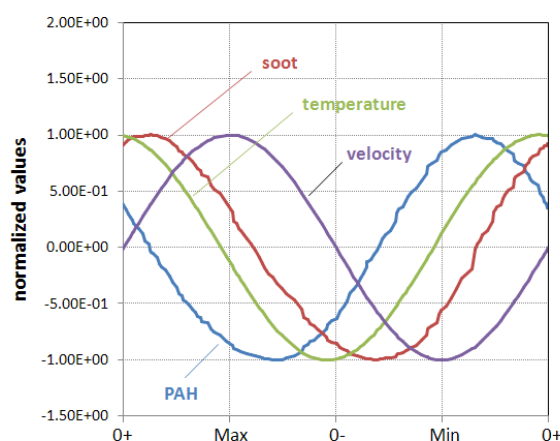


Figure 97. Normalized profiles of inlet velocities, peak temperature, peak PAH mole fraction and peak soot volume fraction values (propane flame, $A_u=30\%$, $f=30$ Hz).

6.7 Conclusions

The effects of strain rate fluctuations on the formation of soot and its precursors (PAH) were numerically investigated in unsteady counterflow diffusion flames. The transport equations governing the dynamic behavior of the flame were numerically solved using a very detailed kinetic scheme and an accurate description of the transport properties.

Several counterflow diffusion flames fed with methane, propane and ethylene were studied, starting from steady-state conditions. The results obtained in steady state conditions confirmed the different propensity to soot formation of the three fuels investigated and the strong effects of the global strain rate on the soot production. The quantitative and qualitative comparisons with experimental measurements were satisfactory, especially for propane flames.

The results obtained from unsteady flames fed with methane confirm the experimental observations obtained by several authors in similar conditions: the smaller PAHs respond in a quasi-steady manner to the instantaneous strain rate at higher frequencies. At high oscillation frequency the large PAHs do not appreciably respond to the fast strain rate fluctuations. Sinusoidal responses, also for large PAHs, can be observed for low or intermediate oscillation frequencies in the instantaneous strain rate. Moreover, the response of the larger PAHs to the frequency changes is much damped and the response of the smallest PAHs is the least damped. For low frequency oscillations and high strain rates the PAH production is largely increased in comparison with the steady flame: this is particularly true for largest PAHs. On the contrary the PAH production becomes insensitive at higher frequencies oscillations. The quantitative agreement with experimental measurements in terms of amplitude of PAH mole fraction oscillations is not completely satisfactory and therefore further investigations are necessary.

The frequency response to externally imposed strain rate harmonic oscillations was successively investigated for the propane flame, in a wide range of conditions. The numerical results confirmed the experimental observations: the oscillations tend to increase the soot production with respect to the steady state conditions. However, the response of the flame can be very complex, depending on the frequency of the imposed oscillations and the initial strain rate. In particular when the imposed frequency is large, PAH and soot do not appreciably respond to the fast strain rate fluctuations. On the contrary, sinusoidal responses can be observed for low or intermediate oscillation frequencies in the instantaneous strain rate. Moreover, the response of soot to the frequency changes is more damped than PAH response, due to the different characteristic chemical times. At low oscillation frequencies and high strain rates the soot production is largely increased in comparison with the steady flame. Fluctuations can strongly affect the spatial distribution of soot within the flame, without changing the maximum soot volume fraction.

Conclusions

The present thesis was mainly focused on the problem of the numerical modelling of interactions between turbulence and chemistry and their effects on the formation of pollutant species in turbulent combustion. The study of turbulent non premixed flames was carried out and the performances of a number of models for turbulence (based on the RANS approach) and turbulence-chemistry interaction were compared, analysed and discussed.

In order to reduce the numerical difficulties related to the simulation of the turbulent motions and minimize the calculation times, axisymmetric, turbulent jet flames were chosen for comparing the different combustion models and analysing how the turbulent fluctuations affect the formation of chemical species. Even for simple jet flames the correct choice of the turbulence model in the context of RANS simulations resulted very important. In particular the application of the so called κ - ϵ realizable model was found the best solution for the correct prediction of the spreading of round jets. As far as the modelling of chemical reaction is concerned, the simulations showed that the assumptions of chemical equilibrium or very fast chemistry are often unsuitable, even for the prediction of temperature and main species. It was evident that the combustion model should allow to take into account finite rate effects and detailed kinetics. The EDC and SLF models were found a good compromise between accuracy and computational time requests. The predictions of temperature and main species in the flames investigated resulted satisfactory. However the SLF and EDC models are not able to correctly predict the formation of pollutant species whose chemistry is characterized by slow times, like nitrogen oxides (NO_x) and soot.

In order to obtain reliable predictions of pollutant emissions from turbulent flames, several approaches were proposed, specifically conceived for each class of pollutant species. A kinetic post-processing procedure (KinPP) was formulated and applied for the numerical prediction of nitrogen oxides emissions from industrial burners. This approach facilitates and makes possible the predictions of NO_x formation with detailed chemistry even in complex geometries. The results of

the NO formation and reduction are promising and the agreement between computations and experiments is satisfactory. The successful prediction of flame structures and NO_x formation supports the proposed approach for the kinetic post-processor. The `KinPP` code already is a very useful tool for the optimal design of new burners with a particular attention to pollutants formation. Prediction of formation of other by-products in turbulent diffusion flames will be the natural extension and application of this tool. A further step in the study is to investigate the detailed effects of the chemical mechanisms. This detailed knowledge will be useful in developing improved combustion devices, such as low-NO wood stoves and waste incinerators.

The formation of carbonaceous particulate (soot) in turbulent flames was numerically investigated as well. Since the interactions between turbulent mixing and soot chemistry are very strong and complex, the attention was shifted from the detailed kinetics to the correct modeling of effects of turbulence on the formation rates of soot particles. Several closure models and strategies for describing the interactions between soot and turbulent mixing were formulated and applied to jet flames fed with ethylene. The model included all the main processes involved in soot formation (nucleation, molecular growth, oxidation and coagulation) through semi-empirical models available in literature. Such kinetic schemes allowed to describe the evolution of soot volume fraction quite accurately, despite their simplicity. Neglecting the effects of turbulent fluctuations of both temperature and composition on the soot source terms resulted in the over-prediction of the soot volume fraction. Only when the interactions between soot chemistry and turbulent mixing were accurately taken into account through the so called *uncorrelated approach*, a satisfactory agreement with the experimental measurements was achieved. The Direct Quadrature Method of Moments was applied in order to remove the hypothesis of monodispersed soot particle distribution, without dramatically increasing the computational time. The agreement with the experimental data was improved by the application of the DQMOM, but only when the effects of turbulence were directly taken into account in the DQMOM formulation. Moreover, the simulations confirmed that the coupling between the soot production rate and the radiative heat loss must be carefully taken into account to accurately model the formation of soot. The predicted soot amount in the turbulent flame was found to be relatively insensitive to the semi-empirical model adopted for describing the nucleation process. A deeper sensitivity analysis to the growth, oxidation and coagulation models could be very useful in a future work to investigate the role of individual soot formation rates to determine the optimal parameters for the semi-empirical soot models that can be used in the simulation of turbulent non-premixed flames.

The effects of turbulence on PAH and soot chemistry were further investigated without recurring to turbulent non premixed flames, which are reactive systems complex to numerically

model and characterized by the existence of many coupled phenomena. Opposed counter-flow diffusion flames (CFDF), which possess much of the physics of turbulent flames, were exposed to harmonic oscillations of the strain rate in order to simulate turbulent fluctuations and their effects on the formation of pollutant species. The numerical analyses were conducted on flames fed with methane, propane and ethylene. The response of the flame to the strain rate oscillations appeared very complex, depending on the ratio between the characteristic time of the imposed oscillations and the characteristic time of each individual chemical species. Strain rate fluctuations strongly affect the spatial distribution of PAH and soot within the flame. The oscillations tend to increase the PAH and soot production with respect to the steady state conditions. In particular, when the imposed frequency is large, PAH and soot do not appreciably respond to the fast strain rate fluctuations. At low oscillation frequencies and high strain rates the soot production is largely increased in comparison with the steady flame. The introduction of the non-dimensional Stokes' number was very useful for better understanding the diffusion-limited frequency response of counter flow diffusion flames and to easily collect and organize the information obtained from the unsteady analysis. The qualitative and quantitative agreement with experimental measurements was satisfactory, but further investigations are necessary to make this methodology more reliable.

References

1. Adams, B. R. and P. J. Smith, *Modeling effects of soot on radiative transfer in turbulent gaseous combustion*, Spring meeting of the Western States Section / The Combustion Institute, 1993, Paper 93S-24.
2. Adams, B. R. and P. J. Smith, *Modeling effects of soot and turbulence-radiation coupling on radiative transfer in turbulent gaseous combustion*, *Combustion Science and Technology* **109** (1995), 121-140.
3. Aksit, I. M. and J. B. Moss, *A hybrid scalar model for sooting turbulent flames*, *Combustion and Flame* **145** (2006), 231-244.
4. Bai, X. S., B. M., F. Mauss and F. L., *Detailed soot modeling in turbulent jet diffusion flames*, Twenty-Seventh Symposium (International) on Combustion, The Combustion Institute, 1998, p. 1623-1630.
5. Bardina, J., J. H. Ferziger and W. C. Reynolds, *Improved subgrid models for large eddy simulation*, AIAA Paper **80** (1980), 1357-1366.
6. Barlow, R. S. and J. Y. Chen, *On transient flamelets and their relationship to turbulent methane-air jet flames*, Twenty-Fourth Symposium (International) on Combustion, The Combustion Institute, 1992, p. 231-237.
7. Barlow, R. S., G. J. Fiechtner, C. D. Carter and J. Y. Chen, *Experiments on the scalar structure of turbulent CO/H₂/N₂ jet flames*, *Combustion and Flame* **120** (2000), 549-569.
8. Barlow, R. S., G. J. Fiechtner, C. D. Carter and J. Y. Chen, *Sandia/ETH-Zurich CO/H₂/N₂ Flame Data - Release 1.1*, www.ca.sandia.gov/TNF, Sandia National Laboratories (2002).
9. Barlow, R. S., A. N. Karpetis, J. H. Frank and J. Y. Chen, *Scalar profiles and NO formation in laminar opposed-flow partially premixed methane/air flames*, *Combustion and Flame* **127** (1998), 2102-2118.

10. Barlow, R. S., N. S. A. Smith, J. Y. Chen and R. W. Bilger, *Nitric Oxide Formation in Dilute Hydrogen Jet Flames: Isolation of the Effects of Radiation and Turbulence-Chemistry Submodels*, *Combustion and Flame* **117** (1999), 4-31.
11. Benson, S. W., *Thermochemical Kinetics (2nd Edition)*, Wiley, New York, 1976.
12. Beretta, A., N. Mancini, F. Podenzani and L. Vigevano, *The influence of the temperature fluctuations variance on NO predictions for a gas flame*, *Combustion Science and Technology* **121** (1996), 193-216.
13. Bilger, R. W., "*Turbulent flows with nonpremixed reactants*", *Turbulent Reacting Flows*, Libby, P. A. and F. A. Williams (Editors), Springer-Verlag, Berlin, 1980, p. 65-113.
14. Bilger, R. W., *The structure of turbulent nonpremixed flames*, Twenty-Second Symposium (International) on Combustion, The Combustion Institute, 1988, p. 475-488.
15. Bilger, R. W., S. H. Starner and R. J. Kee, *On Reduced Mechanisms for Methane-Air Combustion in Nonpremixed Flames*, *Combustion and Flame* **80** (1990), 135-149.
16. Binninger, B., M. Chan, G. Paczkko and M. Hermann, *Numerical Simulation of Turbulent Partially Premixed Hydrogen Flames with the Flamelet Model*, Technical report, Advanced Combustion GmbH, Internal Report (1998).
17. Bird, R. B., W. E. Stewart and E. N. Lightfoot, *Transport phenomena (2nd Edition)*, Wiley, New York, 2002.
18. Bray, K. N. C. and N. Peters, "*Laminar flamelets in turbulent flames*", *Turbulent Reacting Flows*, Libby, P. A. and F. A. Williams (Editors), Academic Press, London, 1994, p. 78-84.
19. Brenan, K. E., S. L. Campbell and L. R. Petzold, *Numerical Solution of Initial-Value Problems in Differential-Algebraic Equation*, North-Holland, New York, 1989.
20. Brookes, S. J. and J. B. Moss, *Measurements of soot production and thermal radiation from confined turbulent jet diffusion flames of methane*, *Combustion and Flame* **116** (1999), 49-61.
21. Brookes, S. J. and J. B. Moss, *Predictions of soot and thermal radiation properties in confined turbulent jet diffusion flames*, *Combustion and Flame* **116** (1999), 486-503.
22. Brown, P. N., G. D. Byrne and A. C. Hindmarsh, *VODE: a variable-coefficient ODE solver*, *SIAM Journal on Scientific and Statistical Computing* **10** (1989), no. 5, 1038-1051.

23. Brown, P. N., A. C. Hindmarsh and L. R. Petzold, *A description of DASP6: A solver for large-scale differential-algebraic systems*, Lawrence Livermore National Laboratories, Report UCRL (1992).
24. Buzzi-Ferraris, G., *Numerical Libraries in C++*, Politecnico di Milano - Available at: <http://www.chem.polimi.it/homes/gbuzzi>.
25. Buzzi-Ferraris, G., *Building numerical libraries the object-oriented way*, Addison Wesley-Longman, New York, 1993.
26. Buzzi-Ferraris, G., *"Numerical Libraries in C++"*, Politecnico di Milano, 2007.
27. Buzzi-Ferraris, G. and D. Manca, *BzzOde - A variable coefficient ODE solver*, Computers and Chemical Engineering **22** (1988), 1595-1621.
28. Buzzi-Ferraris, G. and D. Manca, *BzzOde: a new C++ class for the solution of stiff and non-stiff ordinary differential equation systems*, Computers and Chemical Engineering **22** (1998), no. 11, 1595-1621.
29. Byrne, G. D. and A. M. Dean, *The numerical solution of some kinetics models with VODE and CHEMKIN II*, Computers and Chemistry **17** (1993), 297-302.
30. Choudhury, D., *Introduction to the Renormalization Group Method and Turbulence Modeling*, Fluent Inc. Technical Memorandum TM-107 (1993).
31. Cleary, M. J., *"CMC Modelling of Enclosure Fires"*, The School of Aerospace, Mechanical and Mechatronic Engineering, The University of Sydney, Sydney, 2004.
32. Cuoci, A., A. Frassoldati, G. Buzzi Ferraris, T. Faravelli and E. Ranzi, *The ignition, combustion and flame structure of carbon monoxide/hydrogen mixtures. Note 2: Fluid dynamics and kinetic aspects of syngas combustion*, International Journal of Hydrogen Energy **32** (2007), 3486-3500.
33. Cuoci, A., M. Mehl, G. Buzzi Ferraris, T. Faravelli, D. Manca and E. Ranzi, *Autoignition and burning rates of fuel droplets under microgravity*, Combustion and Flame **143** (2005), 211-226.
34. D'Anna, A. and J. H. Kent, *Modeling of particulate carbon and species formation in coflowing diffusion flames of ethylene*, Combustion and Flame **144** (2006), 249-260.
35. Dally, B. B., D. F. Fletcher and A. R. Masri, *Modelling of Turbulent Flames Stabilised on a Bluff-Body*, Combustion Theory and Modelling **2** (1998), 193.

36. Decroix, M. E. and W. L. Roberts, *Study of transient effects on the extinction limits of an unsteady counterflow diffusion flame*, Combustion Science and Technology **146** (1999), 57-84.
37. Decroix, M. E. and W. L. Roberts, *Transient flow field effects of soot volume fraction in diffusion flames*, Combustion Science and Technology **160** (2000), 165-189.
38. Desam, P. R., *"Subgrid scale model development and validation for thermal nitric oxide prediction in glass furnaces"*, Department of Mechanical Engineering, The University of Utah, Salt Lake City, 2006.
39. Dopazo, C., *"Recent developments in PDF methods"*, Turbulent reactive flows, Libby, P. A. and F. A. Williams (Editors), Academic Press, 1994, p. 375-474.
40. Drake, M. C., S. M. Correa, R. W. Pitz and M. Lapp, *Nitric oxide formation from thermal and fuel-bound nitrogen sources in a turbulent nonpremixed syngas flame*, Twentieth Symposium (International) on Combustion, The Combustion Institute, 1984, p. 1983-1990.
41. Egolfopoulos, F. N. and C. S. Campbell, *Unsteady counterflowing strained diffusion flames: diffusion-limited frequency response*, Journal of Fluid Mechanics **318** (1996), 1-29.
42. Falcitelli, M., S. Pasini, N. Rossi and L. Tognotti, *CFD + reactor network analysis: an integrated methodology for the modelling and optimisation of industrial systems for energy saving and pollution reduction*, Applied Thermal Engineering **22** (2002), no. 8, 971-979.
43. Falcitelli, M., S. Pasini and L. Tognotti, *An algorithm for extracting chemical reactor network models from CFD simulation of industrial combustion systems*, Combustion Science and Technology **174** (2002), 27-42.
44. Ferziger, J. H. and M. Peric, *Computational Methods for Fluid Dynamics*, Springer, Berlin, 2002.
45. FLUENT Inc., *FLUENT 6.3 User's Guide*, 2006.
46. Flury, M., *Experimentelle Analyse der Mischungsstruktur in turbulenten nicht vorgemischten Flammen*, Ph.D. Thesis - ETH Zurich, Switzerland, 1999.
47. Fox, R. O., *Computational models for turbulent reacting flows*, Cambridge University Press, Cambridge, 2003.
48. Frassoldati, A., T. Faravelli and E. Ranzi, *A wide range modeling study of formation and nitrogen chemistry in hydrogen combustion*, International Journal of Hydrogen Energy **31** (2006), no. 15, 2310-2328.

49. Frenklach, M., D. W. Clary, W. C. Gardiner and S. E. Stein, *Detailed kinetic modeling of soot formation in shock-tube pyrolysis acetylene*, Twentieth Symposium (International) on Combustion The Combustion Institute, 1984, p. 887-901.
50. Friedlander, S. K., *Smoke, dust and haze: fundamentals of aerosol behavior*, John Wiley & Sons, New York, 1977.
51. Fuchs, N. A., *Mechanics of Aerosols*, Pergamon, New York, USA, 1964.
52. Gear, C. W., *The automatic integration of ordinary differential equations*, Communications of the America Chemical Society **14** (1971), no. 3, 175-180.
53. Giordano, P. and D. Lentini, *Combustion-Radiation-Turbulence interaction modeling in absorbing-emitting nonpremixed flames*, Combustion Science and Technology **172** (2001), 1-22.
54. Gordon, R. G., *Error bounds in equilibrium statistical mechanics*, Journal of Mathematical Physics **9** (1968), 655-672.
55. Granata, S., F. Cambianica, S. Zinesi, T. Faravelli and E. Ranzi, *Detailed Kinetics of PAH and Soot Formation in Combustion Processes: Analogies and Similarities in Reaction Classes*, European Combustion Meeting (ECM), 2005, p.
56. Granata, S., T. Faravelli and E. Ranzi, *A wide range kinetic modeling study of pyrolysis and combustion of naphthenes*, Combustion and Flame **132** (2003), 533-544.
57. Granata, S., A. Frassoldati, T. Faravelli, E. Ranzi, S. Humer and K. Seshadri, *Polycyclic aromatic hydrocarbons and soot particle formation in liquid fuel combustion*, Chemical Engineering Transactions, AAAS AIDIC Milano (Italy), 2006, p. 275-280.
58. Gregory, P. S., M. G. David, M. Frenklach, N. Moriarty, B. Eiteneer, M. Goldenberg, C. T. Bowman, R. K. Hanson, S. Song, W. C. Gardiner and V. Vitali, *GRI-Mech 3.0*, http://www.me.berkeley.edu/gri_mech/.
59. Grosshandler, W. L., *RADCAL: A narrow-band model for radiation calculations in combustion environments*, NIST Technical note 1402 (1993).
60. Haworth, D. C., M. C. Drake, S. B. Pope and R. J. Blint, *The importance of time-dependent flame structures in stretched laminar flamelet models for turbulent jet diffusion flames*, Twenty-Second Symposium (International) on Combustion, The Combustion Institute, 1988, p. 589-597.

61. Hewson, J. C. and A. R. Kerstein, *Stochastic simulation of transport and chemical kinetics in turbulent CO/H₂/N₂ flames*, *Combustion Theory and Modelling* **5** (2001), 669-697.
62. Hildebrand, F. B., *Introduction to Numerical Analysis (2nd Edition)*, Dover Publications, 1987.
63. Hindmarsh, A. C., *GEAR: Ordinary Differential Equation System Solver*, Report UCID 30001, Rev. 3, Lawrence Livermore Laboratories, Livermore, CA (1974).
64. Hindmarsh, A. C., *LSODE and LSODI: two new initial value differential equation solvers*, *American Chemical Society SIGNUM Newsletters* **15** (1980), 10-11.
65. Hinze, J. O., *Turbulence*, McGraw-Hill Companies, 1975.
66. Hossain, M., J. C. Jones and W. Malalasekera, *Modelling of a bluff-body nonpremixed flame using a coupled radiation-flamelet combustion model*, *Flow, Turbulence and Combustion* **67** (2001), 217-234.
67. Im, H. G., C. K. Law and F. A. Williams, *Response of counterflow diffusion flame to oscillating strain rates*, *Combustion and Flame* **100** (1995), 21-30.
68. Jones, W. P. and B. E. Launder, *The prediction of laminarization with a 2-equation model of turbulence*, *International Journal of Heat and Mass Transfer* **15** (1972), 301.
69. Kee, R. J., J. A. Miller, H. E. Gregory and G. Dixon-Lewis, *A computational model of the structure and extinction of strained, opposed flow, premixed methane-air flames*, *Twenty-Second Symposium (International) on Combustion*, The Combustion Institute, 1988, p. 1479-1494.
70. Kee, R. J., F. Rupley and J. A. Miller, *Report SAND86-8215B - Sandia National Laboratories*, 1987.
71. Kee, R. J., F. Rupley and J. A. Miller, *The Chemkin Thermodynamic Data Base*, Sandia National Laboratories, Livermore (California, USA), 1989.
72. Kent, J. H. and D. Honnery, *Modelling soot turbulent jet flames using an extended flamelet technique*, *Combustion Science and Technology* **54** (1987), 383-397.
73. Kim, J. S. and F. A. Williams, *Extinction of Diffusion Flames with Non-Unity Lewis Number.*, *Engineering Mathematics* **31** (1997), 101-118.
74. Kleiveland, R. N., *"Modelling of soot formation and oxidation in turbulent diffusion flames"*, Department of Energy and Process Engineering, Norwegian University of Science and Technology, Trondheim (Norway), 2005.

75. Kollmann, W., I. M. Kennedy, M. M. and J. Y. Chen, "*Application of a soot model to a turbulent ethylene diffusion flame*", Soot Formation in Combustion - Mechanisms and Models, Springer-Verlag, 1994, p. 503-526.
76. Kronenburg, A., R. W. Bilger and J. H. Kent, *Modeling soot formation in turbulent methane/air jet diffusion flames*, Combustion and Flame **121** (2000), 24-40.
77. Launder, B. E., G. J. Reece and W. Rodi, *Progress in the development of a Reynolds-stress turbulence closure*, Journal of Fluid Mechanics **68** (1975), no. 3, 537-566.
78. Launder, B. E. and D. B. Spalding, *Lectures in Mathematical Models of Turbulence.*, Academic Press, London, England, 1972.
79. Lee, K. B., M. B. Thring and J. M. Beer, *On the rate of combustion of soot in a laminar soot flame*, Combustion and Flame **6** (1962), 137-145.
80. Lentini, D., *Assessment of the Stretched Laminar Flamelet Approach for nonpremixed turbulent combustion*, Combustion Science and Technology **100** (1994), 95-122.
81. Lindstedt, R. P. and S. A. Louloudi, *Joint-scalar transported PDF modeling of soot formation and oxidation*, Thirtieth Symposium (International) on Combustion, The Combustion Institute, 2005, p. 775-783.
82. Liu, F., H. Guo, G. J. Smallwood and O. Gulder, *Numerical modelling of soot formation and oxidation in laminar coflow non-smoking and smoking ethylene diffusion flames*, Combustion Theory and Modelling **7** (2003), 301-315.
83. Liu, F., H. Guo, G. J. Smallwood, O. Gulder and M. D. Matovic, *A robust and accurate algorithm of the Beta-PDF integration and its application to turbulent methane-air diffusion combustion in a gas turbine combustor simulator*, International Journal of Thermal Sciences **41** (2002), no. 8, 763-772.
84. Liu, F., K. A. Thomson, H. Guo and G. J. Smallwood, *Numerical and experimental study of an axisymmetric coflow laminar methane-air diffusion flame at pressures between 5 and 40 atmospheres*, Combustion and Flame **146** (2006), 456-471.
85. Ma, G., J. Z. Wen, M. F. Lightstone and K. A. Thomson, *Optimization of soot modeling in turbulent nonpremixed ethylene/air jet flames*, Combustion Science and Technology **177** (2005), 1567-1602.
86. Magnussen, B. F., *On the structure of turbulence and a generalized Eddy Dissipation Concept for chemical reactions in turbulent flows*, Nineteenth AIAA Aerospace Science Meeting, 1981

87. Magnussen, B. F., *Modeling of Pollutant formation in gas turbine combustor with special emphasis on soot formation and combustion*, Eighteenth International Congress on Combustion Engines, International Council on Combustion Engines, 1989
88. Magnussen, B. F. and B. H. Hiertager, *On mathematical modeling of turbulent combustion*, Sixteenth Symposium (International) on Combustion, The Combustion Institute, 1976, p. 719-727.
89. Manca, D. and G. Buzzi-Ferraris, *BzzMath: an Object Oriented Numerical Project*, Proceedings of ICheaP-7, 2005, p.
90. Manca, D., G. Buzzi-Ferraris, T. Faravelli and E. Ranzi, *Numerical problems in the solution of oxidation and combustion models*, Combustion Theory and Modelling **15** (2001), no. 5, 185-199.
91. Marchisio, D. L. and R. O. Fox, *Solution of population balance equations using the direct quadrature method of moments*, Aerosol Science **36** (2005), 43-73.
92. Marracino, B. and D. Lentini, *Radiation modelling in non-luminous nonpremixed turbulent flames*, Combustion Science and Technology **128** (1997), 23-48.
93. Mauss, F., D. Keller and N. Peters, *A lagrangian simulation of flamelet extinction and re-ignition in turbulent jet diffusion flames*, Twenty-Third Symposium (International) on Combustion, The Combustion Institute, 1990, p. 693-700.
94. McGraw, R., *Description of aerosol dynamics by the quadrature method of moments*, Aerosol Science and Technology **27** (1997), 255-265.
95. McGraw, R. and D. L. Wright, *Chemically resolved aerosol dynamics for internal mixtures by the quadrature method of moments*, Journal of Aerosol Science **34** (2003), 189-209.
96. Moss, J. B., C. D. Stewart and K. J. Young, *Modeling soot formation and burnout in a high temperature diffusion flame burning under oxygen-enriched conditions*, Combustion and Flame **101** (1995), 491-500.
97. Muller, C. M., H. Breitbach and N. Peters, *Partially premixed turbulent flame propagation in jet flames*, Twenty-Fifth Symposium (International) on Combustion, The Combustion Institute, 1994, p.
98. Novoselov, I. V., P. C. Malte, S. Yuan, R. Srinivasan and J. C. Y. Lee, *Chemical reactor network application to emissions prediction for industrial DLE Gas Turbine*, Proceedings of GT2006 ASME Turbo Expo 2006: Power for Land, Sea and Air, 2006

99. Peters, N., *Laminar diffusion flamelet models in non premixed combustion*, Progress Energy Combustion Science **10** (1984), 319-339.
100. Peters, N., *Laminar Flamelet concept in turbulent combustion*, Twenty-First Symposium (International) on Combustion, The Combustion Institute, 1986, p. 1231-1250.
101. Peters, N., *Turbulent Combustion*, Cambridge University Press, Cambridge, 2000.
102. Petzold, L. R., "A description of DASSL: a differential-algebraic system solver", Scientific Computing: Applications of mathematics and computing to the physical sciences, Stepleman, R. (Editor), New York, 1983.
103. Pitsch, H., H. Barths and N. Peters, *Three-dimensional modeling of NO_x and soot formation in DI-Diesel engines using detailed chemistry based on the interactive flamelet approach*, SAE Paper 962057, SAE (1996).
104. Pitsch, H., M. Chen and N. Peters, *Unsteady flamelet modeling of turbulent hydrogen-air diffusion flames*, Twenty-Seventh Symposium (International) on Combustion, The Combustion Institute, 1998, p. 1057-1064.
105. Pitsch, H. and N. Peters, *A consistent flamelet formulation for non-premixed combustion considering differential diffusion effects*, Combustion and Flame **114** (1998), 26-40.
106. Pitsch, H., E. Riesmeier and N. Peters, *Unsteady flamelet modeling of soot formation in turbulent diffusion flames*, Combustion Science and Technology **158** (2000), 389-406.
107. Poinso, T. and D. Veynante, *Theoretical and numerical combustion*, Edwards, Philadelphia, 2001.
108. Pope, S. B., *Pdf methods for turbulent reactive flows*, Progress Energy Combustion Science **11** (1985), 119-192.
109. Pope, S. B., *Turbulent Flows*, Cambridge University Press, Cambridge, 2000.
110. Ranzi, E., *A wide-range kinetic modeling study of oxidation and combustion of transportation fuels and surrogate mixtures*, Energy & Fuels **20** (2006), no. 3, 1024-1032.
111. Ranzi, E., M. Dente, G. Bozzano, A. Goldaniga and T. Faravelli, *Lumping procedures in detailed kinetic models of gasification, pyrolysis, partial oxidation and combustion of hydrocarbon mixtures*, Progress in Energy Combustion Science **27** (2001), 99-139.
112. Ranzi, E., T. Faravelli, A. Frassoldati and S. Granata, *Wide range kinetic modeling study of the pyrolysis, partial oxydation and combustion of heavy n-alkanes*, Industrial and Engineering Chemistry Research **44** (2005), 5170-5183.

113. Ranzi et al., "*CRECK Modeling: C1C30704 Kinetic Scheme*", Politecnico di Milano, 2007.
114. Richter, H., S. Granata, W. H. Green and J. B. Howard, *Detailed modeling of PAH and soot formation in a laminar premixed benzen/oxygen/argon low-pressure flame*, Thirtieth Symposium (International) on Combustion - The Combustion Institute, The Combustion Institute, 2005, p. 1397-1405.
115. Rodi, W., *Turbulence models and their applications in hydraulics - A state of the art review*, IAHR, Delft (The Netherlands), 1980.
116. Roditcheva, O. V. and X. S. Bai, *Pressure effect on soot formation in turbulent diffusion flames*, Chemosphere **42** (2001), 811-821.
117. Santoianni, D. A., M. E. Decroix and W. L. Roberts, *Temperature imaging in an unsteady propane-air counterflow diffusion flame subjected to low frequency oscillations*, Flow, Turbulence and Combustion **66** (2001), 23-36.
118. Sazhin, S. S., *An approximation for the absorption coefficient of soot in a radiating gas*, Fluent Europe (Internal Report) (1994).
119. Seshadri, K. and N. Peters, *Asymptotic structure and extinction of methane-air diffusion flames*, Combustion and Flame **73** (1988), 23-44.
120. Shaddix, C. R. and K. C. Smyth, *Laser-Induced incandescence measurements of soot production in steady and flickering methane, propane and ethylene diffusion flames*, Combustion and Flame **107** (1996), no. 4, 418-452.
121. Shampine, L. F., *Numerical solution of ordinary differential equations*, Stiff Computation, Aiken, R. C. (Editor), Oxford University Press, New York, 1985.
122. Shih, T. H., W. W. Liou, A. Shabbir, Z. Yang and J. Zhu, *A new κ - ϵ eddy-viscosity model for high Reynolds number turbulent flows. Model development and validation*, Computers and Fluids **24** (1995), no. 3, 227-238.
123. Sivathanu, Y. R. and G. M. Faeth, *Temperature / Soot Volume Fraction correlations in fuel-rich region of buoyant turbulent diffusion flames*, Combustion and Flame **81** (1990), 150-165.
124. Skjøth-Rasmussen, M. S., O. Holm-Christensen, M. Østberg, T. S. Christensen, T. Johannessen, A. Jensen and P. Glarborg, *Post-processing of detailed chemical kinetic mechanism onto CFD simulations*, Computers and Chemical Engineering **28** (2004), 2351-2361.

125. Spalding, D. B., *Mixing and chemical reaction in steady confined turbulent flames*, Thirteenth Symposium (International) on Combustion, The Combustion Institute, 1971, p. 649-657.
126. Sreenivasan, K. R., A. R. Antonia and H. Q. Dahn, *Temperature dissipation fluctuations in a turbulent boundary layer*, Physics of Fluids **20** (1977), 1238.
127. Stahl, G. and J. Warnatz, *Numerical investigation of time-dependent properties and extinction of strained methane- and propane-air flamelets*, Combustion and Flame **85** (1991), 285-299.
128. Steele, R. C., P. C. Malte, D. G. Nicol and J. C. Kramlich, *NO_x and N₂O in Lean-Premixed Jet-Stirred flames*, Combustion and Flame **100** (1995), 440-449.
129. Syed, K., C. D. Stewart and J. B. Moss, *Modelling soot formation and thermal radiation in buoyant turbulent diffusion flames*, Twenty-Third International Symposium on Combustion, The Combustion Institute, 1990, p. 1533-1541.
130. Tennekes, H. and J. L. Lumley, *A first course in turbulence*, The MIT Press, 1972.
131. Versteeg, H. K. and W. Malalasekera, *Computational fluid dynamics*, Addison Wesley Longman, 1995.
132. Von Karman, T., *Ober laminare und turbulente Reibung*, Zeitschrift fur angewandte Mathematik und Mechanik **1** (1921), no. 4, 233-252.
133. Warnatz, J., U. Maas and R. W. Dibble, *Combustion. Physical and Chemical Fundamentals, Modeling and Simulation, Experiments, Pollutant Formation*, Springer, Berlin, 1999.
134. Welle, E. J., W. L. Roberts, C. S. Campbell and J. M. Donbar, *The response of a propane-air counter-flow diffusion flame subjected to a transient flow field*, Combustion and Flame **135** (2003), 285-297.
135. Welle, E. J., W. L. Roberts, M. E. Decroix, C. S. Campbell and J. M. Donbar, *Simultaneous particle-imaging velocimetry and oh planar laser-induced fluorescence measurements in an unsteady counterflow propane/air diffusion flame*, Twenty-Eight Symposium (International) on Combustion, The Combustion Institute, 2000, p. 2021-2027.
136. Wen, J. Z., S. Yun, K. A. Thomson and M. F. Lightstone, *Modeling soot formation in turbulent kerosene/air jet diffusion flames*, Combustion and Flame **135** (2003), 323-340.

137. Westbrook, C. K. and F. C. Dryer, *Chemical kinetic modeling of hydrocarbon combustion*, Progress in Energy and Combustion Science **10** (1984), 1-57.
138. Wilcox, D. C., *Turbulence modeling for CFD - 2nd Edition*, DCW Industries, Inc., 2004.
139. Xiao, J., E. Austin and W. L. Roberts, *Relative polycyclic aromatic hydrocarbon concentrations in unsteady counterflow diffusion flames*, Combustion Science and Technology **177** (2005), 691-713.
140. Zhang, C., A. Atreya and K. Lee, *Sooting structure of methane counterflow diffusion flame with preheated reactants and dilution by products of combustion*, Twenty-Fourth Symposium (International) on Combustion, The Combustion Institute, 1992, p. 1049-1057.
141. Zucca, A., *"Modelling of turbulence-chemistry interaction and soot formation in turbulent flames"*, Department of Chemical Engineering, Politecnico di Torino, Torino (Italy), 2004.
142. Zucca, A., D. L. Marchisio, A. A. Barresi and R. O. Fox, *Implementation of the population balance equation in CFD codes for modelling soot formation in turbulent flames*, Chemical Engineering Science **61** (2006), 87-95.

Nomenclature

A	pre-exponential factor [kmol, m, s, K]
a	Planck mean absorption coefficient [m^{-1}]
A_{soot}	specific soot area [m^{-1}]
C_C	correction coefficient
C_k	molar concentration of species k [kmol m^{-3}]
C_p	specific heat [$\text{J kg}^{-1} \text{K}^{-1}$]
D	fuel nozzle diameter [m]
$\underline{\underline{D}}$	rate of strain (deformation) tensor [$\text{kg m}^{-1} \text{s}^{-2}$]
Da	Damköhler number
d_{nuclei}	maximum size of soot primary particles [m]
d_p	soot particle diameter [m]
d_{pp}	diameter of soot primary particles [m]
\hat{E}	specific total energy [$\text{m}^2 \text{s}^{-2}$]
E_j^{att}	activation energy of reaction j [J kmol^{-1}]
\hat{E}_K	specific kinetic energy [$\text{m}^2 \text{s}^{-2}$]

200 Nomenclature

\vec{f}	volume force [J m]
f_v	soot volume fraction
f_v^N	normalized soot volume fraction [-]
g	gravity [m s^{-2}]
\hat{H}_k	specific enthalpy of species k [$\text{m}^2 \text{s}^{-2}$]
$\hat{H}_{s,k}$	specific sensible enthalpy of species k [$\text{m}^2 \text{s}^{-2}$]
j_k	mass flux of species k [$\text{kg m}^{-2} \text{s}^{-1}$]
K_j	kinetic constant of reaction j [kmol, m, s, K]
Ka	Karlovitz number
Le_k	Lewis number of species k
L_j	local abscissas of node j [m]
l_K	Kolmogorov length scale [m]
m_0	soot particle number density [m^{-3}]
m_0^N	normalized soot particle number density
m_k	moment of order k
\dot{m}_{ox}	surface oxidation rate [$\text{kg m}^{-2} \text{s}^{-1}$]
M_p	molecular weight of primary soot particles [kg kmol^{-1}]
n	number density function
N_{AV}	Avogadro's number [kmol^{-1}]
N_C	number of cells
N_E	number of elements
N_F	number of faces
N_P	number of points
N_R	number of reactions

N_s	number of species
\hat{n}	unit vector
P	probability
p	pressure [$\text{kg m}^{-1} \text{s}^{-2}$]
\dot{Q}	volume energy source term [$\text{J m}^{-3} \text{s}^{-1}$]
q	energy flux [$\text{J m}^{-2} \text{s}^{-1}$]
\dot{Q}_R	heat release due to combustion [$\text{J m}^{-3} \text{s}^{-1}$]
\dot{Q}_{rad}	radiative heat transfer source term [$\text{J m}^{-3} \text{s}^{-1}$]
\dot{Q}_R^*	heat release due to combustion [$\text{J m}^{-3} \text{s}^{-1}$]
R	universal gas constant [$\text{J kmol}^{-1} \text{K}^{-1}$]
r	radial coordinate [m]
\dot{r}_j	reaction rate of reaction j [$\text{kmol m}^{-3} \text{s}^{-1}$]
S	surface [m^2]
Sc	Schmidt number
\dot{S}_{m0}	source term in transport equation for soot [$\text{m}^{-3} \text{s}^{-1}$]
\dot{S}_M	source term in transport equation for soot [$\text{kg m}^{-3} \text{s}^{-1}$]
T	temperature [K]
t	time [s]
t'	non dimensional time
T_K	kinetic temperature [K]
T'^2	variance of temperature [K^2]
u	velocity [m s^{-1}]
\hat{U}	specific internal energy [$\text{m}^2 \text{s}^{-2}$]
V	volume [m^3]
V_k	diffusion velocity of species k [m s^{-1}]

w_j	weight of node j [m^{-3}]
W_k	molecular weight of species k
x	space coordinate [m]
X_k	mole fraction of species k
Z	mixture fraction
Z'^2	variance of mixture fraction

Greek symbols

β	soot coagulation function [$\text{m}^3 \text{kg}^{-1/6} \text{s}^{-1}$]
γ	normalized heat loss
Γ	mixture fraction diffusivity [$\text{m}^2 \text{s}^{-1}$]
$\Gamma_{k,mix}$	mass diffusivity of species k into the mixture [$\text{kg m}^{-1} \text{s}^{-1}$]
Γ_t	turbulent viscosity [$\text{kg m}^{-1} \text{s}^{-1}$]
$\Delta \hat{H}_{f,k}^0$	specific formation enthalpy of species k [$\text{m}^2 \text{s}^{-2}$]
ε	dissipation rate of kinetic energy [$\text{m}^2 \text{s}^{-3}$]
κ	turbulent kinetic energy [$\text{m}^2 \text{s}^{-2}$]
λ	thermal conductivity [$\text{J m}^{-1} \text{K}^{-1} \text{s}^{-1}$]
μ	molecular viscosity [$\text{kg m}^{-1} \text{s}^{-1}$]
ν_{ij}	stoichiometric coefficient of species i in reaction j
ρ	density [kg m^{-3}]
σ	Stefan-Boltzmann constant [$\text{J m}^{-2} \text{s}^{-1} \text{K}^{-4}$]
$\underline{\underline{\sigma}}$	stress tensor [$\text{kg m}^{-1} \text{s}^{-2}$]
ξ_j	weighted abscissas of node j [m^{-2}]
$\underline{\underline{\tau}}$	viscous tensor [$\text{kg m}^{-1} \text{s}^{-2}$]

τ_C	chemical time [s]
τ_K	Kolmogorov time scale [s]
τ_{mix}	micromixing time scale [s]
τ_R	residence time [s]
ν	molecular viscosity [$\text{m}^2 \text{s}^{-1}$]
ϕ_H	enthalpy defect [J kg^{-1}]
ϕ_M	soot mass fraction
ϕ_N	number of soot particles per unit mass of gas [kmol kg^{-1}]
χ	scalar dissipation rate [s^{-1}]
ψ	generic scalar variable
$\dot{\Omega}_k$	mass formation rate of species k [$\text{kg m}^{-3} \text{s}^{-1}$]
ω_k	mass fraction of species k

Appendix A

Non adiabatic steady laminar flamelet library

The governing equations of steady laminar flamelets are reported and briefly discussed in the following. Some details about the numerical methods employed for their solution are given and the methodology adopted for the construction of the flamelet library is summarized.

Governing equations of steady flamelets

The steady laminar flamelet equations can be derived from the equations describing the counter flow diffusion flames, by adopting an appropriate transformation from the physical space to mixture fraction space (with Z as the independent variable). The mathematical procedure and the assumption needed for such transformation are described in [105] and [107] and are not here repeated. In the present thesis a simplified set of the mixture fraction space equations is solved, according to the suggestions reported in [103]. In the following the conservation equations of species and energy in the mixture fraction space are summarized:

$$\frac{1}{2}\rho\chi\frac{d^2\omega_k}{dZ^2} + \dot{\Omega}_k = 0 \quad k = 1, \dots, N_s \quad (\text{A.1})$$

$$\frac{1}{2}\rho\chi\frac{d^2T}{dZ^2} - \frac{1}{C_p} \sum_{k=1}^{NC} \hat{H}_k \dot{\Omega}_k + \frac{1}{2C_p} \rho\chi \left[\frac{d\hat{C}_p}{dZ} + \sum_{k=1}^{NS} \hat{C}_{p,k} \frac{d\omega_k}{dZ} \right] \frac{dT}{dZ} = 0 \quad (\text{A.2})$$

The boundary conditions for the fuel (F) and oxidizer (O) sides are:

$$\text{Oxidizer side } (Z = 0) \begin{cases} \omega_k = \omega_{k,O} \\ T = T_O \end{cases} \quad (\text{A.3})$$

$$\text{Fuel side } (Z = 1) \begin{cases} \omega_k = \omega_{k,F} \\ T = T_F \end{cases} \quad (\text{A.4})$$

In the Equations reported above, χ is the scalar dissipation rate, which must be modeled across the flamelet. In the present thesis, the following expression [73] is assumed, which is an extension of a simpler expression [99] to variable density flows :

$$\chi(Z) = \frac{a_s}{4\pi} \frac{3 \left(\sqrt{\frac{\rho_O}{\rho}} + 1 \right)^2}{2 \sqrt{\frac{\rho_O}{\rho}} + 1} \exp \left(-2 \left[\text{erfc}^{-1}(2Z) \right]^2 \right) \quad (\text{A.5})$$

where a_s is the characteristic strain rate, erfc^{-1} is the inverse complementary error function and ρ_O is the density of the oxidizer stream.

Extension to non adiabatic combustion

The extension to non adiabatic combustion requires the introduction of the enthalpy defect, which is defined as the difference between the actual enthalpy and the enthalpy for an adiabatic flame:

$$\phi_H = \hat{H} - \left[\hat{H}_O - Z(\hat{H}_F - \hat{H}_O) \right] \quad (\text{A.6})$$

where \hat{H}_O and \hat{H}_F denotes respectively the enthalpy of oxidizer and fuel streams. A set of laminar flamelets profiles, at different scalar dissipation rates, must be calculated at several fixed values of enthalpy defect. The profiles are organized in shelves, where each shelf contains entries referring to values of χ_{st} , ranging from equilibrium to extinction, plus the pure-mixing (or inert) state, and each shelf refers to a different value of enthalpy defect. Assuming the hypotheses of equal diffusivities, it is relatively easy to calculate the new flamelet profiles corresponding to the assigned enthalpy defect ϕ_H . If the same value of the enthalpy defect is enforced at both the fuel and oxidizer sides, the enthalpy defect is uniform across the whole flamelet.

Many commercial codes assume that flamelet species profiles are unaffected by heat defect, which means that for each enthalpy defect in the flamelet library the species profiles are assumed to be the same for the adiabatic flamelet; only the temperature profile is updated, using a simplified approach, which avoids to recalculate a new set of flamelets [16, 97]. The main disadvantage of this approach is that the effect of the heat losses on the species mass fractions is not taken into account. On the contrary, in this thesis for each enthalpy defect the flamelet profiles (both for temperature and mass fractions) are recalculated from scratch. This approach is very accurate, but requires the calculation of a very large number of laminar flamelet profiles. For example if ~10 enthalpy defects are considered and for each of them ~20 flamelet profiles are generated, the overall number of flamelets to be generated is ~200.

In Figure 98 the resulting organization of the library is reported.

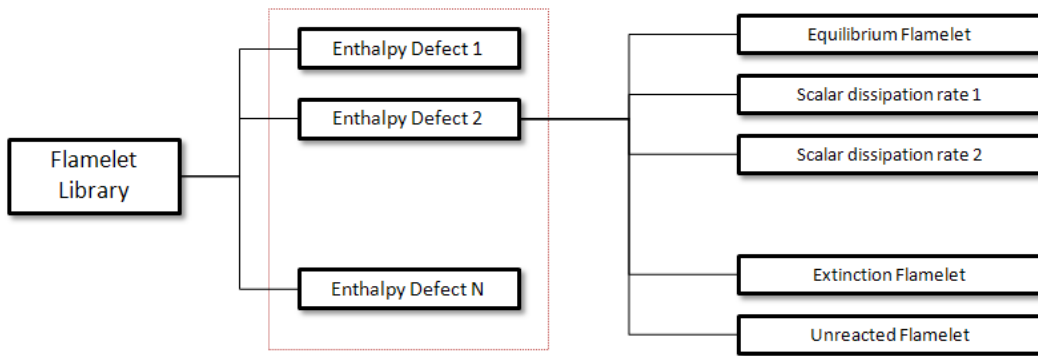


Figure 98. Non adiabatic flamelet library structure.

Transient solution method

The overall model consists of a differential system of the conservation equations with boundary conditions for the dependent variables. The numerical solution of the overall system corresponding to differential equations (A.1) and (A.2) requires particular attention. In the present thesis the equations (A.1) and (A.2) are solved in a transient form, which is obtained by adding the corresponding time derivatives, in order to obtain a parabolic system of partial differential equations, rather than an ordinary differential equation boundary value system. The transient equations are reported in the following and are solved for a time which is long enough to reach steady state conditions:

$$\rho \frac{\partial \omega_k}{\partial t} = \frac{1}{2} \rho \chi \frac{\partial^2 \omega_k}{\partial Z^2} + \dot{\Omega}_k \quad k = 1, \dots, N_s \quad (\text{A.7})$$

$$\rho \frac{\partial T}{\partial t} = \frac{1}{2} \rho \chi \frac{\partial^2 T}{\partial Z^2} - \frac{1}{\hat{C}_P} \sum_{k=1}^{NC} \hat{H}_k \dot{\Omega}_k + \frac{1}{2\hat{C}_P} \rho \chi \left[\frac{\partial \hat{C}_P}{\partial Z} + \sum_{k=1}^{NS} \hat{C}_{P,k} \frac{\partial \omega_k}{\partial Z} \right] \frac{\partial T}{\partial Z} \quad (\text{A.8})$$

Finite difference discretization

The equations reported above are discretized by means of a non uniform spatial grid, in order to obtain a system of ordinary differential equations. The adopted discretization uses conventional finite differencing techniques for non-uniform mesh spacing:

$$\frac{\partial \omega_{k,j}}{\partial t} = \frac{1}{2} \chi_j \frac{\frac{\omega_{k,j+1} - \omega_{k,j}}{x_{j+1} - x_j} - \frac{\omega_{k,j} - \omega_{k,j-1}}{x_j - x_{j-1}}}{\frac{1}{2}(x_{j+1} - x_{j-1})} + \frac{\dot{\Omega}_k}{\rho} \quad k = 1, \dots, N_S \quad (\text{A.9})$$

$$\frac{\partial T_j}{\partial t} = \frac{1}{2} \chi_j \frac{\frac{T_{j+1} - T_j}{x_{j+1} - x_j} - \frac{T_j - T_{j-1}}{x_j - x_{j-1}}}{\frac{1}{2}(x_{j+1} - x_{j-1})} - \frac{\sum_{k=1}^{NC} \hat{H}_{k,j} \dot{\Omega}_{k,j}}{\rho_j \hat{C}_{P,j}} + \frac{\chi_j}{2\hat{C}_{P,j}} \left[\frac{\partial \hat{C}_P}{\partial Z} \right]_j^{cen} + \sum_{k=1}^{NS} \hat{C}_{P,k} \left[\frac{\partial \omega_k}{\partial Z} \right]_j^{cen} \left[\frac{\partial T}{\partial Z} \right]_j^{cen} \quad (\text{A.10})$$

where the first derivative are discretized using the central differencing scheme:

$$\left. \frac{\partial \psi}{\partial x} \right|_j^{cen} = \psi_{j-1} \frac{x_{j+1} - x_j}{(x_j - x_{j-1})(x_{j+1} - x_{j-1})} + \psi_j \frac{x_{j-1} - 2x_j + x_{j+1}}{(x_{j+1} - x_j)(x_j - x_{j-1})} + \psi_{j+1} \frac{x_j - x_{j-1}}{(x_{j+1} - x_j)(x_{j+1} - x_{j-1})} \quad (\text{A.11})$$

Non adiabatic flamelet library construction

After flamelet generation, the flamelet profiles are convoluted with assumed-shape PDFs and then tabulated for look-up in the CFD code. The instantaneous value of any state quantity ψ inside a flamelet can be expressed as a function of the mixture fraction Z , the scalar dissipation rate χ and the enthalpy defect ϕ_H :

$$\psi = \psi(Z, \chi_{st}, \phi_H) \quad (\text{A.12})$$

The corresponding mean value can be obtained by introducing the joint-PDF $P(Z, \chi_{st}, \phi_H)$:

$$\bar{\psi} = \int_{-\infty}^{\infty} \int_0^{\infty} \int_0^1 \psi(Z, \chi_{st}, \phi_H) \cdot P(Z, \chi_{st}, \phi_H) \cdot dZ \cdot d\chi_{st} \cdot d\phi_H \quad (\text{A.13})$$

In presumed PDF approach, a shape for the joint-PDF $P(Z, \chi_{st}, \phi_H)$ is assigned on empirical basis. Many experimental and numerical evidences [14, 99], indicated that mixture fraction and scalar dissipation rate are statistically independent. According to the suggestions proposed by Bray and Peters [18], the joint-PDF can be split in the product of three PDF's of a single variable:

$$P(Z, \chi_{st}, \phi_H) = P(Z) \cdot P(\chi_{st}) \cdot P(\phi_H) \quad (\text{A.14})$$

According to Bilger [13], the result of integration with respect to the mixture fraction is relatively insensitive to the details of the PDF shape, if it is chosen on physical grounds. Usually a β -PDF or a clipped Gaussian PDF are adopted. The integration with respect to χ_{st} is not a problem, as all evidence unanimously indicates a log-normal distribution for the shape of the associated PDF. The enthalpy defect PDF is usually assumed to be a Dirac delta function centered on the local mean value of enthalpy defect ϕ_H [92].

The β -PDF

The β -PDF is the most used approach for modeling the mixture fraction PDF, which is described by the following function:

$$P(Z) = \frac{Z^{a-1} (1-Z)^{b-1}}{\int_0^1 Z^{a-1} (1-Z)^{b-1} dZ} = \frac{\beta(Z)}{\int_0^1 \beta(Z) dZ} \quad (\text{A.15})$$

where a and b are two non-negative parameters and are related to the mean \tilde{Z} and the variance \tilde{Z}^2 of the mixture fraction, calculated by the solver:

$$a = \tilde{Z} \left[\frac{\tilde{Z}(1-\tilde{Z})}{\tilde{Z}^2} - 1 \right] \quad (\text{A.16})$$

$$b = (1-\tilde{Z}) \left[\frac{\tilde{Z}(1-\tilde{Z})}{\tilde{Z}^2} - 1 \right] \quad (\text{A.17})$$

In general the distribution is asymmetric, but approaches a symmetric Gaussian shape when the ratios $\sqrt{\widetilde{Z}^2}/\widetilde{Z}$ and $\sqrt{\widetilde{Z}^2}/(1-\widetilde{Z})$ are small.

The Clipped-Gaussian PDF

The clipped Gaussian PDF is based upon the clipping of a Gaussian function so that the probability is finite only in the allowable region of mixture fraction. A clipped Gaussian PDF contains a Gaussian distribution $G(Z)$ for the turbulent region $0 < Z < 1$ and Dirac delta functions for the intermittent appearance of unmixed fluid at $Z=0$ and $Z=1$. In Favre form it is given by:

$$P(Z) = \alpha_1 \cdot \delta(Z) + (1 - \alpha_1 - \alpha_2) \frac{G(Z)}{I_G} + \alpha_2 \cdot \delta(1 - Z) \quad (\text{A.18})$$

where $\delta(Z - Z_0)$ is the Dirac delta function centered in $Z=Z_0$, whose integral is unity if $Z=Z_0$ and is zero otherwise; the variable I_G is defined as:

$$I_G = \int_0^1 G(Z) dZ \quad (\text{A.19})$$

the unknown free parameters α_1 , α_2 and variance g of the Gaussian distribution, which are function of the mean \widetilde{Z} and the variance \widetilde{Z}^2 of the mixture fraction, can be evaluated using the computationally inexpensive method suggested by Cleary [31]:

$$g = \min \left[\widetilde{Z}^2, \left(\frac{\widetilde{Z}}{2} \right)^2, \left(\frac{1 - \widetilde{Z}}{2} \right)^2 \right] \quad (\text{A.20})$$

$$G(Z) = \begin{cases} \frac{1}{\sqrt{2\pi g}} \exp\left(-\frac{(Z - \widetilde{Z})^2}{2g}\right) & \text{for } \frac{|Z - \widetilde{Z}|}{\sqrt{g}} \leq 2 \\ 0 & \text{for } \frac{|Z - \widetilde{Z}|}{\sqrt{g}} > 2 \end{cases} \quad (\text{A.21})$$

$$\alpha_1 = \left(1 - \frac{\tilde{Z}(1-\tilde{Z}) - \tilde{Z}^{\tilde{u}_2}}{\tilde{Z}(1-\tilde{Z}) - g} \right) (1-\tilde{Z}) \quad (\text{A.22})$$

$$\alpha_2 = \left(1 - \frac{\tilde{Z}(1-\tilde{Z}) - \tilde{Z}^{\tilde{u}_2}}{\tilde{Z}(1-\tilde{Z}) - g} \right) \tilde{Z} \quad (\text{A.23})$$

The log-normal distribution

The log-normal distribution is largely used for describing the PDF of scalar dissipation rate:

$$P(\chi_{st}) = \frac{1}{\sqrt{2\pi}} \frac{1}{\sigma\chi_{st}} \exp\left(-\frac{1}{2\sigma^2} \left(\ln \frac{\chi_{st}}{\tilde{\chi}_{st}} - \frac{\sigma^2}{2}\right)^2\right) \quad (\text{A.24})$$

where it is assumed that $\sigma = 2$ (according to the experimental results by Sreenivasan *et al.* [126]).

Numerical integration

The numerical integration with respect to the enthalpy defect ϕ_H is straightforward, because the associated PDF is simply a Dirac delta function:

$$\begin{aligned} \bar{\psi} &= \int_{-\infty}^{\infty} \int_0^{\infty} \int_0^1 \psi(Z, \chi_{st}, \phi_H) \cdot P(Z) P(\chi_{st}) \delta(\phi_H - \tilde{\phi}_H) \cdot dZ d\chi_{st} d\phi_H = \\ &= \int_0^{\infty} \int_0^1 \psi(Z, \chi_{st}, \tilde{\phi}_H) \cdot P(Z) P(\chi_{st}) \cdot dZ d\chi_{st} \end{aligned} \quad (\text{A.25})$$

On the contrary, the numerical integration with respect to the mixture fraction and the scalar dissipation requires attention and must be performed in an accurate and inexpensive way:

$$\bar{\psi} = \int_0^{\infty} \int_0^1 \psi(Z, \chi_{st}, \tilde{\phi}_H) \cdot P(Z) P(\chi_{st}) \cdot dZ d\chi_{st} = \int_0^{\infty} P(\chi_{st}) d\chi_{st} \int_0^1 \psi(Z, \chi_{st}, \tilde{\phi}_H) \cdot P(Z) \cdot dZ \quad (\text{A.26})$$

Integration with respect to Z. Let us focus the attention on the evaluation of the integral $\int_0^1 \psi(Z, \chi_{st}, \tilde{\phi}_H) \cdot P(Z) \cdot dZ$ with respect the mixture fraction. For the clipped Gaussian PDF the

numerical evaluation of such integral is relatively simple, due to the absence of singularities and can be obtained using the usual quadrature formulas [62]. However, while the formulation of the β -PDF looks simple compared to the clipped Gaussian, the need to numerically determine the integral reported above can be computationally expensive. The numerical integration of the β -PDF encounters difficulties due to the singularity problem at either the oxidizer side (O) or the fuel side (F), depending on the parameters a and b , and the overflow problem when the PDF parameters are sufficiently large:

$$\int_0^1 \psi(Z, \chi_{st}, \tilde{\phi}_H) \cdot P(Z) \cdot dZ = \frac{\int_0^1 \psi(Z, \chi_{st}, \tilde{\phi}_H) \cdot \beta(Z) \cdot dZ}{\int_0^1 \beta(Z) \cdot dZ} \quad (\text{A.27})$$

where $\beta(Z) = Z^{a-1} (1-Z)^{b-1}$. Liu *et al.* [83] suggested to evaluate the integrals at numerator and denominator by using the following approximate solution, which removes the singularities at the boundaries of the integration domain:

$$\begin{aligned} \int_0^1 \Upsilon(Z) \beta(Z) dZ &= \int_0^\varepsilon \Upsilon(Z) \beta(Z) dZ + \int_\varepsilon^{1-\varepsilon} \Upsilon(Z) \beta(Z) dZ + \int_{1-\varepsilon}^1 \Upsilon(Z) \beta(Z) dZ \cong \\ &\cong \Upsilon_{ox} \frac{\varepsilon^a}{a} + \int_\varepsilon^{1-\varepsilon} \Upsilon(Z) \beta(Z) dZ + \Upsilon_{fuel} \frac{\varepsilon^b}{b} \end{aligned} \quad (\text{A.28})$$

where ε is a small parameter (which is usually assumed to be 10^{-6}) and $\Upsilon(Z)$ is a generic function which corresponds to $\psi(Z, \chi_{st}, \tilde{\phi}_H)$ for the integral at numerator and to I for the integral at denominator. The integral $\int_\varepsilon^{1-\varepsilon} \Upsilon(Z) \beta(Z) dZ$ can be now numerically calculated using the conventional quadrature formulas [62].

Integration with respect to χ_{st} . The integration with respect to χ_{st} is simpler to perform. In this work the approach suggested by Marracino and Lentini [92] is adopted. From the (A.26), after the integration with respect to Z :

$$\bar{\psi} = \int_0^\infty P(\chi_{st}) d\chi_{st} \int_0^1 \psi(Z, \chi_{st}, \tilde{\phi}_H) \cdot P(Z) \cdot dZ = \int_0^\infty H(\chi_{st}, \tilde{Z}, \tilde{Z}''^2, \tilde{\phi}_H) P(\chi_{st}) d\chi_{st} \quad (\text{A.29})$$

The integration range in χ_{st} is split into L subranges $[\chi_{l-1/2}, \chi_{l+1/2}]$, with $l=1, 2, \dots, L$ and $\chi_{l-1/2} = 0$, such that χ_l can be considered a representative value for the corresponding interval. The integral is evaluated by the following approximation:

$$\begin{aligned} \int_0^\infty H(\chi_{st}, \tilde{Z}, \tilde{Z}^{n^2}, \tilde{\phi}_H) P(\chi_{st}) d\chi_{st} &= \sum_{l=1}^L \int_{\chi_{l-1/2}}^{\chi_{l+1/2}} H(\chi_{st}, \tilde{Z}, \tilde{Z}^{n^2}, \tilde{\phi}_H) P(\chi_{st}) d\chi_{st} \cong \\ &\cong \sum_{l=1}^L H(\chi_{st}, \tilde{Z}, \tilde{Z}^{n^2}, \tilde{\phi}_H) \int_{\chi_{l-1/2}}^{\chi_{l+1/2}} P(\chi_{st}) d\chi_{st} \end{aligned} \quad (\text{A.30})$$

The approximate evaluation of the integral reported above is not computationally expensive and is accurate even with a limited number of points in the χ_{st} -space, contrary to the large number needed in the Z -space. Now we need to evaluate the integrals:

$$\int_{\chi_{l-1/2}}^{\chi_{l+1/2}} P(\chi_{st}) d\chi_{st} = \int_{\chi_{l-1/2}}^{\chi_{l+1/2}} \frac{1}{\sqrt{2\pi}} \frac{1}{\sigma\chi_{st}} \exp\left(-\frac{1}{2\sigma^2} \left(\ln \frac{\chi_{st}}{\tilde{\chi}_{st}} - \frac{\sigma^2}{2}\right)^2\right) d\chi_{st} \quad (\text{A.31})$$

where $P(\chi_{st})$ is usually assumed to be a log-normal distribution, already reported in (A.24). By

introducing the running integration variable $\theta = \frac{1}{\sqrt{2}\sigma} \left(\ln \frac{\chi_{st}}{\tilde{\chi}_{st}} - \frac{\sigma^2}{2}\right)$, the integral (A.31) becomes:

$$\int_{\chi_{l-1/2}}^{\chi_{l+1/2}} \frac{1}{\sqrt{2\pi}} \frac{1}{\sigma\chi_{st}} \exp(-\theta^2) d\chi_{st} = \frac{1}{\sqrt{\pi}} \int_{\theta_{l-1/2}}^{\theta_{l+1/2}} \exp(-\theta^2) d\theta \quad (\text{A.32})$$

The integral reported above has an analytical solution, which is given by:

$$\frac{1}{\sqrt{\pi}} \int_{\theta_{l-1/2}}^{\theta_{l+1/2}} \exp(-\theta^2) d\theta = \frac{1}{2} [erf(\theta_{l+1/2}) - erf(\theta_{l-1/2})] \quad (\text{A.33})$$

where erf is the error function and:

$$\theta_{l\pm 1/2} = \frac{1}{\sqrt{2}\sigma} \left(\ln \frac{\chi_{l\pm 1/2}}{\tilde{\chi}_{st}} - \frac{\sigma^2}{2}\right) \quad (\text{A.34})$$

Appendix B

Unsteady counter flow diffusion flames: mathematical model

The numerical solution of the counter flow diffusion flames described in Chapter 6 is obtained by solving the unsteady conservation equations of mass, momentum, species and energy. In the following the governing differential and algebraic equations used in the present thesis are derived, summarized and briefly discussed.

Governing equations of counter flow diffusion flames

Since the counter flow diffusion flames investigated in the present work consist of two concentric, circular nozzles directed towards each other, the resulting geometry is axisymmetric. Therefore the conservation equations of mass, momentum, species and energy are more conveniently written in cylindrical coordinates, exploiting the symmetry about the axis.

Conservation equation of mass

The mass conservation equation, already introduced in Chapter 1, in cylindrical coordinates becomes:

$$\frac{\partial \rho}{\partial t} + \frac{\partial}{\partial x}(\rho u) + \frac{1}{r} \frac{\partial}{\partial r}(r \cdot \rho v) = 0 \quad (\text{B.1})$$

From the hypotheses that u and ρ depend on x only, it is possible to obtain:

$$\frac{1}{r} \frac{\partial}{\partial r}(r \cdot v) = 2 \cdot f(x) \quad (\text{B.2})$$

where $f(x)$ is a function of x only. The Equation (B.2) can be integrated in order to obtain the relation between the radial component of velocity v and the radial coordinate r :

$$v = f(x) \cdot r \quad (\text{B.3})$$

$$\frac{\partial v}{\partial r} = f(x) = \frac{v}{r} \quad (\text{B.4})$$

Substituting the (B.2) and the (B.4) in the continuity equation, we obtain:

$$\frac{\partial \rho}{\partial t} + \frac{\partial}{\partial x}(\rho u) + 2\rho \frac{v}{r} = 0 \quad (\text{B.5})$$

If we define for convenience the following two functions:

$$F(x) = \frac{\rho u}{2} \quad (\text{B.6})$$

$$G(x) = -\frac{\rho v}{r} \quad (\text{B.7})$$

the continuity equation can be expressed as:

$$\frac{\partial \rho}{\partial t} = 2 \left(G - \frac{\partial F}{\partial x} \right) \quad (\text{B.8})$$

Conservation equation of momentum

The equation of conservation of momentum, both in axial and in radial directions, can be derived from more general equations, reported in many textbooks [17].

In the axial direction, the equation governing the conservation of momentum is:

$$\rho \frac{Du}{Dt} = -\frac{\partial P}{\partial x} - \left(\frac{1}{r} \frac{\partial}{\partial r} (r \tau_{rx}) + \frac{\partial \tau_{xx}}{\partial x} \right) \quad (\text{B.9})$$

where the components of the stress tensor are defined according to the following expressions:

$$\tau_{rx} = -\mu \left(\frac{\partial u}{\partial r} + \frac{\partial v}{\partial x} \right) \quad (\text{B.10})$$

$$\tau_{xx} = -\mu \left(2 \frac{\partial u}{\partial x} - \frac{2}{3} \nabla \bar{u} \right) \quad (\text{B.11})$$

Substituting the expressions of τ_{rx} and τ_{xx} reported above, the following equation is obtained:

$$\rho u \frac{\partial u}{\partial x} = -\frac{\partial P}{\partial x} + \frac{1}{r} \frac{\partial}{\partial r} \left(r \mu \frac{\partial v}{\partial x} \right) + \frac{\partial}{\partial x} \left[\mu \left(2 \frac{\partial u}{\partial x} - \frac{2}{3} \nabla \bar{u} \right) \right] \quad (\text{B.12})$$

If the (B.4) and the (B.6) are used, after some rearrangements, we obtain:

$$\frac{\partial P}{\partial x} = -4F \frac{\partial}{\partial x} \left(\frac{F}{\rho} \right) + \frac{2\mu}{r} \frac{\partial v}{\partial x} + \frac{\partial}{\partial x} \left[\mu \left(\frac{4}{3} \frac{\partial u}{\partial x} - \frac{4}{3} \frac{v}{r} \right) \right] \quad (\text{B.13})$$

Substituting the (B.7) and the (B.8) in the equation reported above, the final version of the conservation equation for the axial component of moment follows:

$$\frac{\partial P}{\partial x} = -4F \frac{\partial}{\partial x} \left(\frac{F}{\rho} \right) - 2\mu \frac{\partial}{\partial x} \left(\frac{1}{\rho} \frac{\partial F}{\partial x} \right) + \frac{4}{3} \frac{\partial}{\partial x} \left[2\mu \frac{\partial}{\partial x} \left(\frac{F}{\rho} \right) + v \frac{\partial F}{\partial x} \right] \quad (\text{B.14})$$

The conservation equation of momentum in the radial direction is:

$$\rho \frac{Dv}{Dt} = -\frac{\partial P}{\partial r} - \left(\frac{1}{r} \frac{\partial}{\partial r} (r \tau_{rr}) - \frac{\tau_{\theta\theta}}{r} + \frac{\partial \tau_{rx}}{\partial x} \right) \quad (\text{B.15})$$

where the stress tensor components have the following expressions:

$$\tau_{rr} = -\mu \left(2 \frac{\partial v}{\partial r} - \frac{2}{3} \nabla \bar{u} \right) \quad (\text{B.16})$$

$$\tau_{\theta\theta} = -\mu \left(2 \frac{v}{r} - \frac{2}{3} \nabla \bar{u} \right) \quad (\text{B.17})$$

$$\tau_{rx} = -\mu \left(\frac{\partial u}{\partial r} + \frac{\partial v}{\partial x} \right) \quad (\text{B.18})$$

If we substitute the expressions reported above in the conservation equation of momentum:

$$\rho \left(u \frac{\partial v}{\partial x} + v \frac{\partial v}{\partial r} \right) = -\frac{\partial P}{\partial r} + \frac{1}{r} \frac{\partial}{\partial r} \left(r \mu \left(2 \frac{\partial v}{\partial r} - \frac{2}{3} \nabla \bar{u} \right) \right) - \frac{\mu}{r} \left(2 \frac{v}{r} - \frac{2}{3} \nabla \bar{u} \right) + \frac{\partial}{\partial x} \left(\mu \frac{\partial v}{\partial x} \right) \quad (\text{B.19})$$

After some rearrangements, the following equation is obtained:

$$\frac{1}{r} \frac{\partial P}{\partial r} = \frac{\partial}{\partial x} \left(\frac{2F}{\rho} \frac{\partial F}{\partial x} \right) - \frac{3}{\rho} \left(\frac{\partial F}{\partial x} \right)^2 - \frac{\partial}{\partial x} \left[\mu \frac{\partial}{\partial x} \left(\frac{1}{\rho} \frac{\partial F}{\partial x} \right) \right] \quad (\text{B.20})$$

From the conservation equations (B.14) and (B.20), it is evident that both $\frac{\partial P}{\partial x}$ and $\frac{1}{r} \frac{\partial P}{\partial r}$ depend on the coordinate x only:

$$\frac{\partial}{\partial x} \left(\frac{1}{r} \frac{\partial P}{\partial r} \right) = \frac{1}{r} \frac{\partial}{\partial r} \left(\frac{\partial P}{\partial x} \right) = 0 \quad (\text{B.21})$$

This means that the only possibility is:

$$\frac{1}{r} \frac{\partial P}{\partial r} = H = \text{const} \quad (\text{B.22})$$

where H is an eigenvalue of the resulting system (not to be confused with the enthalpy \hat{H}). As a consequence and after some rearrangements, the equation of conservation of momentum in the radial direction becomes:

$$\frac{\partial}{\partial x} \left[\mu \frac{\partial}{\partial x} \left(\frac{G}{\rho} \right) \right] - 2 \frac{\partial}{\partial x} \left(\frac{FG}{\rho} \right) + \frac{3}{\rho} G^2 + H = 0 \quad (\text{B.23})$$

Conservation equations of species

The conservation equations of species have the usual form, which was already introduced in Chapter 1:

$$\rho \left[\frac{\partial \omega_k}{\partial t} + u \frac{\partial \omega_k}{\partial x} \right] = - \frac{\partial}{\partial x} (\rho \omega_k V_k) + \dot{\Omega}_k \quad (\text{B.24})$$

If the definition of variable F is used, the conservation equations become:

$$\rho \left[\frac{\partial \omega_k}{\partial t} + \frac{2F}{\rho} \frac{\partial \omega_k}{\partial x} \right] = - \frac{\partial}{\partial x} (\rho \omega_k V_k) + \dot{\Omega}_k \quad (\text{B.25})$$

Conservation equation of energy

The conservation equation of energy can be obtained from the equation in the general form introduced in Chapter 1. Since the Mach number in counter flow diffusion flames is very small, we neglect the terms associated to the viscous dissipation and to the pressure. Moreover the kinetic and potential energy can be neglected. Under such assumptions, using the conservation equations for species (B.24), the energy equation becomes:

$$\rho \hat{C}_P \left[\frac{\partial T}{\partial t} + u \frac{\partial T}{\partial x} \right] = \frac{\partial}{\partial x} \left[\lambda \frac{\partial T}{\partial x} \right] - \rho \sum_{k=1}^{NC} \hat{C}_{P,k} \omega_k V_k \frac{\partial T}{\partial x} - \sum_{k=1}^{NC} \hat{H}_k \dot{\Omega}_k \quad (\text{B.26})$$

If the definition of variable F is used, the conservation equations become:

$$\rho \hat{C}_P \left[\frac{\partial T}{\partial t} + \frac{2F}{\rho} \frac{\partial T}{\partial x} \right] = \frac{\partial}{\partial x} \left[\lambda \frac{\partial T}{\partial x} \right] - \rho \sum_{k=1}^{NC} \hat{C}_{P,k} \omega_k V_k \frac{\partial T}{\partial x} - \sum_{k=1}^{NC} \hat{H}_k \dot{\Omega}_k \quad (\text{B.27})$$

Governing equations for counter flow diffusion flames

The overall model consists of system of differential and algebraic equations, corresponding to the conservation equations and the boundary conditions for the dependent variables (G, F, H, ω_k, T) . The equations are summarized in the following in a form which will be exploited for their numerical solution:

$$\frac{\partial \rho}{\partial t} = 2 \left(G - \frac{\partial F}{\partial x} \right) \quad (\text{B.28})$$

$$\frac{\partial G}{\partial t} = \frac{\partial}{\partial x} \left[\mu \frac{\partial}{\partial x} \left(\frac{G}{\rho} \right) \right] - 2 \frac{\partial}{\partial x} \left(\frac{FG}{\rho} \right) + \frac{3}{\rho} G^2 + H = 0 \quad (\text{B.29})$$

$$\frac{1}{r} \frac{\partial P}{\partial r} = H = \text{const} \quad (\text{B.30})$$

$$\frac{\partial \omega_k}{\partial t} = -\frac{2F}{\rho} \frac{\partial \omega_k}{\partial x} - \frac{1}{\rho} \left[\frac{\partial}{\partial x} (\rho \omega_k V_k) - \dot{\Omega}_k \right] \quad k = 1, \dots, NS \quad (\text{B.31})$$

$$\frac{\partial T}{\partial t} = -\frac{2F}{\rho} \frac{\partial T}{\partial x} + \frac{1}{\rho \hat{C}_p} \frac{\partial}{\partial x} \left[\lambda \frac{\partial T}{\partial x} \right] - \frac{1}{\hat{C}_p} \sum_{k=1}^{NC} \hat{C}_{p,k} \omega_k V_k \frac{\partial T}{\partial x} - \frac{1}{\rho \hat{C}_p} \sum_{k=1}^{NC} \hat{H}_k \dot{\Omega}_k \quad (\text{B.32})$$

Boundary conditions

The boundary conditions for the fuel (F) and oxidizer (O) streams at the nozzles are:

$$\text{Fuel side } (x = 0) \left\{ \begin{array}{l} F = \frac{\rho_F u_F}{2} \\ G = 0 \\ T = T_F \\ \rho u \omega_k + \rho \omega_k V_k = (\rho u \omega_k)_F \end{array} \right. \quad (\text{B.33})$$

$$\text{Air side } (x = L) \left\{ \begin{array}{l} F = \frac{\rho_O u_O}{2} \\ G = 0 \\ T = T_O \\ \rho u \omega_k + \rho \omega_k V_k = (\rho u \omega_k)_O \end{array} \right. \quad (\text{B.34})$$

The boundary conditions for each chemical species specifies the total mass flux (accounting for diffusion and convection), rather than the species fraction, as adopted in previous works [41]. If gradients exist at the boundary, these conditions allow diffusion into the nozzle and therefore they are able to warrant a more accurate description.

Finite difference discretization

The overall model consists of a differential system of the conservation equations with boundary and initial conditions for the dependent variables. The partial differential equations (B.28)-(B.32) are discretized by means of a non uniform spatial grid. Discretization of the differential equations uses conventional finite differencing techniques for non-uniform mesh spacing. Diffusive terms use central differences. For better convergence, convective terms use upwind differencing, based on the sign of the axial convective velocity:

$$\left. \frac{\partial \psi}{\partial x} \right|_j^{upw} = \begin{cases} \frac{\psi_j - \psi_{j-1}}{x_j - x_{j-1}} & \text{if } F_j > 0 \\ \frac{\psi_{j+1} - \psi_j}{x_{j+1} - x_j} & \text{if } F_j \leq 0 \end{cases} \quad (\text{B.35})$$

where the subscript j is used for indicating the j^{th} point of the grid and ψ is a generic variable. The convective terms can be also written using the central differencing scheme for improving the accuracy:

$$\left. \frac{\partial \psi}{\partial x} \right|_j^{cen} = \psi_{j-1} \frac{x_{j+1} - x_j}{(x_j - x_{j-1})(x_{j+1} - x_{j-1})} + \psi_j \frac{x_{j-1} - 2x_j + x_{j+1}}{(x_{j+1} - x_j)(x_j - x_{j-1})} + \psi_{j+1} \frac{x_j - x_{j-1}}{(x_{j+1} - x_j)(x_{j+1} - x_{j-1})} \quad (\text{B.36})$$

The continuity equation is used as an algebraic equation for evaluating the auxiliary variable F . The continuity equation can be discretized as:

$$\frac{\rho_j - \rho_j^{old}}{t - t^{old}} = 2 \left(\frac{G_j + G_{j-1}}{2} - \frac{F_j - F_{j-1}}{x_j - x_{j-1}} \right) \quad (\text{B.37})$$

where the superscript *old* refers to the value of each variable corresponding to the previous time step. The conservation of momentum in radial direction is written as a differential equation for the auxiliary variable G :

$$\frac{\partial G_j}{\partial t} = \frac{\mu_j \left(\frac{G_{j+1}}{\rho_{j+1}} - \frac{G_j}{\rho_j} \right) - \mu_{j-1} \left(\frac{G_j}{\rho_j} - \frac{G_{j-1}}{\rho_{j-1}} \right)}{\frac{1}{2}(x_{j+1} - x_{j-1})} - 2 \left. \frac{\partial}{\partial x} \left(\frac{FG}{\rho} \right) \right|_j^{upw} + 3 \frac{G_j^2}{\rho_j} + H_j = 0 \quad (\text{B.38})$$

The eigenvalue can be obtained solving the additional algebraic equation of conservation of perpendicular moment:

$$H_{j+1} - H_j = 0 \quad (\text{B.39})$$

The species and energy equations are treated as differential equations, from which the mass fractions and temperature can be obtained:

$$\frac{\partial \omega_{k,j}}{\partial t} = -2 \frac{F_j}{\rho_j} \frac{\partial \omega_k}{\partial x} \Big|_j^{upw} - \frac{1}{\rho_j} \left[\frac{\bar{\rho}_{j+1/j} (\omega_k V_k)_j - \bar{\rho}_{j/j-1} (\omega_k V_k)_{j-1}}{\frac{1}{2} (x_{j+1} - x_{j-1})} - \dot{\Omega}_{k,j} \right] \quad k = 1, \dots, NS \quad (\text{B.40})$$

$$\begin{aligned} \frac{\partial T_j}{\partial t} = & -\frac{2F_j}{\rho_j} \frac{\partial T}{\partial x} \Big|_j^{upw} + \frac{\lambda_j \frac{T_{j+1} - T_j}{x_{j+1} - x_j} - \lambda_{j-1} \frac{T_j - T_{j-1}}{x_j - x_{j-1}}}{\frac{1}{2} \rho_j \hat{C}_{P,j} (x_{j+1} - x_{j-1})} + \\ & - \frac{1}{\hat{C}_{P,j}} \sum_{k=1}^{NC} \left[\frac{1}{2} ((\omega_k V_k)_j + (\omega_k V_k)_{j-1}) \hat{C}_{P,k,j} \frac{\partial T}{\partial x} \Big|_j^{cen} \right] - \frac{1}{\rho_j \hat{C}_{P,j}} \sum_{k=1}^{NC} \hat{H}_{k,j} \dot{\Omega}_{k,j} \end{aligned} \quad (\text{B.41})$$

In the Equations (B.40) and (B.41) reported above, $\bar{\rho}_{j+1/j}$ is the mean density between the point $j+1$ and the point j :

$$\bar{\rho}_{j+1/j} = \frac{1}{2} (\rho_{j+1} + \rho_j) \quad (\text{B.42})$$

The product $(\omega_k V_k)_j$ between the mass fraction and the diffusion velocity is calculated as:

$$(\omega_k V_k)_j = -\Gamma_{k,j} \frac{W_k}{W_{gas}} \frac{X_{k,j+1} - X_{k,j}}{x_{j+1} - x_j} \quad (\text{B.43})$$

Appendix C

BzzDAE class

Before addressing differential-algebraic equations (DAE), it is worth spending some time on the numerical algorithms for the solution of ordinary differential equation (ODE) systems. As the ancestors of DAE packages, ODE solvers share several peculiarities and a common theoretical background with them. Starting from `DIFSUB` [52] and passing to `GEAR` [63], `LSODE` [64], `VODE` [22, 29] and `BzzOde` [27], the improvement in terms of the features and capabilities of ODE solvers has been continuous, mainly in terms of robustness and efficiency. As far as the DAE systems are concerned, besides the well-known `LSODI` routine [64], the most recent decades were characterized by the evolution of the `DASSL` routine [102] into `DASPK` [23] and by the introduction of `BzzDae` [90]. `BzzMathlibrary` [25, 26] comprises the afore mentioned `BzzOde` and `BzzDae` C++classes. `BzzMath` is freeware for non commercial use and can be downloaded directly at <http://www.chem.polimi.it/homes/gbuzzi>. While a more complete discussion is reported elsewhere [28, 33], a rather concise description of the main features of `BzzDae` solver is reported in the following.

`BzzDae` integrates DAE systems in the form

$$\begin{cases} \vec{y}' = \vec{f}_1(\vec{y}, t) \\ \vec{f}_2(\vec{y}, t) = \vec{0} \end{cases} \quad (\text{C.44})$$

On the robustness side, `BzzDae` is characterized by the following features:

1. According to Brenan *et al.* [19] and Brown *et al.* [23], `BzzDae` normalizes the algebraic portion of the Jacobian matrix through a simple a priori division by h . With reference to matrix $\underline{\underline{G}}$, the `BzzDae` formulation exploits the following structure:

$$\underline{\underline{G}} = \begin{bmatrix} \underline{\underline{I}} - hr_0 \frac{\partial \vec{f}_1}{\partial \vec{y}_1} & hr_0 \frac{\partial \vec{f}_1}{\partial \vec{y}_2} \\ \frac{\partial \vec{f}_2}{\partial \vec{y}_1} & \frac{\partial \vec{f}_2}{\partial \vec{y}_2} \end{bmatrix} \quad (\text{C.45})$$

where \vec{y}_1 and \vec{y}_2 are the differential and algebraic variables with h being the step size and r_0 the first coefficient of the BDF method [52]. This simple normalization significantly improves the robustness and precision of the solver.

2. If the model variables are physically bounded, the solver deals with constraints. `DASPK`, a common Fortran routine, allows the user to assign a non negative scalar constraint to the solution vector \vec{y} throughout the integration path. This option has been extended in `BzzDae`, where the user may simply assign maximum and/or minimum constraint vectors. The solver automatically handles the constraints, taking care not to violate the assigned bounds. The control is performed before passing any illegal values to the DAE system routine. The correction vector \vec{b} is accepted only when the non linear system, resulting from the DAE problem, is accurately solved to the assigned precision and when \vec{y} simultaneously complies with the constraints. As a result, the DAE function is always computed with safe \vec{y} values and math errors are avoided a priori.
3. As suggested by Brenan *et al.* [19] the order is reduced when the elements of the Nordsieck vector are not decreasing.
4. Both the order and the step size are reduced when there are convergence problems.
5. The integration order is automatically reduced to one and `BzzDae` restarts from the last successful convergence point when repeated convergence failures occur [28, 90].

The following features contribute to the efficiency of `BzzDae`:

1. Droplet combustion, similar to most of the DAE chemical problems, is characterized by a relevant number of equations and by the need to numerically evaluate the Jacobian matrix $\underline{\underline{J}}$. Therefore, function evaluations have the greatest impact on CPU time. The Jacobian evaluation becomes more and more exacting when the equation number increases. `BzzDae` uses a distinct memory allocation for the Jacobian matrix and its factorization $\underline{\underline{G}} = (\underline{\underline{I}} - hr_0 \underline{\underline{J}})$. A direct consequence is an overall improvement in efficiency since when either a different step size or a method order is chosen, there is no need to reevaluate the

Jacobian matrix and then superimpose its factorization, which is required by the non linear system solver based on the Newton method.

2. `BzzDae` uses the following criterion for updating the Jacobian matrix. It checks whether $\underline{\underline{J}}$ should be updated through the following equation:

$$\bar{y}'_{n+1} \cong \bar{y}'_n + \underline{\underline{J}} \cdot (\bar{y}_{n+1} - \bar{y}_n) + f_t(t_{n+1} - t_n) \quad (\text{C.46})$$

where , \bar{y}'_n , \bar{y}'_{n+1} , \bar{y}_n , \bar{y}_{n+1} are the variables at the n and $n+1$ iterations and f_t is the time derivative of the DAE system. With a large number of equations, the Jacobian numerical evaluation is rather time consuming, so it is advisable to delay the update of $\underline{\underline{J}}$ as far as possible. Conversely, if the system has few equations, it is convenient to evaluate $\underline{\underline{J}}$ more frequently in order to increase the efficiency of the Newton method. On this basis, `BzzDae` updates the Jacobian matrix with a proper frequency dependent on $\underline{\underline{J}}$ dimension.

3. DAE systems characterized by sparse and not necessarily structured Jacobian matrices can be easily solved by exploiting the automatic memory allocation and matrix rearrangement of the C++ classes. Namely, structured systems with a tridiagonal block structure are efficiently solved by `BzzDaeBlockTridiagonal`.

The afore mentioned features improve the overall performance of the `BzzDae` solver not only when dealing with constrained integration variables, but also under the following conditions: highly oscillating problems, that is, Jacobian matrix of the DAE system with complex λ eigenvalues having a negative real part and a large imaginary part ($Re(\lambda) < 0$ and $|Im(\lambda)| \gg 1$); DAE systems with large discontinuities in the derivatives, i.e., discontinuous or piecewise initial conditions or physical properties, IF . . . THEN structures, code branching.